

**FAT AND WATER SIGNALS
IN NUCLEAR MAGNETIC RESONANCE IMAGING**

by

Eleni Kaldoudi

**Dept. of Medical Physics and Bioengineering
University College London**

**Submitted for
The Degree of Doctor of Philosophy
University of London**

November 1993

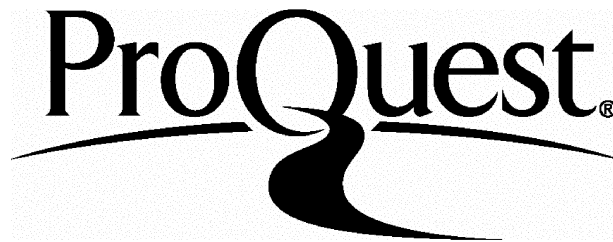
ProQuest Number: 10018509

All rights reserved

INFORMATION TO ALL USERS

The quality of this reproduction is dependent upon the quality of the copy submitted.

In the unlikely event that the author did not send a complete manuscript and there are missing pages, these will be noted. Also, if material had to be removed, a note will indicate the deletion.



ProQuest 10018509

Published by ProQuest LLC(2016). Copyright of the Dissertation is held by the Author.

All rights reserved.

This work is protected against unauthorized copying under Title 17, United States Code.
Microform Edition © ProQuest LLC.

ProQuest LLC
789 East Eisenhower Parkway
P.O. Box 1346
Ann Arbor, MI 48106-1346

ABSTRACT

This thesis is intended to explore fat and water differentiation in nuclear magnetic resonance imaging.

The need to create separate fat and water images is discussed and a critical review of current practices in the field is presented. These techniques include chemical shift imaging, coupled spin mapping and methods based on relaxation time differences. As an extension of this review, alternative slice cycling procedures are proposed that afford an improvement in the conventional chemical shift selective presaturation sequence. A new, hybrid fat or water suppression sequence is studied in detail, including a theoretical description of the role of the sequence parameters, as well as direct experimental comparison with its most closely related conventional fat and water differentiation techniques. The proposed scheme is shown to be robust in normal use and more tolerant than the conventional methods to mis-settings of experimental parameters. *In vivo* demonstration of the method is also performed.

Further work involves the generation of differential fat and water relaxation time maps. A critical review of current, conventional techniques that allow production of longitudinal relaxation calculated images is presented. Novel pulse sequence schemes for the measurement of fat and water longitudinal relaxation times are described, and the accuracy of these measurements is evaluated using phantoms. The results obtained are also being compared with conventional spectroscopic and imaging methods.

ACKNOWLEDGMENTS

I would like to acknowledge the State Scholarships Foundation (Hellas) and the British Council for their financial support, and the University of London Intercollegiate Research Service for use of their excellent NMR imaging facilities at Queen Mary and Westfield College.

The assistance and fellowship of all members of the "greater" NMR group at QMW is greatly appreciated. In particular, I am extremely grateful to Dr. Keith Sales for his warm welcome to the department of chemistry and his lectures; for being so willing to answer all my questions in quantum mechanics. I would also like to thank Drs. Mark A. Horsfield, Tim J. Norwood, Ivan Tkač, Steve R. Williams, and Rick Spink for many useful discussions.

I am extremely grateful to my supervisors for their patience, for their example of scientific rigour, and for giving me the freedom to develop this project as I wished. In particular, I would like to thank Paul S. Tofts for his expert guidance, help and encouragement; Gareth J. Barker, for he showed me the elegance of the NMR phenomenon, shared his deep and wide knowledge about computing, talked me out of my claustrophobia (albeit momentarily) and into ...a whole body MRI scanner, for being there whenever I needed a friend; most of all, I would like to thank Steve C. R. Williams for providing everything, from his expert guidance and a deep friendship to the every day advice and continuous encouragement, the equipment to work, funding to attend meetings, numerous ideas, and priceless support.

I dedicate this thesis to my parents for teaching me common sense and getting me this far with their undemanding support and unconditional love.

Μαμά, Μπαμπά, ευχαριστώ.

CONTENTS

LIST OF FIGURES	7
LIST OF TABLES	10
1. INTRODUCTION	12
2. PRINCIPLES OF NUCLEAR MAGNETIC RESONANCE	14
2.1 Nuclear spin and the Static Magnetic Field	14
2.2 Nuclear Magnetic Resonance	18
2.3 Relaxation and Relaxation Times	22
2.4 Chemical Shift and Scalar Coupling	24
2.5 From Quantum Mechanics ... to the lab!	25
2.6 FID and Quadrature Detection	26
2.7 Signal Sampling and Fourier Transform	28
2.8 Echo Formation and Sampling	33
2.9 Magnetic Field Gradients and the k-Space Formalism	40
2.10 Scanning k-Space and Fourier Imaging Methods	45
2.11 Noise	52
3. FAT AND WATER DIFFERENTIATION IN MRI	54
3.1 Introduction	54
3.2 Reasons for Fat and Water Differentiation in MRI	56
3.2.1 Physiological Implications of Water & Fat Distributions	56
3.2.2 Dynamic Range Problems	58
3.2.3 Chemical Shift Artifacts	60
3.3 MRI Techniques for Fat and Water Differentiation	64
3.3.1 Methods Based on Relaxation Time Differences	64
3.3.2 Chemical Shift Imaging	66
3.3.3 Coupled Spin Imaging	77
3.3.4 Methods Based on Other Physical Parameters	78
3.4 Discussion	78
4. "SLICE CYCLING" TECHNIQUES FOR THE CHEMICAL SHIFT SELECTIVE PRESATURATION SEQUENCE	83
4.1 Introduction	83
4.2 Theoretical Analysis	86

4.3	Experimental Methods	97
4.4	Results and Discussion	99
4.5	Conclusions	105
5.	A CHEMICAL SHIFT SELECTIVE INVERSION RECOVERY (CSS-IR) SEQUENCE FOR FAT AND WATER DIFFERENTIATION IN MRI ..	107
5.1	Introduction	107
5.2	Theory	108
5.3	Experimental Methods	120
5.3.1	Fat Suppression	122
5.3.2	Water Suppression	124
5.3.3	<i>In Vivo</i> Studies	127
5.4	Results and Discussion	128
5.4.1	Fat Suppression	128
5.4.2	Water Suppression	135
5.4.3	<i>In Vivo</i> Studies	142
5.5	Conclusions	145
6.	LONGITUDINAL RELAXATION TIME MEASUREMENTS IN MRI	147
6.1	Introduction	147
6.2	Reasons for Relaxation Time Measurements in MRI	149
6.3	T ₁ Measurements in MRI	151
6.3.1	Progressive Saturation and Saturation Recovery	151
6.3.2	Inversion Recovery	152
6.3.3	Two-Point Measurements and Hybrid Schemes	156
6.3.4	Variable Tip Angles	158
6.3.5	Single-Shot Techniques	159
6.4	General Considerations	163
6.5	Discussion	166
7.	METHODS FOR DIFFERENTIAL FAT AND WATER LONGITUDINAL RELAXATION TIME MEASUREMENTS IN MRI	168
7.1	Introduction	168
7.2	The Sequences	169
7.3	Experiments and Results	175
7.3.1	Spectroscopic T ₁ Measurements	176
7.3.2	Conventional T ₁ Maps	176

7.3.3 Fat and Water T1 Maps	183
7.4 Discussion	187
SUMMARY	193
PUBLICATIONS ARISING FROM THIS WORK	195
APPENDICES	196
Appendix 1 Phase Cycling	197
Appendix 2 Longitudinal Magnetization after a Train of β° Pulses	202
Appendix 3 Statistical Analysis	206
REFERENCES	209

Fig. 4.8.	The effect of the proposed 4-step slice cycling procedure for $T_1=500$ ms	96
Fig. 4.9.	Oil-suppressed phantom images acquired using conventional PRESAT methods and the proposed slice cycling procedures	100
Fig. 4.10.	Water-suppressed phantom images acquired using conventional PRESAT methods and the proposed slice cycling procedures	101
Fig. 4.11.	Oil signal intensity plotted against the slice number for the oil-suppressed conventional PRESAT methods and proposed schemes	102
Fig. 4.12.	Water signal intensity plotted against the slice number for the water-suppressed conventional PRESAT methods and proposed schemes	103
Fig. 4.13.	Water-suppressed phantom images and the result of the masking procedure	104
Fig. 5.1.	CSS-IR pulse sequence diagram	109
Fig. 5.2.	Longitudinal magnetization in a train of inverting pulses as it approaches a steady state	111
Fig. 5.3.	Steady state magnetization as a function of pulse repetition time	111
Fig. 5.4.	Null point as a function of pulse repetition time	113
Fig. 5.5.	Null point for the CSS-IR sequence as a function of the number of slices	113
Fig. 5.6.	Maximum number of slices for the IR and CSS-IR experiment	114
Fig. 5.7.	Inversion time as a function of T_1 for the IR and CSS-IR sequences	115
Fig. 5.8.	Longitudinal magnetization just before excitation as a function of the assumed T_1 for the IR and CSS-IR experiments	117
Fig. 5.9.	Longitudinal magnetization just before excitation as a function of the tip angle of the chemical shift selective pulse for the PRESAT and CSS-IR experiments	118
Fig. 5.10.	Minimum number of pulse repetitions to reach steady state as a function of the number of slices	119
Fig. 5.11.	Pulse sequence diagrams for all techniques used	121
Fig. 5.12.	Representation of the phantom used for water suppression experiments	125
Fig. 5.13.	Oil suppressed phantom images	129
Fig. 5.14.	Oil signal plotted against the T_1 value used to calculate inversion time	131
Fig. 5.15.	Oil signal plotted against the tip angle of the chemical shift selective pulse	133
Fig. 5.16.	Water signal plotted against the bandwidth of the chemical shift selective pulse	134
Fig. 5.17.	Water suppressed phantom images	136
Fig. 5.18.	Water signal plotted against the T_1 value used to calculate inversion time	138
Fig. 5.19.	Oil signal plotted against the bandwidth of the chemical shift selective pulse	140
Fig. 5.20.	Signal intensity plotted against the T_1 value used to calculate inversion time	141
Fig. 5.21.	Fat suppressed images of the abdominal region of a live normal rat	143
Fig. 5.22.	Water suppressed images of the abdominal region of a live normal rat	144

Fig. 6.1.	Schematic representation of partial volume effects	148
Fig. 6.2.	Magnitude representation and contrast reversal in IR experiments	154
Fig. 6.3.	Calculated T1 map of the head of a preserved shark species	157
Fig. 6.4.	Recovery of longitudinal magnetization in a multiple read-out sequence	162
Fig. 7.1.	Single slice chemical shift selective, PS-IR imaging sequence (slice selection during refocusing)	170
Fig. 7.2.	Single slice chemical shift selective, PS-IR imaging sequence (slice selection during excitation)	170
Fig. 7.3.	Double spin echo, chemical shift selective, PS-IR imaging sequence	172
Fig. 7.4.	Chemical shift dependent slice selection	174
Fig. 7.5.	Conventional single slice PS-IR image derived T1 values plotted against the corresponding spectroscopic T1 values	181
Fig. 7.6.	Phantom images and T1 maps using conventional multiple slice PS-IR and a single slice version (slice selection during refocusing)	182
Fig. 7.7.	Phantom images using conventional multiple slice PS and the two single slice versions (slice selection during refocusing or excitation)	184
Fig. 7.8.	Phantom images using single slice conventional PS, with slice selection during refocusing and spoiler gradients	185
Fig. 7.9.	Differential fat and water phantom T1 maps using the proposed single slice methods	188
Fig. 7.10.	Differential fat and water phantom T1 maps using the proposed double spin echo methods	190
Fig. A.1.	Removing dc-offset by a 2-step phase cycling procedure	199
Fig. A.2.	Removing quadrature errors by a 2-step phase cycling procedure	200

LIST OF TABLES

Table 3.1. Conventional MRI techniques for fat and water differentiation	80
Table 4.1. Slice selection order for the proposed 4-step slice cycling procedure.....	92
Table 5.1. Oil and water signal corresponding to the images of Fig. 5.13	130
Table 5.2. Oil and water signal corresponding to the images of Fig. 5.17	137
Table 7.1. Spectroscopic T1 measurements of the phantom compartments	177
Table 7.2. T1 values as measured by conventional multi-slice PS-IR imaging	179
Table 7.3. T1 values as measured by conventional single slice PS-IR imaging	180
Table 7.4. T1 values as measured by conventional single slice PS-IR imaging	186
Table 7.5. T1 values as measured by the proposed single slice PS-IR methods	189
Table 7.6. T1 values as measured by the proposed double spin echo PS-IR methods	191
Table A.1. Phase cycling procedure used in the imaging sequences presented in this study	198

CHAPTER 1

INTRODUCTION

The first nuclear magnetic resonance (NMR) experiments were carried out in 1945 by Bloch, Hansen and Packard [1.1] at Stanford, and Purcell, Torrey and Pound [1.2] at Harvard. The "elegance" of the phenomenon and its potential for a wide variety of applications were immediately perceived and the dawn of the field that would soon encompass scientists from nearly all disciplines was marked by the award of the 1952 Nobel Prize in Physics to Bloch and Purcell for their fundamental research. The understanding of relaxation processes [1.3–1.5], the discovery of spin-spin coupling [1.6], chemical shift [1.7, 1.8] and spin echoes [1.9] soon followed. Together with a number of more recent innovations, such as the introduction of Fourier transforms [1.10] and two-dimensional spectroscopy [1.11], these advances have rendered NMR a versatile tool for studying the chemistry and structure of both solids and liquids. The importance of the technique was recently underlined by the award of the 1991 Nobel Prize in Chemistry to Ernst, for "his contributions to the development of high resolution NMR spectroscopy" [1.12].

The major biochemical and medical interest has, however, arisen from the possibility of making non-invasive measurements in-vivo. These studies have progressed along two parallel and perhaps complimentary paths, namely localized spectroscopy and imaging. Whilst localized spectroscopy methods can provide chemical and metabolic information at a single defined location, imaging techniques measure the total intensity of the nuclear magnetization as a function of position. Since its invention in 1973 [1.13, 1.14], magnetic resonance imaging (MRI) has rapidly developed to become one of the major forces in medical imaging due to a plethora of reasons, in particular the fact that the image contrast depends on a number of factors. These include parameters specific to the phenomenon (such as relaxation times, chemical shift and spin coupling) as well as macroscopic motion and temperature. Imaging pulse sequence schemes are continuously being devised to manipulate one or more of these parameters resulting in a wide variety of both medical and non-medical applications. MRI has primarily been used to gain structural information and recent advances in hardware have allowed microscopic resolution of around 2 μm for specially favoured samples [1.15]. Apart from information on structure and chemical composition, MRI provides the basis for a wide range of dynamical studies, expanding from perfusion and diffusion measurements [1.9] to velocity mapping and angiograms [1.16]. Metabolical and

functional information for various parts of biological systems has also been achieved through manipulation of relaxation time differences and susceptibility effects. Probably the most spectacular recent advance is the application of MRI to neurofunctional imaging [1.17].

Although NMR imaging of various nuclei has been reported in several medical and biological studies, e.g. [1.18], attention is primarily focused on the hydrogen nucleus, not only because of its high inherent sensitivity but also because of its abundance in biological systems. Although the human body contains protons in numerous different chemical environments, unless special line-narrowing techniques are used, the only spins that contribute to an NMR image are those that are undergoing rapid motion, that is water protons and protons of mobile lipids.

The aim of this work was to study fat and water signals in proton nuclear magnetic resonance imaging. An introduction to the principles of the NMR phenomenon is presented in Chapter 2, where the intention is to refresh the reader's knowledge of the basic concepts involved in a NMR imaging experiment. Attention is then drawn to fat and water protons, their different NMR responses, the reasons that demand their differentiation and the conventional ways to achieve it. The critical discussion presented in Chapter 3 aims to provide an overview of the different categories of MRI techniques that differentiate between fat and water, and has also formed the basis of two recent publications [1.19, 1.20]. Following this review of current practice in the field, Chapter 4 involves studies for the improvement of a commonly used conventional technique for fat or water signal suppression, also introducing the new concept of "slice cycling". Subsequently, a new, robust, hybrid sequence for fat and water differentiation is proposed and extensively studied both in theory and experiment (Chapter 5). Parts of this work have also appeared in press [1.21-1.23]. The two final chapters can be regarded as a separate section, where the concept of differential fat and water relaxation time maps is introduced. Chapter 6 is devoted to a background critical review of the conventional methods for longitudinal time measurements in MRI and it has also formed the basis for a recent publication [1.24]. The final chapter presents initial work on original methods for generating differential fat and water longitudinal relaxation time maps, also addressing related technical considerations. This part of work is currently in progress, intending to encompass differential transverse and rotating frame relaxation time mapping of fat and water protons. This thesis has been written, intentionally, in a style that mimics typical texts within the field of MRI where, at the risk of some minor reiteration, each chapter contains the aims, introduction, theoretical analysis and experimental results, discussion and references relating to that specific body of work.

CHAPTER 2

PRINCIPLES OF NUCLEAR MAGNETIC RESONANCE

The nuclear magnetic resonance phenomenon is based on the spin property of nucleons and their interaction with external magnetic fields. The sample for an NMR experiment is an ensemble of nuclei that exhibit non-zero spin. This sample is placed in an external static magnetic field of typical strength values in the range of 0.1 to 14 Tesla. Magnetic resonance is induced by coherent electromagnetic waves (for example in the frequency range of 4-600 MHz for the field strengths above and when the hydrogen nucleus is considered), transmitted perpendicular to the external magnetic field by means of a transmitter coil. The same coil can, in turn, act as a receiver, where a resonant electromotive force is induced. This is the NMR signal, which, on detection, can be processed to yield a spectrum or an image.

As a phenomenon at the sub-atomic level, nuclear magnetic resonance can be described thoroughly only in terms of quantum mechanical theory. A classical model of the phenomenon is, however, adequate to describe efficiently most of the simple experiments, and is extensively used in conventional NMR imaging.

In this chapter only an outline of the principles of NMR and MRI is presented, and the analysis is confined to the proton, the hydrogen nucleus. Detailed aspects of the subject and other related fields are well covered in specialized texts on quantum mechanics [2.1, 2.2], the principles of NMR phenomenon [2.3–2.8], NMR imaging [2.9, 2.10] and instrumentation [2.11], as well as signal processing and image reconstruction [2.12–2.14] and general mathematics [2.15, 2.16].

2.1 NUCLEAR SPIN AND THE STATIC MAGNETIC FIELD

In quantum mechanics, elementary particles are assigned an inherent property of "spin", which is an additional degree of freedom and does not correspond very closely to anything in classical mechanics [2.1, 2.2, 2.17]. This spin property gives rise to the spin angular momentum \mathbf{J} , which should be pictured as due to some internal motion of the particle. As with the orbital angular momentum in quantum mechanics, \mathbf{J} is quantized and the discrete values of its magnitude are given in terms of the spin quantum number I :

$$J = \hbar \sqrt{I(I+1)} \quad (2.1)$$

The constant \hbar is equal to $h/2\pi$, where h is Planck's constant. Individual elementary particles such as nucleons have a spin quantum number of $1/2$. The coupling of the spin (and orbital) angular momenta of the protons and neutrons comprising a nucleus, however, gives rise to a total nuclear spin angular momentum. Its magnitude is again expressed by Eqn. (2.1), but the spin quantum number can now take several different values: half-integer for nuclei with odd mass number, integer for nuclei with even mass number but odd atomic number and zero when both mass and atomic numbers are even.

In order to describe fully the vector quantity \mathbf{J} , its orientation must also be determined. This is accomplished by information about the projection of \mathbf{J} along a given direction, which is conventionally taken to be the z axis. The magnitude of the projection J_z is also quantized and is described in terms of a second quantum number, m_s :

$$J_z = \hbar m_s \quad (2.2)$$

The spin quantum number, m_s , is limited to the $(2I+1)$ values $\{-I, -I+1, \dots, I-1, I\}$. From the physical point of view, this limitation is explained if one considers the requirement that the projection of a vector must always be less or equal to its magnitude. The fact that the maximum absolute value, $\hbar I$, for the projection is always less than the magnitude of the spin angular momentum vector, is a result of the Uncertainty Principle. In the case of the angular momentum vector, this states that at the limit in which any one of the three components J_x , J_y , and J_z of the vector is completely determined, the other two are completely undetermined. Therefore, the spin angular momentum can never be "seen" parallel to any of the three axes.

Associated with the spin angular momentum is the intrinsic magnetic moment $\bar{\mu}$, which is proportional to \mathbf{J} :

$$\bar{\mu} = \gamma \mathbf{J} \quad (2.3)$$

The constant of proportionality γ , known as the gyromagnetic ratio, has a unique value for each different isotope, expressing basically the charge-to-mass ratio of the nucleus.

As \mathbf{J} is quantized, μ will also be:

$$\mu = \gamma \hbar \sqrt{I(I+1)} \quad (2.4)$$

and

$$\mu_z = \gamma \hbar m_s \quad (2.5)$$

For nuclei of spin $1/2$, such as the proton, their spin quantum number m_s can take two possible values, $-1/2$ or $+1/2$. Therefore, their magnetic moment vector can have only two possible orientations with respect to the z -axis, as shown in Fig. 2.1.

If an external static magnetic field of strength B_0 is applied along z , the nuclear magnetic moment will interact with it. The energy of interaction is given by the quantum mechanical Zeeman Hamiltonian operator, and effectively can be regarded as the scalar product of the nuclear magnetic moment and the external magnetic field vectors:

$$E = -\vec{\mu} \cdot \vec{B}_0 = -\mu_z B_0 = -\gamma \hbar m_s B_0 \quad (2.6)$$

Equation (2.6) indicates a splitting of the energy state giving rise to $(2I+1)$ different levels, each corresponding to a particular value of the spin quantum number m_s . Restricting this analysis to protons, there are only two different energy levels, namely:

$$E_{1/2} = -\frac{1}{2} \gamma \hbar B_0 \quad (2.7)$$

and

$$E_{-1/2} = +\frac{1}{2} \gamma \hbar B_0 \quad (2.8)$$

The energy difference ΔE between these states (equal to $\hbar \gamma B_0$ and usually referred to as the Zeeman energy splitting) is directly proportional to the external magnetic field. A diagrammatic representation of the energy splitting and its relation to B_0 is given in Fig. 2.2.

Any individual proton can be in either energy state, but statistical theory favours the lower energy. As a consequence, if a large ensemble of protons (n) is considered, there will be a slight excess population (Δn) in the lower energy level, that is, with magnetic moments aligned in the same direction as the applied static magnetic field. This population follows a Boltzmann distribution [2.7, 2.9]:

$$\frac{\Delta n}{n} = \frac{1 - \exp(-\gamma \hbar B_0 / kT)}{1 + \exp(-\gamma \hbar B_0 / kT)} \approx \frac{\gamma \hbar B_0}{2 k T} \quad (2.9)$$

where k is Boltzmann's constant, and T is known as the "spin temperature", which at thermal equilibrium is equal to the absolute temperature of the macroscopic sample. The final approximation in Eqn. (2.9) holds under the assumption that $\gamma \hbar B_0 \ll kT$, which is true for the conventional NMR experiment. Although in standard experimental conditions this excess turns out to be of the order of only 1 in every 10^6 nuclei, it

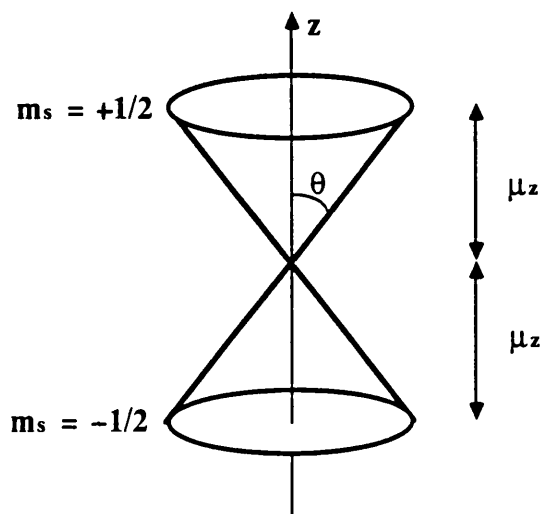


Figure 2.1. Nuclear magnetic moment vector for a nucleus of spin $1/2$, for example the proton. Two possible orientations are allowed, parallel or anti-parallel with respect to z axis, at an angle θ , where $\cos\theta = \sqrt{3}/3$. The direction in the xy plane cannot be specified, therefore there is equal probability to find the magnetic moment vector anywhere on the surface of the two cones.

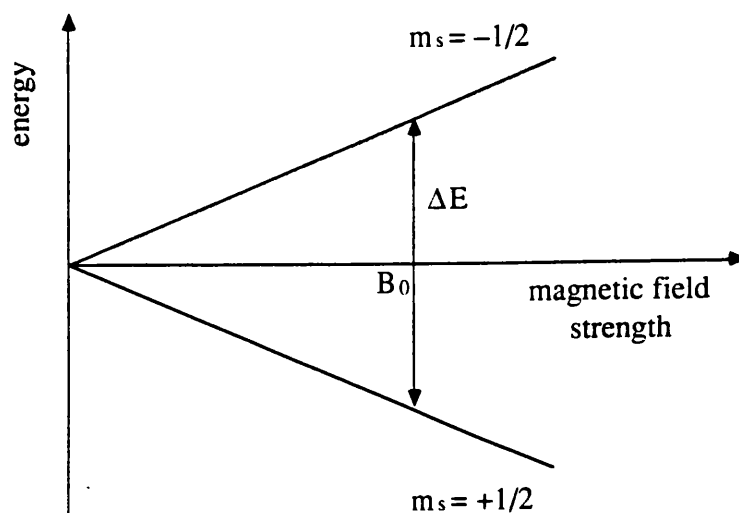


Figure 2.2. The nuclear spin energy for a single nucleus of spin $1/2$, plotted as a function of the strength of the external static magnetic field. The splitting between the two energy levels is directly proportional to the strength of the magnetic field.

nevertheless results in a macroscopic net magnetization M_0 along the direction of the external field. Using Eqn. (2.5), this is given by:

$$M_0 = \Delta n |\mu_z| = \frac{n \gamma^2 \hbar^2 B_0}{4kT} \quad (2.10)$$

This model of two different energy states is adequate to describe the fate of the projection of the nuclear magnetic moment along the direction of the static magnetic field and the generation of a net macroscopic magnetization along the static field. However, it does not give any information about the transverse components of the nuclear magnetic moments. Quantum mechanical theory shows [2.6, 2.8] that although the exact values of the x and y components of the nuclear magnetic moment of an individual spin cannot be determined accurately at any point in time, the expectation value of the projection of the moment on the xy plane appears to move with an angular frequency, ω_0 , termed the Larmor frequency:

$$\omega_0 = -\gamma B_0 \quad (2.11)$$

The direction of precession turns out to be clockwise, with respect to the z-axis, for spins with $\gamma > 0$, and anti-clockwise for spins with $\gamma < 0$. This precessional motion implies that, were a coil placed around an axis on the xy plane, an individual spin would theoretically induce an electromotive force at the Larmor frequency. However, different spins in the sample are characterized by different wavefunctions, and as a result they exhibit a different "phase" for the precession of the expectation value of the magnetic moment projection on the xy plane. Statistical averaging over all spins indicates a total absence of coherence, therefore no net signal is detected.

2.2 NUCLEAR MAGNETIC RESONANCE

Consider a time varying field of strength B_1 applied along a direction perpendicular to the static magnetic field, for example along the x-axis. Assume a resonance condition where the frequency of the field B_1 equals the precession frequency, ω_0 , of the projection of the expectation value of the nuclear magnetic moment on the transverse plane. For the typical values of static magnetic fields used in NMR experiments, this frequency is in the radiofrequency range, thus the electromagnetic field is conventionally referred to as a radiofrequency (RF) pulse. It can be shown that for the RF wavelengths and the transmitter coils used, in the close proximity to the spin ensemble only the magnetic component of the wave need be considered [2.3, 2.18].

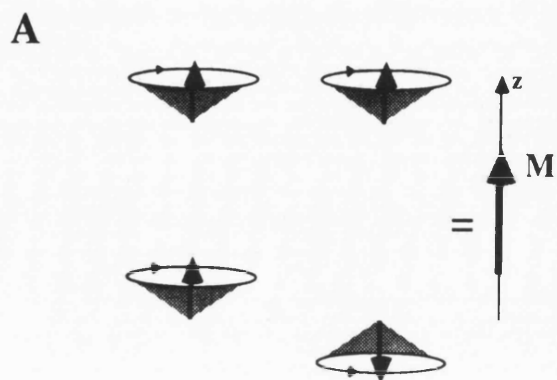
Observing the system from a reference frame ($x'y'z$) that rotates clockwise about the z axis at the same resonance frequency, ω_0 , and just before the RF field is applied, the nuclear magnetic moment is viewed as static, at a fixed but random orientation with respect to the $x'y'$ rotating plane and at fixed orientation with respect to the z axis. In this rotating frame, therefore, the nuclear spin can be regarded as if it is not experiencing an external magnetic field (since it is not moving). Application of an RF pulse of frequency ω_0 along the x -axis of the laboratory frame produces effectively a static magnetic field B_1 along the x' axis of the rotating frame. The nuclear spins experiencing the apparently static magnetic field B_1 will behave exactly as described above. That is, the magnetic moment will be quantized along the axis of field application, its possible different orientations along the x' axis given by Eqn. (2.5). Eventually, the thermal equilibrium distribution will be achieved, giving a net magnetization component along the x' axis, as described by Eqn. (2.10) where the field B_1 has to be considered instead of B_0 . In practice, the strength of the RF field is orders of magnitude less than the static magnetic field, therefore this net magnetization component along x' can be considered negligible. Additionally, the duration of the pulse is usually assumed too short to allow thermal equilibrium in B_1 to be established.

Each individual magnetic moment will precess about the x' axis and on the $y'z$ plane at a resonance frequency ω_1 given by an expression similar to Eqn. (2.11). However, as at the starting point of pulse application there is a measurable projection of the magnetic moment along the z axis, the precessional motion of all spins during the pulse is coherent. The result is that there is a net magnetization component on the $y'z$ plane, precessing with angular frequency ω_1 . The angle of precession is given by:

$$\theta = \omega_1 T_p = \gamma B_1 T_p \quad (2.12)$$

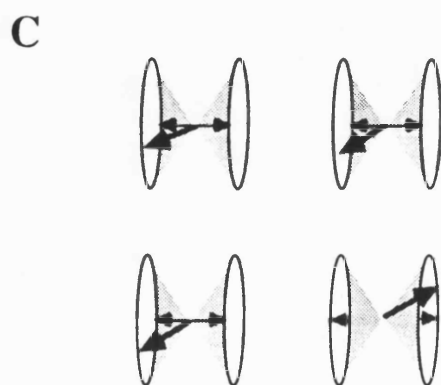
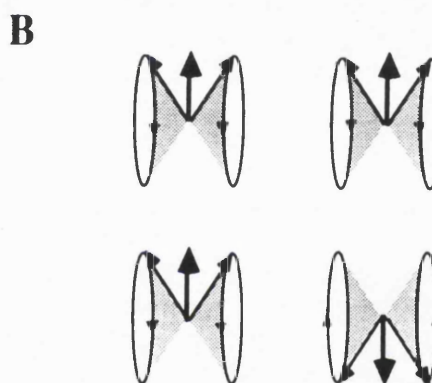
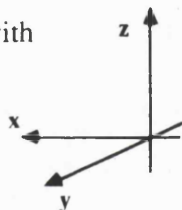
where T_p is the duration of the pulse.

A 90° RF pulse, for example, is of sufficient strength and precise duration (according to Eqn. (2.12)) to allow 90° precession of the magnetic moment projection on the $y'z$ plane, which results in a measurable magnetic moment projection along y' and a net magnetization component along y' . At the end of the pulse, and viewing the system from the laboratory frame, the nuclear magnetic moments return to their previous state, coupled only with the static magnetic field of strength B_0 . Once again, the equilibrium magnetization along the z axis starts to reform, while for each individual spin the projection of the expectation value of the magnetic moment on the xy plane is precessing at the Larmor frequency ω_0 . However, this precessional motion is now coherent, thus creating a net magnetization component on the xy plane, which induces an electromotive force (EMF) in a coil placed around an axis on the same plane. This



Initially the 4 spins are in thermal equilibrium distribution, with an excess of population with magnetic moments parallel to the static field. The shaded cones indicate the possible positions of the magnetic moment vector.

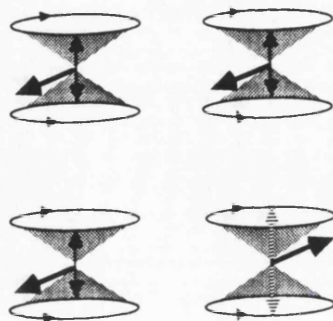
A RF pulse applied along x at the Larmor frequency quantizes the magnetic moments along x' . The moments start precessing about x' on the shaded cones. Because of their previous quantization, each magnetic moment has equal probability of being at either one of the two positions indicated with the two vectors.



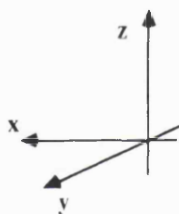
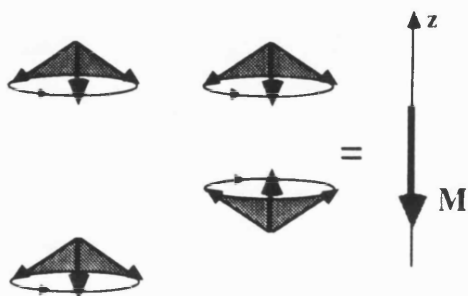
The precession of the magnetic moments during the pulse application is, therefore, coherent. Thermal equilibrium has not yet been established, therefore there is no excess of population in either of the two orientations.

Figure 2.3. Simplified pictorial representation of the effect of a RF pulse on an ensemble of nuclear magnetic moments in a static magnetic field along z .

continued ...

D

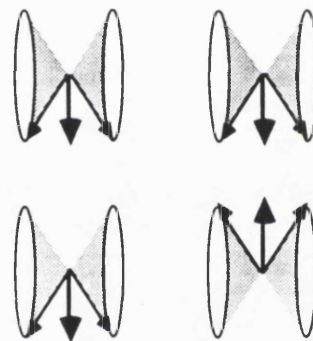
The RF field is left on till the moments precess through an angle of 180° .

**F**

... continued

Figure 2.3. Simplified pictorial representation of the effect of a RF pulse on an ensemble of nuclear magnetic moments in a static magnetic field along z.

When the magnetic moments have precessed through 90° , the RF field is switched off. Because of the previous quantization, the moment has equal probability of being at either one of the two positions indicated by the vectors, and the precession in the static field along z is coherent, creating a net x'y' component. Thermal equilibrium has not yet been established.

E

When the RF is switched off, the moments start precessing about z. The precession is coherent, but equal probabilities exist to find them at 180° opposite to each other. Statistical averaging results in zero transverse magnetization. Because of the previous quantization, the initial excess population has been temporarily inverted.

EMF, an oscillating voltage at the Larmor frequency, forms the detected NMR signal. A pictorial representation of the effect of a 90° and a 180° RF pulse on a proton ensemble is given in Fig. 2.3. It should be noted that this is only a simplified description, the full mathematical treatment can be expressed only in terms of quantum statistical mechanics, e.g. References [2.3–2.6].

2.3 RELAXATION AND RELAXATION TIMES

Whenever the energy state of a spin system is changed, for example by changing the overall static magnetic field or after application of a RF pulse, several processes occur to bring the spins back to equilibrium with their environment. These relaxation mechanisms have their origin in the time dependent magnetic or electric fields at the nucleus, which arise primarily from the random thermal motion present in the sample. Detailed descriptions of the relaxation mechanisms and their mathematical treatment in terms of quantum mechanical statistics have been given elsewhere [2.3, 2.7, 2.19]. Two major kinds of relaxation are usually distinguished in the NMR experiment, namely longitudinal and transverse relaxation.

Longitudinal or spin-lattice relaxation refers to the processes by which the spin system achieves the thermal equilibrium population distribution, the interaction between magnetic dipoles being one of the predominant mechanisms. Longitudinal relaxation is responsible for the finite time required for the generation of the excess of spin population in the lower energy state when a spin ensemble is placed in a static magnetic field, or when the strength of this field is changed. Similarly, whenever the population distribution in the energy states is disturbed by means of a RF pulse, longitudinal relaxation re-establishes the thermal equilibrium condition. In any case, the final result is the generation of a net magnetization component along the axis of the applied field, whose maximum value at thermal equilibrium is M_0 , as given by Eqn. (2.10). For a large number of systems of practical interest, spin-lattice relaxation is generally a first-order process. The magnetization recovery towards its equilibrium value M_0 is exponential and is characterised by a time constant T_1 :

$$\frac{dM_z}{dt} = -\frac{M_z - M_0}{T_1} \quad (2.13)$$

T_1 relaxation time can, thus, be considered as the lifetime of the spin system in the excited energy state and is inversely proportional to the decay rate of longitudinal magnetization.

Transverse relaxation refers to the loss of the spin coherence created by a pulse and originates in various processes, one of them being the return of spins in their

original thermal equilibrium distribution (i.e. longitudinal relaxation) [2.20]. However, even if transitions between the energy states do not occur, the spin coherence is gradually lost due to energy interactions amongst the spins. Most of these spin-spin relaxation mechanisms are of the same nature as those of longitudinal relaxation, with dipole-dipole interaction again predominant. However, there are some additional contributions to spin-spin relaxation, and the most important of these is due to chemical or physical transfer of excited nuclear spins from one chemically distinguishable environment to another, where they continue to precess with a new random phase. The end result of transverse relaxation is the decay of the net transverse relaxation component, and for that reason the decay of the NMR signal. In proton NMR of biological systems, transverse relaxation is generally a complex function of time and can be resolved into two or more exponential components. With some approximation, however, it can be considered as a first-order process and an average time constant T_2 is then ascribed to the decay of the transverse magnetization, M_{xy} :

$$\frac{dM_{xy}}{dt} = -\frac{M_{xy}}{T_2} \quad (2.14)$$

T_2 relaxation time can, thus, be considered as the lifetime of the net xy magnetization component or, in other words, of the observed NMR signal. As accuracy is inversely proportional to the time allowed for a measurement (Uncertainty Principle), NMR signal measurements will have an inherent uncertainty because of the finite T_2 relaxation time. In practice, any static field inhomogeneity (due, for example, to non-uniform static magnetic field or susceptibility effects within different regions of the sample) gives rise to a spread of precession frequencies for a given nucleus and therefore a loss in phase coherence. The result is an additional decay of the transverse magnetization with an overall effective transverse relaxation time $T_2^* < T_2$.

T_1 and T_2 relaxation times reflect the structure and dynamics of molecules [2.9]. In biological systems, relaxation times generally increase proportionally to the amount of free water present in the tissue. Additionally, any increase in paramagnetic centre concentration, enhances relaxation as their unpaired electron greatly favours dipole-dipole interactions. As a consequence, differences in water content (or mobility) and changes of paramagnetic concentrations are some of the major sources of contrast, and thus information, in biological proton NMR imaging.

2.4 CHEMICAL SHIFT AND SCALAR COUPLING

The discussion so far has assumed that the presence of the sample does not modify the applied static magnetic field. However, this is not strictly true, and any individual nuclear spin experiences a static magnetic field slightly altered by interactions with the surrounding electronic cloud, as well as other neighbouring nuclear spins. The result is that the precession frequency of the nuclear moment is slightly altered, the difference between the apparent resonance frequency and the one calculated through Eqn. (2.11) being a characteristic fingerprint of the chemical environment of the nucleus.

The atomic and molecular electrons that surround the nucleus exhibit a total magnetic moment (due to both spin and orbital angular momentum) which interacts with the external magnetic field in a similar way to the nuclear spin magnetic moment [2.21]. The result is that the electrons are forced to circulate around the nucleus about the direction of the static magnetic field at their characteristic Larmor frequency, given by an expression similar to Eqn. (2.11). This circulating motion of electric charges induces a secondary magnetic field at the site of the nucleus, which depends upon the number and distribution of the moving electrons. Therefore, nuclei at chemically distinct sites, which have different electronic distributions, experience slightly different effective magnetic fields, and thus resonate at slightly different frequencies. The secondary magnetic field created by the moving electrons is also directly proportional to the angular frequency of the electron motion, that is, directly proportional to the external static magnetic field. Therefore, the overall effective field, B_{eff} , experienced by the spin can be expressed as:

$$B_{eff} = (1-\sigma) B_0 \quad (2.15)$$

where σ is the shielding constant. In general, σ is a tensor quantity because of the anisotropy in the molecular shielding, but in the case of liquids only the isotropic part is left unaveraged by the rapid thermal molecular motion, so σ reduces to a scalar value. The frequency difference between two groups of nuclei that experience different chemical environments is known as the chemical shift. To overcome the static field dependency, the chemical shift is usually quoted as a relative difference in frequency from some reference compound and is expressed as a dimensionless number, δ , in parts per million (ppm):

$$\delta = \frac{\omega - \omega_{ref}}{\omega_{ref}} \times 10^6 \quad (2.16)$$

where ω and ω_{ref} are the resonance frequencies of the nucleus in the chemical environment of interest and in a reference compound respectively. For proton NMR, tetramethylsilane (TMS) is usually the reference compound and the chemical shift of water protons, for example, relative to that is 4.8 ppm.

Intramolecular nuclear spins are also involved in another effect known as scalar or J coupling. This indirect interaction between adjacent nuclear spins arises via the shared electrons in covalent chemical bonds. The nuclear spin magnetic moment induces a slight electron polarization which is then transmitted to the neighbouring nuclei via electron delocalization. The magnitude of the nuclear magnetic moment is independent of the strength of the external magnetic field, however it takes various orientations according to Eqn. (2.5). According to the relative orientations of the two spins involved in the interaction, the local magnetic field at the site of the spin of interest is slightly altered, either reduced or enhanced. The spin ensemble will, therefore, exhibit as many frequencies as the different orientations of the coupled nucleus. The separation of the frequencies is given by the coupling constant J, which is characteristic of the two coupled spins. It can be shown that J coupling is not observable when the two spins involved are chemically equivalent, that is, they have the same chemical shift and the same J coupling constants with the neighbouring nuclei [2.5].

2.5 FROM QUANTUM MECHANICS ... to the lab !

The simplified and qualitative description of the nuclear magnetic resonance phenomenon that has been presented so far is rigorously treated in terms of the density matrix formalism of quantum statistical mechanics [2.3–2.6, 2.22, 2.23]. A more pictorial approach is that of the product operator formalism, which is based on the decomposition of the density matrix into a linear combination of products of spin angular momentum operators [2.24, 2.25]. However, when the simple spin systems involved in conventional imaging are considered, a classical approach to the NMR phenomenon is adequate and is usually favoured because of its simplicity and clear visualization of the process [2.3, 2.25, 2.26].

In this classical vector model the spin ensemble is represented by a single vector, \bar{M} , the sum of all the individual nuclear magnetic moments. When no external field is applied, the individual nuclear moments are randomly oriented and cancel out, so there is no net magnetization. In the presence of a static magnetic field and at thermal equilibrium, the longitudinal component of the net magnetization, M_z , reflects the excess, M_0 , of nuclear spins at the lower energy state as given by Eqn. (2.10). The incoherence of the nuclear spins is expressed as a zero transverse component, M_{xy} . Application of a RF pulse results in a rotation of the net magnetization component about

the axis of the pulse application through an angle which is proportional to the strength and duration of the pulse, as given by Eqn. (2.12). At the end of the pulse, any transverse component of the magnetization precesses about the z axis at the Larmor frequency, and induces an electromotive force in a receiver coil [2.27].

2.6 FID AND QUADRATURE DETECTION

Consider the simple experiment where a 90° RF pulse is applied to a proton ensemble which is in thermal equilibrium, i.e. $\vec{M}_0 = M_0 \hat{z}$. The orientation of the transmitter coil is such that the direction of the B_1 magnetic field at time zero is along the x axis, that is, along the x' axis of the rotating frame. The pulse generates transverse magnetization which starts a clockwise precession at the Larmor frequency, ω_0 . Thus, at time t following the pulse the transverse magnetization is given by:

$$\vec{M}(t) = \exp(-t/T_2^*) [-M_0 \sin(\phi + \omega_0 t) \hat{x} + M_0 \cos(\phi + \omega_0 t) \hat{y}] \quad (2.17)$$

where ϕ is the phase difference between the x' axis of the rotating frame and the x axis of the laboratory frame at the end of pulse application. This precession of the net transverse magnetization is termed "free induction decay" (FID). It is apparent from Eqn. (2.17) that the net magnetization decays exponentially with a time constant T_2^* due to the effective transverse relaxation. In a perfectly homogeneous static magnetic field, the FID decay constant would be the transverse relaxation time T_2 .

A coil placed around the x axis experiences a time dependent magnetic flux Φ proportional to $[-\exp(-t/T_2^*) M_0 \sin(\phi + \omega_0 t)]$. An electromotive force, proportional to the rate of change of the magnetic flux (i.e. $EMF \propto -d\Phi/dt$), is thus induced in the coil, and, assuming that $1/T_2^* \ll \omega_0$ it is given by:

$$EMF(t) \propto \omega_0 M_0 \exp(-t/T_2^*) \cos(\phi + \omega_0 t) \quad (2.18)$$

This oscillating voltage can be amplified and is fed into a phase sensitive detector (PSD), where it is multiplied by a reference oscillation of frequency ω_r and phase θ , generated in the receiver electronics. The output of the PSD is the NMR signal, given by:

$$S(t) = A M_0 \exp(-t/T_2^*) \cos(\phi + \omega_0 t) \cos(\theta + \omega_r t) \quad (2.19)$$

where A is a constant that relates to the characteristics of the receiver electronic circuit and encompasses the constant (i.e. Larmor frequency, ω_0) which results from the

previous differentiation. Given that $\exp(i\beta) = \cos\beta + i\sin\beta$, $\forall \beta \in \mathfrak{R}$, Eqn. (2.19) becomes:

$$S(t) = \frac{AM_0}{4} \exp(-t/T_2^*) \left\{ \exp[+i((\omega_0 + \omega_r)t + (\phi + \theta))] + \exp[-i((\omega_0 + \omega_r)t + (\phi + \theta))] + \right. \\ \left. + \exp[+i((\omega_0 - \omega_r)t + (\phi - \theta))] + \exp[-i((\omega_0 - \omega_r)t + (\phi - \theta))] \right\} \quad (2.20)$$

This signal is passed through filters to remove the high frequency components and the remainder is:

$$S(t) = \frac{AM_0}{4} \exp(-t/T_2^*) \left\{ \exp[+i(\Delta\omega t + \phi - \theta)] + \exp[-i(\Delta\omega t + \phi - \theta)] \right\} \quad (2.21)$$

where $\Delta\omega$ is the difference between the Larmor frequency and the reference frequency, i.e. $\Delta\omega = \omega_0 - \omega_r$. Note that such a signal detection cannot distinguish between Larmor frequencies ω_0 positioned below or above the reference frequency ω_r . Thus, Larmor frequencies, for example, lower than the reference frequency will "fold" into the final spectrum. One solution is to position the reference frequency well above or below the expected Larmor frequency range. However, the noise will still fold, thus degrading the overall signal-to-noise ratio by a factor of $\sqrt{2}$. The elegant way to solve the problem is quadrature detection. The principle requires a second detector, at exactly 90° to the first, for example on the $-y$ axis. The EMF induced in this second detector is then given by:

$$\text{EMF}(t) \propto -\omega_r M_0 \exp(-t/T_2^*) \sin(\phi + \omega_r t) \quad (2.22)$$

In practice, quadrature detection is performed in the receiver electronic circuit without the physical involvement of a second detector. The initial signal given by Eqn. (2.18), after amplification, is fed into two phase sensitive detectors with a relative phase offset of 90° . The output of the two PSDs is then:

$$\text{PSD}_1(t) = A M_0 \exp(-t/T_2^*) \cos(\phi + \omega_r t) \cos(\theta + \omega_r t) \quad (2.23a)$$

$$\text{PSD}_2(t) = -A M_0 \exp(-t/T_2^*) \cos(\phi + \omega_r t) \sin(\theta + \omega_r t) \quad (2.23b)$$

where θ is the common phase of the two reference oscillations. As the two detectors have a 90° phase difference, the total signal can be described using complex notation:

$$\begin{aligned}
 S(t) &= \text{PSD}_1(t) + i \text{PSD}_2(t) = \\
 &= \frac{AM_0}{2} \exp(-t/T_2^*) \left\{ \exp[-i((\omega_0 + \omega_r)t + (\phi + \theta))] + \exp[+i((\omega_0 - \omega_r)t + (\phi - \theta))] \right\}
 \end{aligned}
 \tag{2.24}$$

The two signals are passed through filters to remove the high frequency components and the remainder is:

$$S(t, \psi) = \frac{AM_0}{2} \exp(i\psi) \exp(-t/T_2^*) \exp(i\Delta\omega t)
 \tag{2.25}$$

where $\psi = \phi - \theta$. Detailed descriptions of phase sensitive and quadrature detection, as well as an analysis of the electronics involved can be found in texts such as References [2.11, 2.27, 2.28].

2.7 SIGNAL SAMPLING AND FOURIER TRANSFORM

To extract the frequency response spectrum from the time dependent signal induced in the receiver, Fourier transform (FT) methods are employed and the calculations involve digital computers. Therefore the continuous time domain analogue signal must be sampled and digitized before further computer manipulation.

Invoking the sampling theorem [2.12], a continuous function of time can be adequately represented by a finite number, N , of discrete samples taken at regular time intervals, T , under the condition that its Fourier transform is non-zero over a finite frequency range. The sampling rate, $1/T$, and the number of samples, N , specify the frequency bandwidth and resolution, respectively, in the subsequent frequency domain spectrum. In order to define a signal of a certain frequency a minimum of two points per cycle of the time domain signal must be sampled. Therefore the sampling rate should be at least twice the maximum frequency present in the time domain signal, which can generally be easily estimated in any specific NMR experiment. Therefore, the maximum detectable frequency for a given sampling rate is $f_{\max} = 1/(2T)$ in Hz, and is known as the Nyquist frequency. Components of the signal with frequencies higher than the Nyquist frequency give rise to artifacts in the FT spectrum, as their apparent frequency is reduced by an integral multiple of the Nyquist frequency, Fig. 2.4. The frequency resolution is limited by how long the FID is sampled, as components of the magnetization with different frequencies have to be observed for a long enough time for their phase difference to become distinguishable. Considering that the maximum detectable frequency is $1/(2T)$, the frequency resolution, in Hz, is equal to $1/(NT)$.

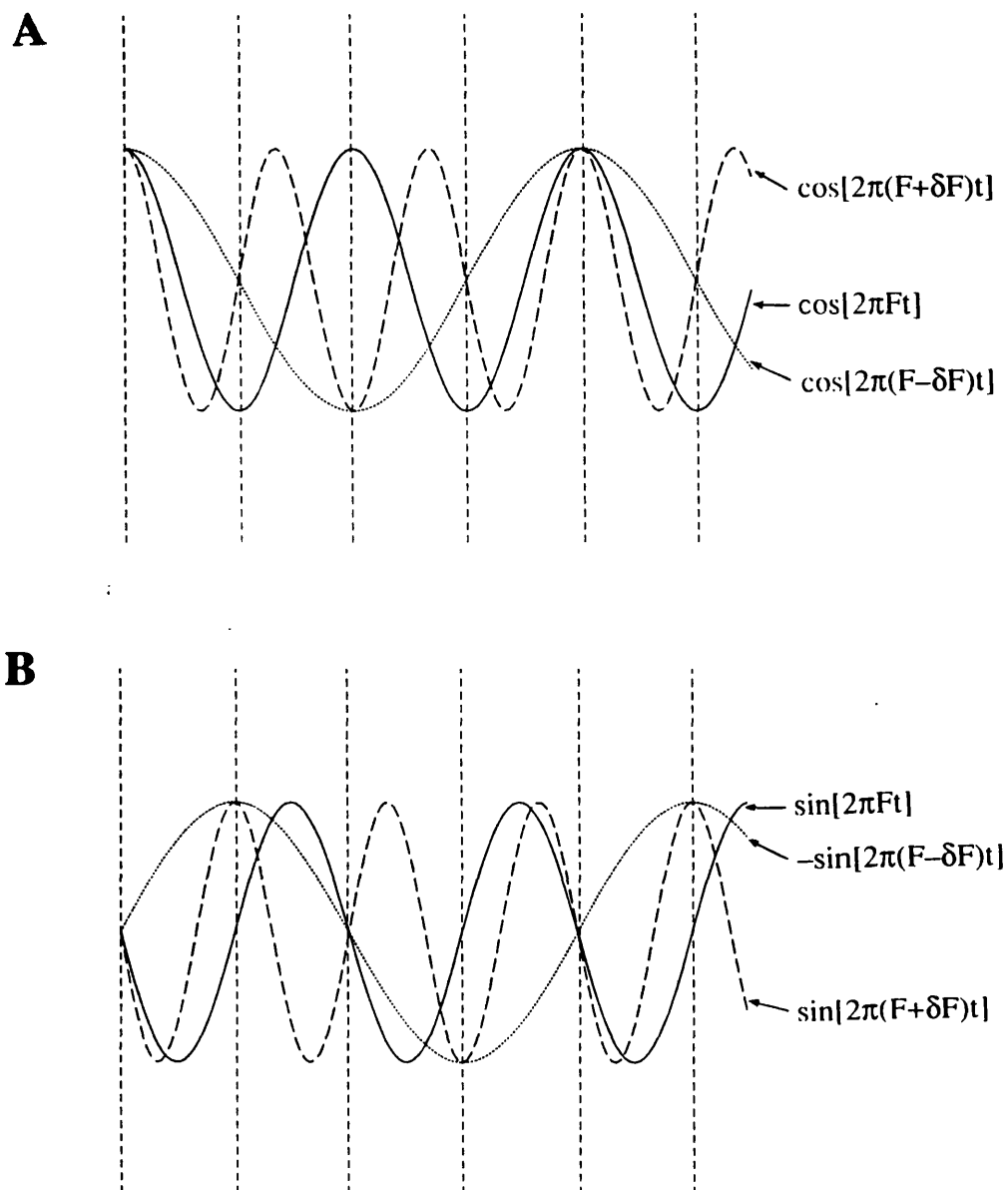


Figure 2.4. Aliasing of frequencies above the Nyquist frequency F in the case of quadrature detection. The sampling rate is $1/T=2F$ and the sampling points are denoted with the vertical dashed lines. **(A)** For a cosine wave the sampled ordinates of a frequency $F+\delta F$ (dashed curve) are the same as for a frequency $F-\delta F$ (dotted curve). **(B)** For the equivalent sine wave of the second detector in quadrature, the sampled ordinates for the wave of frequency $F+\delta F$ (dashed curve) are the same as for an inverted sine wave of frequency $F-\delta F$ (dotted curve). After quadrature detection, the actual wave of frequency $F+\delta F$ is aliased as a ghost frequency of $-(F-\delta F)$. In this graph the damping effect of the effective transverse relaxation has been ignored.

As it is sampled, the continuous time domain signal of Eqn. (2.25) is converted into a function $S_D(\tau)$ of discrete time τ . If the first sample is assumed to occur at $t=0$, then:

$$\begin{aligned} S_D(\tau) &= S(\tau T) && \text{for } \tau = 0, 1, 2, \dots, N-1 \\ S_D(\tau) &= 0 && \text{otherwise} \end{aligned} \quad (2.26)$$

The frequency spectrum can then be recovered by the discrete Fourier transform $F(v)$ of the time domain signal which is given by:

$$\begin{aligned} F(v) &= f_D\{S_D(\tau)\} = \frac{1}{N} \sum_{\tau=0}^{N-1} S_D(\tau) \exp(-i2\pi \frac{v}{N} \tau) && \text{for } v = 0, 1, 2, \dots, N-1 \\ F(v) &= f_D\{S_D(\tau)\} = 0 && \text{otherwise} \end{aligned} \quad (2.27)$$

where v/N may be identified with frequency measured in cycles per sampling interval over the given range, i.e. $v/(NT)$ in Hz. For consistency with the signal expressions that use the concept of angular frequency, the frequency spectrum $F(\omega_D, \psi)$ in terms of the discrete angular frequency $\omega_D = 2\pi v/(NT)$ is given by:

$$\begin{aligned} F(\omega_D, \psi) &= \frac{1}{N} \sum_{\tau=0}^{N-1} \frac{AM_0}{2} \exp(i\psi) \exp(-\tau T/T_2^*) \exp(i\Delta\omega\tau T) \exp(-i\omega_D\tau T) \\ &&& \text{for } \omega_D = 0, \frac{2\pi}{NT}, 2 \frac{2\pi}{NT}, 3 \frac{2\pi}{NT}, \dots, (N-1) \frac{2\pi}{NT} \\ F(\omega_D, \psi) &= 0 && \text{otherwise} \end{aligned} \quad (2.28)$$

where Eqn. (2.25) has been used to expand $S_D(\tau)$.

In practice, the computation of Eqn. (2.28) can be very time consuming, and most computers used in NMR experiments now employ fast discrete Fourier transform (FDFT) algorithms, such as the Cooley-Tukey algorithm and its modifications [2.29, 2.30].

To summarize, the final input into the computer is a discrete function of time which can be thought as an approximation to the underlying continuous time domain signal initially induced in the receiver. Following numerical computation, the output of the Fourier transform is a discrete function in the frequency domain. This again can be regarded as an approximation to the FT of the continuous time domain signal. For simplicity, only the continuous time domain function and its FT will be considered in

this analysis hereafter. Thus, the frequency spectrum $F(\omega, \psi)$ of the time-domain signal $S(t, \psi)$ can be recovered through its Fourier transformation $f\{S(t, \psi)\}$:

$$F(\omega, \psi) = f\{S(t, \psi)\} = \int_0^{\infty} S(t, \psi) \exp(-i\omega t) dt \quad (2.29)$$

The integrating limits correspond to the duration of the FID observation, which starts at zero time and it is assumed to last till the signal has completely dephased (equivalent to infinity). Expanding Eqn. (2.29) and using the signal expression as given by Eqn. (2.25), it can be shown that $F(\omega, \psi)$ is a complex function and its real, $\text{Re}\{F(\omega, \psi)\}$, and imaginary, $\text{Im}\{F(\omega, \psi)\}$, parts are given by:

$$\text{Re}\{F(\omega, \psi)\} = \frac{AM_0}{2} \left[\cos\psi \frac{T_2^*}{1 + (\omega - \Delta\omega)^2 (T_2^*)^2} + \sin\psi \frac{(\omega - \Delta\omega) (T_2^*)^2}{1 + (\omega - \Delta\omega)^2 (T_2^*)^2} \right] \quad (2.30a)$$

$$\text{Im}\{F(\omega, \psi)\} = \frac{AM_0}{2} \left[\sin\psi \frac{T_2^*}{1 + (\omega - \Delta\omega)^2 (T_2^*)^2} - \cos\psi \frac{(\omega - \Delta\omega) (T_2^*)^2}{1 + (\omega - \Delta\omega)^2 (T_2^*)^2} \right] \quad (2.30b)$$

The initial transverse magnetization phase ϕ and the phase θ of the reference signal can easily be made equal, i.e. $\psi = \phi - \theta = 0$, for example by shifting the time origin of the signal observation. Then the equations for the final signal and its Fourier transformation simplify to give:

$$S(t) = \frac{AM_0}{2} \exp(-t/T_2^*) \exp(-i\Delta\omega t) \quad (2.31)$$

and

$$\text{Re}\{F(\omega)\} = \frac{AM_0}{2} \frac{T_2^*}{1 + (\omega - \Delta\omega)^2 (T_2^*)^2} \quad (2.32a)$$

$$\text{Im}\{F(\omega)\} = \frac{AM_0}{2} \frac{(\omega - \Delta\omega) (T_2^*)^2}{1 + (\omega - \Delta\omega)^2 (T_2^*)^2} \quad (2.32b)$$

The graphical representation of Eqns. (2.32a) and (2.32b) is shown in Fig. 2.5. The real part of the FT corresponds to a Lorentzian lineshape curve and is known as the

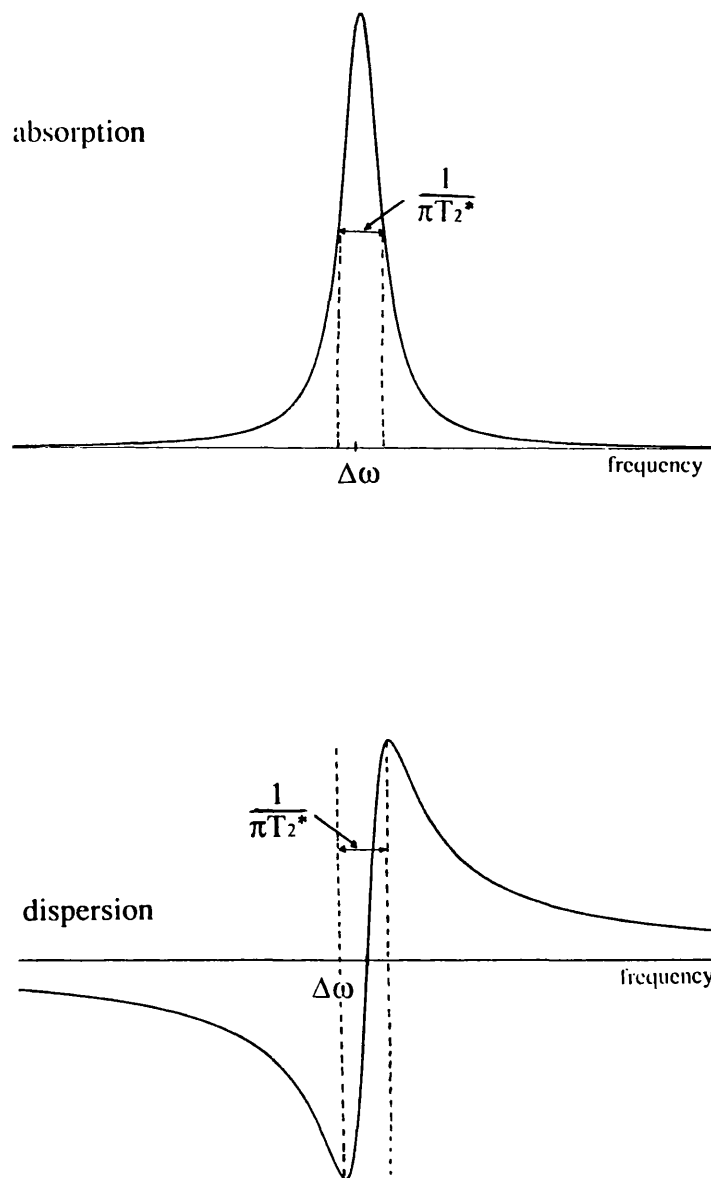


Figure 2.5. Graphical representation of the real (absorption) and imaginary (dispersion) parts of the Fourier transform of an FID, as given by Eqns. (2.32). The width of the absorption line at half-height, and the peak-to-trough separation of the dispersion line are equal to $1/(\pi T_2^*)$ in Hz.

"absorption" signal, while the imaginary part gives the "dispersion" signal. The set of Eqns. (2.30) carry effectively the same information, but in this case both real and imaginary parts are admixtures of absorption and dispersion signals. In practice, such "contaminations" may also arise from other sources (such as mis-settings of the origin of the FID in time and off-resonance effects of finite radiofrequency pulses) and are usually frequency dependent. The pure absorption and dispersion signals can generally be recovered by "phase correction" procedures, which can be manual or based on iterative computer algorithms [2.31, 2.32].

2.8 ECHO FORMATION AND SAMPLING

In several NMR applications and considering the finite time required for switching the electronics (i.e. switch off the transmitter and on the receiver), the effective transverse relaxation time of the sample can be prohibitively short for the required number of samples. Moreover, in imaging experiments, application of magnetic field gradients for spatial encoding further increases the decay constant of the FID. This latter problem can be solved by employing mechanisms that lead to the formation of a "spin echo" at a specified time TE after the excitation pulse. As it will be shown, sampling the full echo enables the recovery of the absorption spectrum simply by calculating the modulus of the Fourier transform. Additionally, full echo sampling results, after Fourier transformation, in double the signal amplitude as compared to sampling the FID, save for transverse relaxation. Spin echoes can generally be formed using additional pulses (RF echo) or employing magnetic field gradient reversal (gradient echo).

A common method of RF echo formation involves application of a 180° RF pulse at a time TE/2 after the initial excitation pulse, Fig. 2.6 [2.33, 2.34]. For example, consider an extension of the simple experiment described above, where the direction of the B_1 field for the 180° pulse is along the y' axis. Immediately after the 90° pulse (applied along x') the magnetization is aligned along a direction which forms an angle ϕ with the y' axis. Due to static magnetic field homogeneities, the individual components of the magnetization precess at different resonance frequencies. Therefore, as observed from a frame rotating at the Larmor frequency, they spread out during the time interval TE/2. The subsequent 180° pulse inverts the spins, which continue to precess at their individual frequencies but now converging. After a further time TE/2 all magnetization components are aligned once again along a direction which forms an angle ϕ with the y' axis, thus forming an echo. Then the spins spread out again, in the same way as after the 90° pulse. As all phase shifts are refocused, the echo peak amplitude depends only on the spin-spin relaxation during the time TE. A simplified diagrammatic

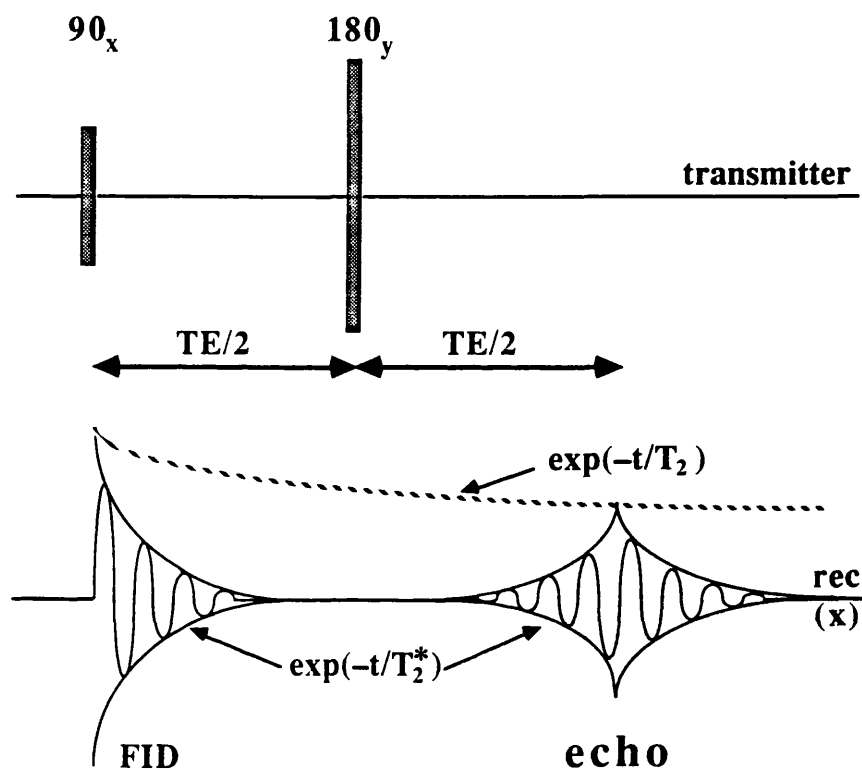


Figure 2.6. The free induction decay signal following a $90^\circ(x)$ excitation pulse and the spin echo formed by means of a refocusing $180^\circ(y)$ pulse. In both the FID and the full echo, the signal decays due to the effective transverse relaxation time T_2^* . However, the maximum amplitude of the echo decays only due to transverse relaxation, T_2 .

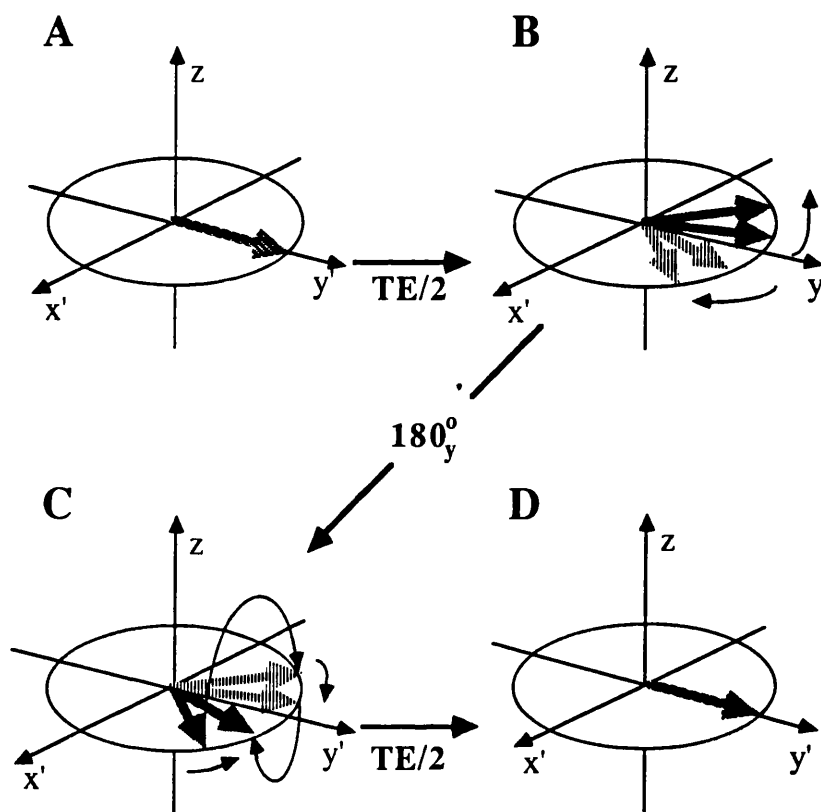


Figure 2.7. A vector diagram illustrating the formation of a RF spin echo. A frame rotating at the Larmor frequency is assumed. (A) The net magnetization is aligned along y , immediately after, for example, a $90^\circ(x)$ excitation pulse. (B) During the time $TE/2$ the individual spin vectors spread out due to differences in their frequencies, which arise from local inhomogeneities in the static magnetic field, susceptibility differences and chemical shifts. (C) An $180^\circ(y)$ pulse inverts the spins, which continue to precess in their individual frequencies, but now converging. (D) After a further $TE/2$ time the spin vectors refocus to form a spin echo. Scalar couplings are assumed to be negligible in the spin system considered. (CPMG, [2.34])

representation of the spin precession and the formation of an echo as a result of the refocusing 180° pulse is shown in Fig. 2.7. A similar echo can be formed after an RF pulse of an arbitrary tip angle, though the amplitude of the echo depends on the tip angle of the pulse. A detailed, generalized description of the echoes formed by trains of pulses is given in Reference [2.20]. It should be noted that the echo amplitude is generally modulated by the J-coupling constant when coupled spins are present and the refocusing pulse is experienced by the entire coupled system [2.35].

Spin dephasing and refocusing can also be induced by magnetic field gradient reversal, and such an echo is usually termed a "gradient echo" [2.36]. The process involves application of a magnetic field gradient along an arbitrary axis, Fig. 2.8. Spins at different positions along the axis of the gradient experience different static magnetic fields, and precess at different resonance frequencies. The result is an overall dephasing, and the accumulated phase is proportional to the product of the time integral of the applied gradient. Gradient reversal forces the spins to rephase and an echo is formed when the overall accumulated phase compensates the phase gained during the first period of gradient application. The process of gradient echo formation is schematically illustrated in Fig. 2.9. As no spin inversion occurs, phase shifts due to B_0 inhomogeneities, susceptibility differences and chemical shifts will not be refocused. The peak amplitude of the gradient echo, therefore, depends on the effective relaxation time T_2^* , and is modulated by the chemical shifts and scalar couplings of the spins present. Although this degrades the signal-to-noise ratio (as compared to an equivalent RF echo) and can induce artifacts due to chemically shifted spins (as described in a later chapter), it may prove an advantage when contrast dependent on T_2^* , susceptibility differences, or chemical shift is desired. Furthermore, gradient echoes can prove useful in certain clinical applications, where multiple refocusing pulses can result in excessive RF power deposition. Their dependence, however, on magnetic field homogeneity and chemical shift limits their widespread use. In the signal analysis hereafter, a RF spin echo (for example, that of Fig. 2.6) will be assumed, and, for convenience as well as consistency with literature, it will simply be referred to as spin echo.

If the time origin is placed at the centre of the spin echo and acquisition begins at that point, the signal is given by an expression similar to Eqn. (2.25), the only difference being that at echo formation the magnitude of the net magnetization has already been attenuated by transverse relaxation during the time interval TE and this is expressed by the additional factor $\exp(-TE/T_2)$. Fourier transformation of the signal from the second half of the echo yields frequency spectra described by Eqns. (2.30). Assuming T_2 effects during the echo formation are negligible, the signal from the entire echo can be described by:

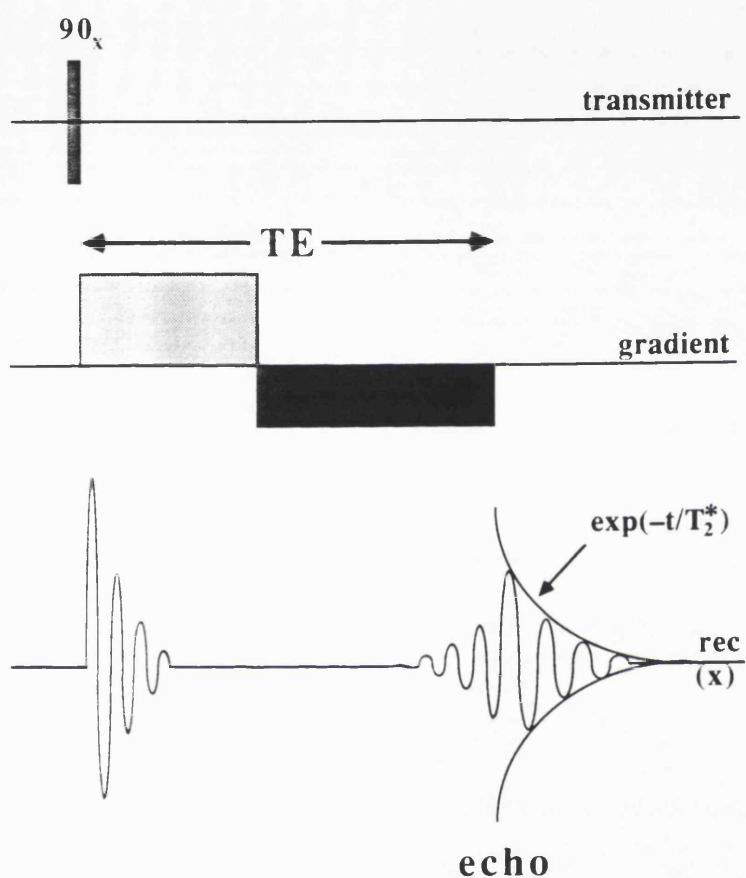


Figure 2.8. The free induction decay signal following a $90^\circ(x)$ excitation pulse and the spin echo formed by means of magnetic field gradient reversal. The echo is formed at the end of the gradient pulse. The positive and negative gradient lobes have the same time integral. The FID as well as the first half of the echo are characterized by the combined damping effect of the magnetic field gradient and the effective transverse relaxation time T_2^* . During the second half of the echo the signal decays only due to the effective relaxation time T_2^* .

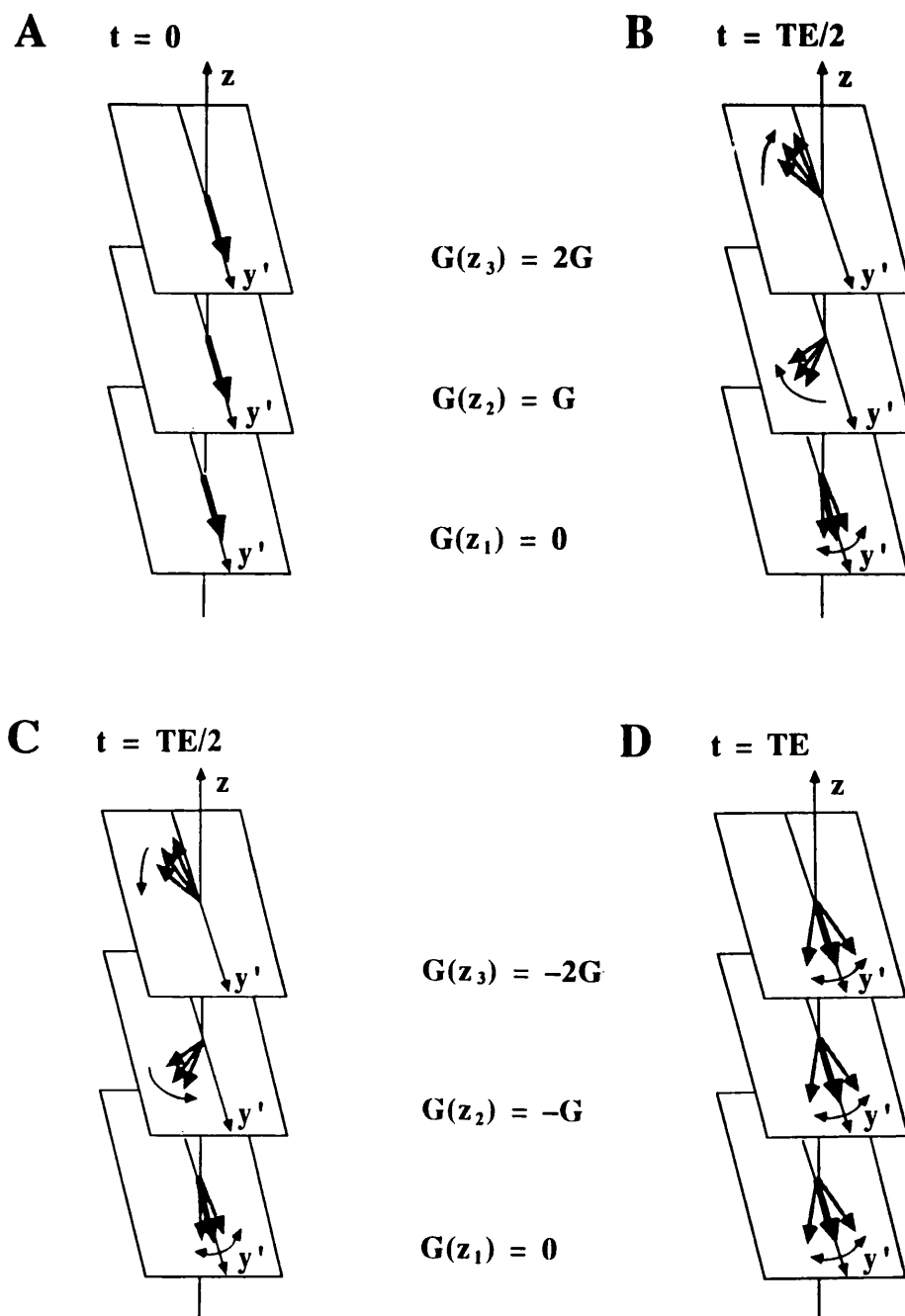


Figure 2.9. A vector diagram illustrating the formation of a gradient echo. (A) The net magnetization is aligned along y' , immediately after a $90^\circ(x)$ excitation pulse. A magnetic field gradient applied along z forces spins at different locations to precess at different frequencies. (B) Spins at different planes normal to z accumulate different phase shifts. (C) The magnetic field gradient is reversed, inducing the same phase shifts but in the opposite direction. (D) The echo is formed when the phase shift induced by the first part of the gradient is exactly compensated for by the second, reversed gradient. Phase shifts due to local static magnetic field inhomogeneities, susceptibility differences and chemical shifts are not refocused.

$$S(t,\psi) = \frac{AM_0}{2} \exp(-TE/T_2) \exp(i\psi) \exp(t/T_2^*) \exp(i\Delta\omega t) \quad -\infty < t < 0 \quad (2.33a)$$

$$S(t,\psi) = \frac{AM_0}{2} \exp(-TE/T_2) \exp(i\psi) \exp(-t/T_2^*) \exp(i\Delta\omega t) \quad 0 \leq t \leq +\infty \quad (2.33b)$$

If the transverse relaxation time is short compared to the observation time, the signal is modulated by the T_2 exponential decay, leading to loss of resolution [2.37], which, however, can be recovered by deconvolution methods extracting T_2 information at the same time [2.38]. Fourier transformation of Eqns. (2.33) involves integration over the entire observation time, from before echo formation has started ($-\infty$), till the signal has completely dephased again ($+\infty$).

$$\begin{aligned} F(\omega,\psi) &= f\{S(t,\psi)\} = \int_{-\infty}^{+\infty} S(t,\psi) \exp(-i\omega t) dt = \\ &= \int_{-\infty}^0 S(t,\psi) \exp(-i\omega t) dt + \int_0^{+\infty} S(t,\psi) \exp(-i\omega t) dt = \\ &= \int_{-\infty}^0 (AM_0/2) \exp(-TE/T_2) \exp(i\psi) \exp(t/T_2^*) \exp(i\Delta\omega t) \exp(-i\omega t) dt + \\ &+ \int_0^{\infty} (AM_0/2) \exp(-TE/T_2) \exp(i\psi) \exp(-t/T_2^*) \exp(i\Delta\omega t) \exp(-i\omega t) dt \end{aligned} \quad (2.34)$$

Performing the integration in Eqn. (2.34), it can be shown that $F(\omega,\psi)$ is a complex function and its real, $\text{Re}\{F(\omega,\psi)\}$, and imaginary, $\text{Im}\{F(\omega,\psi)\}$ parts are given by:

$$\text{Re}\{F(\omega,\psi)\} = A M_0 \exp(-TE/T_2) \cos\psi \frac{T_2^*}{1 + (\omega - \Delta\omega)^2 (T_2^*)^2} \quad (2.35a)$$

$$\text{Im}\{F(\omega,\psi)\} = A M_0 \exp(-TE/T_2) \sin\psi \frac{T_2^*}{1 + (\omega - \Delta\omega)^2 (T_2^*)^2} \quad (2.35b)$$

If $\psi = \phi - \theta = 0$ (i.e. if phase correction is performed) the FT reduces to a real spectrum:

$$\operatorname{Re}\{F(\omega)\} = A M_0 \exp(-TE/T_2) \frac{T_2^*}{1 + (\omega - \Delta\omega)^2 (T_2^*)^2} \quad (2.36a)$$

$$\operatorname{Im}\{F(\omega)\} = 0 \quad (2.36b)$$

If only the second half of the echo is sampled then the absorption spectrum would be given by Eqn. (2.32a) allowing for an additional exponential term to account for transverse relaxation during TE. Comparing Eqns. (2.36a) and (2.32a), it is apparent that the amplitude of the full echo spectrum is double the amplitude of the spectrum resulting from sampling only the second half of the echo. Most interesting is the fact that the pure absorption line can be readily recovered by taking the modulus of the complex FT, that is:

$$\begin{aligned} M(\omega) &= |F(\omega)| = (\operatorname{Re}\{F(\omega)\}^2 + \operatorname{Im}\{F(\omega)\}^2)^{1/2} = \\ &= A M_0 \exp(-TE/T_2) \frac{T_2^*}{1 + (\omega - \Delta\omega)^2 (T_2^*)^2} \end{aligned} \quad (2.37)$$

2.9 MAGNETIC FIELD GRADIENTS AND THE k-SPACE FORMALISM

Since the resonance frequency is proportional to the strength of the applied magnetic field, a magnetic field gradient across a sample gives rise to a range of resonance frequencies. Although this simple fact had been pointed out in the early days of NMR spectroscopy [2.39], only in 1973 was the imposition of a magnetic field gradient used to produce spatial distribution maps of the contributing spins [2.40, 2.41]. Initially, images were limited to small objects. The first whole body proton NMR image was published in 1977 [2.42] and these early results were followed rapidly by a variety of imaging techniques.

The principle of magnetic resonance imaging (MRI) lies in the effects a linear magnetic field gradient creates when superimposed on the static field during the conventional NMR experiment. In the presence of a static magnetic field B_0 , the spins in the sample resonate at $\omega_0 = \gamma B_0$. If the local spin density is given by the function $\rho(\bar{r})$, then there will be $\rho(\bar{r})dV$ spins in a volume element dV , and the macroscopic net magnetization arising from this voxel can be calculated considering Eqn (2.10), and is given by:

$$dM_0 = \alpha \rho(\bar{r}) dV \quad (2.38)$$

where, considering Eqn. (2.10), the constant of proportionality α is:

$$\alpha = \frac{\gamma^2 \hbar^2 B_0}{4kT} \quad (2.39)$$

The signal arising from this voxel can then be calculated using Eqn. (2.25), and is given by:

$$dS(t) = B \rho(\bar{r}) dV \exp(i\Delta\omega t) \quad (2.40)$$

where the constant of proportionality is either $B = (A\alpha/2) \exp(i\psi) \exp(-t/T_2^*)$ in the case of sampling an FID, or $B = (A\alpha/2) \exp(i\psi) \exp(-TE/T_2) \exp(-t/T_2^*)$ when a spin echo is considered. A spatially varying magnetic field $G(\bar{r})$ applied across the sample creates a spread of resonance frequencies that exhibit the same spatial dependence. For the common example of a linear magnetic field gradient, the local Larmor frequency at position \bar{r} is thus defined as:

$$\omega(\bar{r}) = \gamma B_0 + \gamma G(\bar{r}) \cdot \bar{r} \quad (2.41)$$

Consider applying such a magnetic field gradient for a time interval, i.e. from $t=T_a$ to $t=T_b$. The signal arising from a voxel is then:

$$dS(t) = B \rho(\bar{r}) dV \exp\left(i\gamma \int_{T_a}^{T_b} G(\bar{r}, t) \cdot \bar{r} dt\right) \quad (2.42)$$

where the reference frequency is assumed to be $\omega_r = \gamma B_0$. Thus the integrated signal over the whole sample volume is:

$$S(t) = B \int_V \rho(\bar{r}) \exp\left(i\gamma \int_{T_a}^{T_b} G(\bar{r}, t) \cdot \bar{r} dt\right) d\bar{r} \quad (2.43)$$

or

$$S(t) = B \int_V \rho(\bar{r}) \exp(i \bar{k}(t) \cdot \bar{r}) d\bar{r} \quad (2.44)$$

where the vector quantity $\bar{k}(t)$ is the integral of the magnetic field gradients over the duration of their application:

$$\bar{K}(t) = \gamma \int_{T_a}^{T_b} G(\bar{r}, t) dt \quad (2.45)$$

Equation (2.44) suggests that $\bar{K}(t)$ can be seen as a vector of "spatial-frequency" coordinates. That is, Eqn. (2.44) can be rewritten as:

$$S(t) = B S'(\bar{K}(t)) \quad (2.46)$$

where $S'(\bar{K}(t))$ is the ^{3D} Fourier transform $f\{\rho(\bar{r})\}$ of the spatial spin distribution function $\rho(\bar{r})$. The function of the spatial distribution of the object $\rho(\bar{r})$ can be considered as a sum of sinusoids with different frequencies. The received signal as described by Eqn. (2.46) is the Fourier transform of this function, that is, the spectrum of individual spatial frequencies $\bar{K}(t)$. A three-dimensional inverse FT of $S(t)$ as given by Eqn. (2.46), therefore, gives the spatial spin density distribution of the object $\rho(\bar{r})$.

It is apparent that sampling the time domain signal is equivalent to sampling the spatial frequency spectrum, which, in the general case, is three-dimensional. The sampling procedure follows the same basic principles as described before, the only difference being that now the process occurs in the "frequency" domain. Once again the sampling theorem [2.12] requires that the sampling of k-space along any axis should be at equal intervals, Δk , not exceeding $1/(2r_{max})$, where r_{max} is the field of view (FOV) at this particular direction. It should be noted that in practice the magnetic field gradient is zero in the middle of FOV, extending from maximum negative value to maximum positive value over the entire FOV. In this case, r_{max} is half the FOV, as it always represents the distance along which the magnetic field gradient changes from zero to maximum value. The extent of k-space sampling, that is, the number of samples N , determines the spatial resolution, which is given by $1/(N\Delta k)$. A schematic representation of a k-space grid and a numerical example for the relation between the k-space sampling rate and the number of samples with the spatial resolution and the field of view is given in Fig. 2.10. In this figure, it is assumed that an NMR imaging experiment encodes the spatial spin distribution of an object with uniform density into the FID by employing magnetic field gradients along the two orthogonal in-plane directions x and y . The k-space grid shown corresponds to one of the two detectors in quadrature. The sampling interval along each direction is determined by the required field of view, $2x_{max}=32$ cm and $2y_{max}=20$ cm (where the gradients are assumed to extend from negative to positive values over the FOV). Therefore, $\Delta k_x = 1/(2x_{max}) = 0.032$ cm⁻¹ and $\Delta k_y = 1/(2y_{max}) = 0.050$ cm⁻¹. The number of points sampled along each direction of k-space determines the image resolution, i.e., $1/(2N_x\Delta k_x) = 2$ cm along x and $1/(2N_y\Delta k_y) = 2.5$ cm along y . The remaining three

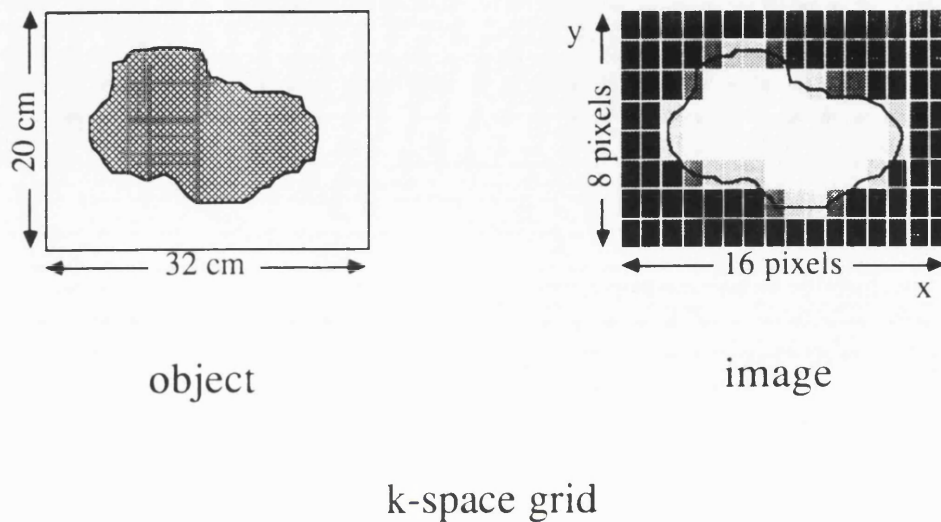


Figure 2.10. Schematic representation of a 2D object, its spin density distribution as mapped in an NMR image, and a k-space grid corresponding to this image. The object is assumed to have uniform spin density distribution. An NMR imaging experiment encodes the spatial spin distribution into the signal by employing magnetic field gradients along the two orthogonal in-plane directions x and y . The k-space grid shown corresponds to one of the two detectors. The image is displayed using a grey scale, different scale levels denoted by different tones of shading, while the outline of the object is drawn only for clarity.

quadrants are sampled only when full k-space echoes are acquired. It should be noted that k-space can be sampled irregularly, but interpolation algorithms must be used to place the acquired data points into the regular rectangular grid before the conventional multidimensional Fourier transform is performed.

Although the concept of spatial frequency is essential for the understanding of image formation in Fourier NMR methods, it may not be intuitively related to the actual experimental parameters. Invoking Eqn. (2.45), therefore, the spatial frequency sampling interval Δk_r for any given encoding direction r (where r is x , y , or z) can be expressed as, (assuming a rectangular gradient waveform):

$$\Delta k_r = \gamma (G_r \Delta T_r + \Delta G_r T_r - \Delta G_r \Delta T_r) \quad (2.47)$$

where ΔG_r and ΔT_r is the difference in the gradient strength, G_r , and gradient duration, T_r , respectively, between subsequent data points along the corresponding spatial encoding axis r . It is apparent that the k-space sampling interval Δk can be altered by keeping constant the gradient strength while changing the duration of the gradient between the signal samples or vice versa. Theoretically there is no limit to the maximum value of Δk , thus there is no limit as to the minimum achievable field of view, as well as the maximum achievable resolution. In practice maximum limits are imposed to the value of Δk due to hardware limitations in terms of maximum gradient strength, as well as to maximum gradient duration due to spin relaxation. However, the fact that the same sampling interval can be achieved for various combinations of difference in gradient strength and gradient duration provides the possibility to optimize FOV and spatial resolution for a given experimental set-up.

Similarly to the FT of the FID signal (see Eqns. (2.30)), the Fourier transform of Eqn. (2.46) is a complex function whose real and imaginary parts are admixtures of "absorption" and "dispersion" signals. This admixture appears as a "phase twist" across the spatial distribution map according to the shift theorem [2.10, 2.12]. Sampling a full "k-space echo" results in a FT whose both real and imaginary parts are "absorption" signals (see Eqns. (2.35)). Then, the phase shift can be easily corrected or a modulus image can be created. In analogy to the concept of spin echo, a k-space echo involves sampling negative spatial frequencies which can be created by gradient reversal, as it will be shown in the examples presented in the following section.

Detailed descriptions of the k-space formalism can be found in texts such as References [2.10, 2.43–2.48].

As shown in the previous analysis, the spatial encoding can be a three-dimensional procedure with the FID (or spin echo) carrying information from the entire imaging volume. However, the final map of the spin density distribution is generally

displayed as a series of two-dimensional "slices" of the object. This slice selection can also be achieved by means other than simultaneous encoding of all three spatial dimensions in the NMR signal, which is a rather time consuming process for most k-space scanning schemes. An alternative method for slice selection involves an oscillating magnetic field gradient with a time dependent amplitude applied in a direction normal to the desired slice [2.49]. The gradient has zero-field contribution only in the image plane, thus signal averaging over the gradient time dependence removes signal from everywhere except the slice of interest. However, the most established and extensively used way to select a plane is by selective excitation [2.50, 2.51]. This involves application of a narrow frequency bandwidth RF pulse in the presence of a magnetic field gradient that creates a spread of resonance frequencies in the direction normal to the desired plane. A detailed treatment of selective excitation is given in Reference [2.10], while some of its considerations will be presented in a later chapter. In the following analysis, slice selection along the z axis is always assumed unless otherwise stated, and spatial encoding is, therefore, required only for the remaining two dimensions, i.e., x and y axes. As a result, the k-space grid, as well as the Fourier transform, become two-dimensional. It should be noted that the orthogonal axes along which the spatial encoding is performed in a magnetic resonance imaging experiment can take any arbitrary orientation in space, and x, y, and z are used only for convenience.

2.10 SCANNING k-SPACE AND FOURIER IMAGING METHODS

Different imaging methods can be grouped together according to the way they scan k-space, which is determined by their gradient pulse sequence and signal sampling scheme. There is an infinite number of ways to scan k-space, each having advantages and disadvantages in terms of image quality, time efficiency, hardware and software requirements concerning the gradient pulse sequence implementation and the sampling procedures, as well as data computation. Most established and routinely used Fourier imaging methods are based on the k-space scanning schemes of projection reconstruction (PR), spin-warp, and echo-planar (EPI) imaging methods.

The first published NMR image was obtained using a projection reconstruction method [2.40]. A schematic pulse sequence diagram for the 2D spin echo version of this method is shown in Fig. 2.11.A. The excited magnetization within a slice is forced into a spin echo and the signal is selected in the presence of two orthogonal gradients. The vector sum of their time integral defines the line in the two-dimensional k-space grid along which the sampling occurs. The gradient reversal assures the formation of the k-space echo. The very first data point corresponds to the maximum negative k value along the line defined by the gradient combination. As the sampling continues, the

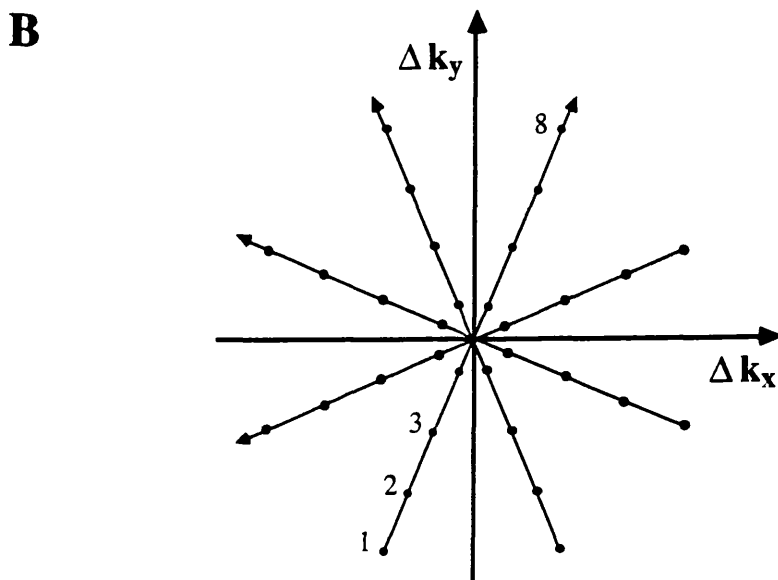
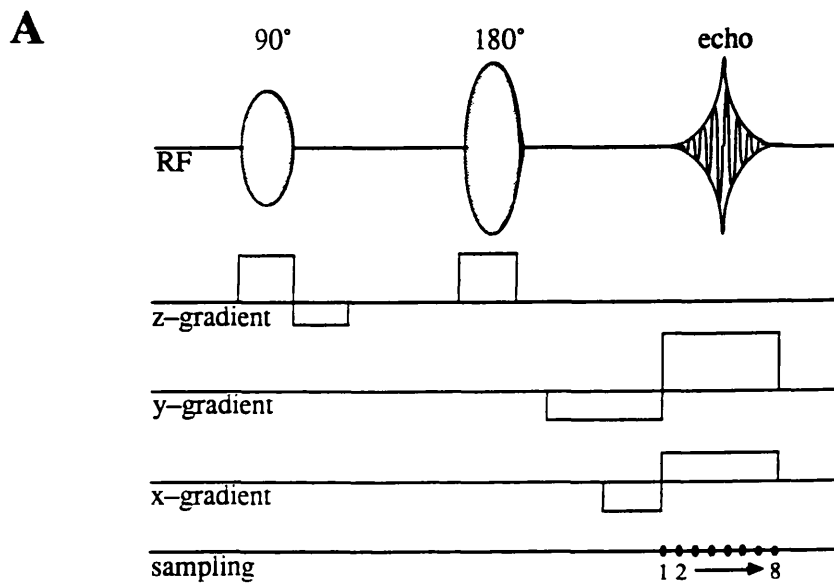


Figure 2.11. (A) Pulse sequence diagram for a 2D, spin echo, projection reconstruction imaging experiment. The slice selection is performed along z by means of selective excitation. The sequence is repeated for different combinations of the time integral values of the gradients along x and y . (B) Schematic representation of the corresponding k -space grid. Each line corresponds to a different sequence repetition, while the arrows indicate the direction of the sampling within each experiment.

positive gradient cancels incrementally the effects of the previously applied negative gradient pulse, and the data points correspond to negative k values closer to zero. When the positive gradient has completely compensated the previously applied negative lobe, the data points correspond to positive k values which systematically increase till the end of the acquisition. A series of experiments are performed with different gradient combinations so that the line defined by their vector sum is "rotated" to cover the full k -space. The corresponding k -space grid and the sampling direction is schematically shown in Fig. 2.11.B. It is apparent that k -space is not sampled in the regular way required for application of the conventional 2D FT, and interpolation of the acquired points into a rectangular grid is required. In practice, however, the reconstruction of the final image is achieved by a different procedure, whereby a one-dimensional FT is performed for every sampled line of k -space, thus yielding a line integral projection of the object. The 2D image is then recovered from all the projections by means of mathematical techniques commonly used in X-ray computer assisted tomography [2.14, 2.52].

A schematic pulse sequence diagram for a 2D, spin echo, spin-warp experiment [2.36, 2.53] is shown in Fig. 2.12.A. The excited magnetization within a selected slice is left to evolve in the presence of a gradient along one of the in-plane directions, for example y . This process, known as "phase encoding", encodes into the final signal a single spatial frequency along the y -axis. Invoking Eqn. (2.45), it is apparent that the encoded spatial frequency k_y depends on the strength and duration of the applied gradient. Therefore, in order to encode all the desired spatial frequencies along the y direction, the same experiment must be repeated for different values of the gradient integral. The k -space echo formation in this direction is formed by stepping the phase encoding gradient for both positive and negative values. The spatial encoding in the remaining in-plane direction, x , is performed in a similar way as in the projection reconstruction method and it is known as "frequency-encoding". The k -space echo along x is again formed by gradient reversal prior to acquisition. This compensating (or "defocusing") gradient lobe is usually placed before the refocusing RF pulse in order to avoid high strain in the gradient coil hardware as well as additional gradient echoes formed by magnetization excited by a non-perfect 180° refocusing pulse. In that case the polarity of the gradient is reversed, to account for the fact that the refocusing pulse effectively inverts the accumulated phase of the precessing spins. It should be pointed out that the spatial encoding process is the same along both in-plane directions, the only difference being in the time interval between sampling subsequent k -space points. In this respect, the terms "phase encoding" and "frequency encoding" are misleading, however they are extensively used both in practice as well as in the literature of the NMR field, and, for convenience, they will also be adopted hereafter. Figure 2.12.B

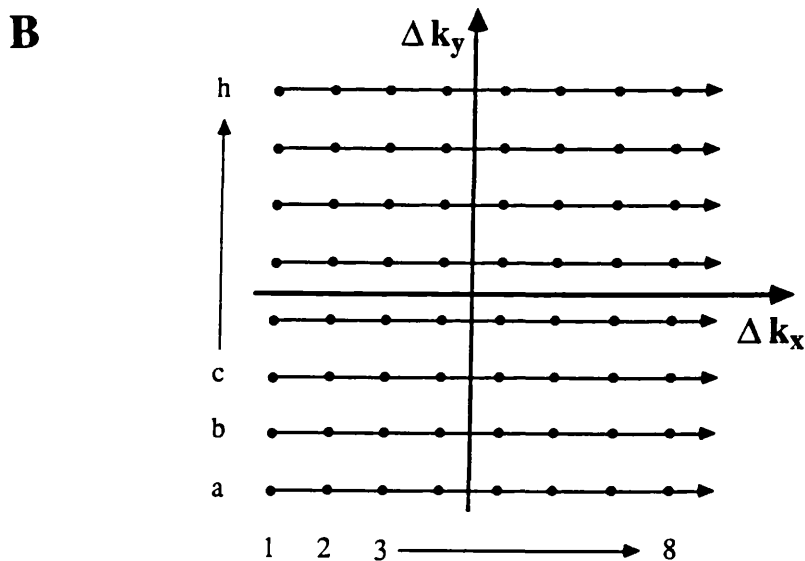
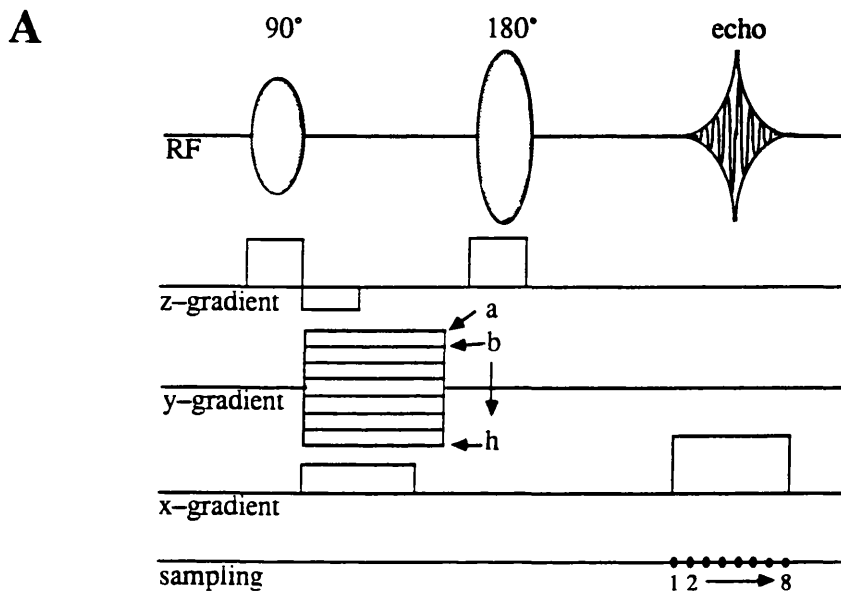


Figure 2.12. (A) Pulse sequence diagram for a 2D, spin echo, spin-warp imaging experiment. The slice selection is performed along z by means of selective excitation. The sequence is repeated for different values of the "phase encoding" gradient along y , (indicated by different letters). (B) Schematic representation of the corresponding k -space grid. Each line corresponds to a different sequence repetition, while the arrows indicate the direction of the sampling within each experiment.

shows the corresponding k-space grid and the sampling direction for the spin-warp imaging experiment. This characteristic sampling of one line of the rectangular k-space grid per sequence repetition is a common feature for a large number of conventional imaging sequences in current practice [2.10]. These include extensions of the simple spin-warp experiment to allow for relaxation time measurements and chemical shift imaging (such as methods reviewed and proposed in the following chapters), stimulated echo imaging [2.54, 2.55], as well as fast imaging techniques [2.48] based on steady-state-free-precession [2.56, 2.57] and low-angle excitation [2.58]. Calculating the two dimensional inverse FT of the observed signal as given by Eqn. (2.46), it can be shown [2.10] that the pixel intensity, I , in the final image is proportional to the maximum amplitude of the observed signal as given by Eqn. (2.43), that is:

$$I = C \rho \exp(-TE/T_2) \quad (2.48)$$

where ρ is the proton density function averaged over the volume of the corresponding voxel, while C encompasses constants that relate to the hardware characteristics as well as constants arising from the Fourier transformation.

Another major group of imaging techniques involves scanning the k-space in a single experiment. This can be achieved by a series of spin echoes after a single excitation, where the spatial encoding procedure for each echo is the same as for each sequence repetition of the spin-warp experiment [2.59]. Alternatively, single-shot k-space scanning can be achieved by frequent reversal of at least one of the magnetic field gradients, which can be done in various ways resulting in k-space trajectories that can differ significantly. Many such pulse sequence schemes have been proposed, including the well know family of echo-planar (EPI) imaging sequences. Figure 2.13 shows the pulse sequence diagram and the corresponding k-space grid for a modification of the first proposed EPI imaging sequence [2.60]. The signal from the selected slice is sampled in the presence of gradients along both in-plane directions. One of them (in this example along x) is a low strength, constant gradient, forcing the sampling along x direction from zero towards larger k_x values. At the same time, the first lobe of the alternating gradient along y forces the k-space trajectory to move from zero towards higher k_y values. The second lobe progressively cancels the effect of the first lobe, and the trajectory moves progressively back to zero, and then towards negative k_y values. The combination of the two gradients results in the "zig-zag" sampling pattern shown in Fig. 2.13.B. Note that although the alternating gradient ensures k-space echo formation along the y direction, no k-space echo is formed along x , therefore modulus imaging is not possible. Additionally, the data points have to be interpolated into a rectangular grid prior to application of the conventional 2D Fourier transform. Those problems have

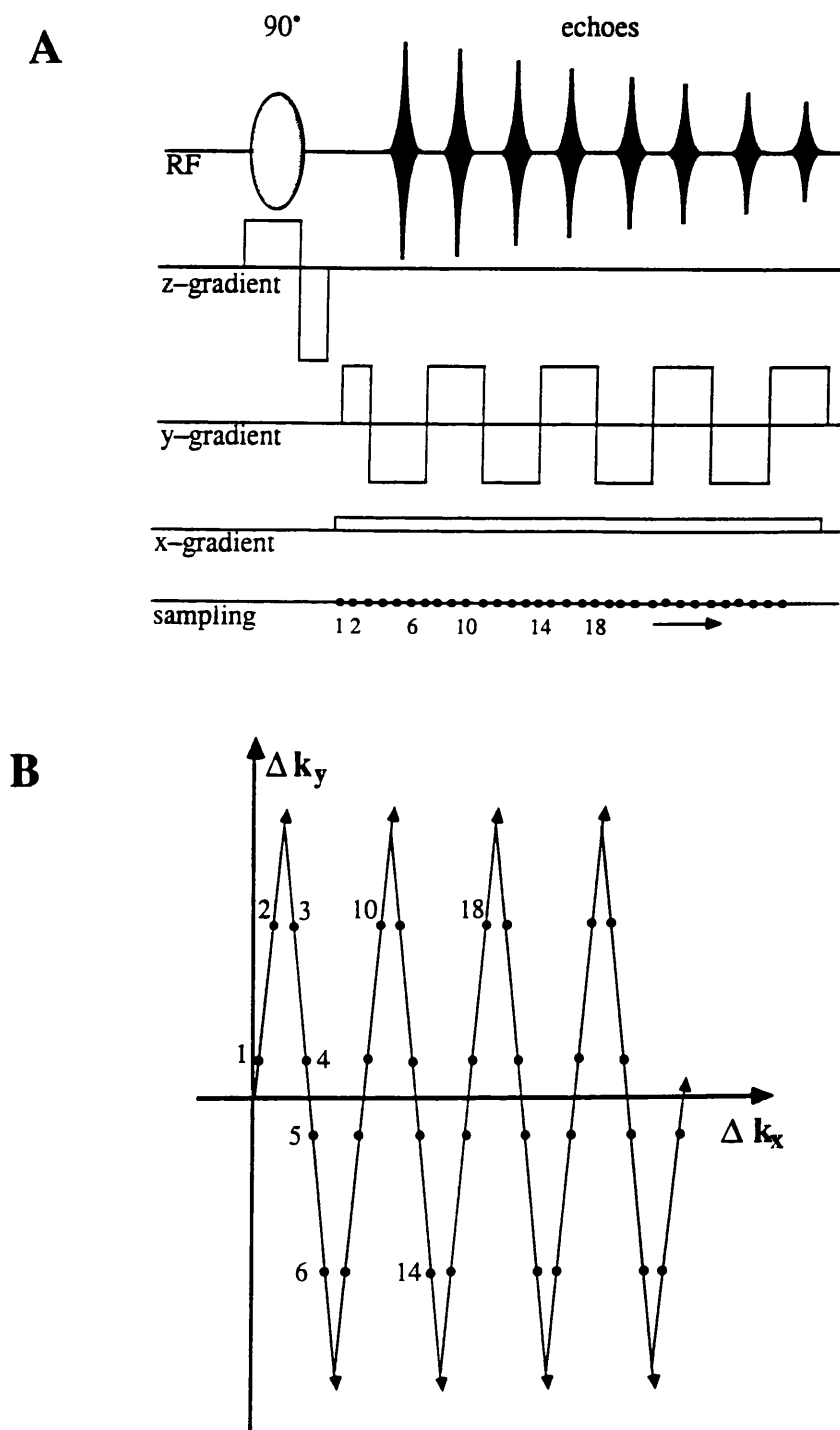


Figure 2.13. (A) Pulse sequence diagram for a 2D, echo-planar imaging experiment. The slice selection is performed along z by means of selective excitation. The maximum amplitude of the gradient echoes is progressively reduced due to the combined effect of the effective transverse relaxation and the dephasing induced by the constant gradient along x . (B) Schematic representation of the corresponding k -space grid. The arrows indicate the direction of the sampling.

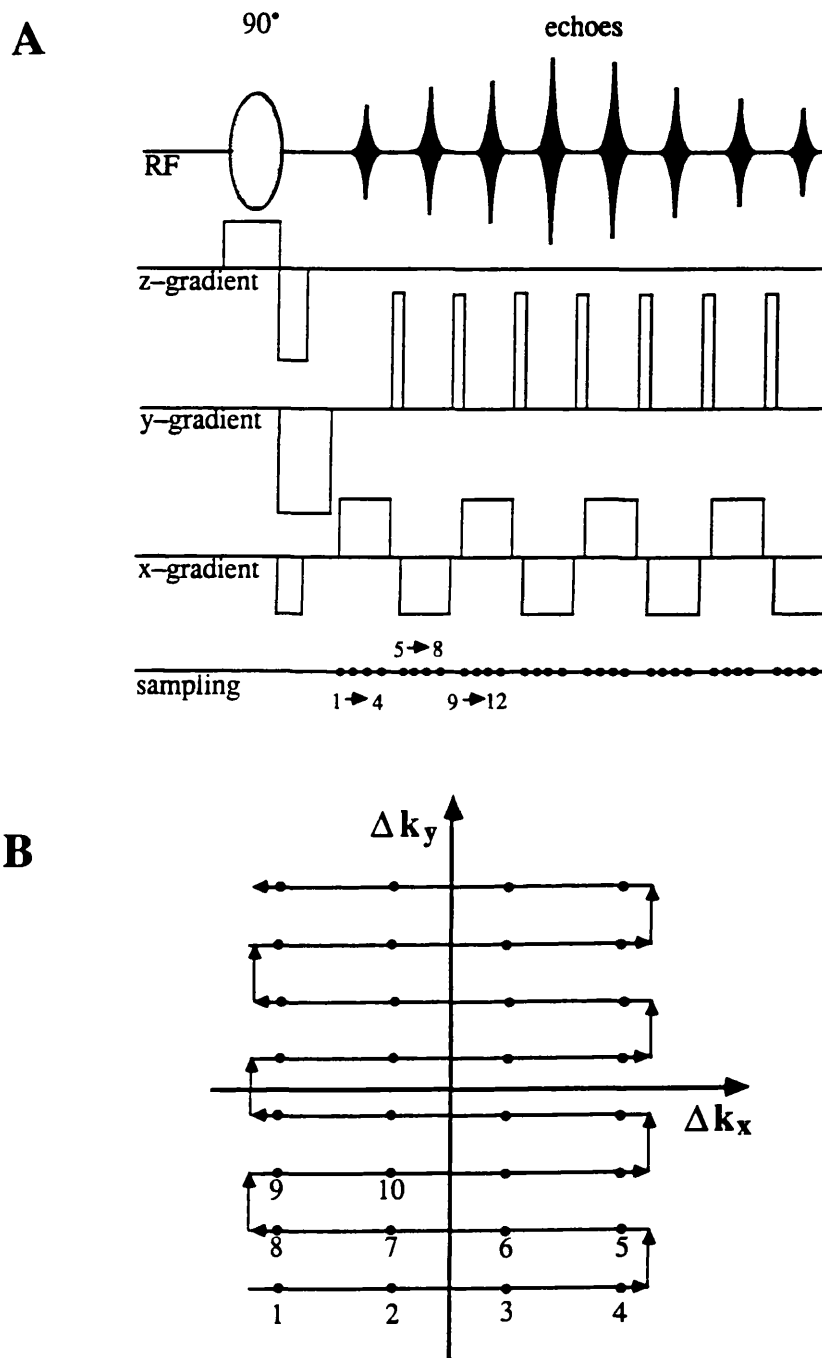


Figure 2.14. (A) Pulse sequence diagram for a modified 2D, echo-planar imaging experiment. The slice selection is performed along z by means of selective excitation. The maximum amplitude of the gradient echoes is progressively reduced due to the effective transverse relaxation, and is also modulated by the dephasing effects induced by the gradient along y which varies from maximum negative towards maximum positive values in the course of the experiment. (B) Schematic representation of the corresponding k -space grid. The arrows indicate the direction of the sampling.

been dealt with in several subsequent modifications of EPI, and such a pulse sequence diagram is shown in Fig. 2.14 together with the corresponding k-space grid [2.61]. The sampling occurs in the presence of one gradient only (for example along x) thus a line of the rectangular k-space grid is scanned in a fashion similar to the spin-warp experiment. The k-space echo along this direction is formed by gradient reversal which also creates a gradient spin echo. Then a very short, intense pulse of the second gradient, along y, forces the trajectory to the next k-space line. The echo formation in this direction is ensured by a preceding reversed gradient lobe, with time integral equal to half of the total time integral of the subsequent gradient pulses. Data re-arrangement is required to account for the reversed scanning of every alternate line.

2.11 NOISE

Combining Eqns. (2.10), (2.11) and (2.19), it is readily shown that the signal in the NMR experiment is proportional to the square of the Larmor frequency:

$$S \propto \omega_0^2 \quad (2.49)$$

This is one of the most important reasons for the development of high static magnetic field systems, both for spectroscopic and imaging studies. However, this simple equation does not take into account the noise that is generated during the experiment.

The noise in NMR can arise from various external sources, the sample, the receiver coil and the receiver electronic circuit. Although there may be some systematic sources of noise with characteristic frequency (e.g. some external transmission in the RF region which is strong enough to be picked up by the receiver), the noise in the NMR experiment generally arises from the randomly fluctuating currents due to the Brownian motion of electrolytes within the sample and the electrons within the receiver coil, and as such it is independent of the signal amplitude [2.62]. The noise, however, increases with static magnetic field strength, although there is some disagreement concerning the order of the dependence [2.3, 2.63–2.66]. In summary, and considering Eqn. (2.49), the dependence of the signal-to-noise ratio (S/N) for biological NMR imaging to the operating frequency is likely to be complex, being proportional to $\omega_0^{3/2}$ or $\omega_0^{7/4}$ at low static magnetic fields, switching to a linear dependence at higher field strengths [2.9].

The fact that the noise is independent of the NMR signal amplitude, while the signal is proportional to the imaging volume (Eqn. (2.38)), implies that the S/N is directly proportional to the voxel size, thus imposing limits to the maximum achievable spatial resolution for a specific experimental set-up [2.66]. The S/N can be improved by

signal averaging: the signal is coherent and will increase linearly with the number of the successive experiments that are co-added, however the random noise fluctuations increase proportionally to the square root of the number of co-added experiments [2.62, 2.67]. Although signal averaging increases the overall experimental time, it can also be combined with phase cycling procedures to cancel artifacts arising, for example, from imbalances in the two channels of the quadrature detector or from imperfect RF pulses (see Appendix 1).

Noise from sources such as thermal motion is expected to be statistically independent in the time domain and with a Gaussian probability density distribution centred around zero [2.68, 2.69]. In the 2D FT spin-warp image reconstruction technique used in this study, the Gaussian density distribution in the time domain will be also retained in both the real and imaginary parts of the Fourier transformed data [2.12]. In the modulus image, however, the probability density function of the noise magnitude shows a Rayleigh distribution [2.12]. Consequently, if σ is the standard deviation of zero mean noise in either the real or imaginary parts of the transformed signal, in the magnitude image and due to the Rayleigh probability density distribution, the mean value of noise will be 1.25σ with a standard deviation of 0.66σ [2.69]. This can result in a positive bias to measurements of low intensity signals which, however, can be removed by special correction procedures [2.70, 2.71].

CHAPTER 3

FAT AND WATER DIFFERENTIATION IN MRI

3.1 INTRODUCTION

The predominant signals in most medical, biological, and industrial applications of proton magnetic resonance imaging arise from water and lipid molecules. For example, an industrial application of MRI involves studying the properties of sedimentary rock in relation to the water/oil saturation state [3.1]. In biological systems, water is the principal component of most cells, and the basic constituent of extracellular fluids, such as plasma, lymph, urine, as well as interstitial, synovial, amniotic and cerebrospinal fluid. Protons in large structural proteins give rise to extremely broad lines, which, in the presence of a narrow intense water peak, are not observed in conventional MRI experiments, and lipids are the only "mobile" molecules, other than water, to contribute to a conventional, biological proton image [3.2]. In plants, lipids appear primarily in the form of oils, while in mammals they are deposited as fatty droplets in the cells of adipose tissue which is located throughout the body (e.g. bone marrow, subcutaneous, orbital, mammary or abdominal fat), and also within various organs, such as liver, kidney, and muscle [3.3].

The water molecule consists of two hydrogen atoms symmetrically bound to an oxygen atom via ionic bonds, Fig. 3.1. As the natural abundance of hydrogen is 99.985% H-1, hydrogen nuclei can be considered as protons. The symmetry of the molecule ensures that the two protons experience the same electronic shielding, therefore have the same Larmor frequency, i.e. the same chemical shift. Due to their chemical equivalence scalar coupling is not observed.

Lipids are water-insoluble organic molecules that derive their distinctive properties from the hydrogen-carbon nature of a major portion of their structure. Adipose tissue stores lipids in the form of fatty acids, mainly in triglycerides, Fig. 3.2 [3.3, 3.4], while crude oil mostly consists of alkanes, (C_nH_{2n+2}) [3.5]. The major contribution to the proton NMR signal arises from the methylene groups ($-CH_2-$) of the long fatty chains with minor contributions from unsaturated protons ($-HC=CH-$), and protons of the methyl group ($-CH_3$). The electronic shielding is slightly different for the protons in the various groups of the fatty molecules, and as a result they exhibit a range of chemical shifts, which, however, are distinctively different from that of water protons. Generally, the majority of resonance frequencies for the fat protons lie within a

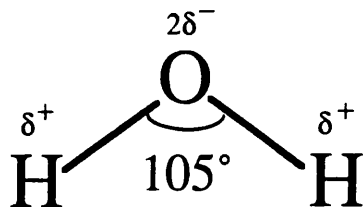


Figure 3.1. The structure of the water molecule, showing the polar bonds between the hydrogen and oxygen atoms.

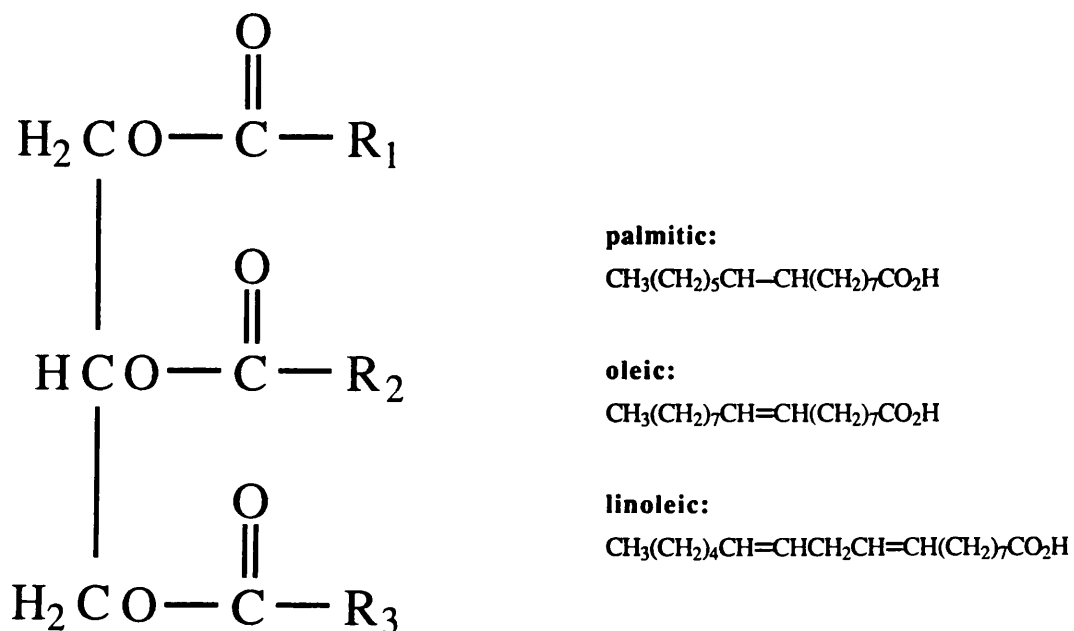


Figure 3.2. Molecular structure of a triglyceride. R1, R2, and R3 refer to the long carbon chains of three different fatty acids, which can be saturated or unsaturated and can occur in any combination. The formulae of 3 free fatty acids that are commonly found in adipose tissue are also shown.

~2 ppm range, centred ~3.6 ppm below the water resonance [3.6]. Figure 3.3 shows a proton NMR whole-body spectrum of a normal adult rat obtained at 4.7T, showing the water and fat peaks. Although coupling occurs between non-equivalent nuclei of the same or different isotopes, considering the low natural abundance of carbon-13 (the only carbon isotope with non-zero nuclear magnetic moment), scalar coupling should mainly be expected between the protons of the ethyl group (CH_3CH_2-), and the value of the J constant is in the range of 7-8 Hz [3.7].

Relaxation times are usually different for fat and water in tissues, a detailed review of the related literature is given in Ref. [3.8]. In particular, T_1 of fat is significantly shorter than the T_1 values of most of the non-fatty tissues. As measured at 1.5T, for example, T_1 values are about 260 ms for fat and in the range of 500-920 ms for various non-fatty tissues, such as brain parenchyma, kidney, spleen, liver, cardiac and skeletal muscle [3.8].

3.2 REASONS FOR FAT AND WATER DIFFERENTIATION IN MRI

The need to create separate maps of fat and water distribution has been apparent since the early days of MRI [3.9, 3.10]; the major reasons are summarized below.

3.2.1 Physiological Implications of Water and Fat Distributions

Normally, basic knowledge of anatomy is sufficient to interpret the areas on a clinical MR image that correspond to lean tissue, such as muscle and brain and to distinguish them from fatty tissue. However, in certain disease states there is some ambiguity as to whether signal from certain areas corresponds to fat or water protons or a combination of the two. Such examples include cases of fatty infiltration of the liver [3.11] or heart [3.12] as well as studies of bone marrow patterns with age or after transplantation and irradiation [3.13–3.15] or the distinction between various kinds of tumours on the basis of their lipid content [3.16]. Also, during the acute phase of multiple sclerotic plaque formation, free cholesterol esters that appear as the myelin sheath of the neuronal axon disintegrates may be the only "MRI visible" lipid within the central nervous system [3.17].

Calculation of the fat and fat-free content of the body is often desirable; an example, where MRI is perhaps the only applicable technique, is the study of fetal fat and its correlation to normal fetal growth [3.18]. Moreover, relaxation times in clinical MRI provide a source of additional diagnostic information and enable tissue characterization and quantitation as well as choice of optimum sequence parameters. However, this potential may be limited in cases where fat and water are present within

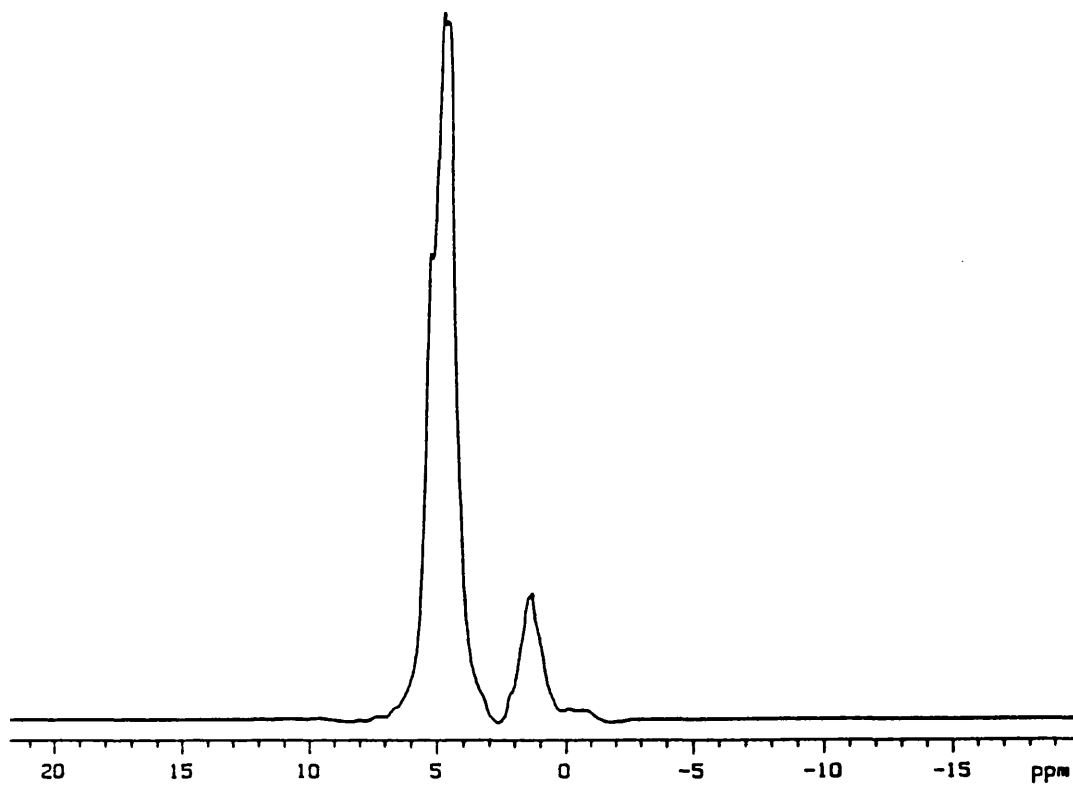


Figure 3.3. *In vivo* proton NMR spectrum of a normal adult rat (whole body) obtained at 4.7T, showing the "water" (at ~5 ppm) and "fat" (at ~1.5 ppm) resonance peaks.

the same imaging voxel due to their physiological distribution or as a result of chemical shift artifact.

3.2.2 Dynamic Range Problems

The sampling and digitization of the NMR signal is performed via an analogue-to-digital converter (ADC), which converts the initially analogue signal into a binary sequence [3.19]. The number of bits in the ADC defines the dynamic range of the receiver circuit. Typical ADCs have 12 or 16 bits, one of them being reserved for sign information. Therefore, the dynamic range for a 12-bit ADC, for example, is $(2^{11}-1):1$, or 2047:1. Generally, the gain of the receiver circuit is adjusted so that the signal of maximum intensity in a NMR experiment nearly fills the ADC, i.e. corresponds to an intensity of ~ 2000 for a 12-bit ADC. Then any signal of relative intensity less than 1 cannot be detected. The dynamic range of the system can be further limited by the display system, which for a typical computer screen corresponds to an 8-bit word, that is, 255:1. This limited dynamic range can result in loss of fine detail in intensity, especially when both fat and water signals are present.

Although the proton density is fairly similar in a wide range of body tissues, it is often significantly increased in fatty tissue (e.g. proton density ratio of 1.46:1 for fat and muscle, respectively, in the human thigh [3.20]), resulting in a higher NMR signal. Due to its significantly shorter T_1 , fat signal is often further enhanced relative to water when, for example, short repetition times are used in order to reduce overall imaging time. In the resulting conventional image, anatomical detail of fine structures near bulk fat deposits, e.g. renal cortex or optical nerve, may be lost. It should be noted that the dependence of signal intensity on proton density and relaxation times is specific to the pulse sequence involved. For the example of the spin echo experiment, the signal intensity is given by:

$$I = C \rho \exp(-TE/T_2) \{ 1 - \exp(-TR/T_1) \} \quad (3.1)$$

which is derived directly from Eqn. (2.48) by taking into account the partial relaxation of the magnetization in the interval TR between successive excitation pulses. Furthermore, it has recently been reported by several groups that imaging sequences which employ trains of refocusing pulses, such as fast spin echo methods [3.21], result in significant enhancement of the fat signal due to J-coupling effects while the water signal can be reduced because of magnetization transfer [3.22–3.24]. The opposite situation is also possible, when intense signal from water compartments "dynamically" suppresses low intensity signal from small fat deposits, for example in imaging of the

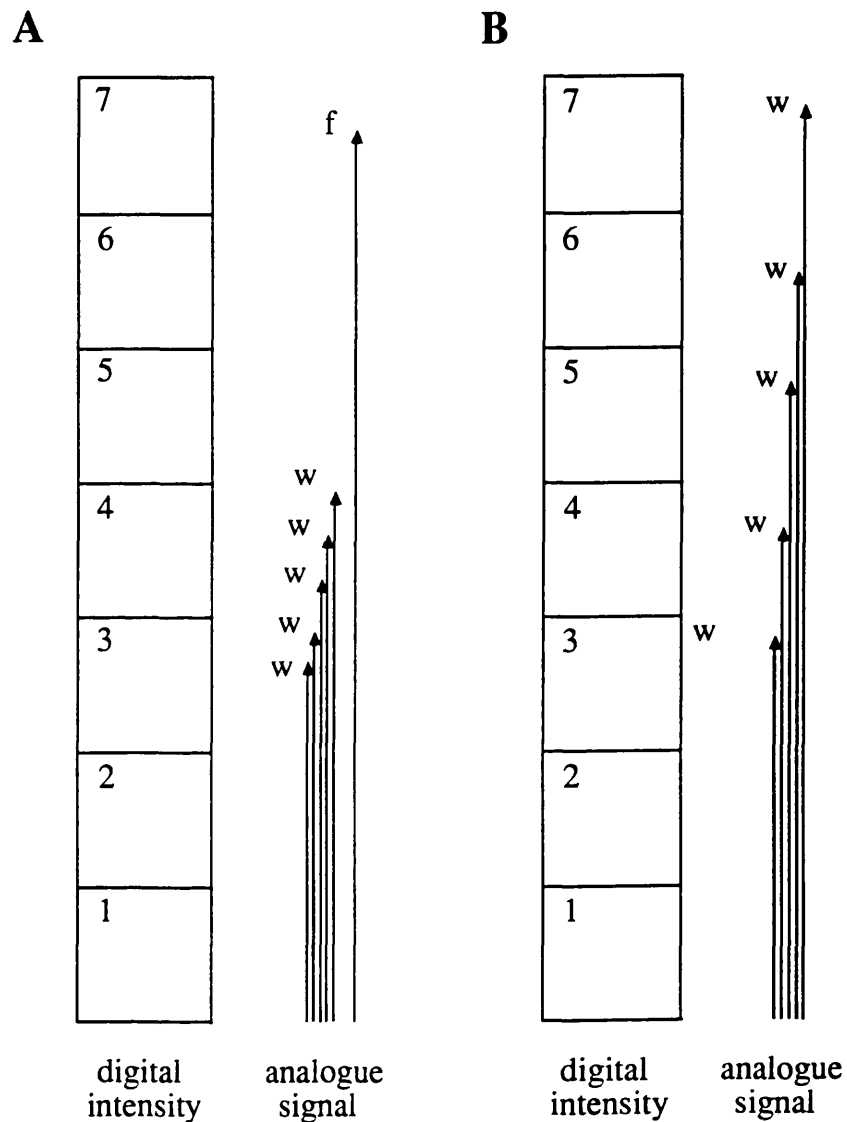


Figure 3.4. A diagrammatic representation of a 4-bit ADC, which results in a dynamic range of $2^3-1:1$, i.e. 7:1. **(A)** The gain is adjusted so that the maximum signal from fat (f) nearly fills the ADC, corresponding to a digital reading of "7". A range of weaker water signals (w) is dynamically suppressed to fit within a limited range of values, corresponding to a reading of either "3" or "4". **(B)** In the absence of fat, the same signal from water is adjusted to fit the whole ADC range, the individual components correspond to a range of digital readings.

lipid deposits in blood vessels. A diagrammatic representation of the problems due to limited dynamic range of the electronics is illustrated in Fig. 3.4.

3.2.3 Chemical Shift Artifacts

The chemical shift difference between fat and water protons can lead to image artifacts at boundaries when water-filled compartments or tissue are adjacent to fatty deposits. In clinical imaging, examples are the organs in the abdominal region surrounded by subcutaneous and peritoneal fat, breast, heart, intervertebral disks, optic nerve, and bone marrow [3.25]. These artifacts, usually referred to under the general term of chemical shift artifact, appear in various forms according to the spatial encoding technique involved in the imaging sequence, and their intensity generally depends on static magnetic field strength, gradient strength and pixel frequency resolution. Chemical shift artifacts primarily arise from k-space sampling schemes that "mix" spatial and spectral information. They can also be due to slice selection using selective irradiation, as well as echo amplitude modulation in gradient spin echo imaging sequences.

The description of image reconstruction through k-space sampling given in Chapter 2 is based on the assumption that the precession frequency of a spin is only related to its spatial location via the applied magnetic field gradients. A more complete k-space formalism, however, treats image reconstruction from NMR signals modulated by both spatial and spectral frequencies [3.26]. This generalized description takes into account the fact that the signal is actually a function of both spatial frequency and time, $S(\mathbf{k}, t)$. Therefore, the Fourier transform is a function of both spatial location and resonance frequency, $F(\mathbf{r}, \omega)$. The two variables are mixed only when sampled simultaneously. Since the time-domain is sampled during the course of signal acquisition, the mixing of the two variables occurs only in the k-space sampling schemes that involve traversing k-space during signal acquisition. It follows that the "mixing" is limited to the spatial direction that is sampled during signal acquisition.

In the reconstructed image, the inability to distinguish in this specific direction between the chemical shift and the frequency difference induced by a field gradient, will appear as a misregistration of the fat image relative to water. This can be calculated as follows: Considering the chemical shift of $\delta=3.6$ ppm between fat and water protons, their resonance frequencies in the absence of magnetic field gradients, $\omega_0(\text{fat})$ and $\omega_0(\text{water})$, respectively, obey the relationship:

$$\omega_0(\text{water}) = \omega_0(\text{fat}) + \Delta\omega \quad (3.2)$$

where $\Delta\omega$ can be expressed in terms of the chemical shift using Eqns. (2.11) and (2.16), and is given by:

$$\Delta\omega = \delta \gamma B_0 \times 10^{-6} \quad (3.3)$$

Consider a linear magnetic field gradient of amplitude G applied along the r direction. Expanding Eqn. (2.41) to account for chemical shifts, the linear frequency distribution created by the gradient is:

$$\omega(r) = \omega_0 + \gamma(1-\sigma) Gr \approx \omega_0 + \gamma Gr \quad (3.4)$$

where σ is the shielding constant of the species to be imaged. Water at position r would then exhibit a frequency $\omega(\text{water}, r)$ given by:

$$\omega(\text{water}, r) = \omega_0(\text{water}) + \gamma Gr \quad (3.5)$$

or, using Eqn. (3.2):

$$\omega(\text{water}, r) = \omega_0(\text{fat}) + \gamma G \left(r + \frac{\Delta\omega}{\gamma G} \right) \quad (3.6)$$

Equations (3.4) and (3.6) suggest that the water resonance at a spatial position r along the direction of the applied gradient is equal to the fat resonance frequency at a different position $\{r + (\Delta\omega/\gamma G)\}$, therefore the misregistration of the fat signal relative to water is given by:

$$\Delta r = -\frac{\Delta\omega}{\gamma G} = -\frac{\delta B_0}{G} \times 10^{-6} \quad (3.7)$$

This chemical shift artifact and the misregistration between fat and water signals is illustrated in Fig. 3.5. For the same resolution and field-of-view, increasing the gradient strength results in a smaller relative misregistration of the chemically shifted signals. As the static field and spatial resolution increase, the misregistration can become equivalent to several image pixels and create dark/bright rings in the interfaces of the two components [3.25]. Considering the examples of k -space sampling schemes presented in Chapter 2, for the spin-warp experiment of Fig. 2.12, and the echo planar sequence of Fig. 2.14, chemical shift misregistration appears only in the frequency encoding direction (x -axis in both figures), as for the remaining in-plane direction a particular value of k is reached prior to signal acquisition. Therefore the artifact will

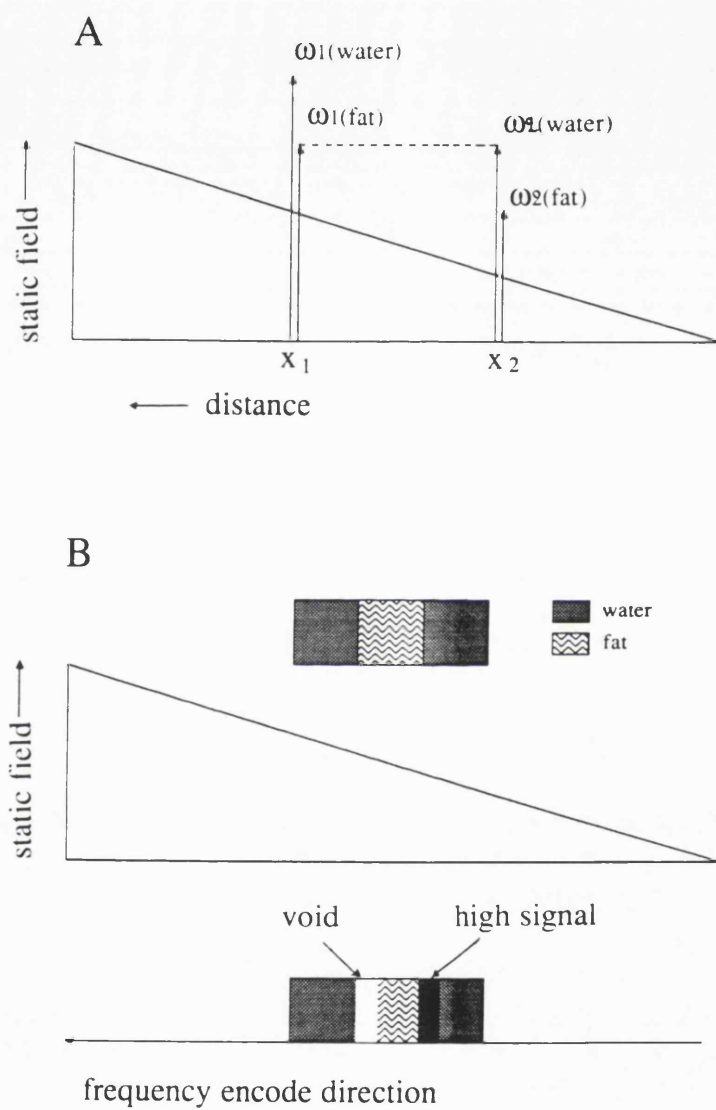


Figure 3.5. Diagrammatic representation of the chemical shift artifact. (A) Signal from fat protons at position x_1 can be misinterpreted as signal from water protons at position x_2 , as $\omega_1(\text{fat}) = \omega_2(\text{water})$. (B) A diagrammatic example of the relative misregistration and the bright/dark interface of fat and water images in the frequency encode direction due to the chemical shift artifact.

appear as the dark/bright interface of Fig. 3.5 along the frequency encoding direction. In the projection reconstruction technique of Fig. 2.11 and the echo planar sequence of Fig. 2.13, the misregistration occurs along all k-space trajectories, resulting in a blurring at the interfaces of the two components.

Additional boundary artifacts can appear when a gradient spin echo is used. Such an echo does not refocus the dephasing due to chemical shift differences. After excitation and during the entire echo time, TE, the two components precess at different resonance frequencies accumulating phase at different rates. The two components are in phase only if:

$$TE(\text{in-phase}) = \frac{2\lambda\pi}{\Delta\omega} \quad \lambda=0, 1, 2, 3, \dots \quad (3.8)$$

For any other values for the echo time, the signals from fat and water are out of phase at echo formation, and they become completely anti-phase for:

$$TE(\text{out-of-phase}) = \frac{(2\lambda+1)\pi}{\Delta\omega} \quad \lambda=0, 1, 2, 3, \dots \quad (3.9)$$

At the interfaces of fat and water compartments, voxels are likely to contain a mixture of both components, therefore, if the in-phase condition is not fulfilled the two components can combine destructively, resulting in boundaries of low signal intensities [3.27, 3.28]. Recently it has been reported that, at 1.5T, gradient echo techniques gave an unacceptable level of chemical shift artifact in the imaging of lumbar spine [3.29].

When slice selection is performed by application of a frequency selective pulse in the presence of a magnetic field gradient, the misregistration of fat and water signals as given by Eqn. (3.7) can lead to non-planar slices and erroneous superposition of anatomical structures from different positions along the slice selection direction [3.30, 3.31].

3.3 MRI TECHNIQUES FOR FAT AND WATER DIFFERENTIATION

Many MRI methods have been proposed that create separate fat and water images or suppress contribution from one or the other. To distinguish between the two components, the techniques take advantage of one or more of their several different responses in NMR, such as relaxation times, chemical shift or scalar coupling, as well as other chemical and physical differences.

3.3.1 Methods Based on Relaxation Time Differences

A commonly used technique in clinical MRI is the T₁-null method [3.20, 3.32], which is based on the inversion recovery sequence. A 180° RF pulse initially inverts the magnetization and T₁ relaxation causes it to increase from a negative value, passing through zero as it returns towards thermal equilibrium. If a 90° read-out pulse is applied at a time when the net magnetization is passing through zero, no transverse component is generated and hence no signal results. Since T₁ relaxation times of fat are usually much shorter than those of water in other tissues, the inversion time, TI, can be adjusted to minimize ^{either} contribution to the total signal. As all the pulses are slice selective, the effect of the pulse sequence is confined within a single slice and therefore, data from several slices can be obtained within the same repetition time by repeating the same regime using different frequency offsets for all the pulses [3.33] (see also Fig. 3.6.B). There are no special demands on field homogeneity, hardware or data processing and the technique can be easily performed in any NMR imaging system.

Non-fatty tissues, however, tend to exhibit a wide range of longer T₁ values [3.8], and it is rather difficult to find an inversion time where all water signal would be eliminated. Therefore, in most cases the water T₁-null method is applied for fluid water attenuation only [3.34, 3.35], and then it is known as FLAIR (FLuid Attenuated Inversion Recovery). The long inversion time generally required, however, increases the overall repetition time, while it allows only a few slices to be accommodated within every repetition time. The number of slices acquired can be increased by employing more time-efficient multi-slice acquisition schemes. For example, the inversion pulses for a number of slices can be applied during the inversion time of the first slice, while the imaging part of the sequence for all the inverted slices follows subsequently as a set [3.33], Fig. 3.6.C. Alternatively, the inversion pulse and the read-out part of the sequence can be applied without any inversion time delay and are repeated for the number of times that can fit into the repetition time, ensuring that each inversion pulse does not correspond to the slice that the immediately following imaging sequence selects, but to a slice of a later read-out experiment, the duration of the intermediate number of experiments allowing for the desired inversion time [3.36], Fig. 3.6.D.

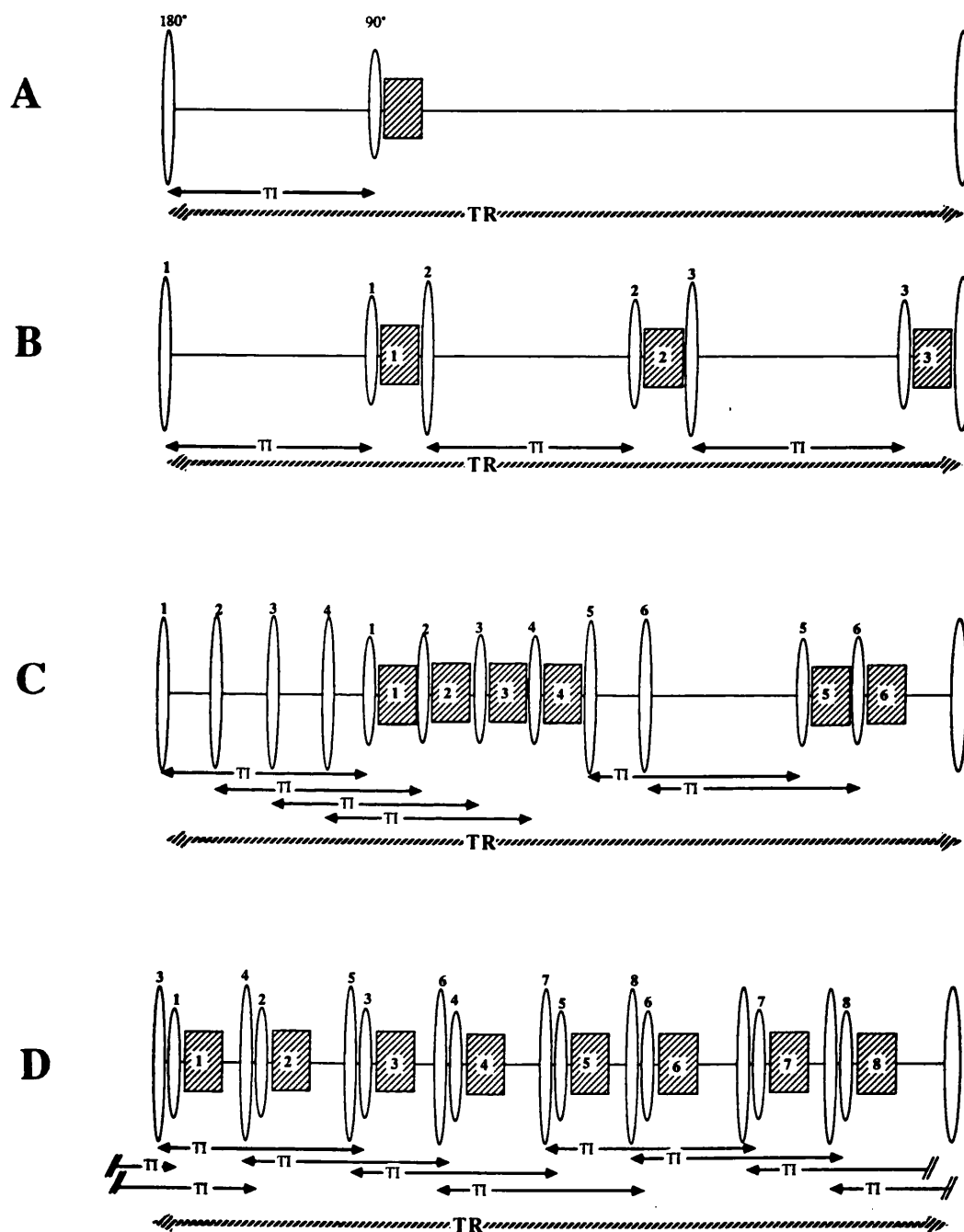


Figure 3.6. Diagrammatic representation of various slice selection schemes for the IR sequence. Only the inversion and excitation pulses are shown, while the shaded box represents the rest of the imaging experiment. All pulses are slice selective. The numbers above each pulse and within the box indicate the slice number. (A) Single slice sequence. (B) Conventional multi-slice scheme. (C) and (D) Multiplexed multi-slice schemes.

The T₁-null method is, however, most commonly used with short inversion times for fat suppression and in this case is known as STIR (Short inversion Time Inversion Recovery) [3.32]. STIR has become a very popular sequence in biomedical MRI since it not only suppresses the unwanted signal from fat but can also produce high T₁ contrast for the remaining water signal. Due to the short inversion time, the overall imaging time is comparable to that of the conventional imaging experiments, though attempts have been made to decrease it even further by reducing the repetition time [3.37] and the tip angle of the excitation pulse [3.38]. A major limitation, however, is the necessity for prior knowledge or estimation of the fat T₁ values which can be different in various anatomical locations or between different individuals [3.37]. Another drawback of the method is that the signal-to-noise ratio (S/N) may be greatly reduced relative to conventional spin echo images, as the water magnetization has partially relaxed when the 90° read-out pulse is applied. For example, in a clinical study [3.39], a STIR sequence with a repetition time of 1560 ms and an inversion time of 150 ms was used to suppress signal from orbital fat (mean T₁ of 215 ms) while imaging the optic nerve (white matter mean T₁ of 385 ms) at 0.5T. It can be calculated that the S/N ratio for this STIR image is only 37% of that for a spin echo image at the same repetition time.

Discrimination between fat and water on the basis of the transverse relaxation time is not commonly used, as their range of T₂ values in different tissue often overlap [3.8]. Nevertheless, a conventional multi-echo sequence can be used to calculate T₂ values for all the imaging voxels and thus discriminate between tissues of different T₂ range by appropriately windowing the resulting T₂-calculated image [3.40]. In cases where the T₂ values of the fat are known to be distinctively different from the surrounding tissues, this method may be used to produce separate fat and water distribution maps.

3.3.2 Chemical Shift Imaging

Separate fat and water images can be produced by a wide variety of pulse sequences that selectively image protons of a specific resonance frequency (chemical shift imaging), i.e. either protons from the water molecule or from the major groups of the fat molecule. It should be noted that a small proportion of adipose tissue does consist of water in the form of capillaries and ^{between} collagen fibers. In a proton spectrum, this water accounts to the ~31% of the fat protons, and the same composition can be assumed for each fatty tissue imaging voxel [3.41].

A number of chemical shift imaging techniques use selective irradiation where a narrow-band frequency selective pulse is applied in the absence of any magnetic field gradient. The frequency of the pulse and its spectral excitation profile can be adjusted to

allow either the water or the fat protons to be on resonance. The pulse is thus made effective over the entire imaging volume for spins of only one of the chemical species. Another group of chemical shift imaging techniques takes advantage of the phase difference created by the different precession rates of the excited, chemically shifted species. Finally, techniques have been devised that distinguish between the two components by virtue of the chemical shift artifact in the frequency encoding or slice selection direction during a conventional imaging experiment.

Selective Irradiation

A simple chemical shift imaging sequence using selective irradiation is shown in Fig. 3.7. The frequency selective 90° pulse applied in the absence of any gradient excites the spins of one of the two resonance peaks while slice selection is achieved during the refocusing 180° pulse [3.42]. Alternatively, chemical shift selection can be achieved during the refocusing pulse, with the 90° pulse being slice selective [3.43]. The effective difference between the two sequences is limited to hardware considerations. For example, eddy currents induced by switching off the gradients may degrade the static field homogeneity, thus necessitating a long delay prior to application of the chemical shift selective pulse. This delay can be more easily accommodated within the period before acquisition rather than the time $TE/2$ following excitation. Irrespective of the choice, two experiments are needed in order to create both fat and water images. If required, it is possible, however, to acquire both images during the same experiment, where water and lipid protons are excited sequentially by means of two frequency-selective 90° pulses at the appropriate frequency offsets. A single, slice-selective 180° refocusing pulse then generates two echoes, which occur with a time difference equal to the time separation of the excitation pulses [3.44]. The diagram of this pulse sequence is shown in Fig. 3.8. The two echoes appear in reverse order of the corresponding signal excitation, resulting in a differential T_2 weighting of the two images. The major drawback of these methods is that they are single-slice: as the chemical shift selective pulse is applied over the entire imaging volume, the sequence can only be repeated for different slice frequency offsets after time for the required longitudinal relaxation has been allowed.

Selective irradiation can also be used to saturate the signal from one component. First, a frequency selective 90° pulse is applied in the absence of any gradient to selectively perturb the spins from the unwanted resonance into the transverse plane. The conventional spin echo, spin warp experiment that follows is experienced only by the spins left unaffected during the first part of the sequence [3.45]. Saturation can be enhanced by the application of a magnetic field gradient (spoiling or spoiler gradient) immediately after the chemical shift selective pulse, to rapidly dephase the undesired

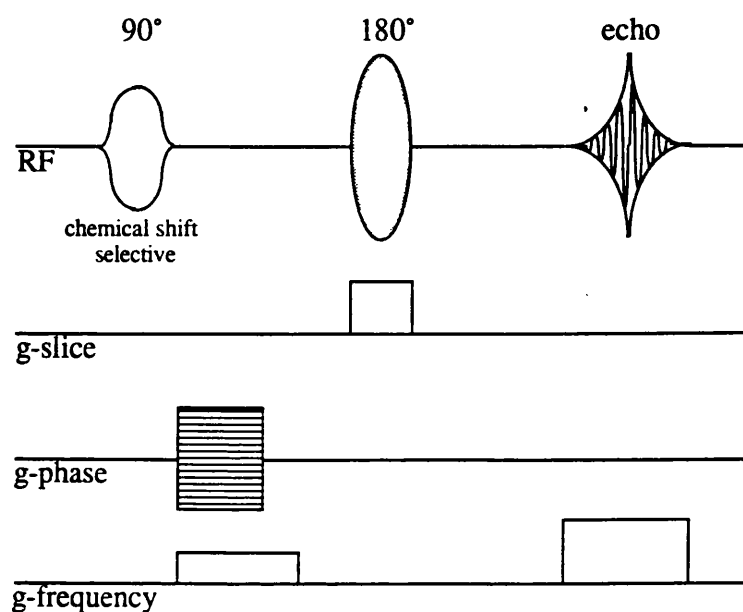


Figure 3.7. Simple chemical shift selective pulse sequence, where the chemical shift selection is achieved during radiofrequency excitation. The sequence selects a single slice and produces an image of either fat or water.

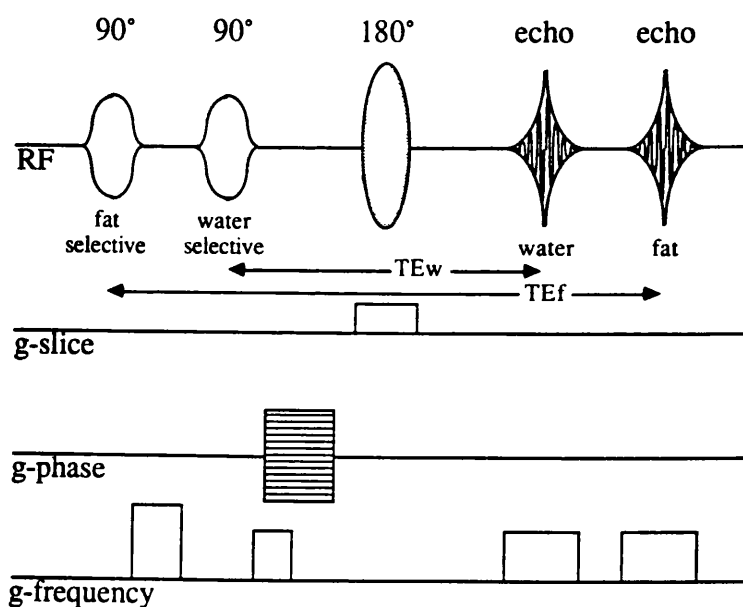


Figure 3.8. Double-pulse chemical shift imaging sequence. Fat and water protons are excited separately by the two chemical shift selective pulses. The sequence is single slice, but it produces both fat and water images simultaneously, though differentially T₂ weighted as indicated by the two different echo times TE_f (for fat) and TE_w (for water).

magnetization [3.46]. Finally, if the spin echo part of the sequence is repeated with different frequency offsets for the slice selective pulses, several slices can be obtained while spins with the unwanted chemical shift remain saturated [3.47]. It should be noted however, that as the saturated magnetization relaxes, it will gradually appear in later slices. It can be shown that the shorter the T_1 values of the saturated component (e.g. in fat suppression), the more pronounced the differential suppression across the slices. This problem may create confusion in clinical studies, especially as slices are often selected not in their spatial order but in a "first-odd-then-even" mode. In order to avoid this problem, most clinical systems use a modification of the initial presaturation method, where the chemical shift selective pulse and the subsequent spoiling gradient are applied before every slice selection. The penalty is the slightly increased overall imaging time (or reduced number of slices) and additional RF power deposition.

Selective irradiation can be also employed in stimulated echo (STE) imaging. The stimulated echo is formed at the end of a 90° - $TE/2$ - 90° - T_M - 90° - $TE/2$ pulse sequence [3.48]. In a typical STE experiment, the magnetization is initially tipped into the transverse plane by a first 90° pulse and it dephases during the time interval $TE/2$, at the same time phase encoding is performed. The following 90° pulse rotates the magnetization in a plane parallel to the longitudinal axis. During the time interval T_M the spins continue to precess (preserving the previously acquired phase information) while T_1 relaxation occurs. The third 90° pulse rotates once again the plane of precession, and the magnetization refocuses to form the stimulated echo after a further time $TE/2$. Only the spins that experience all three pulses will contribute to the stimulated echo. In general, any of the three pulses can be made chemical shift selective [3.49], and a schematic diagram of one such pulse sequence with an extension to multiple slice imaging is shown in Fig. 3.9. The first pulse performs the selection of the desired component, while repetition of the last pulse at different slice frequency offsets results in a multi-slice data set of stimulated echo images. It should be noted that as the delay T_M is different for the various slices, they will be differentially T_1 weighted. Selective irradiation in STE imaging may offer an additional approach to multi-slice chemical shift imaging. However, the method is not always favourable for clinical applications because of the major drawback inherent in STE imaging, namely the fact that the stimulated echo has only half the signal intensity of the echo created by the equivalent spin echo experiment.

In all the figures that show diagrammatic representations of pulse sequences using selective irradiation (Fig. 3.7-3.9), the frequency selective pulse has been drawn as a shaped Gaussian [3.50], which excites a Gaussian shaped range of frequencies. It should be noted, however, that a variety of other frequency selective pulses exist. Common examples include the long, weak rectangular [3.51] and the $\sin x/x$ (i.e. sinc)

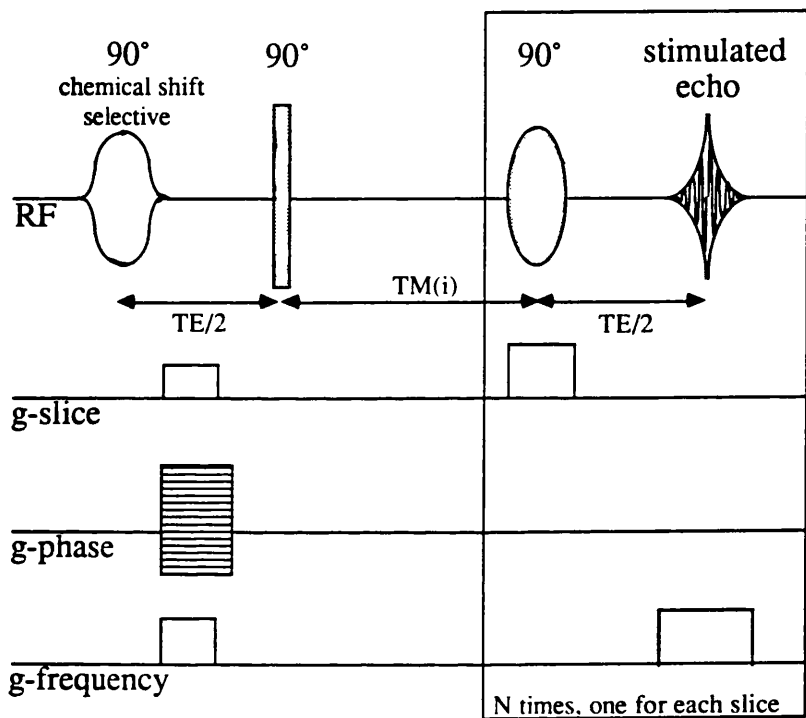


Figure 3.9. Stimulated echo pulse sequence for chemical shift imaging. The selection of the desired component is performed by the first, chemical shift selective pulse. Repetition of the last part of the sequence, within the box, for different pulse frequency offsets yields an N-slice set of images, each with a different TM, hence different T₁-weighted.

shaped [3.52] pulse. However, these may cause irradiation of unwanted frequencies since both exhibit an excitation pattern with sidelobes that may extend far from resonance. Selective pulses specially tailored to match the line-shape of the component in question have also been presented [3.53, 3.54]. Frequency selection can also be achieved without the necessity for shaped radiofrequency waveforms by the use of two or more short, rectangular pulses separated by an appropriate chemical shift evolution delay [3.55–3.57]. The simplest example of such a sequence involves the use of a $45^\circ\text{-}\tau\text{-}45^\circ$ pulse regime where the component of interest is placed on resonance and experiences a net 90° pulse whereas the resonance to be suppressed is allowed to evolve through 180° during τ therefore returning to longitudinal magnetization on application of the second pulse.

Asymmetric Spin Echoes

A large selection of chemical shift imaging techniques are based on "asymmetric" spin echo imaging sequences that use the phase difference induced in the excited spins of the two resonances, due to their different rates of precession, Fig. 3.10. In a $90^\circ\text{-TE}/2\text{-}180^\circ\text{-TE}/2$ spin echo sequence, immediately after the 90° pulse water and fat protons are aligned, i.e. they are in-phase. Because of the difference in their resonance frequencies, however, water protons will precess faster than fat protons and in the time interval $TE/2$ water protons will be at a phase of $\Delta\phi = (TE \Delta\omega)/2$ ahead of fat protons, where $\Delta\omega$ is the difference of angular frequencies between fat and water protons as given by Eqns. (3.2) and (3.3). Application of the 180° pulse reverses their relative positions, effectively placing the water spins at a $\Delta\phi$ phase behind fat. The fast precessing water spins progressively diminish this phase difference, and all protons are once again in-phase exactly after a further time $TE/2$, at the centre of the spin echo. Subsequently, they dephase and rephase again and the time interval for the in-phase and out-of-phase conditions is given by Eqns. (3.8) and (3.9). More specifically, the first time the two components will be out of phase after the formation of the spin echo is given by:

$$\Delta\tau = \frac{\pi}{\Delta\omega} \quad (3.10)$$

In order to create separate fat and water images, a spin echo imaging sequence can be used where the time delay between the refocusing 180° pulse and the acquisition is varied [3.58, 3.59]. The sequence is repeated twice and two images are collected. In the first image, acquired using the conventional spin echo mode (symmetric spin echo), fat and water protons are in-phase and the signal is the sum of both components.

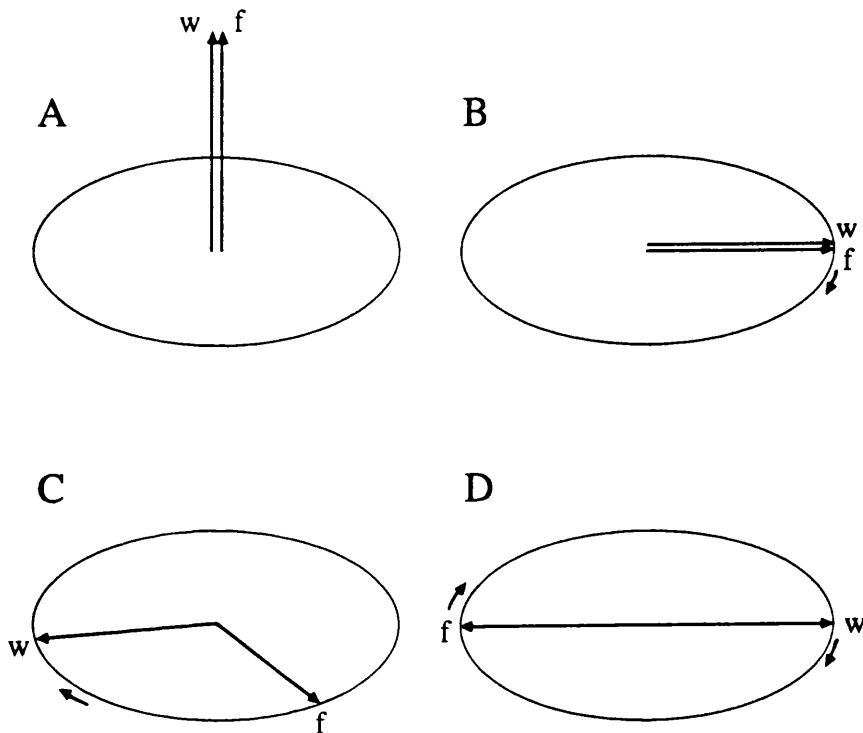


Figure 3.10. The phase difference induced in the excited spins of fat (f) and water (w) as they precess at different frequencies. Immediately after the equilibrium magnetization (A) is excited, both components are in phase (B). As the system evolves and the water protons precess faster than the fat protons a phase difference appears (C) and at a time $\Delta\tau$, or odd multiples thereof, the relative phase difference between fat and water magnetization is 180° (D).

Considering Eqn. (2.48), the signal intensity (e.g. phase corrected real part of the spin echo FT) can be expressed as:

$$I(\text{symmetric}) = K(w) \rho(w) + K(f) \rho(f) \quad (3.11)$$

where $\rho(f)$ and $\rho(w)$ are the proton densities of fat and water, respectively, while $K(w)$ and $K(f)$ encompass the constant C of Eqn. (2.48) and exponential terms that relate to the relaxation characteristics of each component. In the second experiment, the effective echo time is $TE + \Delta\tau$ (asymmetric spin-echo experiment), so that the fat and water magnetizations are 180° out of phase. Assuming on resonance condition with the water spins, the resulting signal can then be expressed as:

$$I(\text{asymmetric}) = K(w) \rho(w) - K(f) \rho(f) \quad (3.12)$$

Adding or subtracting the two images thus yields a water-only or fat-only image, respectively:

$$I(\text{symmetric}) + I(\text{asymmetric}) = 2 K(w) \rho(w) \quad (3.13a)$$

$$I(\text{symmetric}) - I(\text{asymmetric}) = 2 K(f) \rho(f) \quad (3.13b)$$

Problems with this technique may arise from inhomogeneous magnetic fields and magnetic susceptibility differences within the object, as well as flow and diffusion, all of which induce further regional phase differences. In order to overcome these problems, the data from the two experiments can be represented in magnitude mode prior to addition and subtraction. This, however, suffers from the "absolute value" artifact, where the data set that results from summation is always an image of the component which gives the stronger signal for each individual voxel. Similarly, the data set that results from subtraction depicts the component within each voxel that gives the weaker signal. For example, if Q represents the stronger signal and q the weaker signal, irrespective of the component, then $q < Q$, and assuming magnitude representation, Eqns. (3.11) and (3.12) yield:

$$|I(\text{symmetric})| = |Q + q| = Q + q \quad (3.14a)$$

$$|I(\text{asymmetric})| = |Q - q| = |q - Q| = Q - q \quad (3.14a)$$

Upon data summation or subtraction, Eqns (3.14) yield:

$$|I(\text{symmetric})| + |I(\text{asymmetric})| = 2 Q \quad (3.15a)$$

$$|I(\text{symmetric})| - |I(\text{asymmetric})| = 2 q \quad (3.15b)$$

To overcome this difficulty, various algorithms have been proposed to phase correct the original data, so that the asymmetric echo technique can be successfully used even in cases with regional field inhomogeneities and without employing magnitude mode representation. One such method involves acquiring an additional asymmetric spin echo corresponding to a 360° phase evolution between the two components [3.60]. Any phase differences between this additional image and the symmetric spin echo experiment are due exclusively to factors other than chemical shift, and they can be used for correction of the initial data sets. Similarly, phase errors can be recovered by information obtained when comparing the asymmetric echo corresponding to a 180° phase difference with an additional asymmetric echo that corresponds to a -180° (or 270°) phase difference [3.61]. Another technique determines the cause of phase changes based on the assumption that the field inhomogeneity (which is the primary cause of phase errors) varies smoothly over the image, whilst the boundaries between areas of fat and water cause sharp phase changes [3.62].

Another drawback of the asymmetric spin echo technique is that the overall imaging time required is at least double that of the conventional imaging methods, even in the case where only one of the components is of interest. To address this problem, multiple echo modifications have been proposed that allow for both in-phase and opposed-phase images to be acquired within the same experiment, thus reducing the imaging time of the conventional asymmetric echo technique by a factor of 2 [3.63, 3.64].

Methods Based on Chemical Shift Artifacts

Several methods have been devised that create separate fat and water images by utilising any of the various kinds of chemical shift artifact. A first group of techniques considers the relative displacement of fat and water signals along the spatial direction which is encoded during acquisition. Reversing the direction of the gradient involved causes the displacement to appear in the opposite direction. Separate fat and water images can then be obtained by data manipulation which involves subtraction of the two data sets, shifting to account for the relative chemical shift displacement and adding them back to the original sets. The method, first applied to projection reconstruction imaging [3.65, 3.66] and then demonstrated for the conventional spin warp experiment [3.67], requires linear magnetic field gradients and extensive data manipulation, which may

include iterative processes that can result in noise accumulation and registration errors [3.67].

The idea of the gradient reversal can also be implemented in the slice-selection direction [3.68, 3.69]. In a conventional spin echo experiment and because of the chemical shift separation between the two components, the slice where fat protons are excited is displaced with respect to the slice where water protons are excited, and this displacement is given by Eqn. (3.7). Increasing the static magnetic field strength causes an increase in the relative displacement to such an extent that, for certain values of the frequency bandwidth of the slice selective pulses, fat and water protons can be excited in completely separate slices where the "fat-slice" corresponds to lower slice-selection gradient values. If ΔF_p is the frequency bandwidth of the slice selective pulse (in Hz), the threshold condition for selecting fat and water in slices that do not overlap is expressed by:

$$\Delta F_p \leq \frac{\Delta\omega}{2\pi} \quad (3.16)$$

or, using Eqn. (3.3):

$$\Delta F_p \leq \frac{\delta \gamma B_0}{2\pi} \times 10^{-6} \quad (3.17)$$

If the slice-selection gradient is reversed during the 180° pulse, fat and water protons will again experience the pulse in separate slices, only this time the "fat-slice" will be in the reverse direction (always corresponding to lower slice-selection gradient values). By properly adjusting the transmitter frequency for the 180° pulse, one of the chemically shifted species is irradiated in two different slices by the 90° and 180° pulse respectively, while the spins of the remaining chemical shift are affected within the same slice by both pulses. Only the spins that experience both pulses are refocused during acquisition, while signal from the other component is eliminated. The technique requires good static field homogeneity and gradient linearity and can function in a multi-slice mode.

Spectroscopic Imaging

In the group of chemical shift imaging methods one should also include spectroscopic imaging sequences where a complete NMR spectrum is obtained from each imaging voxel and a spatial map of any of the spectral lines can be reproduced [3.70, 3.71]. A diagram of such a sequence is shown in Fig. 3.11, where spatial encoding within the selected slice is performed by two independently incremented phase

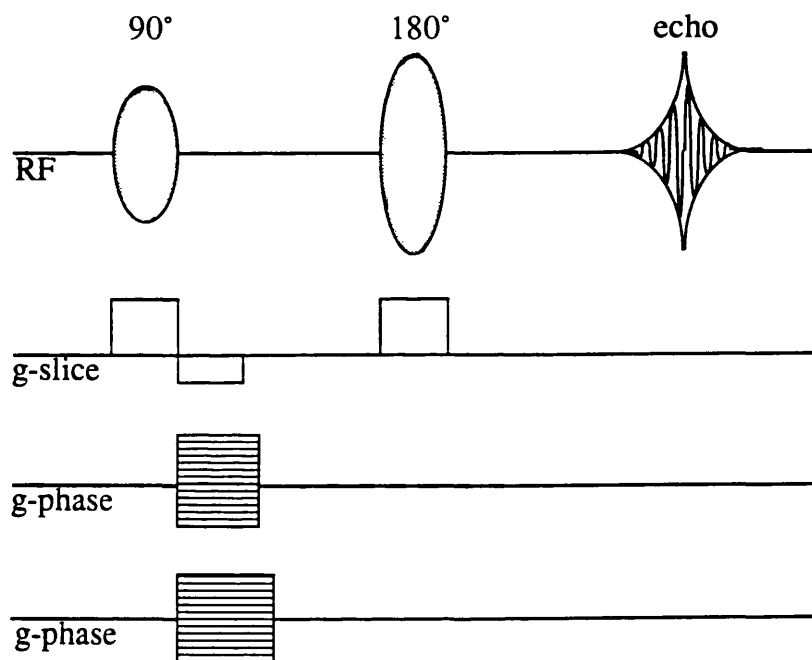


Figure 3.11. Pulse sequence for 2D spectroscopic imaging. The spatial encoding within each slice is achieved by two independently stepped phase-encoding gradients and the signal is acquired in the absence of any gradient, thus giving spectral information for each imaging voxel.

encoding gradients. The signal is acquired in the absence of all gradients and, on three-dimensional Fourier transformation, gives the spatial distribution of each spectral line. Spectroscopic imaging techniques, although providing extra spectral information, tend to require long imaging times to achieve acceptable spatial resolution. Such techniques can be justified when mapping of several resonance frequencies is required but they are not favoured for differentiation of simple, two component fat and water systems.

3.3.3 Coupled Spin Imaging

To overcome the requirement for both good static field homogeneity and high spectral resolution in many chemical shift imaging methods, a number of techniques that exploit the field independent parameter of scalar coupling (J) between protons in some groups of the fat molecule have been reported. The splittings in the fat peak due to proton spin-spin coupling have a mean frequency difference of $J \approx 7$ Hz. Following a 90° excitation pulse coupled spins precess at different rates (difference of $2\pi J$ in radians) in a similar way as that described in Fig. 3.10. Provided that a refocusing 180° is experienced by all coupled spins in question, the spin-spin coupling is not affected and the dephasing of the coupled spins continues during the entire echo time in a conventional spin echo sequence [3.72]. Following Eqn.(3.9), at echo times given by:

$$\text{TE}(\text{out-of-phase}) = \frac{2\lambda+1}{2J} \quad \lambda=0, 1, 2, 3, \dots \quad (3.18)$$

the two frequency components of the coupled spins are exactly out of phase and they cancel each other. At any other time they produce a net vector sum, the maximum being when they are exactly in phase, i.e. for echo times being an integer multiple of $1/J$, see Eqn. (3.8). It is apparent that subtraction of two conventional spin echo images acquired with two different echo times to correspond to the in-phase and out-of-phase condition for the coupled spins results in an image of the distribution of coupled spins. Both in-phase and out-phase images can be acquired in one sequence repetition using a four echo, multiple echo sequence [3.73]. Although the resulting coupled spin image gives the spatial distribution of fat, S/N is relatively poor as only a fraction of the fat protons contribute to the image. Furthermore, as the echo time for the in-phase condition must be at least of the order of ~ 150 ms (i.e. $1/J$, for a mean J of 7 Hz), the S/N can be further degraded due to T_2 relaxation.

More elaborate pulse schemes have also been used to exploit the phenomenon of multiple quantum coherence transfer in order to suppress the signal from water and other non-coupled spins [3.74–3.76]. But as with the previously mentioned method, the fat images are derived by difference techniques whether by direct subtraction of image data sets or phase cycling of the receiver to leave only the desired component. Therefore

these methods are inherently sensitive to problems relating to motion and dynamic range. Finally, a water image can only be produced indirectly through further data manipulation.

3.3.4 Methods Based on Other Physical Parameters

In addition to conventional fat/water differentiation techniques discussed so far, there have been other recent MRI studies that explore chemical and physical differences of the two components. In a study reporting the first MR images of natural abundance carbon-13 (C-13) in biological tissues [3.77], images from an oxtail were shown to closely correlate with fat-only, proton images. However, the limitations connected with C-13 MRI, which include low sensitivity, low concentration and coupling, may prohibit its extensive use for fat imaging. A more recent, promising approach that involves the use of diffusion weighted imaging to suppress the mobile tissue water relative to less mobile lipids has been reported. The technique has been used to produce MR images of lipid deposits in atherosclerotic lesions of excised human aorta [3.78].

3.4 DISCUSSION

Fat and water imaging by magnetic resonance techniques is now commonplace in the clinical environment. The T₁-null technique is commonly used in clinical imaging of various organs and regions, such as the musculoskeletal system [3.79]. Asymmetric spin echo methods are also popular, recent examples being the imaging of prostatic tumours [3.80] and the studies of bone marrow in Hodgkin's disease patients receiving radiotherapy [3.81]. Selective irradiation methods for chemical shift imaging generally require longer imaging time since most of them are single slice protocols, therefore they are not extensively used. However, selective presaturation can function in a multi-slice mode, and has therefore been used to suppress fat in a variety of clinical studies, for example in the imaging of focal liver disease [3.82]. It has also been reported as a useful tool for differentiating benign lipomas from malignant tumours on the basis of their fat content [3.83]. Coupled spin filtration techniques, although not widely used, have been applied to studies of the nervous system during demyelinating disease [3.17]. With the advent of high field systems, the principle of gradient reversal in the slice selection direction in order to select fat and water in two different slices has recently become more popular. It has already been shown to be particularly useful for lipid suppression in MR angiography [3.84]. However, no individual method has yet proven to be successfully applicable to all anatomical regions and on every system configuration. Table 3.1 summarizes the different groups of methods for fat and water differentiation and highlights the major advantages and disadvantages of each regime.

A potential approach to multi-slice chemical shift imaging is the use of the recently designed two-dimensional pulses which select both a desired slice thickness and the required chemical shift simultaneously using an elaborately shaped radiofrequency pulse in the presence of an oscillating magnetic field gradient [3.85]. Hybrid techniques that combine the asymmetric spin echo experiment with an inverting pulse [3.86] or frequency selective irradiation [3.87] have been proposed to enhance the suppression of both fat and motion artifact, although they may compound the limitations of each individual method. Two related pulse sequence schemes have recently been proposed to completely cancel the signal from fat tissue (as opposed to fatty cells only) [3.41]. This study takes into account the fact that the water protons of fatty tissue amount to ~31% of the total fat protons for each fatty tissue imaging voxel. Partial chemical shift selective inversion of the fat resonance creates inverted fat magnetization equal in magnitude but with opposite sign to the water component in the same voxel. Alternatively, fast repetition of the selective, partial inversion pulse creates a steady-state condition for the fat magnetization (see also Appendix 2) with a value equal to the water component of the same voxel. A subsequent asymmetric spin echo experiment adjusted to correspond to the out-of-phase condition cancels the signal from fatty tissue.

As high magnetic field strength systems are becoming more popular, the need for fat and water differentiation in order to avoid chemical shift artifacts is increasing. At the same time, the improved spectral resolution favours chemical shift imaging techniques, although the additional imaging time often required still imposes limitations. Hence, future prospects lie with the combination of chemical shift selection with high speed imaging techniques. Such sequences have already been proposed [3.88–3.91] and their further investigation and application to elucidate the extent of disease in mankind will dictate their long term popularity. Inevitably, different regimes will be optimal for the observation of different conditions.

TABLE 3.1		
METHOD	PROS	CONS
T1-null Method [3.20, 3.32]	<ul style="list-style-type: none"> * no special requirements for high or homogeneous static magnetic field * multiple-slice * high T1 contrast 	<ul style="list-style-type: none"> * not true fat- or water-only images, but suppression of component with certain T1 * prior knowledge/estimation of T1 values required * may result in poor S/N
T2-calculated Images [3.40]	<ul style="list-style-type: none"> * no special requirements for high or homogeneous static magnetic field * multiple-slice 	<ul style="list-style-type: none"> * not true fat- or water-only images, but images of components with certain T2 * range of T2 values for fat and water often overlap
Selective Excitation [3.42–3.44]	<ul style="list-style-type: none"> * true fat- or water-only images 	<ul style="list-style-type: none"> * requires static field high and homogeneous enough to resolve the two resonances * single-slice
Selective Excitation Using Stimulated Echo Imaging [3.49]	<ul style="list-style-type: none"> * true fat- or water-only images * multiple-slice 	<ul style="list-style-type: none"> * requires static field high and homogeneous enough to resolve the two resonances * differential T1 weighting across the slices * inherent poor S/N
Selective Suppression [3.45–3.47]	<ul style="list-style-type: none"> * true fat- or water-only images * multiple-slice 	<ul style="list-style-type: none"> * requires static field high and homogeneous enough to resolve the two resonances * may result in differential suppression across the slices

Table 3.1 continued...

Table 3.1 ...continued...

METHOD	PROS	CONS
Asymmetric Spin-Echo [3.58]	<ul style="list-style-type: none"> * true fat- or water-only images * lower static field requirements than most other chemical shift imaging techniques * multiple-slice 	<ul style="list-style-type: none"> * phase-correction algorithms, relatively extensive post-processing which may result in degradation of the image motion artifacts * at least two experiments required even if only one component is of interest * may suffer from dynamic range problems
Asymmetric Multiple-Echo Spin-Echo [3.63]	<ul style="list-style-type: none"> * true fat- or water-only images * lower static field requirements than the other chemical shift imaging techniques * multiple-slice * inherent B_0 information available for phase-correction 	<ul style="list-style-type: none"> * phase-correction algorithms, relatively extensive post-processing * data-manipulation may result in degradation of the image by motion artifacts * may suffer from dynamic range problems
Gradient Reversal in Slice Selection Direction [3.68]	<ul style="list-style-type: none"> * true fat- or water-only images * multiple-slice 	<ul style="list-style-type: none"> * requires static field high and homogeneous enough to resolve the two resonances * requires gradient linearity * slice number and thickness limitations

Table 3.1 ...continued...

Table 3.1 ...continued.

METHOD	PROS	CONS
Spectroscopic Imaging [3.70, 3.71]	<ul style="list-style-type: none"> * true fat- or water-only images * multiple-slice * extra spectral information 	<ul style="list-style-type: none"> * requires static field high and homogeneous enough to resolve the two resonances * longer imaging times to achieve the same spatial resolution * relatively extensive post-processing (3D)
Coupled-Spin Imaging [3.73–3.76]	<ul style="list-style-type: none"> * no special requirements for high or homogeneous static magnetic field 	<ul style="list-style-type: none"> * data-manipulation may result in degradation of the image by motion artifacts * may suffer from dynamic range problems
C-13 Imaging [3.77]	<ul style="list-style-type: none"> * water-excluded images 	<ul style="list-style-type: none"> * inherent limitations, such as low sensitivity, low concentration, scalar coupling * no water-only images
Diffusion-Weighted Imaging [3.78]	<ul style="list-style-type: none"> * fat images * multiple-slice 	<ul style="list-style-type: none"> * poor S/N * motion artifact * no direct water-only images

Table 3.1. A summary of the main advantages and disadvantages of conventional magnetic resonance imaging techniques for fat and water differentiation.

The "title" for each subcategory is followed by the original references relating to that method.

CHAPTER 4

"SLICE CYCLING" TECHNIQUES FOR THE CHEMICAL SHIFT SELECTIVE PRESATURATION SEQUENCE

4.1 INTRODUCTION

Selective presaturation chemical shift imaging is a popular method for fat and water differentiation in clinical MRI, as it provides water or fat suppressed multi-slice data sets in an overall imaging time comparable to that of the conventional spin echo experiment. The multi-slice version of the method was initially proposed [4.1] as shown in Fig. 4.1, with a single presaturating pulse followed by a series of spin echo experiments for different slice offsets, and will be referred to as PRESAT-1 hereafter. However, the major limitation of this technique is that as the saturated magnetization relaxes, it gradually re-appears in later slices. This differential suppression across the slices is most pronounced for short T₁ components, for example fat. The problem becomes more complex, when, in order to minimize saturation effects due to possible overlapping of adjacent slices, the slices are selected not in their spatial order but in a "first-odd-then-even" mode. Furthermore, differential suppression can be a major problem for certain image processing algorithms, such as contour detection and segmentation techniques that are based on thresholding [4.2]. In such applications, reduction of intense signals is often desired to avoid dynamic range problems, but differential variation of the suppression imposes limitations to the threshold values used to characterize and follow different contours and structures across slices.

In order to avoid this differential suppression, most clinical systems use a modification of the sequence, shown in Fig. 4.2, and referred to as PRESAT-2 hereafter. In this sequence the chemical shift selective pulse and the subsequent spoiling gradient are applied before every slice selective spin echo experiment, thus ensuring the same suppression of the unwanted component across the slices. The sequence, however, has two limitations:

- (i) It can result in increased imaging time (or, alternatively, less slices available), due to the extra time required for presaturation pulses and gradients prior to each slice selection. The minimum duration of this presaturation is typically in the order of 10-20 ms. For example, a Gaussian pulse with a frequency bandwidth of approximately 4 ppm is in the range of 2-20 ms, for static magnetic fields of 4.7-0.5 T, respectively. The minimum possible duration of the spoiling gradient can be calculated considering the minimum gradient time integral required to create a

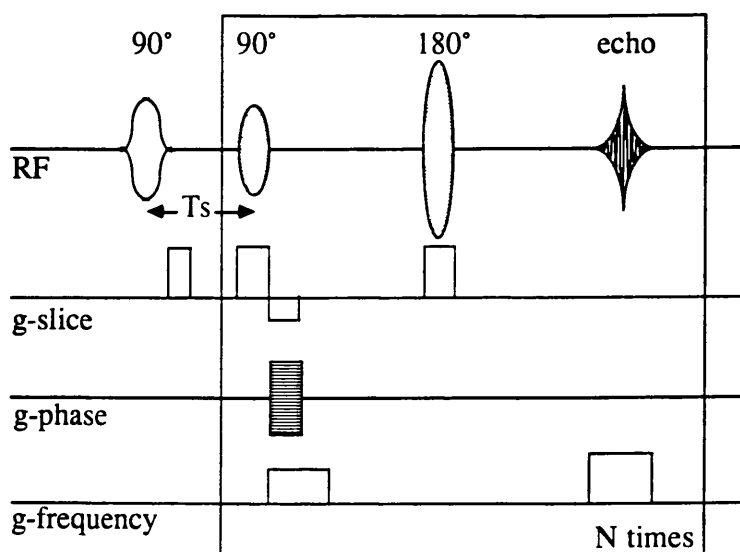


Figure 4.1. Pulse sequence diagram for the PRESAT-1 method. The initial chemical shift selective pulse and the subsequent spoiler gradient saturate the unwanted component. A series of spin echo experiments follow to select different slices.

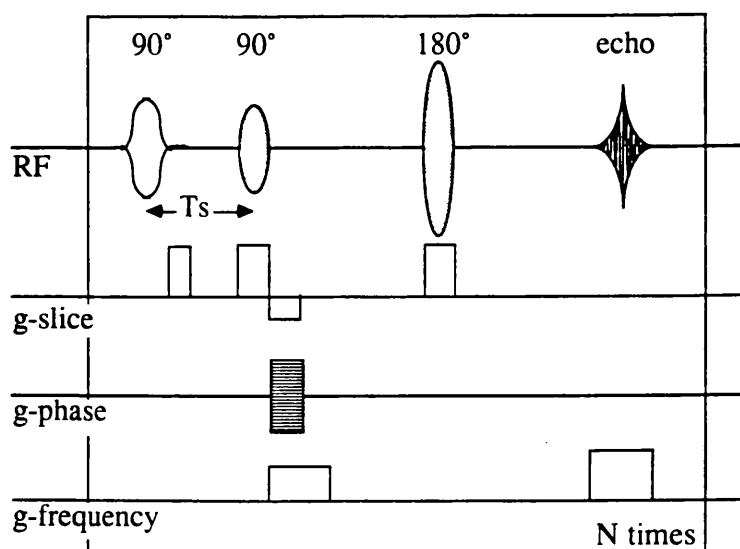


Figure 4.2. Pulse sequence diagram for the PRESAT-2 method. The saturating chemical shift selective pulse and the subsequent spoiler gradient are repeated before each one of the spin echo experiments performed to select different slices.

spread of magnetization phases that average to zero over the size of the voxel in the direction of the gradient application. In proton imaging, for a typical example of 1mm voxel dimension in the direction along which the spoil gradient is applied, and a gradient strength of 10mT/m, the minimum spoil gradient duration is approximately 2.5 ms. Therefore, a typical duration for the presaturation part is usually less than 30-40% of the total sequence duration when a spin echo regime is employed (assuming typical echo times of 30 ms and longer). In a gradient echo experiment, however, with a typical echo time of 10 ms, repetition of the presaturation part prior to each slice selection effectively doubles the sequence duration.

- (ii) The second limitation of the PRESAT-2 sequence concerns the extra power dissipated in the sample due to the additional pulses. This power is proportional to the square of the tip angle of the pulse [4.3, 4.4]. Assuming that the duration of the chemical shift selective pulse is similar to the slice selective ones, repetition of the saturating pulse prior to each slice selection accounts for the ~17% of the total RF power deposition when a spin echo is employed. However, if a gradient echo experiment is performed, the presaturating pulses represent 50% of the total power dissipated, which may be unacceptable.

In this chapter, two slice selection cycling procedures are proposed for the PRESAT-1 sequence that reduce the differential suppression across the slices without use of additional saturation pulses. Both techniques take advantage of the additional repetitions of the sequence often required to enhance signal-to-noise ratio in high resolution imaging, and to allow for phase cycling procedures (see Appendix 1). The principle of the proposed methods is that in every sequence repetition, the slice selection order is altered. The result is that the differential suppression is "distributed" differently across the slices, and is eventually "smoothed out" after signal averaging. The proposed slice cycling schemes are particularly beneficial in high resolution imaging where many averages are generally required. In such cases a large number of slices is usually desired (to give a similarly high resolution in the slice selection direction), while gradient echoes are often employed to keep the overall experimental time within reasonable limits. In such cases, PRESAT-2 would result in significant increase of both experimental time and power deposition. In this study, the proposed cycling procedures are evaluated using phantoms and compared to the two conventional presaturation schemes, for both water and fat suppression.

4.2 THEORETICAL ANALYSIS

The longitudinal magnetization $M_z(t)$ at time t after a 90° pulse can be calculated by integrating Eqn. (2.13), and is given by:

$$M_z(t) = M_0 \left[1 - \exp\left(-\frac{t}{T_1}\right) \right] \quad (4.1)$$

where M_0 and T_1 are the thermal equilibrium magnetization and the longitudinal relaxation time, respectively. (A more detailed treatment for the general case of longitudinal magnetization after a train of β° pulses is given in Appendix 2.)

Consider a set of N slices with spatial position indicated as 1, 2, 3, ..., n , ..., N . For simplicity, it is assumed that the slices are selected in their spatial order and not in the "first-odd-then-even" mode. Applying Eqn. (4.1) for the initially saturated component in the PRESAT-1 sequence of Fig. 4.1, the relaxed longitudinal magnetization $M_1(n)$ at the beginning of the n th subsequent spin echo experiment which corresponds to the n th slice is given by:

$$M_1(n) = M_0 \left[1 - \exp\left(-\frac{T_s + (n-1)(TE+T_D)}{T_1}\right) \right] \quad (4.2)$$

where T_s is the interval between the presaturating pulse and the excitation pulse in the following spin echo experiment, TE the echo time and T_D the delay between successive spin echo experiments. In theory, no extra delay is required between signal acquisition and the next 90° pulse, therefore T_D should be equal to the second half of the acquisition time. In practice, however, it is possible that a considerable delay between successive experiments is required to allow, for example, for data transfer or balancing the RF channel duty cycle. The delay T_s is at least equal to the spoil gradient duration, although it may be longer in order to ensure that any eddy currents from switching off the spoil gradient will not degrade the selection of the following slice. Figure 4.3.A shows $M_1(n)$ plotted as a function of the number of spin echo experiments, i.e. number of slices, for a set of timing parameters also used in the experimental evaluation that follows: $T_s=25$ ms, $TE=30$ ms, $T_D=30$ ms, and $T_1=280$ ms. The variation in the relaxed longitudinal magnetization across the slices is even more complicated, and therefore confusing, if the "first-odd-then-even" slice selection scheme is assumed, as shown in Fig. 4.3.B. In PRESAT-2, by comparison, the recovered longitudinal magnetization of the saturated component is the same for every slice and depends only on its T_1 value and the time interval T_s :

$$M(n) = M_0 \left[1 - \exp\left(-\frac{T_s}{T_1}\right) \right] \quad (4.3)$$

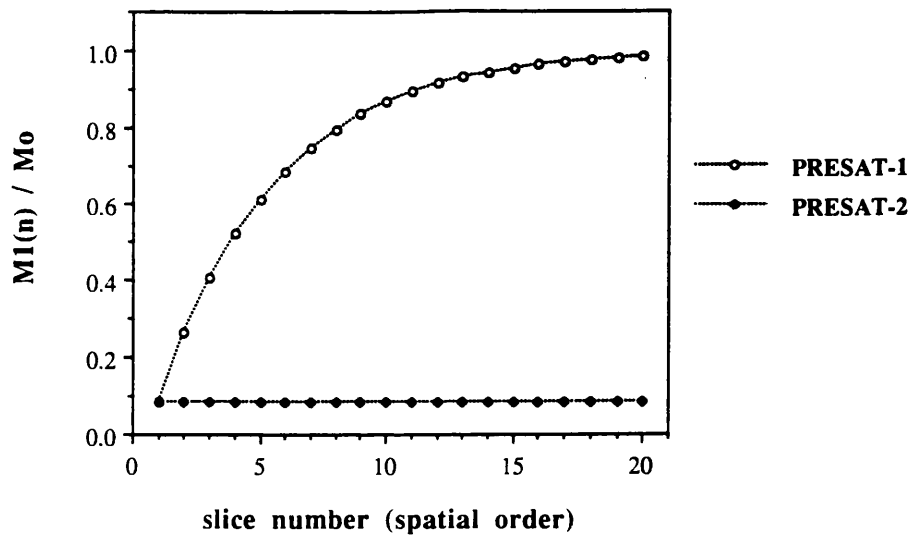
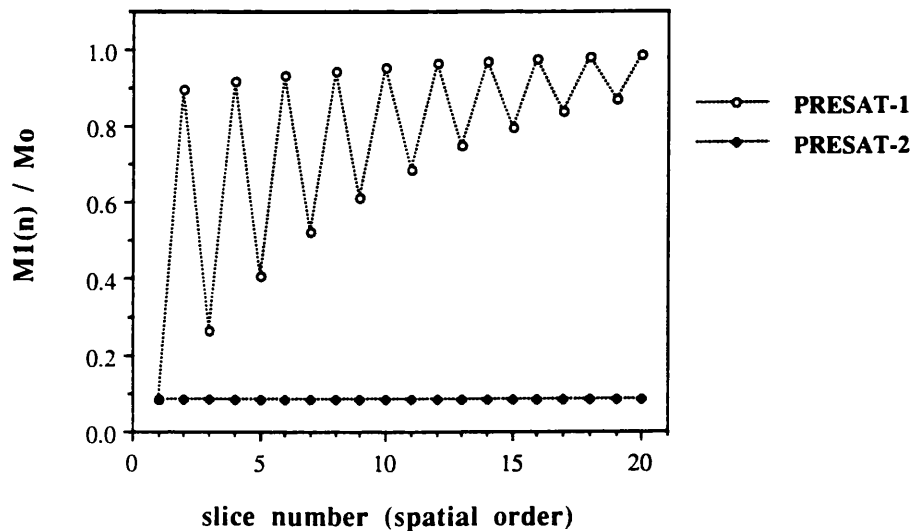
A**B**

Figure 4.3. The residual longitudinal magnetization of the initially saturated component of 280 ms T_1 , as a fraction of its thermal equilibrium value M_0 , plotted against the slice number for PRESAT-1 and PRESAT-2 sequences ($T_s=25$ ms, $T_E=30$ ms, and $T_D=30$ ms). (A) The slices are selected in their spatial order. (B) The slices are selected in a "first-odd-then-even" fashion. Note that the plots are meaningful at discrete points only, the lines have been drawn for clarity.

From Eqn. (4.2) it is apparent that the initially saturated magnetization recovers exponentially across the slices. However, Fig. 4.3.A indicates that during the first few slices the re-growth of the magnetization can be approximated with a linear function. This can be also be shown mathematically using the Taylor expansion theorem, according to which an exponential function can be expanded as a MacLaurin series. Assuming that the absolute value of the exponent is much less than 1, the exponential can then be approximated by a linear function:

$$\exp(x) \approx 1 + x \quad |x| \ll 1 \quad (4.4)$$

Using Eqns. (4.2) and (4.4), the longitudinal magnetization prior to the nth slice is given by:

$$M_1(n) \approx M_0 \frac{T_s + (n-1)(TE+T_D)}{T_1} \quad (4.5)$$

where it is assumed that:

$$T_s + (n-1)(TE+T_D) \ll T_1 \quad (4.6)$$

For a given set of timing parameters there can exist a limited number of slices, for which the condition (4.6) is satisfied. For the example of Fig. 4.3, condition (4.6) is satisfied for the first 3-4 slices (with an error in the value of the relaxed longitudinal magnetization of ~4.4% for the 1st slice, ~16% for the 2nd, ~28% for the 3rd, and ~41% for the 4th). For another typical example of $T_s=20$ ms, $TE=30$ ms, and negligible T_D , the recovery of a saturated component of $T_1=500$ ms could be considered linear, with some approximation, through a 10 slice data set (with an error of ~2% for the 1st slice, ~15% for the 5th, and ~32% for the 10th slice).

Assuming that condition (4.6) is satisfied, consider repeating the same experiment, with the temporal order of slice selection reversed, that is, the last slice is selected first and so on. If n always indicates the spatial position of the slices, the longitudinal magnetization of the saturated component in the beginning of the experiment for the nth slice can be calculated using Eqn. (4.5):

$$M_2(n) \approx M_0 \frac{T_s + (N-n)(TE+T_D)}{T_1} \quad (4.7)$$

where N is the total number of slices. Adding the signal of the two experiments yields a constant residual signal for the saturated component across all slices, and this is indicated by the relaxed longitudinal magnetization:

$$\begin{aligned} M_1(n) + M_2(n) &\approx M_0 \frac{T_s + (n-1)(TE+T_D)}{T_1} + M_0 \frac{T_s + (N-n)(TE+T_D)}{T_1} = \\ &= M_0 \frac{2T_s + (N-1)(TE+T_D)}{T_1} \end{aligned} \quad (4.8)$$

which is independent of n . As before, Eqn. (4.8) holds only when the inequality (4.6) is fulfilled, for example, for the 10-slice data set of the numerical example given above (saturated component of $T_1=500$ ms, $T_s=20$ ms, $TE=30$ ms, and negligible T_D). Even then, some variation across the slices should still be expected, due to the approximation inherent in Eqn. (4.5). For this particular example, the result of the proposed slice cycling procedure is shown in Fig. 4.4, where the recovered longitudinal magnetization of the saturated component is plotted against the number of slices. For comparison, the result of the PRESAT-2 method has also been plotted. It is apparent that the proposed slice cycling procedure smooths out the variable suppression across the slices. For this example, there is an increase of the residual magnetization from 4% in the first slice up to 44% in the 10th slice for the PRESAT-1 sequence. Using the same sequence and the proposed slice cycling procedure, the suppression varies only from 24% to 26.5%. The penalty, however, is a significant increase in the mean value of the relaxed magnetization as compared to the PRESAT-2 sequence. For the example of Fig. 4.4, the residual magnetization in PRESAT-2, as calculated using Eqn. (4.3), is only 4%, while the mean residual magnetization using PRESAT-1 and the proposed slice cycling procedure is 25.5%.

If the linear condition is not satisfied, it is expected that the proposed cycling procedure will still reduce to a certain degree the variation of the saturated component. Figure 4.5 shows the procedure for a 12-slice set for the timing parameters of Fig. 4.3, i.e. $T_s=25$ ms, $TE=30$ ms, $T_D=30$ ms, and $T_1=280$ ms, where the linear approximation can be made within a ~30% error only for the first 3 slices. For this example, the residual magnetization varies from 8.5% in the first slice up to 91.5% in the 12th slice for the PRESAT-1 sequence. Using the same sequence and the proposed slice cycling procedure, the range becomes 50%-71.5%, which, while reduced, is still significant. Compared to the residual magnetization of 8.5% in the PRESAT-2 method, the slice cycling procedure results in a residual magnetization with a mean value of 63.5%.

The least possible variation of the residual magnetization can be ensured by applying the slice cycling procedure well within the linear region of the exponential

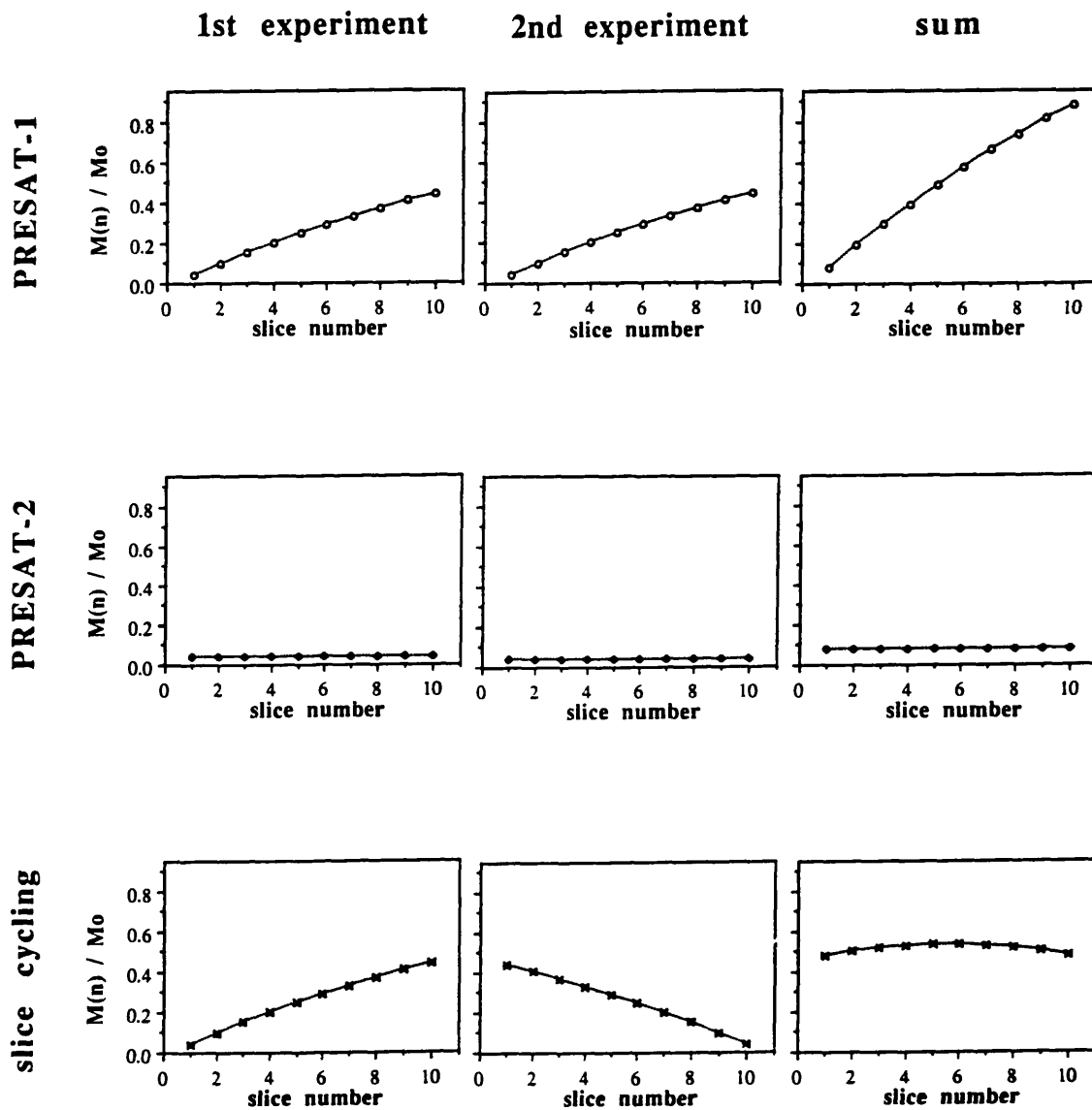


Figure 4.4. The effect of the proposed 2-step slice cycling procedure on the residual longitudinal magnetization of a saturated component of $T_1=500$ ms ($T_s=20$ ms, $TE=30$ ms, and negligible T_D). The slices are selected in their spatial order. Note that the plots are meaningful at discrete points only, the lines have been drawn for clarity.

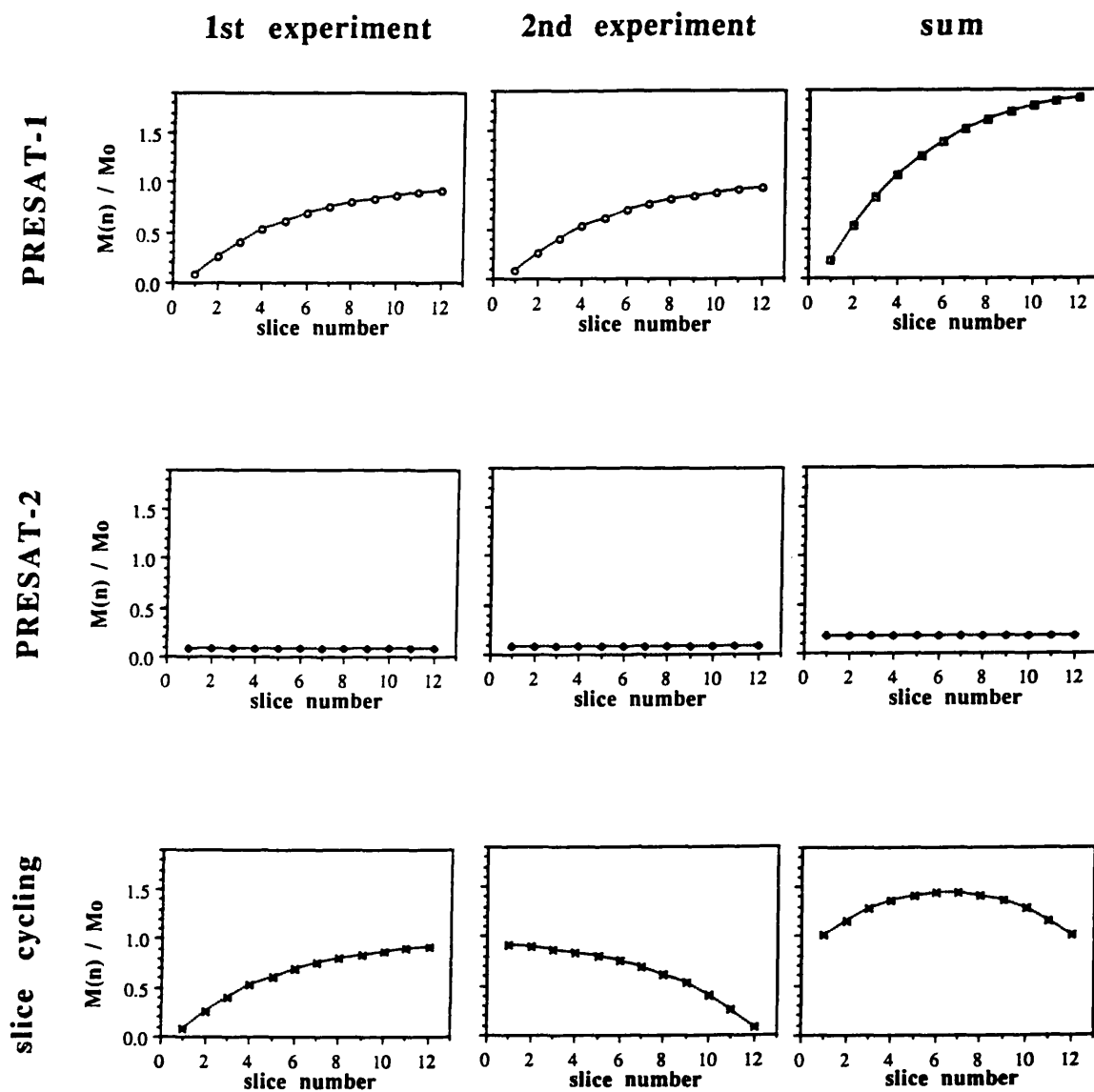


Figure 4.5. The effect of the proposed 2-step slice cycling procedure on the residual longitudinal magnetization of a saturated component of 280 ms T_1 , ($T_s=25$ ms, $TE=30$ ms, and $T_D=30$ ms). The slices are selected in their spatial order. Note that the plots are meaningful at discrete points only, the lines have been drawn for clarity.

magnetization re-growth curve. This can be achieved by estimating the number of slices that correspond to this region for every particular parameter set and applying a saturating pulse prior to every such set of slices. Such a hybrid presaturation scheme, however, would still result in increased imaging time and extra RF power deposition compared to PRESAT-1. As an alternative, a 4-repetition slice cycling procedure is proposed for the PRESAT-1 sequence, which can be combined with the commonly used 4-step CYCLOPS phase cycling procedure described in Appendix 1. In this procedure the total number of slices is divided into four sub-sets, Fig. 4.6.A. The exponential magnetization re-growth curve is, therefore, divided into four corresponding sub-regions, Fig. 4.6.B, and each one of them can be approximated with a linear function. Then, for each sequence repetition the slice selection order is arranged so that by the end of the complete sequence all four slice sub-sets have experienced each one of the four linear sub-regions of the exponential curve (and each one of the phase cycling steps). Table 4.1 summarizes the 4-step slice cycling procedure for the case of a 12-slice data set.

TABLE 4.1				
order of slice selection	1st repetition	2nd repetition	3rd repetition	4th repetition
1	1 (1)	12 (12)	4 (7)	9 (6)
2	2 (3)	11 (10)	5 (9)	8 (4)
3	3 (5)	10 (8)	6 (11)	7 (2)
4	4 (7)	9 (6)	1 (1)	12 (12)
5	5 (9)	8 (4)	2 (3)	11 (10)
6	6 (11)	7 (2)	3 (5)	10 (8)
7	7 (2)	6 (11)	10 (8)	3 (5)
8	8 (4)	5 (9)	11 (10)	2 (3)
9	9 (6)	4 (7)	12 (12)	1 (1)
10	10 (8)	3 (5)	7 (2)	6 (11)
11	11 (10)	2 (3)	8 (4)	5 (9)
12	12 (12)	1 (1)	9 (6)	4 (7)

TABLE 4.1. The slice selection order for each of the four repetitions of the 4-step slice cycling procedure, for the normal (outside the parentheses), as well as the "first-odd-then-even" (within the parentheses) slice selection schemes.

The numbers indicate the spatial position of the slices.

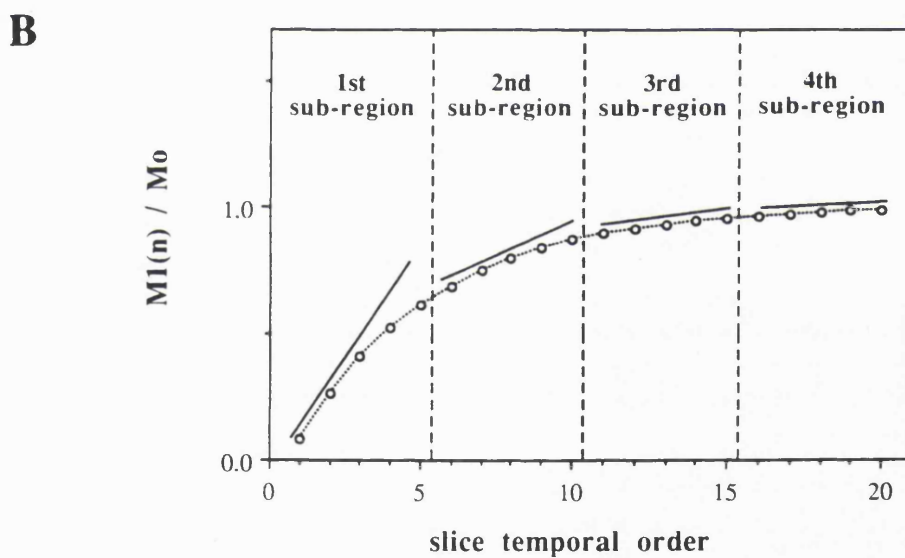
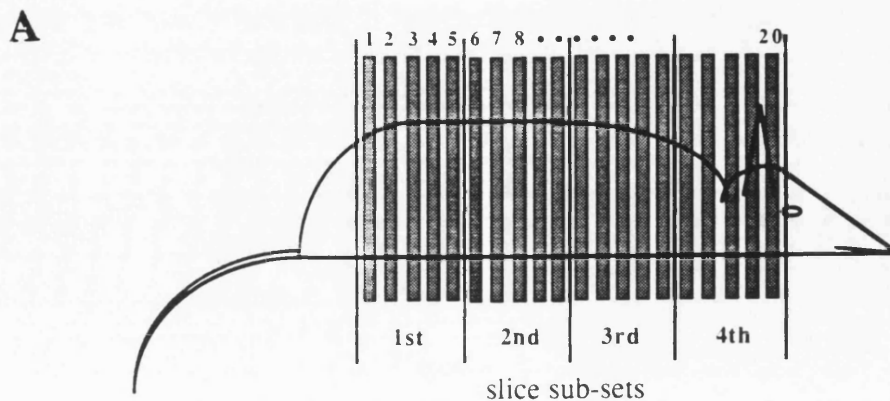


Figure 4.6. (A) The total number of slices divided into 4 sub-sets when the slices are selected in their spatial order. In the case of "first-odd-then-even" fashion, the division into the sub-sets assumes the temporal slice order, and the 1st, 2nd, 3rd and 4th sub-sets would respectively be {1,3,5,7,9}, {11,13,15,17,19}, {2,4,6,8,10}, and {12,14,16,18,20}. (B) The exponential magnetization re-growth curve for a saturated component of 280 ms T_1 ($T_s=25$ ms, $TE=30$ ms, and $T_D=30$ ms) showing the four sub-regions between the vertical dashed lines.

For the parameter set of $T_s=25$ ms, $TE=30$ ms, $T_D=30$ ms, $T_1=280$ ms and 12 slices, the results of the proposed 4-step slice cycling procedure are shown in Fig. 4.7, where the relaxed longitudinal magnetization of the saturated component is plotted against the slice number for the four sequence repetitions and their sum. For comparison, the result of the PRESAT-2 method has also been plotted. The maximum variation of residual magnetization for the PRESAT-1 with the 4-step slice cycling procedure is now reduced to 59%-67.5%, compared to the 50%-71.5% range of the 2-step cycling scheme. When compared to the residual magnetization of 8.5% in the PRESAT-2 method, this slice cycling procedure results in the same mean residual magnetization of 63.5%, as the 2-step cycling scheme. Finally, the result of the proposed 4-step slice cycling procedure for the example of $T_1=500$ ms, $T_s=20$ ms, $TE=30$ ms, and negligible T_D is shown in Fig. 4.8, for a 12-slice data set. The variation of residual magnetization across the slices ranges from 28.6% to 30%.

Although the proposed slice cycling procedures reduce significantly the variation of the residual magnetization across the slices, the mean value of this residual magnetization (which depends on the parameter set) is still considerably higher than in the PRESAT-2 method. This may not be a major problem when only reduction of fat or water signals is required in order, for example, to overcome dynamic range problems. However, if maximum possible suppression of the unwanted component is desired, the proposed 4-step slice cycling procedure can provide the necessary information so that "masking" post-processing techniques can be employed to null the signal from the unwanted component.

Such an algorithm can be based on the fact that although the signal of the saturated component in each slice changes considerably for every repetition of the 4-step procedure, the signal from the component which is not saturated should remain constant. Thus if the signal intensity from two different repetitions of the 4-step cycling procedure is compared in a pixel-by-pixel basis, the pixels that show the same signal intensity (within a predetermined range of values to account for variations due to noise) have contribution from the unsaturated component only. A difference between the intensities of the pixels larger than the predetermined threshold indicates contribution from the saturated component. For the algorithm to be successful, the maximum possible change in the signal intensity of the saturated component is desired. This occurs when the first and the last sub-regions of the exponential re-growth curve are considered. For a cycling scheme such as that in Table 4.1, this maximum change corresponds to the 1st and 2nd sequence repetition for the 1st and 4th slice sub-sets, and to the 3rd and 4th sequence repetition for the 2nd and 3rd slice sub-sets. The post-processing, therefore, involves a computer program whose input is the separate images derived from the 4 steps of the cycling procedure, and the sum image, while the output

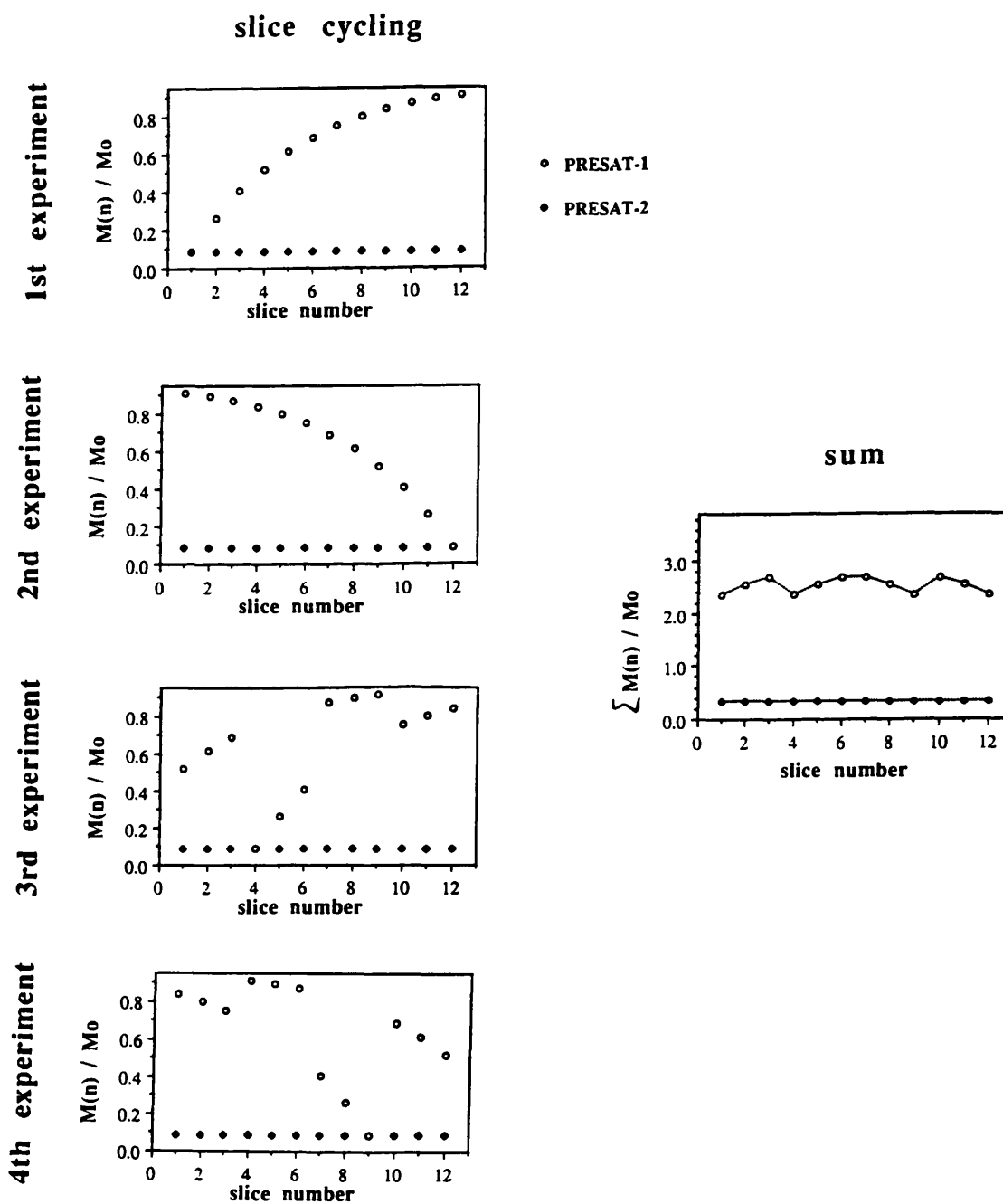


Figure 4.7. The effect of the proposed 4-step slice cycling procedure on the residual longitudinal magnetization of a saturated component of 280 ms T_1 ($T_s=25$ ms, $TE=30$ ms, and $T_D=30$ ms). The slices are selected in their spatial order.

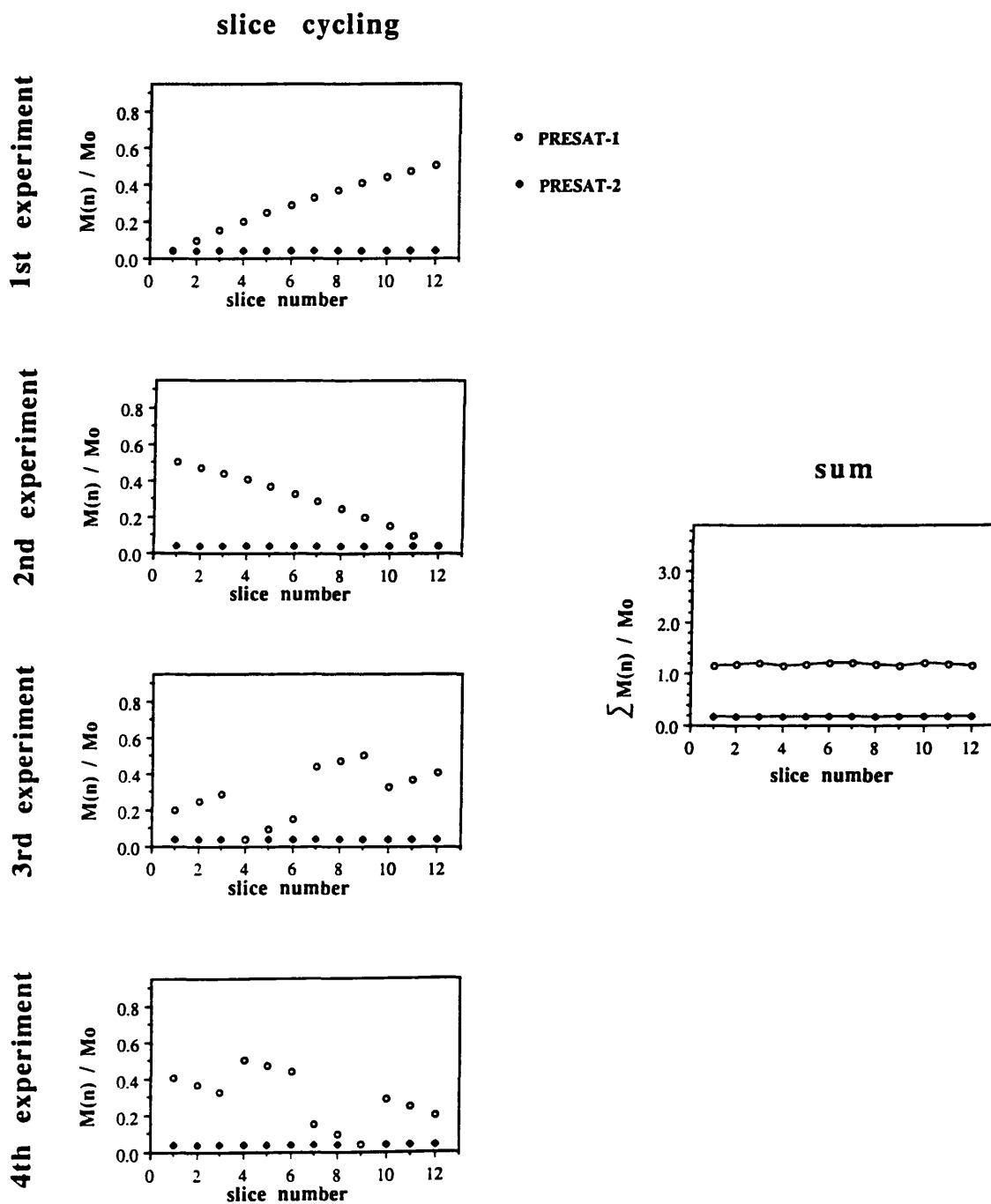


Figure 4.8. The effect of the proposed 4-step slice cycling procedure on the residual longitudinal magnetization of a saturated component of 500 ms T_1 ($T_s=20$ ms, $TE=30$ ms, and negligible T_D). The slices are selected in their spatial order.

is a corrected image. For each slice a decision is made as to which slice sub-set it belongs, and then a signal intensity comparison is performed on a pixel-by-pixel basis considering the pair of images with the maximum difference in the saturated magnetization as described above. If the signal intensity of the equivalent pixels is the same, to within a range of values determined by the noise, then the corresponding "mask" pixel is set to 1, indicating a pixel with no contribution from the saturated component. If the difference between the intensities of the compared pixels is more than the threshold, then the "mask" pixel is set to 0. The sum image is then multiplied pixel-by-pixel by the "mask" image, leaving unaffected the pixels of the desired magnetization component, while setting to zero ("masking") those pixels which have contributions from the saturated magnetization.

4.3 EXPERIMENTAL METHODS

The proposed slice cycling procedures were evaluated for their ability to smooth out the variation of the suppression across the slices in the PRESAT-1 method using a two-compartment phantom. The study was performed on a SISCO-200 NMR imaging spectrometer (Spectroscopy Imaging Systems Corporation, Fremont, California), equipped with a 4.7 T, 33 cm bore superconducting magnet (Oxford Instruments Ltd, Oxford, UK), and the HPAG18 SISCO magnetic field gradient set (100 mT/m, 18 cm inner diameter). An imaging coil with an inner diameter of 8 cm was used.

The phantom consisted of a glass tube (~1 cm outer diameter, ~3.5 cm height) inside a glass beaker (~2.5 cm outer diameter, ~3.5 cm height). The inner tube contained distilled water doped with ~0.4 g/l copper sulphate (CuSO₄) to give a solution with a T₁ of ~500 ms. The beaker contained mineral oil (Aldrich Chemical Co. Ltd., Gillingham SP8 4JL, England) with a mean T₁ value of ~280 ms. The T₁ value of each component was measured by the standard spectroscopic version of the inversion recovery technique [4.5]. A pilot spectrum from the phantom, acquired prior to the imaging experiments, showed that the oil resonance frequencies occurred within a ~2 ppm (400 Hz) range, centred ~3.6 ppm (720 Hz) upfield from the water peak (shimmed to 0.5 ppm full width at half maximum height).

For the imaging experiment, 12 cross-sectional slices of ~1 mm thickness and 1.4 mm separation centre-to-centre were acquired through the middle of the object. A series of imaging sequences was performed:

- (i) standard spin echo (SE) sequence,
- (ii) conventional PRESAT-1 sequence,
- (iii) conventional PRESAT-2 sequence,

- (iv) PRESAT-1 sequence, with the proposed 2-step slice cycling procedure, and
- (v) PRESAT-1 sequence, with the proposed 4-step slice cycling procedure.

The presaturation sequences were repeated twice, saturating the fat or the water protons. All imaging experiments were performed with a 4x4 cm field of view, 128x128 data matrix and 4 signal averages per phase encoding step to enhance signal-to-noise ratio and allow for the phase cycling procedure described in Appendix 1. The acquisition time, echo time and repetition time were kept constant for all sequences at the values of 7 ms, 30 ms and 2000 ms, respectively. Slice selection used the "first-odd-then even" ordering, and was performed with 5000 μ s five-lobe sinc pulses in the presence of 24.4 mT/m linear magnetic field gradient, giving a slice thickness of 0.96 mm. Chemical shift selection was performed by 2850 μ s Gaussian pulses of 700 Hz effective frequency bandwidth, i.e. 3.5 ppm at 4.7 T. The interval between the presaturation pulse and the following spin echo experiment was 25 ms. For the number, pattern, duration, and time separation of the RF pulses employed, a minimum delay time of $T_D=30$ ms between subsequent sequence repetitions was required in order to remain within the duty cycle of the system's M3011 RF amplifier (185-205 MHz, 1 KW, American Microwave Technology Inc.).

The pulse sequence program supplied by the manufacturer (VNMR software, Varian Associates Inc.) was used for the standard spin echo experiment, while all the other sequences and slice cycling schemes were implemented using the C programming language and libraries supplied by the manufacturer. In the slice cycling methods, the signal from the different repetitions of the cycling procedure was stored in separate files. Data re-ordering, summation and Fourier transformation were accomplished using macros developed in the "viewit" programming environment (viewit is an array programming language with function support, developed by C. Potter, Beckman Institute, Urbana, IL 61801). Further post-processing for "masking" involved development of C programmes based on the UNC image processing software and libraries (University North Carolina, USA).

4.4 RESULTS AND DISCUSSION

Three representative slices from each of the 12-slice data sets acquired with the sequences listed above, are shown in Fig. 4.9 (for the case of oil suppression) and in Fig. 4.10 (for the case of water suppression). The slices are the 1st, 6th, and 12th in temporal order of selection. Considering the "first-odd-then-even" selection scheme, this temporal order corresponds to spatial positioning of 1st, 11th, and 12th, respectively. The chemical shift artifact is well illustrated in the spin echo images, where the oil signal is displaced relative to water in the frequency encode direction and a bright/dark ring appears at the interface of the two components because of the superposition of the mis-registered signals. The PRESAT-2 images show the efficient suppression of the saturated component in all three slices. The differential regrowth of the saturated magnetization is apparent in the PRESAT-1 images, particularly in this case for the oil component (Fig. 4.9). Both slice cycling procedures reduce the differential suppression of the saturated component across the slices.

The signal of the saturated component was calculated for all images by measuring the mean signal intensity from a 64 pixel region of interest (i.e. 0.6 mm^2) and by normalizing to the signal of the same region in the equivalent spin echo image (in order to show fractional suppression). Figure 4.11 shows the residual oil signal as a function of the slice number for the 2-step and the 4-step slice cycling procedures, as well as for the conventional PRESAT-1 and PRESAT-2 images in the case of oil suppression. The slices are shown in the order of temporal selection. The residual oil signal in the PRESAT-1 images varies from 16% in the first slice up to 100% (i.e. no suppression) in the last. In the images acquired with the 2-step slice cycling procedure (Fig. 4.11.A) the variation is reduced to the range 52% to 84%. In the images acquired with the 4-step slice cycling procedure (Fig. 4.11.B) the variation is further reduced to a range of 62% to 70%.

Figure 4.12 shows the residual water signal as a function of the slice for the 2-step and the 4-step slice cycle, as well as the conventional PRESAT-1 and PRESAT-2 images in the case of water suppression. The residual water signal in the PRESAT-1 images varies from 7% in the first slice up to 80% in the last. In the images acquired with the 2-step slice cycling procedure (Fig. 4.12.A) the variation is reduced to a range of 40% to 53%. In the images acquired with the 4-step slice cycling procedure (Fig. 4.12.B) the variation is further reduced to a range of 43% to 49%.

Finally, Fig. 4.13 shows the results of the simple "masking" algorithm described previously, for the first slice of the data sets for the case of ω_h ^{water} suppression. The post-processing procedure is designed to null the signal of all the pixels in the initial image that have significant signal contribution from the saturated component, therefore, partial volume and chemical shift artifacts are not removed.

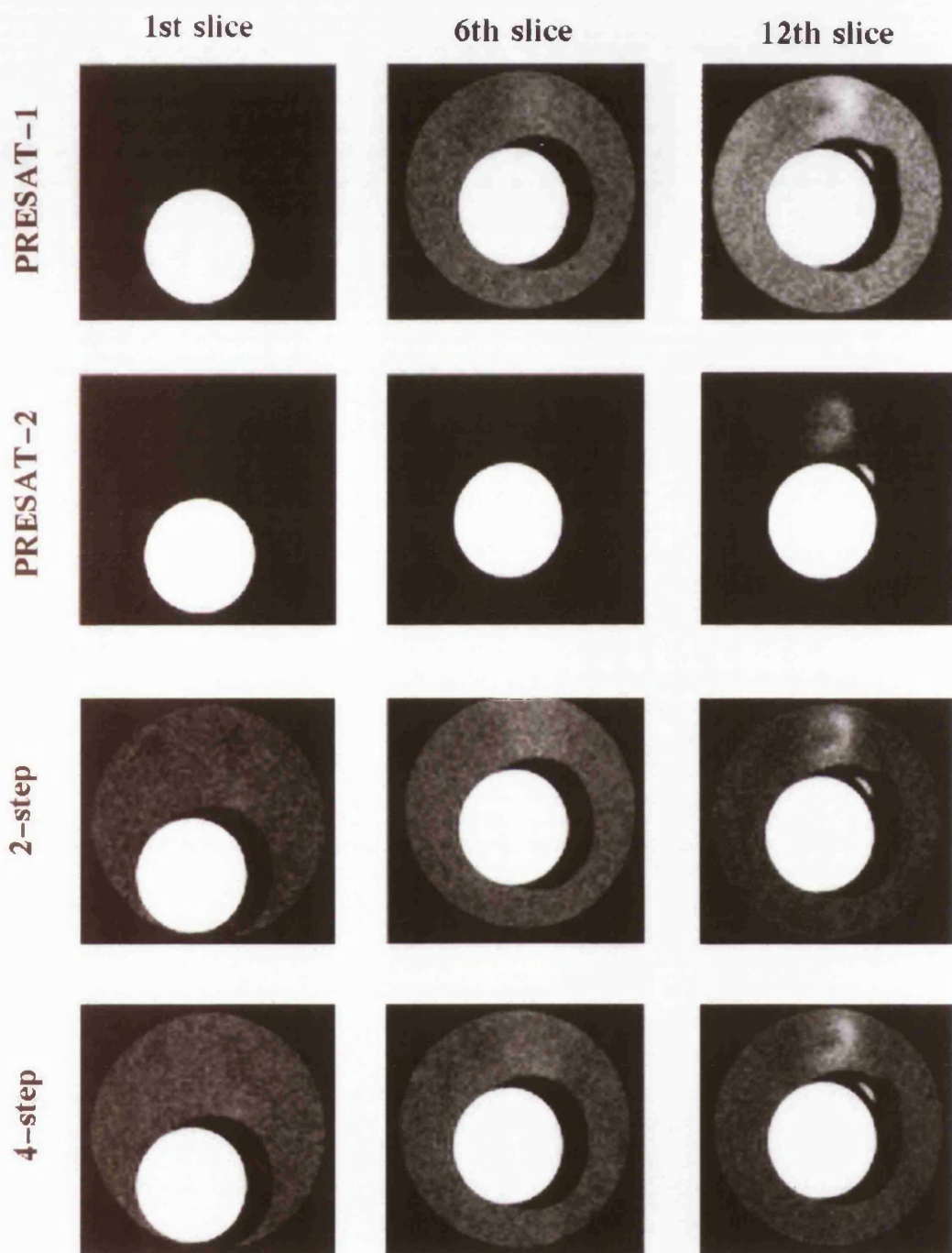


Figure 4.9. Phantom images of the 1st, 6th, and 12th slices (temporal order), acquired using a spin-echo, and oil-suppressed conventional PRESAT-1, and PRESAT-2 sequences, as well as oil-suppressed PRESAT-1 with the proposed 2-step and 4-step slice cycling procedures.

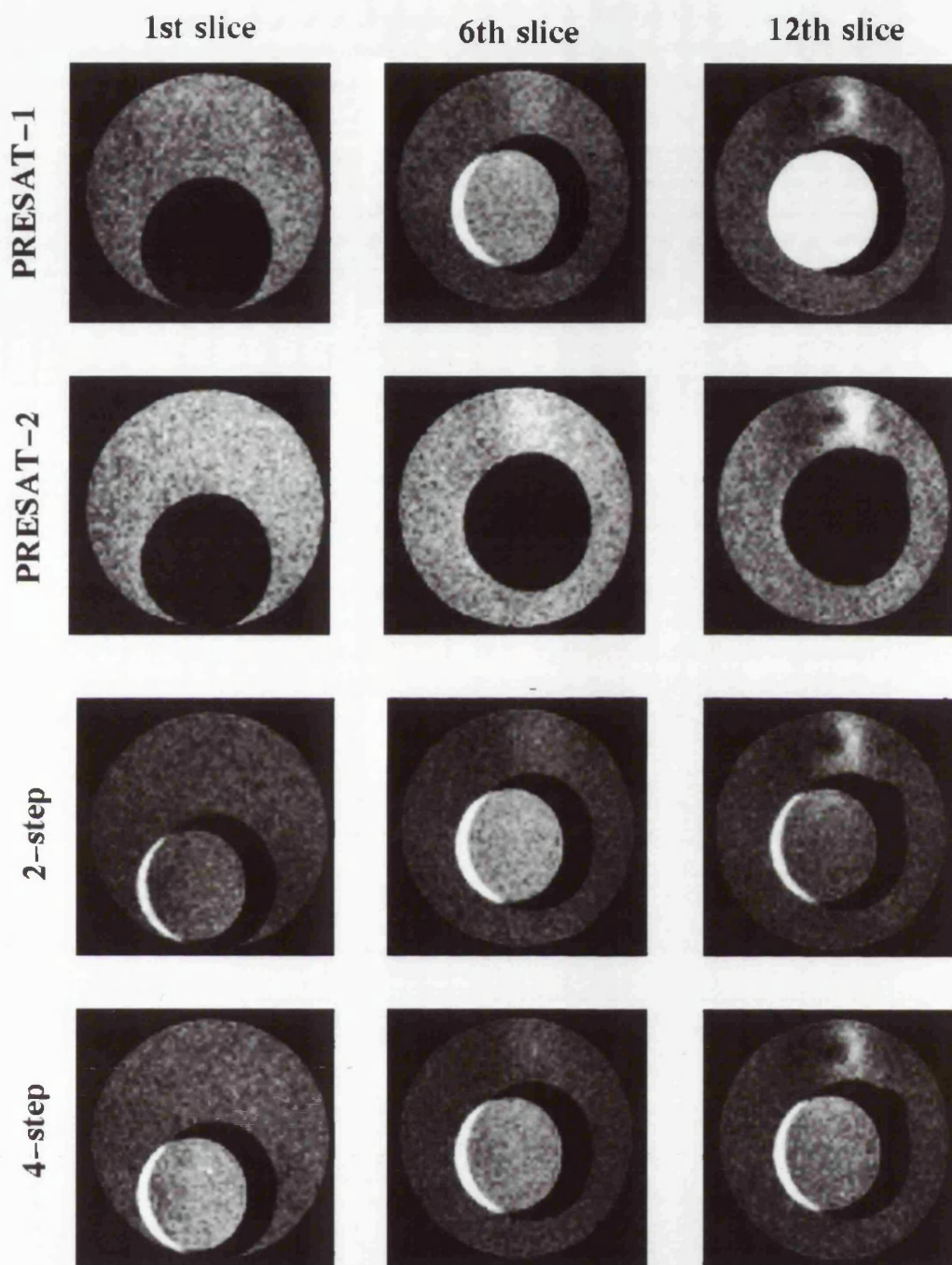


Figure 4.10. Phantom images of the 1st, 6th, and 12th slices (temporal order), acquired using a spin echo, and water-suppressed conventional PRESAT-1 and PRESAT-2 sequences, as well as water-suppressed PRESAT-1 with the proposed 2-step and 4-step slice cycling procedures.

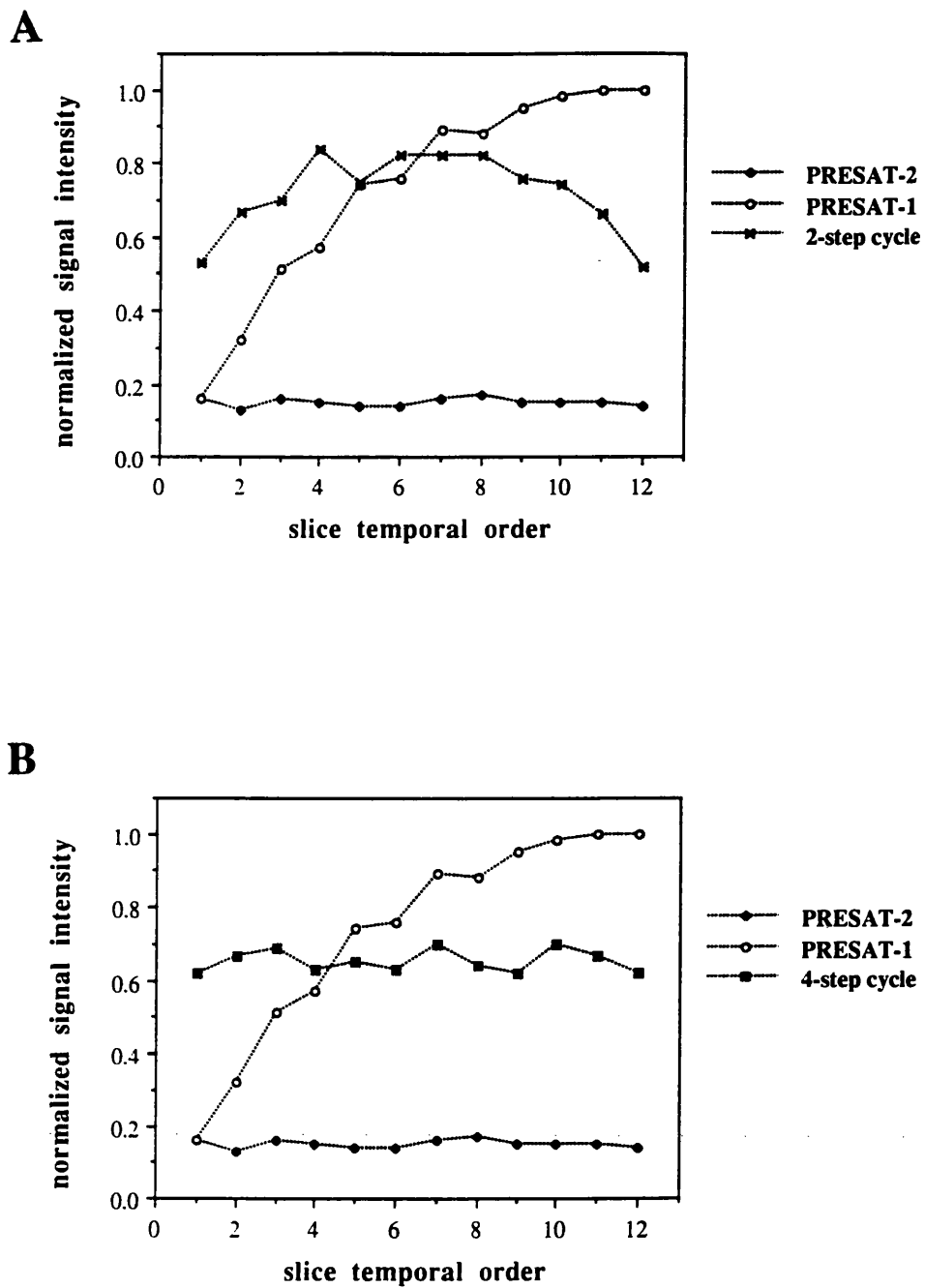


Figure 4.11. Normalized oil signal intensity plotted against the slice temporal order for the oil-suppressed conventional PRESAT-1, PRESAT-2, and PRESAT-1 with the proposed 2-step (A), and 4-step (B) slice cycling procedure.

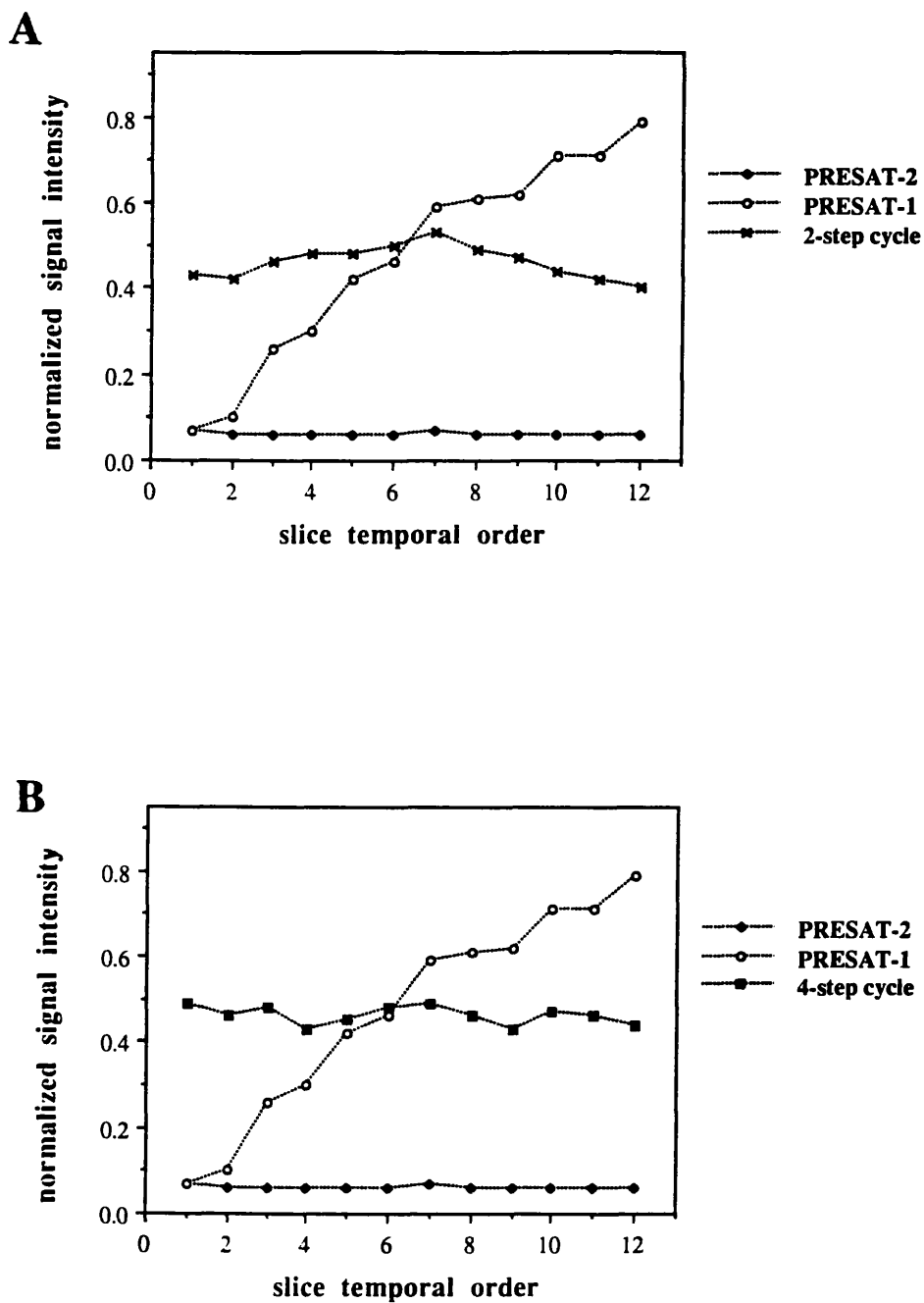


Figure 4.12. Normalized water signal intensity plotted against the slice temporal order for the water-suppressed conventional PRESAT-1, PRESAT-2, and PRESAT-1 with the proposed 2-step (A), and 4-step (B) slice cycling procedure.

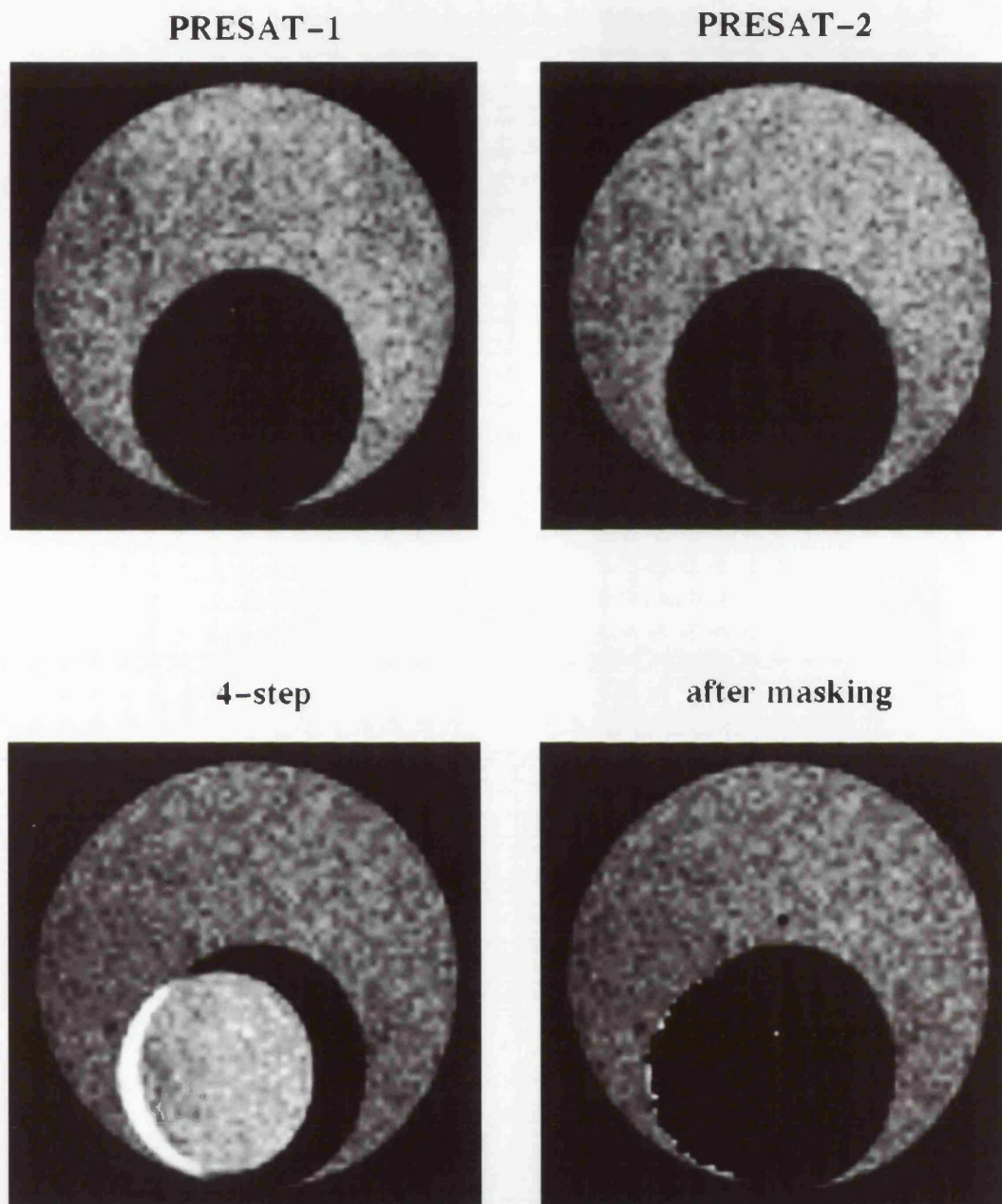


Figure 4.13. Phantom images of the 1st slice, acquired using water-suppressed conventional PRESAT-1 and PRESAT-2 sequences, as well as water-suppressed PRESAT-1 with the 4-step slice cycling scheme, and the result of the "masking" post-processing procedure.

4.5 CONCLUSIONS

Presaturation sequences are commonly used in clinical MRI. For example, fat and water presaturation has been used to better assess the degree of normal fatty bone marrow replacement in fractured vertebral bodies [4.6], while fat presaturation has proved better than spin echo sequences in determining focal liver disease and improving assessment of venous systems [4.7]. The multi-slice presaturation scheme which involves a single presaturation procedure followed by a series of spin echo experiments to select different slices (PRESAT-1) results in differential suppression of the unwanted component across the slices due to T₁ relaxation. Although repetition of the presaturation procedure prior to each slice selection (PRESAT-2) overcomes this problem, the overall imaging time is increased and there is considerable extra RF power deposition, especially when gradient echoes are employed.

Two slice cycling procedures are proposed that can be combined with the PRESAT-1 sequence to smooth out the differential suppression across the slices. The proposed 2-step slice cycling procedure requires two repetitions of the sequence with reverse slice selection order. The reduction in the variation is maximal when the T₁ of the saturated component and the timing parameters of the sequence are such that the exponential regrowth of the magnetization over the slice set can be approximated with a linear function. In other cases the 2-step cycling scheme is still expected to reduce the variation of the suppression to some degree, especially for the central slices (temporal order).

The proposed 4-step slice cycling procedure requires 4 repetitions of the sequence with a more complicated re-ordering of the slices, as explained previously. The variation of the suppression across the slices is further reduced. A more important feature of the 4-step slice cycling scheme, however, is that it can supply the necessary information for a post-processing algorithm to create true fat or water images. Such a simple algorithm has been described and implemented in this phantom study, resulting in images where all pixels that have signal contribution from the suppressed component are "masked" out. Alternatively, the pixels that do not contain any signal from the suppressed component can be set to zero, resulting in an image of the suppressed component, which, however, will suffer a relatively poor S/N. This simple masking procedure does not correct for the chemical shift artifact or partial volume effects at the interfaces of the two components. However, it can result in complete suppression of fat tissue, ^{in cases} where pixels contain a mixture of fat and water and a simple chemical shift selective, fat suppression is not efficient to cancel all signal [4.8].

True correction of the data to give fat-only or water-only images could also be achieved, although this would require rather more elaborate post-processing. The four sequence repetitions of the 4-step slice cycling procedure are images of the saturated

component at four different points of its T_1 recovery curve, and they can be used to create a T_1 map of the saturated component. The process would involve a three parameter fit of the data from the 4 experiments, the unknown variables being the spin density of the unsuppressed component, the spin density of the suppressed component and the T_1 of the suppressed component in every pixel (similar fitting procedures have already been used in various NMR experiments, e.g. [4.9]). This information can then be used to generate synthetic images of the saturated component, at arbitrary points of the relaxation curve. Furthermore, it is also possible to create images of the saturated component with a different T_1 weighting for different slices, so that they correspond exactly to each one of the sequence repetitions of the slice cycling procedure. Direct subtraction of the synthetic images from the acquired ones would result in an image of the desired component only, free from chemical shift artifacts and partial volume effects.

The proposed slice cycling techniques are expected to be most beneficial in imaging applications that require signal averaging and a relatively large number of slices, but the available imaging time is restricted. Such an example is high resolution, gradient echo imaging. Slice cycling, however, can be employed in a similar fashion in any other multi-slice imaging sequence with a single initial preparation period. Such a straightforward application would be in FLAIR imaging [4.10, 4.11], where in order to reduce imaging time a non-selective inverting pulse is usually applied prior to acquisition of a number of slices, the penalty being the differential suppression of fluid across the slices.

CHAPTER 5

A CHEMICAL SHIFT SELECTIVE INVERSION RECOVERY (CSS-IR) SEQUENCE FOR FAT AND WATER DIFFERENTIATION IN MRI

5.1 INTRODUCTION

Imaging time, software and hardware limitations, and the multi-slice requirement of most routine clinical MRI examinations often restrict the wide use of many of the proposed techniques for fat and water differentiation. The two most commonly used methods are the selective presaturation (PRESAT) sequence, and the T₁-null method based on the inversion recovery sequence (IR).

Presaturation chemical shift imaging sequences [5.1–5.3] require radiofrequency and static magnetic fields homogeneous enough to allow differentiation between the resonance frequencies of fat and water protons over the whole imaging volume. Nevertheless, PRESAT sequences can function in a multi-slice mode, where the initial selective pulse and the subsequent spoiling magnetic field gradient are performed before the selection of each individual slice. The T₁-null IR method [5.4, 5.5] has no special hardware or software requirements, works in a multi-slice mode and can be implemented on most clinical systems irrespective of both the static magnetic field strength and homogeneity. One significant disadvantage, however, is that suppression of the unwanted component is heavily dependent on its T₁, which has to be either measured or at least estimated prior to the experiment. Moreover, if the unwanted magnetization exhibits a range of T₁ values, suppression may be inadequate. Thus the technique has been extensively used only with a short inversion time (STIR) to achieve suppression of fat protons. As water exhibits a wide range of T₁ values in tissues, the use of ^{the} T₁-null method has been limited to "fluid attenuation" (FLAIR) rather than true water suppression [5.6, 5.7]. Even so, when applied in the conventional multi-slice mode, the long inversion (TI) and repetition (TR) times required allow only for a few slices to be selected within one sequence repetition.

A new, hybrid chemical shift selective inversion recovery pulse sequence scheme is proposed. It combines the principle of the T₁-null method with selective irradiation of either the water or the fat protons to produce multi-slice data sets with enhanced suppression of the unwanted component and without the limitations of the original techniques, namely the T₁-null inversion recovery (IR) and the chemical shift pre-saturation (PRESAT) sequences. Compared to IR, the suppression of the unwanted component by the hybrid sequence is less strongly dependent on the T₁ of the

magnetization, thus permitting the efficient use of the technique in cases where the T₁ values of the unwanted component are not accurately known or even when there is a relatively wide range of T₁ values (e.g. water protons). Furthermore, the inversion time required by this hybrid sequence is generally shorter than in the conventional IR, thus allowing the imaging of more slices within the same repetition time, as well as manipulation of the contrast for the unsuppressed component to be T₁ and/or T₂ weighted, depending on the repetition and echo times, respectively. When compared to PRESAT, the hybrid sequence is more able to tolerate mis-settings in the tip angle and the frequency bandwidth of the selective pulse, thus reducing the rather stringent static and radiofrequency field requirements of this conventional chemical shift imaging method. The hybrid sequence is evaluated both using phantoms and *in vivo*, and is compared to conventional T₁-null IR and PRESAT imaging. This hybrid sequence will be referred to as CSS-IR (Chemical Shift Selective - Inversion Recovery) hereafter. The sequence, when considered for fat-suppression, can also be regarded as a specific case of the Selective Partial Inversion Recovery (SPIR) method [5.8], which has recently been implemented in the clinical evaluation of breast disease [5.9].

5.2 THEORY

The pulse sequence diagram for CSS-IR is shown in Fig. 5.1. The initial 180° pulse is chemical shift selective, causing only protons of the unwanted chemical shift, that is either the protons in the water molecule or the methyl and methylene protons of fat, in the whole sample to be inverted while leaving the rest of the magnetization unperturbed. A slice selective 90° pulse is then applied at a time T_{ICSS-ir} when the inverted magnetization passes through the null point and causes only "non-inverted" protons within that slice to be excited. The sequence can be immediately repeated to select another slice.

As the inverting 180° pulse is applied in the absence of all gradients (in order to achieve chemical shift selection), its effect is not confined to a single slice. Therefore the selected protons over the whole imaging volume experience a train of inverting pulses, with an effective repetition time:

$$T_{\text{Reff}} = \frac{TR}{N} \quad (5.1)$$

where N is the number of slices. This is similar to the PRESAT sequence, where the protons that are suppressed experience a train of 90° saturating pulses with the same effective repetition time, T_{Reff}. It is apparent that in a single slice experiment, T_{Reff}

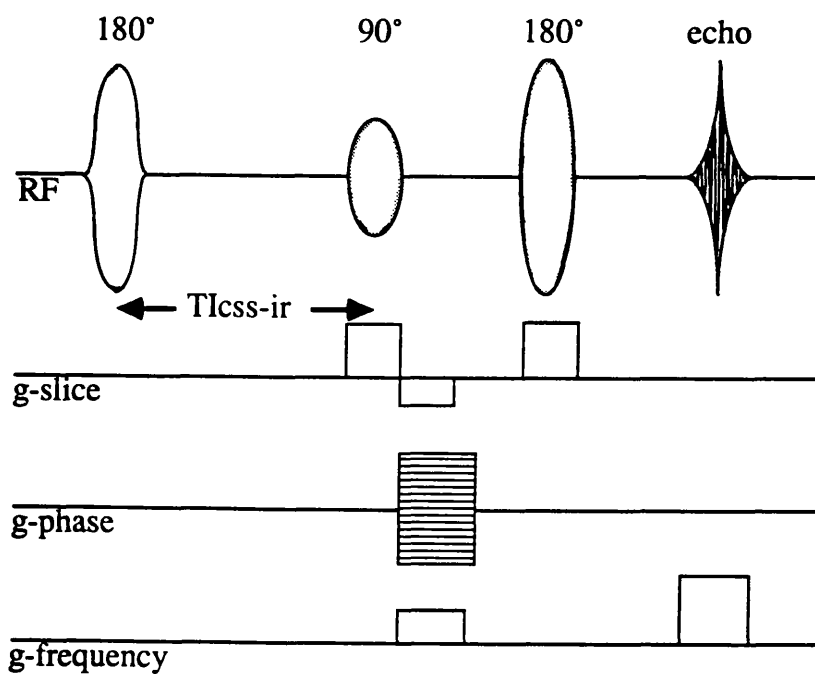


Figure 5.1. Diagrammatic representation of the CSS-IR hybrid pulse sequence. The chemical shift selective 180° pulse inverts only the protons of either the fat or water resonance, and the inversion time, TI_{css-ir} , corresponds to the "null-point" for this magnetization. TE is the echo time.

equals the total sequence repetition time, thus, at this limit, T_{Reff} equals T_R , as in the conventional IR experiment.

The inversion time which corresponds to the time when the inverted magnetization passes through zero (denoted by T_I hereafter) can be calculated considering the relaxation of the longitudinal magnetization M_z , as described by the Bloch equation:

$$\frac{dM_z}{dt} = -\frac{M_z - M_0}{T_1} \quad (5.2)$$

where M_0 is the longitudinal thermal equilibrium magnetization. The following analysis assumes negligible steady-state-free-precession (SSFP) effects.

In the general case of a train of β^* pulses applied with a repetition time of T , the longitudinal magnetization, M_n , just after the n th pulse can be calculated by integrating Eqn. (5.2) with appropriate limits (a detailed derivation is given in Appendix 2):

$$M_n(\beta^*) = \frac{M_0 \cos(\beta) (1 - e^{-T/T_1}) + M_0 \cos^n(\beta) e^{-n(T/T_1)} (1 - \cos(\beta))}{1 - \cos(\beta) e^{-T/T_1}} \quad (5.3)$$

After many pulse repetitions, a steady state is reached and the longitudinal magnetization is given by:

$$M_{ss}(\beta^*) = M_0 \cos(\beta) \frac{1 - e^{-T/T_1}}{1 - \cos(\beta) e^{-T/T_1}} \quad (5.4)$$

In the case of a train of inverting pulses, the longitudinal magnetization M_n and its steady state value M_{ss} can be directly derived from Eqns. (5.3) and (5.4) respectively, by setting the tip angle β^* equal to 180° :

$$M_n = M_0 \frac{e^{-T/T_1} - 1 + 2(-1)^n e^{-n(T/T_1)}}{1 + e^{-T/T_1}} \quad (5.5)$$

and

$$M_{ss} = M_0 \frac{e^{-T/T_1} - 1}{e^{-T/T_1} + 1} \quad (5.6)$$

Figure 5.2 shows the magnetization M_n just after each inverting pulse as it approaches its steady state value. This graph has been computed assuming a T_1 of 200 ms (a typical

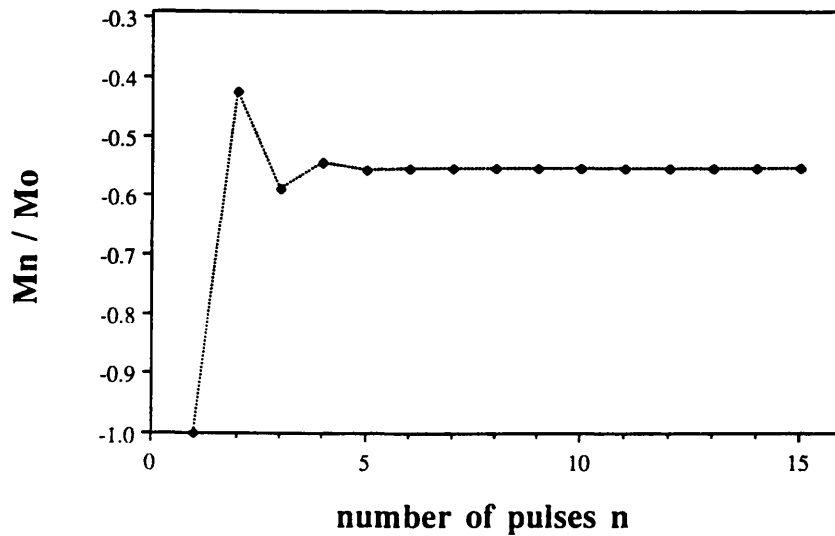


Figure 5.2. M_n , as a fraction of the thermal equilibrium magnetization M_0 , just after each inverting pulse, as it approaches a steady-state. The T_1 is assumed to be 200 ms and the pulse repetition time is 200 ms. Note that the graph consists of discrete points, the dotted line is drawn only for clarity.

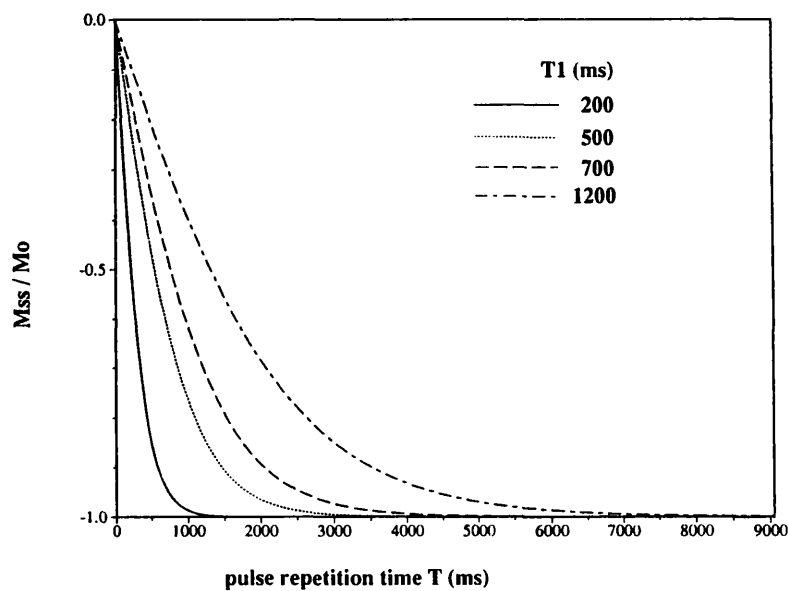


Figure 5.3. The value of the steady state magnetization M_{ss} as a function of the pulse repetition time, for a range of T_1 values chosen to correspond to the typical range of proton T_1 values encountered *in vivo*.

value for fat protons *in vivo*) and an effective repetition time of 200 ms. For the same T_1 , the shorter the pulse repetition time T , the lower the magnitude of the steady state magnetization M_{ss} , as shown in Fig. 5.3.

The time of the null point, TI , for the steady state condition can then be calculated from Eqns. (5.2) and (5.6):

$$TI = T_1 \ln 2 - T_1 \ln(1 + e^{-T/T_1}) \quad (5.7)$$

This dependence of TI on the T_1 and the inverting pulse effective repetition time is also shown in Fig. 5.4. It is apparent that as the pulse repetition time increases, TI becomes dependent mainly on the T_1 . This is the case for the conventional T_1 -null IR technique, (either the STIR or FLAIR version), where the total repetition time TR is long enough so that $e^{-TR/T_1} \approx 0$, and the inversion time TI can be approximated by the most frequently used expression:

$$TI_{ir} = T_1 \ln 2 \quad (5.8)$$

However, for typical values of total repetition time and number of slices, TR_{eff} in the CSS-IR sequence is short enough so that the above approximation does not hold, and the inversion time is then given by Eqn (5.7), where $T=TR_{eff}$, that is:

$$TI_{css-ir} = T_1 \ln 2 - T_1 \ln(1 + e^{-TR_{eff}/T_1}) \quad (5.9)$$

Thus, the inversion time that corresponds to the null point for CSS-IR sequence is a function of T_1 , repetition time and number of slices, and this dependency is illustrated in Fig. 5.5, where TI_{css-ir} is plotted against the number of slices for a range of repetition times assuming a T_1 of 200 ms. Comparing Eqns. (5.8) and (5.9), it can be shown that TI_{css-ir} is generally shorter than TI_{ir} , which makes the CSS-IR sequence more time-efficient than the conventional IR sequence. The result is that for the same repetition time, more slices can be selected using the hybrid sequence, as shown in Fig. 5.6.A for the case of the STIR experiment. When FLAIR is considered, the relatively long inversion time allows for a more time efficient slice selection scheme, where the inversion pulses for later slices are accommodated within the inversion time corresponding to the first slice [5.10] (see also section 3.3.1). Even so, the CSS-IR generally affords more slices in the same total repetition time, as shown in Fig. 5.6.B for magnetization of 700 ms T_1 .

Figure 5.7 shows the calculated inversion time as a function of T_1 for both IR and CSS-IR sequences, using Eqns. (5.2) and (5.9) respectively, for a range of

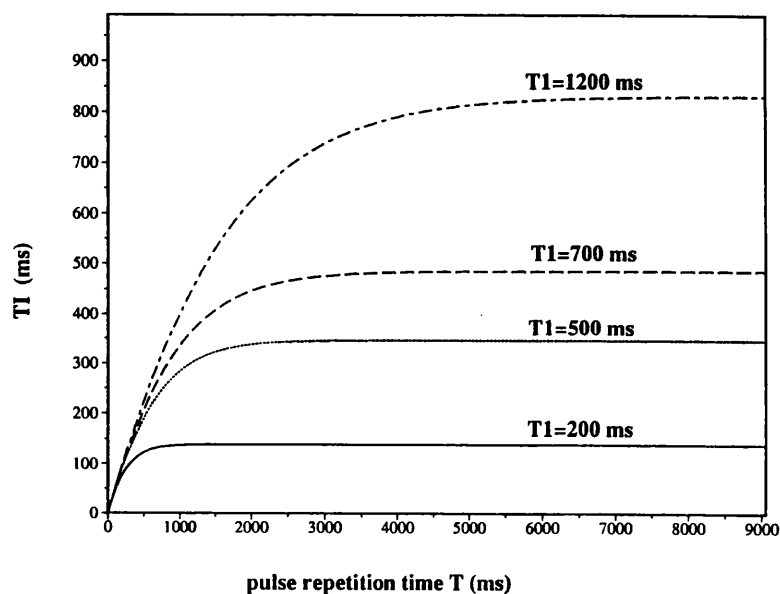


Figure 5.4. The inversion time TI that corresponds to the null point as a function of the inverting pulse repetition time, for a typical range of proton T_1 values.

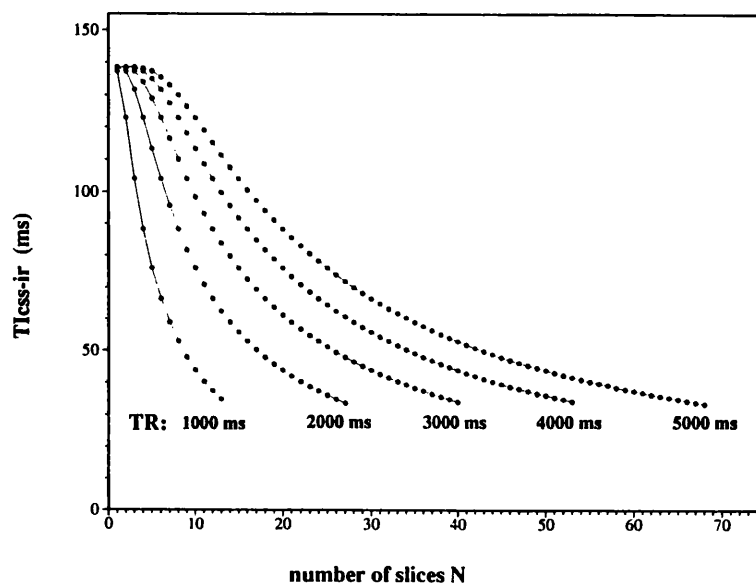


Figure 5.5. The inversion time, $TI_{\text{css-ir}}$, as a function of the number of slices, N , for a range of sequence repetition times, TR . The total imaging time of the spin echo part of the sequence is 40 ms, and $T_1=200$ ms. The curves terminate where $N(TI_{\text{css-ir}}+TE) = TR$, i.e. when no more slices can be fitted within the repetition time. The plot is meaningful at discrete points only.

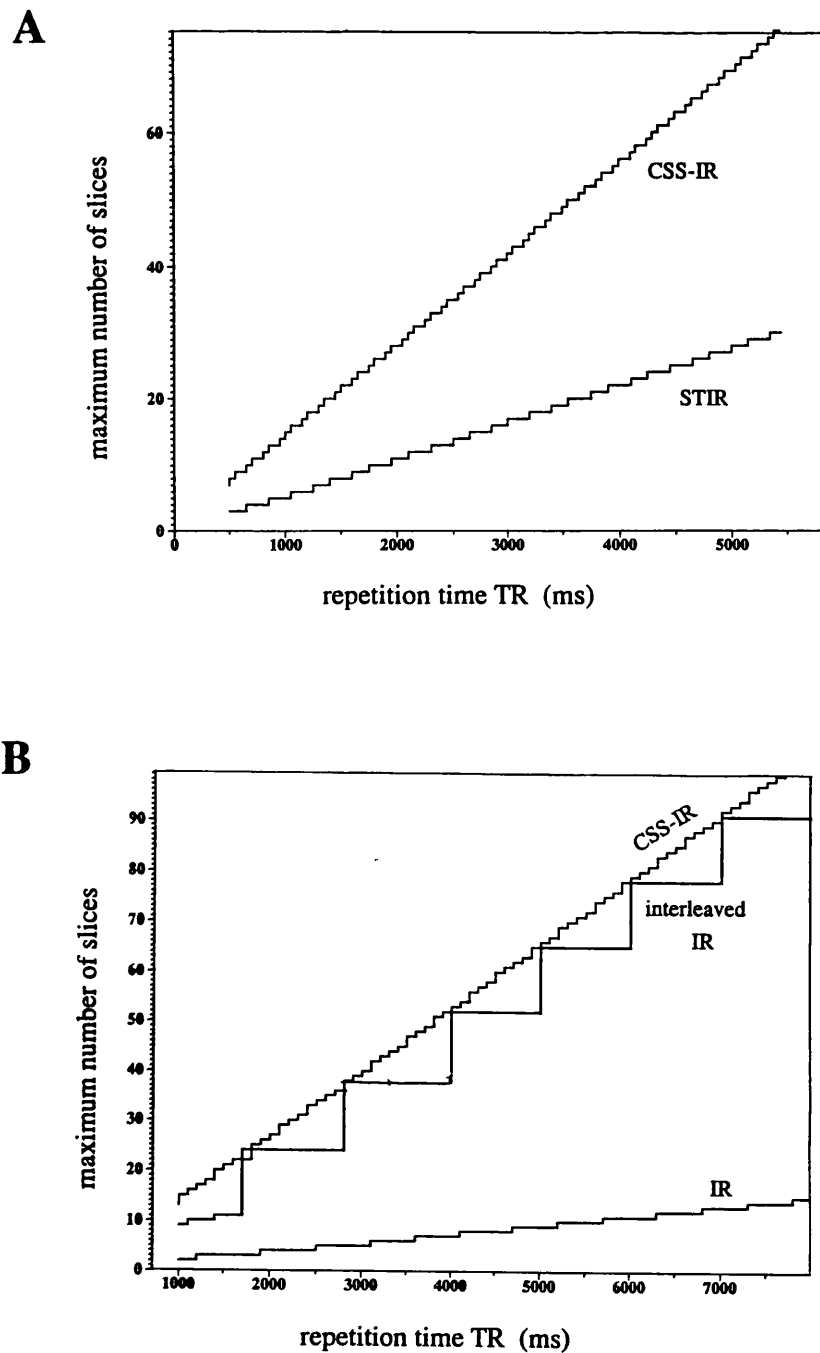


Figure 5.6. The maximum number of slices which can be selected within a repetition time TR for (A) the STIR and CSS-IR sequences for fat magnetization of $T_1=200$ ms, and (B) for the conventional multi-slice IR (Fig. 3.6.B), an IR sequence that employs a multiplexed (interleaved) slice selection scheme (Fig. 3.6.C), and the hybrid CSS-IR sequence, for water magnetization of $T_1=700$ ms. It is assumed that the total imaging time of the spin echo part of all sequences is 40 ms.

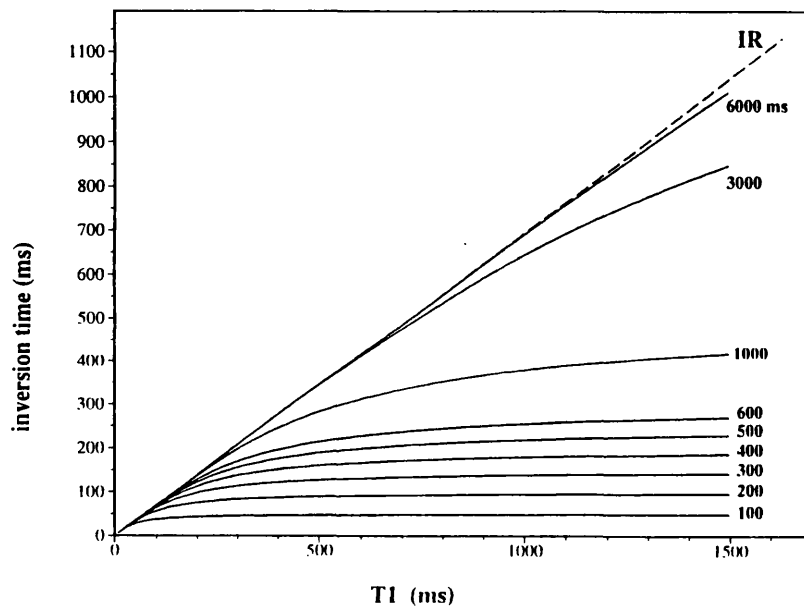


Figure 5.7. The calculated inversion time as a function of T_1 for IR (dashed line) and CSS-IR (solid lines), for a typical range of effective repetition times, T_{Reff} .

common values of TR_{eff} . Differentiation of Eqns. (5.2) and (5.9) shows that the rate of change of the inversion time as a function of T_1 for IR is always greater than the rate of change of the inversion time for CSS-IR. The hybrid sequence thus requires a smaller range of inversion times than IR to null signal from magnetization exhibiting a particular range of T_1 values, so the suppression is less dependent on the range of T_1 values present or on the accuracy of the measured or estimated T_1 . This may be particularly important in the case of water suppression, as water protons exhibit a rather wide range of T_1 values *in vivo*. An example is shown in Fig. 5.8, where the residual longitudinal magnetization at the time the read 90° pulse is applied, is plotted against the "assumed" T_1 used to calculate the null point for magnetization that exhibits a range of actual T_1 values. For this graph only the absolute value of the magnetization was considered, in order to match the magnitude mode representation in the conventional NMR imaging experiment.

An additional advantage of the hybrid sequence is that it can tolerate greater mis-settings of the tip angle of the chemical shift selective pulse than PRESAT. Figure 5.9 shows the magnitude of longitudinal magnetization ($T_1=200$ ms) at the time when the 90° slice selective pulse is applied, derived from Eqn. (5.4) as a function of the effective tip angle of the previous chemical shift selective pulse, for both PRESAT and CSS-IR. For this particular example the range of tip angles that result in a residual magnetization of less than 5% of its thermal equilibrium value are indicated by the arrows on the graph. For CSS-IR, this range is 42% of the nominal 180° value for the chemical shift selective pulse, whereas for PRESAT this range is only 12% of the nominal 90° value.

All the above arguments assume a steady state condition, so the need arises to determine how many repetitions of the CSS-IR sequence are required to reach it (see also Appendix 2). If it is assumed that the steady state condition is reached when the difference between the M_n and the steady-state magnetization M_{ss} is less than or equal to a predetermined value $\alpha\%$ of M_{ss} , then:

$$\frac{|M_n - M_{ss}|}{M_{ss}} \leq \frac{\alpha}{100} \quad (5.10)$$

or, substituting M_n and M_{ss} from Eqns. (5.5) and (5.6) respectively, the minimum number of sequence repetitions for the magnetization to be within $\alpha\%$ of the steady state value M_{ss} is:

$$n_{ss} \geq -\frac{T_1}{TR_{\text{eff}}} \ln \left(\frac{1}{2} \frac{\alpha}{100} (1 - e^{-TR_{\text{eff}}/T_1}) \right) \quad (5.11)$$

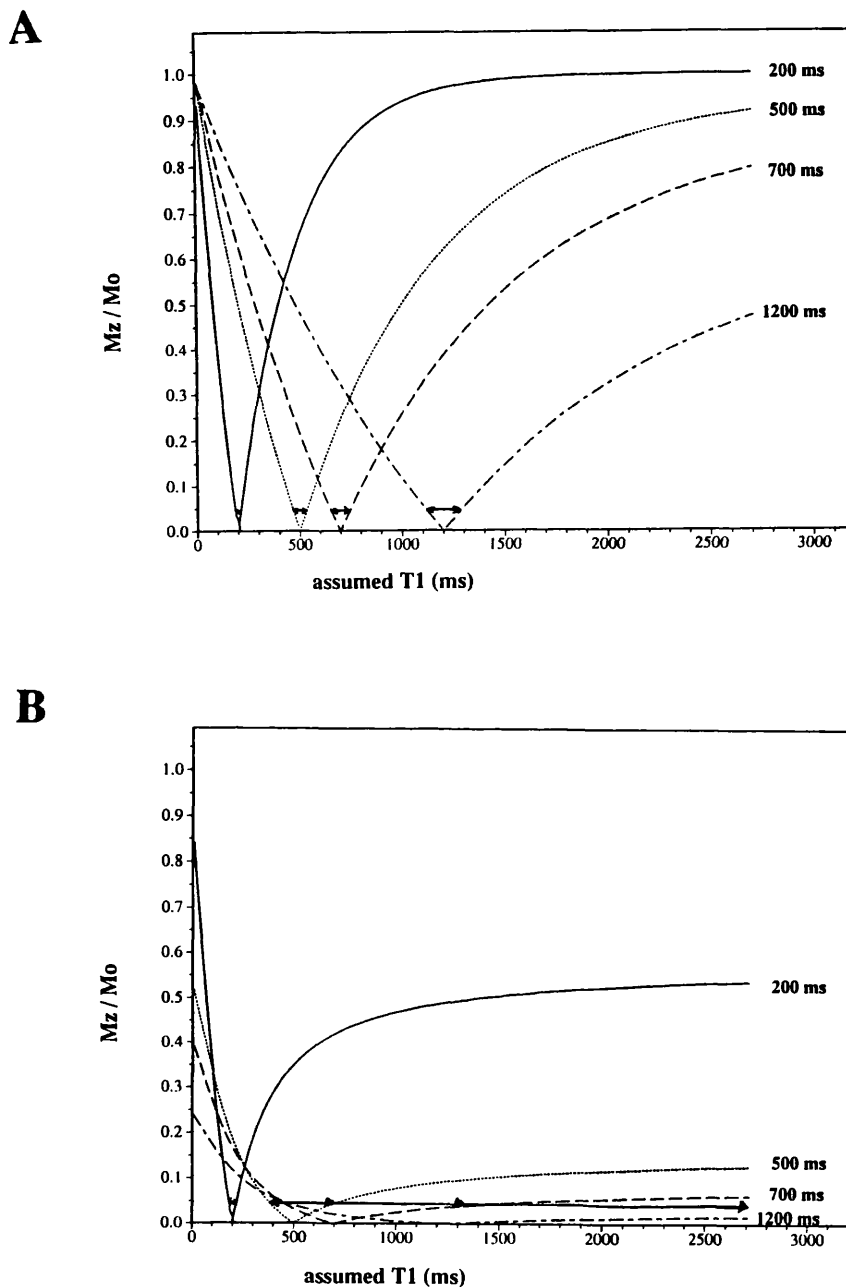


Figure 5.8. The amplitude of longitudinal magnetization M_z (as a fraction of its thermal equilibrium value M_0) just before the application of the 90° slice selective pulse, plotted against the "assumed" T_1 value used to calculate the inversion time, for a range of actual T_1 values, and for: (A) the conventional IR sequence, $TR=6000$ ms, and (B) the hybrid CSS-IR sequence, $T_{\text{Reff}}=600$ ms. The arrows indicate the range of assumed T_1 values for which the magnetization of each particular T_1 component is less than 5% of its thermal equilibrium value.

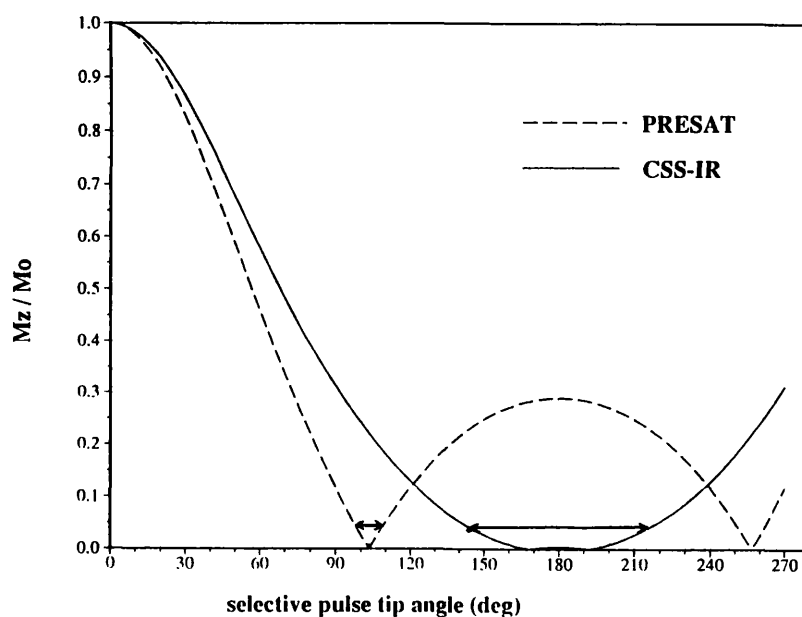


Figure 5.9. The amplitude of longitudinal fat magnetization M_z (as a fraction of its thermal equilibrium value M_0) just before the application of the 90° slice selective pulse, plotted against the tip angle of the chemical shift selective pulse for PRESAT (dashed line) and CSS-IR (solid line). The arrows indicate the range of tip angles for which the suppressed magnetization is less than 5% of its thermal equilibrium value. A T_1 of 200 ms, a T_{Reff} of 200 ms and a delay of 25 ms between the saturating pulse and the spin echo part of the experiment in the PRESAT are assumed.

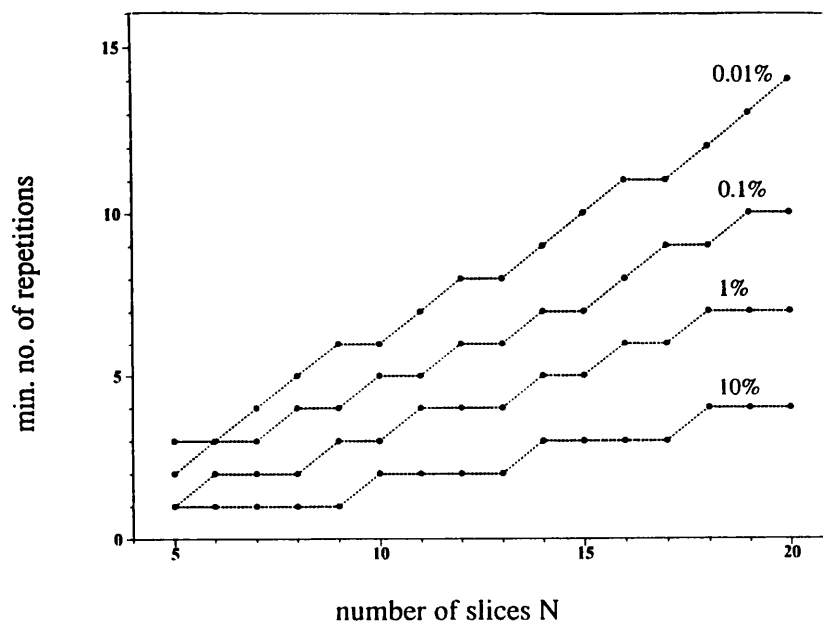


Figure 5.10: The minimum number of pulse repetitions required for the magnetization to reach within $\alpha\%$ of its steady-state value as a function of the number of slices. It is assumed that the magnetization has a T_1 of 200 ms and the total repetition time of the sequence is 3000 ms.

Note that only the repetition of the chemical shift selective pulse is of importance for the generation of the steady-state magnetization, thus n_{ss} refers to the number of repetitions of the chemical shift selective pulse and not to the number of complete sequence repetitions. For conventional imaging conditions, n_{ss} is usually very small compared to the total number of sequence repetitions (phase encoding and signal averaging), therefore steady state for the unwanted magnetization can be achieved within the first few encoding steps. Alternatively, n_{ss} can be accommodated as dummy scans at the beginning of the experiment with negligible increase of the total imaging time. Figure 5.10 shows the minimum number of the chemical shift selective pulse repetitions required for magnetization of $T_1=200$ ms to reach within $\alpha\%$ of its steady-state value as a function of the number of slices, for an overall sequence repetition time of 3000 ms.

To give an example of the timing for the CSS-IR sequence; in a clinical case from the literature [5.11] a STIR sequence with $TR=1560$ ms and $TI_{ir}=150$ ms was used to suppress signal from the orbital fat (mean T_1 of 215 ms) in a 6-slice image set of the optic nerve (white matter mean T_1 of 385 ms) in a 0.5 T clinical system. For the same data set with the same repetition time, the hybrid fat-suppression sequence would require an inversion time of $TI_{css-ir}=94$ ms (as opposed to 150 ms), while 9 dummy scans would be enough for the fat magnetization to reach a value with less than 0.01% difference from its steady state value.

5.3 EXPERIMENTAL METHODS

The hybrid CSS-IR sequence was evaluated, using phantoms, for its ability to suppress fat and water without degrading the S/N ratio for the remaining signal. The performance of the sequence was studied for its dependence on the estimated T_1 of the unwanted magnetization, as well as its dependence on the homogeneity of the static magnetic field, B_0 , and radiofrequency field, B_1 . Finally, CSS-IR was demonstrated *in vivo* by imaging the abdominal region of a normal, adult rat.

All experiments involved direct comparison with the most closely related conventional MRI methods for fat and water differentiation, that is, the T_1 -null IR (simply referred to as IR hereafter) and the chemical shift selective presaturation techniques. A single-slice chemical shift imaging method [5.12] (CSI) was also performed, as well as a conventional spin-echo imaging experiment. A diagrammatic representation of the pulse sequences is given in Fig. 5.11, where the shaded box represents the conventional spin-echo, spin-warp part of the imaging experiment, common to all sequences used. The study was performed on a SISCO-200 NMR imaging spectrometer (Spectroscopy Imaging Systems Corporation, Fremont, California), equipped with a 4.7 T, 33 cm bore superconducting magnet (Oxford

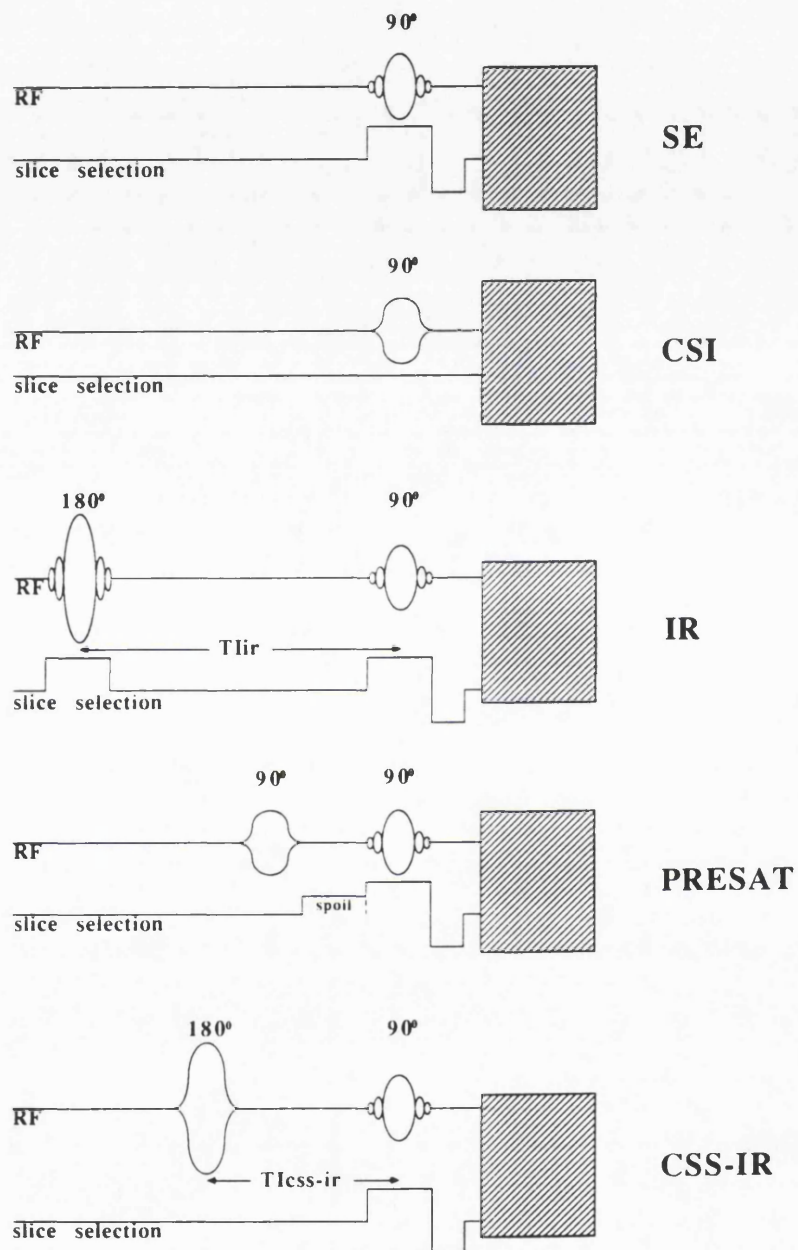


Figure 5.11. Pulse sequence diagrams for all techniques used. **SE:** conventional spin echo; **CSI:** single-slice chemical shift imaging sequence; **IR:** conventional inversion recovery; **PRESAT:** presaturation chemical shift selective imaging sequence; **CSS-IR:** proposed hybrid sequence. The shaded box, common to all sequences, represents the conventional spin-warp, spin echo experiment.

Instruments Ltd, Oxford, UK), and the STD33 SISCO magnetic field gradient set (20 mT/m, 33 cm inner diameter). An imaging coil with an inner diameter of 9 cm was used for all phantom and *in vivo* experiments.

5.3.1 Fat Suppression

Fat Suppression

The aim of this part of the study was to demonstrate the ability of the CSS-IR sequence to suppress fat in the images of a water/oil phantom, in direct comparison to the conventional MRI fat-suppression techniques already mentioned. The phantom used consisted of a glass tube (~1cm outer diameter, ~3.5 cm height) inside a glass beaker (~2.5 cm outer diameter, ~3.5 cm height). The inner tube contained mineral oil (Aldrich Chemical Co. Ltd., Gillingham SP8 4JL, England). The beaker contained distilled water doped with ~0.6 g/l copper sulphate (CuSO₄) to give a solution with a T₁ of ~360 ms. The mineral oil had a mean T₁ of ~200 ms. The T₁ value of each component was measured by the standard spectroscopic version of the inversion recovery technique [5.13]. A pilot spectrum from the phantom, acquired prior to the imaging experiments, showed that the oil resonance frequencies occurred within a ~2 ppm (400 Hz) range, centred ~3.6 ppm (720 Hz) upfield from the water peak (shimmed to 0.5 ppm full width at half maximum height).

For the imaging experiment, the phantom was placed vertically and 10 cross-sectional slices of 2 mm thickness and 3 mm centre-to-centre separation were acquired through the middle of the object. A series of imaging sequences was performed:

- (i) standard spin echo sequence,
- (ii) single-slice chemical shift imaging sequence, whereby only the desired component (i.e. water) was selectively excited in the absence of all magnetic field gradients by a chemical shift selective 90° pulse prior to a 180° slice selective refocusing pulse,
- (iii) conventional short inversion time inversion recovery, with T_{1ir}=139 ms,
- (iv) selective presaturation sequence, saturating the fat before each slice selective excitation of the sequence (with 25 ms delay between the presaturating pulse and the following spin echo part of the sequence),
- (v) the new hybrid sequence, where the frequency offset of the chemical shift selective pulse was set to the centre of the fat resonance and the inversion time was calculated using Eqn. (5.9) to null the signal from fat protons, i.e. T_{1css-ir}=75 ms. 12 dummy scans were incorporated at the beginning of the experiment to allow for the fat magnetization to reach less than 0.01% difference from its steady state value, Eqn. (5.11).

The standard spin echo, the conventional inversion recovery, and the single slice chemical shift selective pulse sequence programs were supplied by the manufacturer (VNMR software, Varian Associates Inc.), while all the rest of the sequences were implemented using the C programming language and the libraries supplied by the manufacturer. Post-processing and display were accomplished by the UNC image processing software (University North Carolina, USA).

All imaging experiments were performed with a 4x4 cm field of view, 256x128 data matrix and 4 signal averages per phase encoding step to enhance signal-to-noise ratio and to allow for the phase cycling procedure described in Appendix 1. The acquisition, echo, and repetition time were kept constant for all sequences at 15 ms, 30 ms, and 2000 ms, respectively. Slice selection was performed with 5000 μ s five-lobe sinc pulses in the presence of 11.7 mT/m linear magnetic field gradient, giving a slice thickness of 2 mm, while the chemical shift selection used 2500 μ s Gaussian pulses of 800 Hz effective frequency bandwidth, i.e. 4 ppm at 4.7 T.

The oil signal was calculated for all images by measuring the mean signal intensity from a 25 mm² (i.e. 512 pixels) region of interest, while the noise was determined by measuring the mean intensity from a 200 mm² (i.e. 4096 pixels) region of interest in the background. The standard error of the mean signal intensity (SEM) was calculated as the standard deviation of the mean divided by the square root of the number of pixels in the area of interest [5.14]. It should be noted that all images were magnitude images, therefore there should be expected a positive bias to the measurements of any low-level signal, such as the suppressed oil signal [5.15, 5.16]. However, no effort was made to correct this positive bias, as the main concern in this study was a relative evaluation of the efficiency of different methods to suppress the oil signal, and not the deduction of absolute values.

T₁ Dependency

Fat suppression in both IR and CSS-IR sequences depends on the accuracy of the determination of the fat T₁, as discussed in the theory (Figs. 5.7 and 5.8). A series of experiments was performed to study the dependency of fat-suppression on the accuracy of the estimated fat T₁ value, that is the sensitivity of fat-suppression to the inversion time used.

The hybrid CSS-IR and the conventional IR sequence were performed as above. The experiments were then repeated for a range of different inversion times, T_{ICSS-ir} and T_{Iir}. These TI values were calculated using Eqns. (5.9) and (5.8) respectively, assuming hypothetical T₁ values for the oil ranging up to $\pm 60\%$ of the actual T₁ value of 200 ms (hypothetical T₁ values ranged from 80 to 300 ms). The oil signal in all experiments was measured as before.

B1 Dependency

The aim of this part of the study was to investigate the dependency of fat-suppression on the effective tip angle of the fat selective pulse, as discussed in the theory (Fig. 5.9). The hybrid CSS-IR and the conventional PRESAT sequence were performed as in the first part of the study. The experiments were then repeated for a range of different effective tip angles for the chemical shift selective pulses, i.e. the 90° saturation pulse in the PRESAT sequence, and the 180° inversion pulse in the new sequence respectively. The tip angles were calculated to be within a range from -44% to +41% of the nominal value for the fat selective pulse in both sequences, i.e. from 50° to 127° for the presaturating pulse in PRESAT, and from 101° to 254° for the inverting pulse in CSS-IR. Note that although variations in B1 are generally relatively small for conventional imaging coils in clinical systems, the radiofrequency field can be greatly degraded in surface coil imaging.

B0-Homogeneity Dependency

As both PRESAT and CSS-IR sequences employ chemical shift selective pulses, the suppression depends on the spectral resolution of the two resonances. Sufficient suppression can always be ensured by the use of a rather broad frequency selective pulse to excite or invert, respectively, the whole range of the unwanted resonances. However, in situations where the spectral resolution is degraded, for example by regional B0 inhomogeneities, such a pulse may also suppress part of the desired signal. This experiment was, therefore, intended to study the effects of PRESAT and the hybrid fat-suppression technique on the water signal in such cases.

The hybrid CSS-IR and the conventional PRESAT sequence were performed as in the first part of the study. The experiments were then repeated for a range of different effective bandwidths of the chemical shift selective pulses (centred on the oil resonance). The bandwidths were calculated to cover the whole possible range of frequency selection, from suppressing just the oil peak (2 ppm), to suppressing the whole spectrum (10 ppm).

5.3.2 Water Suppression

Water Suppression

The aim of this part of the study was to demonstrate the ability of the CSS-IR sequence to suppress water in the images of a water and oil phantom, in direct comparison to the conventional MRI water-suppression techniques already mentioned. The phantom consisted of several glass tubes (~1 cm outer diameter, ~3.5 cm height) within a glass beaker (~4.5 cm outer diameter, ~4 cm height). Each phantom compartment contained either mineral oil (Aldrich Chemical Co. Ltd., Gillingham SP8

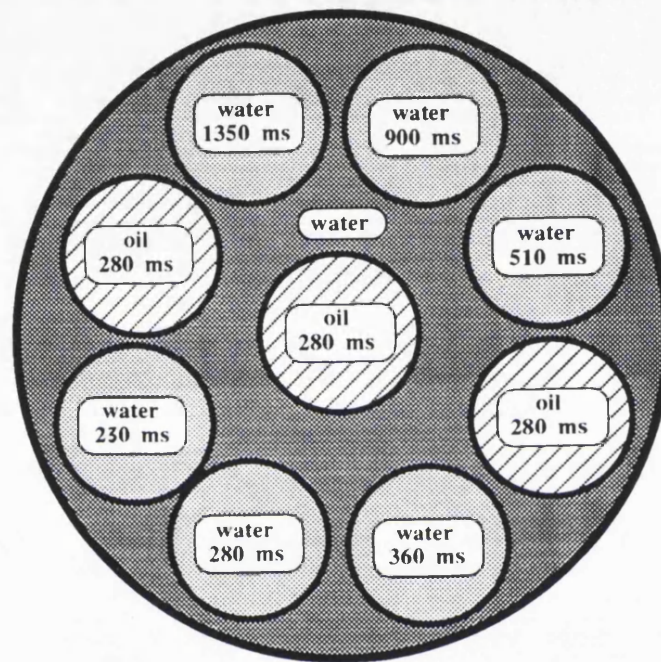


Figure 5.12. Schematic diagram of a cross section of the phantom used for the water suppression part of the experimental study.

4JL, England), or water doped with copper sulphate (CuSO_4) in a range of concentrations to give water T_1 values in a range similar to that found in clinical MRI. A schematic diagram of a cross-section of the phantom is shown in Fig. 5.12. The T_1 value of each component (also shown in Fig. 5.12) was measured by the standard spectroscopic version of the inversion recovery technique [5.13]. A pilot spectrum from the phantom, acquired prior to the imaging experiments, showed that the oil resonance frequencies occurred within a ~ 2 ppm (i.e. 400 Hz) range, centred ~ 3.6 ppm (i.e. 720 Hz) upfield from the water peak (shimmed to 0.5 ppm full width at half maximum height). The mean T_1 value of the water resonance peak was measured to be ~ 650 ms.

For the imaging experiment, the phantom was placed vertically and 10 cross-sectional slices of 2 mm thickness and 3 mm centre-to-centre separation were acquired through the middle of the object. The series of imaging sequences of Fig. 5.11 was performed, while the acquisition, echo and repetition times were kept constant at 5 ms, 30 ms, and 3000 ms, respectively. The inversion time for the IR and the hybrid sequence was calculated to correspond to the null point of the mean magnetization $T_1=650$ ms, that is, $T_{\text{IIR}}=450$ ms and $T_{\text{ICSS-IR}}=133$ ms. As the multi-slice selection was performed in the conventional fashion (simply repeating the same experiment to select a different slice within the repetition time), the inversion time of 450 ms and the repetition time of 3000 ms allowed only for 5 slices to be selected in the IR experiment. All imaging experiments were performed with a 6x6 cm field of view, 128x128 data matrix and 4 signal averages per phase encoding step to enhance signal-to-noise ratio and allow for the phase cycling procedure described in Appendix 1. Slice selection was performed with 5000 μs five-lobe sinc pulses in the presence of 11.7 mT/m linear magnetic field gradient, giving a slice thickness of 2 mm, while the chemical shift selection used 2500 μs Gaussian pulses of 800 Hz effective frequency bandwidth, i.e. 4 ppm at 4.7 T.

The water signal was calculated for all images by measuring the mean signal intensity from a 14 mm² (i.e. 64 pixels) region of interest, while the noise was determined by measuring the mean intensity from a 112 mm² (i.e. 512 pixels) region of interest in the background. The standard error of the mean signal intensity (SEM) was calculated as before.

T₁ Dependency

A series of experiments was performed to study the dependency of water-suppression on the estimated water T_1 value for the hybrid CSS-IR and the conventional IR techniques. Both sequences were performed as above, using the mean water T_1 value for the calculation of the inversion time. The experiments were then repeated for a range of different inversion times, calculated to correspond to the null point of each one of the water phantom compartments with T_1 values of 230 ms, 280 ms, 360 ms, 510

ms, 900 ms, and 1350 ms, respectively. The water signal in all experiments was measured as before. It should be noted that in the IR experiments the number of slices that could be selected within the repetition time of 3000 ms was reduced to 8 slices for the case of 360 ms "assumed" T_1 , 6 slices for the case of 510 ms T_1 , 4 for the case of 900 ms T_1 , and 2 slices for the case of 1350 ms "assumed" T_1 .

B₀-Homogeneity Dependency

This experiment was intended to study the effects of both the PRESAT and the hybrid water-suppression technique on the remaining fat signal in cases where the spectral resolution is degraded and broad frequency chemical shift selective pulses are used. The hybrid CSS-IR and the conventional PRESAT sequence were performed as in the first part of this study. The experiments were then repeated for a range of different effective bandwidths of the chemical shift selective pulses (centred on the water resonance). The bandwidths were calculated to cover the whole possible range of frequency selection, from suppressing just the water peak (2 ppm), to suppressing the whole spectrum (12.5 ppm). The oil signal in all experiments was measured as before.

IR with a non-Selective Inversion Pulse

It is expected that even in the extreme case of a non-selective (hard) inversion pulse, there should be a wide range of inversion times for the CSS-IR sequence that would result in good suppression of long T_1 components (i.e. water) while preserving a considerable residual signal for short T_1 components (e.g. fat), as is also shown in Fig. 5.8.B. Therefore, the CSS-IR sequence was performed with a non-selective inversion pulse of 2500 Hz bandwidth (12.5 ppm) and for a range of inversion times corresponding to the null point of each water phantom component, as well as the longer T_1 values of 2000 and 3000 ms. The water and oil signal in all experiments was measured as before. It should be noted that when the inversion pulse in the CSS-IR sequence is no longer chemical shift selective, the acronym CSS-IR is not appropriate. In such cases the sequence should more appropriately be referred to as "modified IR".

5.3.3 *In Vivo* Studies

A normal 350 g adult male Wistar rat was placed in the magnet in a prone position, under anaesthesia induced and maintained by 1% (v/v) halothane in oxygen flowing at a rate of 1 l/min. A series of inversion recovery spectra were obtained with a range of inversion times from which the T_1 of bulk fat was estimated to be ~326 ms.

To demonstrate fat-suppression, 15 axial slices, 2.4 mm thick, in the abdominal region were acquired using a spin echo sequence with $TR=3000$ ms, a conventional IR with $TR=5115$ ms and $TI_{ir}=226$ ms, PRESAT with $TR=3000$ ms and the CSS-IR

sequence with $TR=3000$ ms and $T_{I_{css-ir}}=85$ ms. All imaging experiments were performed with $TE=30$ ms, 8x8 cm field of view, 256x256 data matrix and 4 signal averages per phase encode step.

To demonstrate water suppression in the extreme case of a non-selective inversion pulse, 10 axial slices, 2.4 mm thick, in the abdominal region were acquired using a conventional spin echo and a CSS-IR with a non-selective inversion pulse, i.e. modified IR sequence. The repetition time was 3000 ms for both sequences. An inversion time of 144 ms was used for the CSS-IR, calculated assuming a T_1 value of 2000 ms to correspond to the fluid of the bladder. A conventional IR experiment was also performed, with an inversion time of 1385 ms. Despite the longer repetition time of 6000 ms, only 4 slices could be afforded with the IR sequence. All imaging experiments were performed with $TE=30$ ms, 7x7 cm field of view, 256x256 data matrix and 4 signal averages per phase encode step.

5.4 RESULTS AND DISCUSSION

5.4.1 Fat Suppression

Fat Suppression

The 5th slice from each 10-slice data set is shown in Fig. 5.13. The chemical shift artifact is well illustrated in the spin echo image, where the fat signal is displaced relative to water in the frequency encode (horizontal) direction. A bright/dark ring appears at the interface of the two components because of the superposition of the mis-registered signals. In the IR image, the degradation of the image quality is apparent as signal from the water compartment is significantly suppressed. Images acquired using the single slice chemical shift selective sequence, the fat presaturation and the CSS-IR sequence, on the other hand, exhibit both good fat suppression and image quality.

The oil and water signals for all sequences are given in Table 5.1. If a 100% suppression is defined to be the suppression of the high signal in the spin-echo experiment down to the noise level, the three conventional fat-suppression techniques and the new hybrid sequence result in about 99% suppression for the oil signal.

T₁ Dependency

Figure 5.14 shows the residual oil signal in the IR and CSS-IR sequence images as a function of the "assumed" value of oil T_1 used to calculate the inversion time for both sequences. In the IR images, suppression of the oil signal greater than 95% is achieved only over a limited T_1 range of 80 ms round the actual oil T_1 value of 200 ms, and drops down to 74% or 78%, respectively, for "assumed" T_1 values 60% shorter or

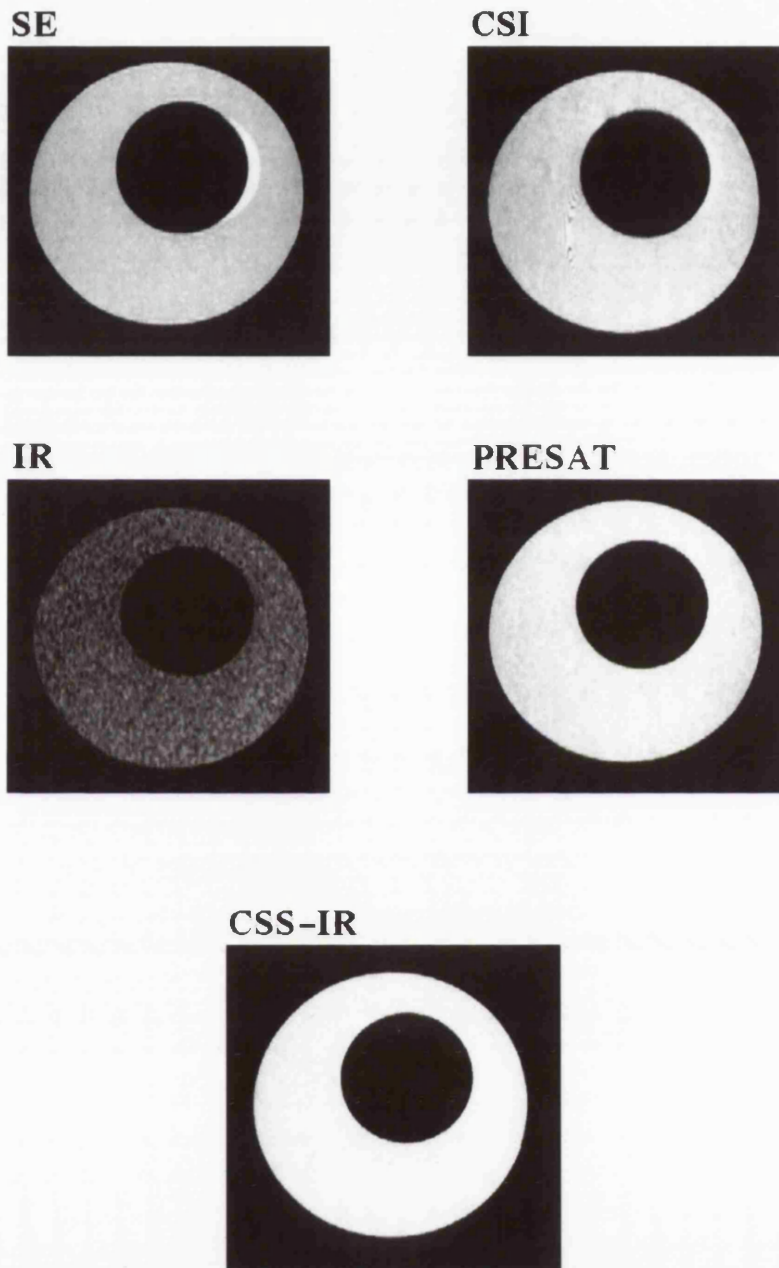


Figure 5.13. Phantom images from the middle slice of each data set acquired using a spin echo sequence (SE), and fat-suppressed CSI, IR, PRESAT, and CSS-IR sequences. The phantom consists of a tube containing oil within a beaker full of water.

TABLE 5.1		
	oil signal	water signal
spin echo	110.3 ± 0.4	306.8 ± 0.4
csi	12.2 ± 0.2	297.5 ± 0.4
ir	12.1 ± 0.2	51.1 ± 0.3
presat	12.5 ± 0.3	298.7 ± 0.4
css-ir	12.5 ± 0.2	307.8 ± 0.4
noise	11.5 ± 0.1	11.5 ± 0.1

Table 5.1. Fat and water signal, as well as noise mean intensities (arbitrary units) corresponding to the images in Fig. 5.13. The mean intensities and the standard error of the mean (SEM) have been calculated as described in the text .

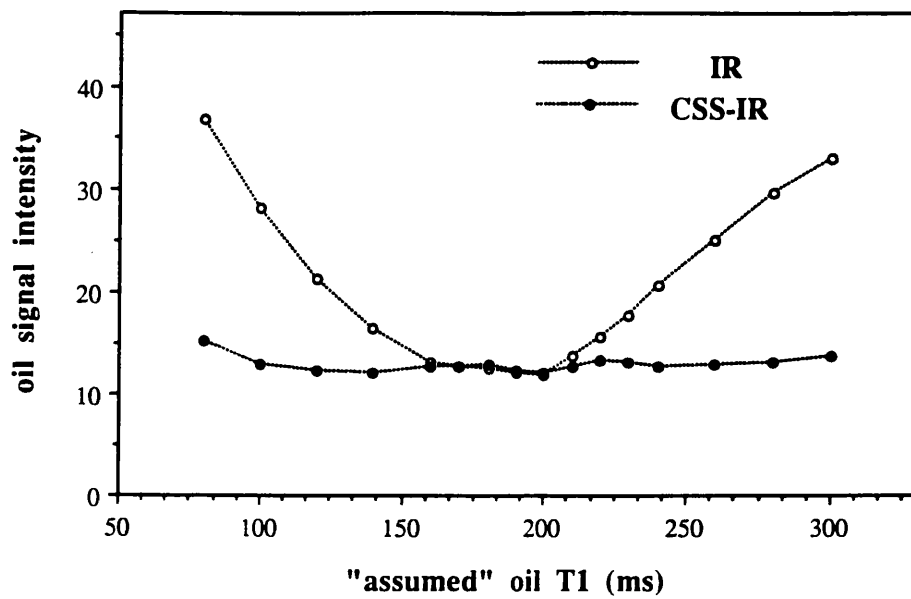


Figure 5.14. Measured oil signal intensity (arbitrary units) plotted against the "assumed" value of oil T1 (used to calculate the inversion time) for both the conventional IR and the CSS-IR sequence.

longer than the actual oil T_1 . In contrast, the CSS-IR sequence gives a fat-suppression greater than 95% over the whole range of the "assumed" T_1 values used in this series of experiments (i.e. 220 ms). These results show that fat-suppression by the proposed hybrid sequence is relatively independent of the value of fat T_1 , as predicted by the theoretical analysis (see Fig. 5.7).

B1 Dependency

Figure 5.15 shows the residual oil signal in the PRESAT and CSS-IR sequence images as a function of the effective tip angle for the selective pulse. For the PRESAT sequence fat-suppression is greater than 95% only for the limited range of effective tip angles from 80° to 101° , which corresponds to a mis-setting of -11% to 12% of the nominal 90° value. For the extreme value of 50° used in this experiment (-44% mis-setting), the fat-suppression drops as low as 54%. The CSS-IR sequence, on the other hand, shows the same efficient performance of more than 95% fat-suppression for the much wider range of effective tip angles from 113° to 213° . This corresponds to a mis-setting of -37% to 18% of the desired 180° value. Even for the extreme values of 101° or 254° (-44% and 41% mis-setting), fat-suppression is as high as 91% and 81% respectively. These results show that fat-suppression by the proposed hybrid sequence is high for a significantly wider range of tip angles for the fat selective pulse, as predicted by the theoretical analysis (see Fig. 5.9).

B0-Homogeneity Dependency

Figure 5.16 shows the water signal in the images from both the PRESAT and the CSS-IR sequences as a function of the effective frequency bandwidths for the chemical shift selective pulses. All experiments showed fat-suppression equal to or better than 99%, so the oil signal has not been plotted. Selective pulses centred on the oil resonance with bandwidths up to 6 ppm should not affect the water protons whose resonances lie within a 0.5 ppm range centred 3.6 ppm away. This agrees with the experimental results for both sequences, as presented in Fig. 5.16. Pulses with frequency bandwidths wider than 6 ppm are expected to affect both the oil and water resonances, and this can be seen in Fig. 5.16, where the water signal is progressively suppressed as the pulse becomes less selective. However, the remaining water signal in the images acquired with the hybrid sequence is always significantly larger than in the corresponding PRESAT images. Although in the PRESAT sequence, all the "selected" magnetization excited by the primary 90° pulse is completely saturated, in the CSS-IR sequence the magnetization affected by the chemical shift selective pulse is merely inverted and is nulled only if the inversion time corresponds to its null point. Since water generally has a much longer T_1 relaxation time than fat, then even if it is all

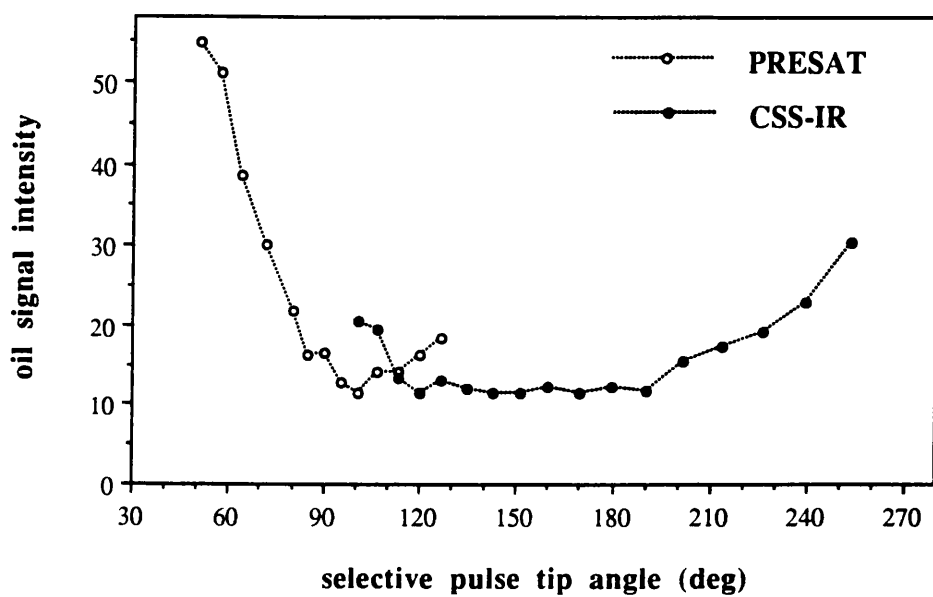


Figure 5.15. Measured oil signal intensity (arbitrary units) plotted against the effective tip angle of the chemical shift selective pulse, for the PRESAT and the CSS-IR sequence.

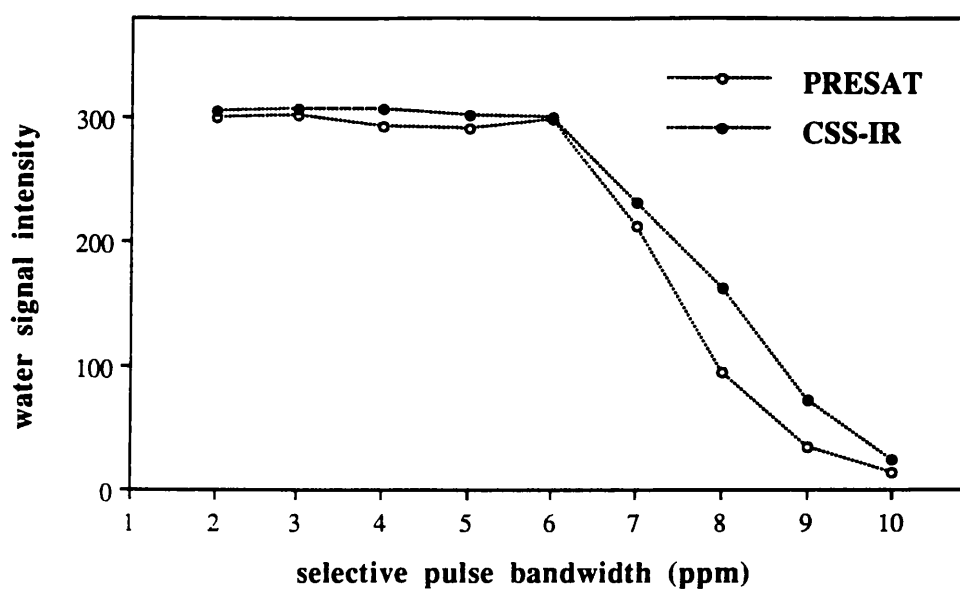


Figure 5.16. Water signal intensity (arbitrary units) plotted against the bandwidth of the chemical shift selective pulses (centred on the oil resonance), for the PRESAT and the hybrid CSS-IR sequence.

inverted by the selective pulse of the CSS-IR sequence it will still yield some residual signal, the value of which depends upon the water T_1 and the sequence parameters.

5.4.2 Water Suppression

Water Suppression

The central slice from the data set acquired with each sequence is shown in Fig. 5.17. The chemical shift artifact is again apparent in the spin echo image. In the IR image, water suppression is efficient only for the water component of $T_1=900$ ms. Images acquired using the CSS-IR sequence, on the other hand, exhibit good water suppression for all phantom compartments, and only the shorter T_1 components of 280 ms and 230 ms give a slight signal.

The oil and water signals of the phantom compartments for all sequences are given in Table 5.2. If a 100% suppression is defined as before, the single slice chemical shift selective sequence results in about 99% suppression of the water signal in all phantom compartments. The PRESAT sequence results in water suppression equal to or better than 95%. This poorer performance of PRESAT relative to CSI may be due to some mis-setting of the tip angle of the chemical shift selective pulse. Such a mis-setting would not affect the water signal in the CSI method, as the pulse is not affecting the water resonance. In the PRESAT sequence, however, mis-setting of the tip angle of the saturating pulse would result in some residual magnetization of the unwanted component. The IR sequence produces significant effect only for the components with T_1 close to the mean T_1 value used to calculate the inversion time, resulting in 89% suppression for the 1350 ms T_1 component, 92% for $T_1=900$ ms, and 86% for $T_1=510$ ms. The suppression for the remaining components is as low as 44%, 31% and 13% for the T_1 values of 360, 280, and 230 ms, respectively. On the other hand, water suppression with the new sequence is much less dependent on T_1 . The CSS-IR sequence results in a water suppression of more than 95% for the T_1 components of 1350 and 900 ms, 90% for T_1 values of 510 and 360 ms, and 88% and 82% for the T_1 components of 280 ms and 230 ms, respectively.

T_1 Dependency

Figure 5.18 shows the residual water signal in the IR and CSS-IR sequence images as a function of the "assumed" value of water T_1 used to calculate the inversion time for both sequences. In the IR experiment, each one of the water components is efficiently suppressed only when the inversion time is calculated to correspond to its T_1 value. For long T_1 components, the graph shows that the best suppression is achieved for assumed T_1 values shorter than the actual T_1 value of the component. This is due to the fact that the repetition time of the sequence is relatively short compared to the long T_1

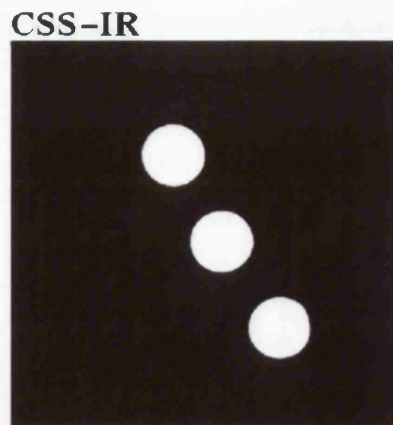
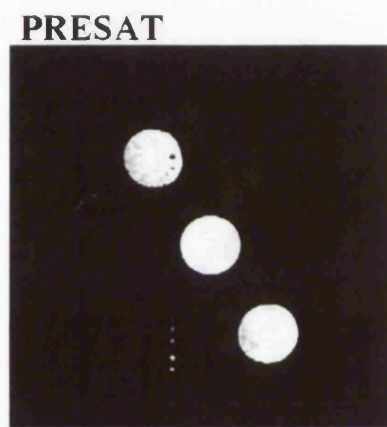
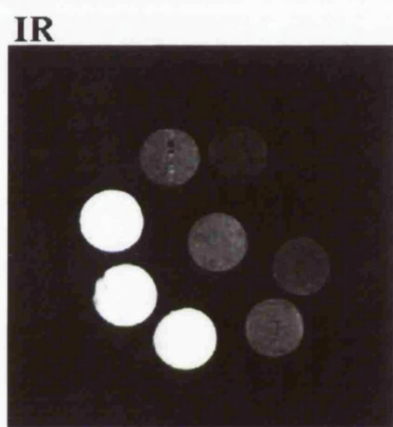
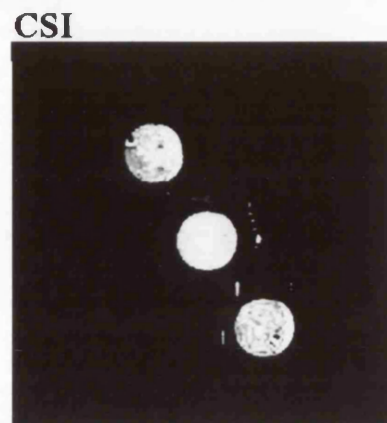
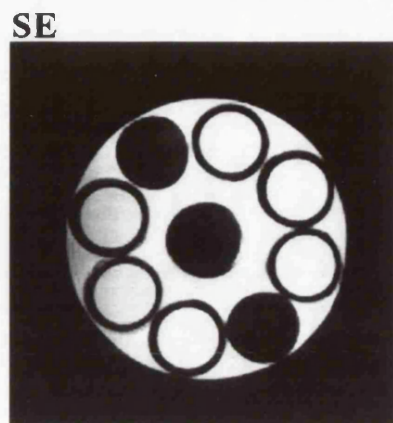


Figure 5.17. Phantom images from the 5th slice of data set acquired using a spin echo sequence (SE), CSI, conventional IR, PRESAT, and CSS-IR sequences. The phantom is the one shown in Fig. 5.12.

TABLE 5.2					
	spin echo	csi	ir	presat	css-ir
oil	309 ± 1.8	305 ± 1.8	226 ± 1.7	308 ± 1.7	305 ± 1.8
water 1350 ms	935 ± 2.1	18 ± 0.7	110 ± 0.7	45 ± 0.7	31 ± 0.8
water 900 ms	934 ± 2.2	16 ± 0.7	91 ± 1.1	56 ± 1.0	47 ± 1.1
water 510 ms	924 ± 2.1	20 ± 1.0	139 ± 0.7	49 ± 0.7	97 ± 0.8
water 360 ms	933 ± 2.1	14 ± 0.7	530 ± 2.2	52 ± 0.7	100 ± 0.8
water 280 ms	777 ± 1.7	17 ± 1.0	544 ± 2.1	48 ± 0.7	106 ± 1.7
water 230 ms	704 ± 1.7	19 ± 0.7	614 ± 1.6	49 ± 1.7	135 ± 1.7
noise	14 ± 0.6	14 ± 0.6	14 ± 0.6	14 ± 0.6	14 ± 0.6

Table 5.2. Oil and water signal, as well as noise mean intensities (arbitrary units) corresponding to the images in Fig. 5.17. The mean intensities and the standard error of the mean (SEM) have been calculated as described in the text .

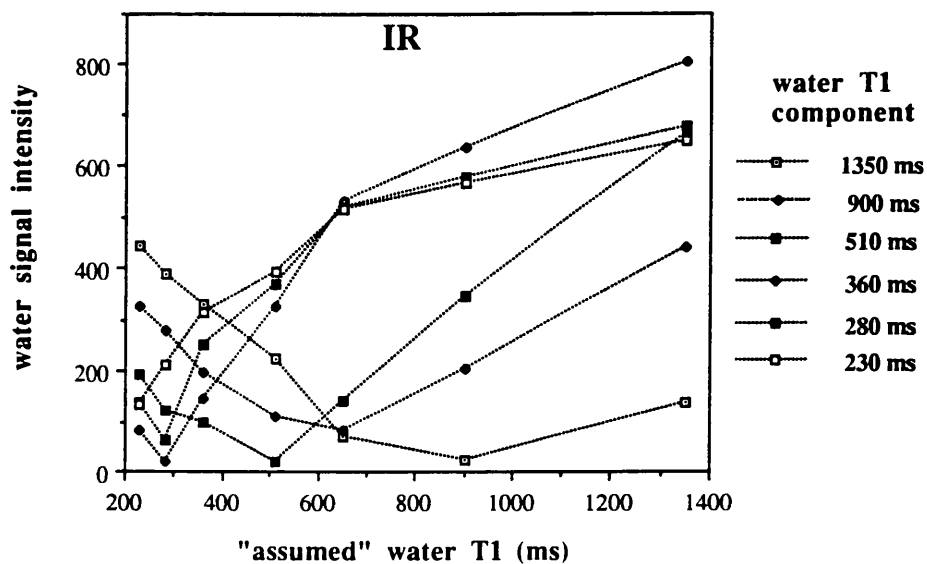
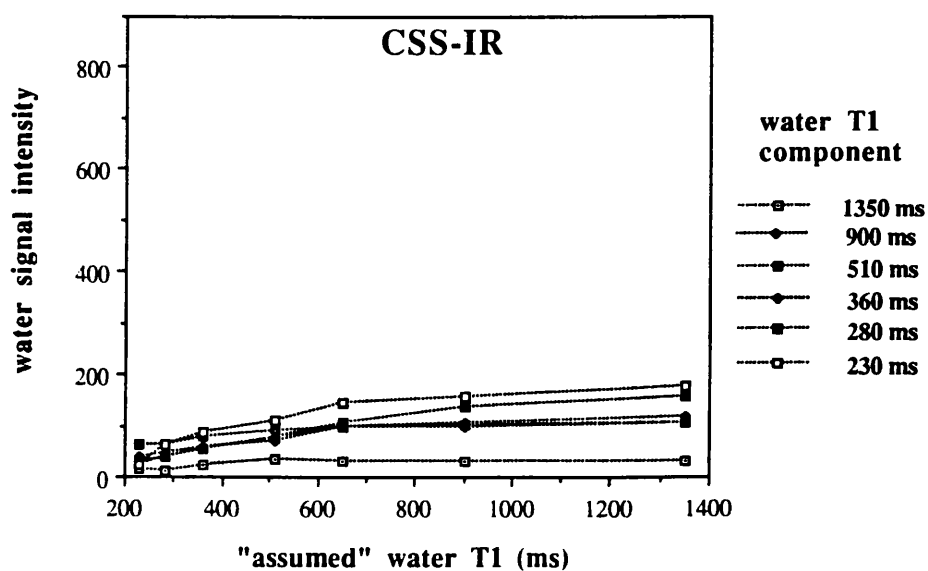
A**B**

Figure 5.18. Measured water signal intensity (arbitrary units) plotted against the "assumed" value of T₁ (used to calculate the inversion time) for (A) the conventional IR, and (B) the CSS-IR sequence.

values of some of the phantom compartments. In such cases the approximate Eqn. (5.8) used to calculate the inversion time for the IR sequence does not hold and the actual null point (as calculated by Eqn. (5.7)) is significantly shorter. For example, the error in the calculation for the null point of the 900 ms and 1350 ms T_1 components for a TR of 3000 ms is 5% and 17.5%, respectively.

The CSS-IR sequence gives efficient water suppression for all the phantom compartments and for the entire range of the "assumed" T_1 values used in this series of experiments. Specifically, the suppression of the component with $T_1=1350$ ms is greater than 98% over the whole range of the assumed T_1 values. The suppression of the 900 ms, 510 ms, and 360 ms T_1 components is always greater than 90%, while the suppression of the 280 ms and 230 ms T_1 components is greater than 90% for shorter assumed T_1 values (in the range from 230 ms to 510 ms) and between 80% and 90% for longer assumed T_1 values. These results show that water suppression by the proposed hybrid sequence is relatively independent of the value of water T_1 , especially for longer T_1 components, as predicted by the theoretical analysis (see Fig. 5.8.B).

Bo-Homogeneity Dependency

Figure 5.19 shows the oil signal in the water suppressed images acquired using the PRESAT and the CSS-IR sequences as a function of the effective frequency bandwidths for the chemical shift selective pulses. Selective pulses centred on the water resonance with bandwidths up to 3 ppm should not affect the oil protons whose resonances lie within a 2 ppm range centred 3.6 ppm away. This agrees with the experimental results for both sequences, as presented in Fig. 5.19. Pulses with frequency bandwidths greater than 3 ppm are expected to affect both the oil and water resonances, and this can be seen in Fig. 5.19, where the oil signal is progressively suppressed as the pulse becomes less selective. However, the remaining oil signal in the images acquired with the hybrid sequence is always significantly larger than in the corresponding PRESAT images. This is due to the fact that the oil magnetization is only inverted in the CSS-IR sequence, and has already relaxed to a positive value when the spin echo part of the sequence is applied (as the inversion time has been calculated to null longer T_1 components). A significant reduction of the oil S/N is, however, expected, and it is dependent on the oil T_1 , the "assumed" water T_1 value used for the calculation of the inversion time and the effective repetition time of the inverting pulse.

IR with a non-Selective Inversion Pulse

Figure 5.20.A shows the water and the oil signal in the images acquired using the CSS-IR sequence with a non-selective inversion pulse as a function of the "assumed" T_1 value used to calculate the inversion time. The oil, with a short T_1 value

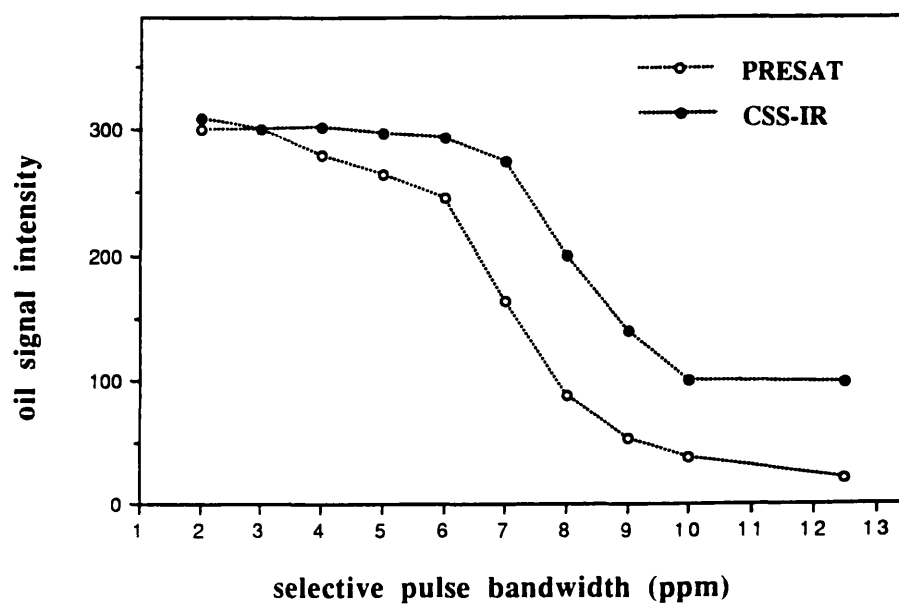
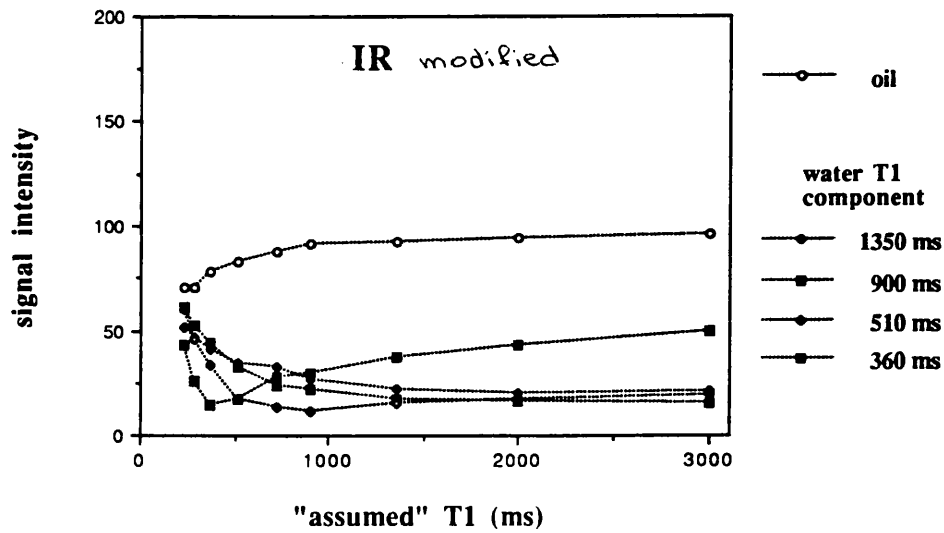


Figure 5.19. Oil signal intensity (arbitrary units) plotted against the bandwidth of the chemical shift selective pulses (centred on the water resonance), for the PRESAT and the hybrid CSS-IR sequence.

A



B

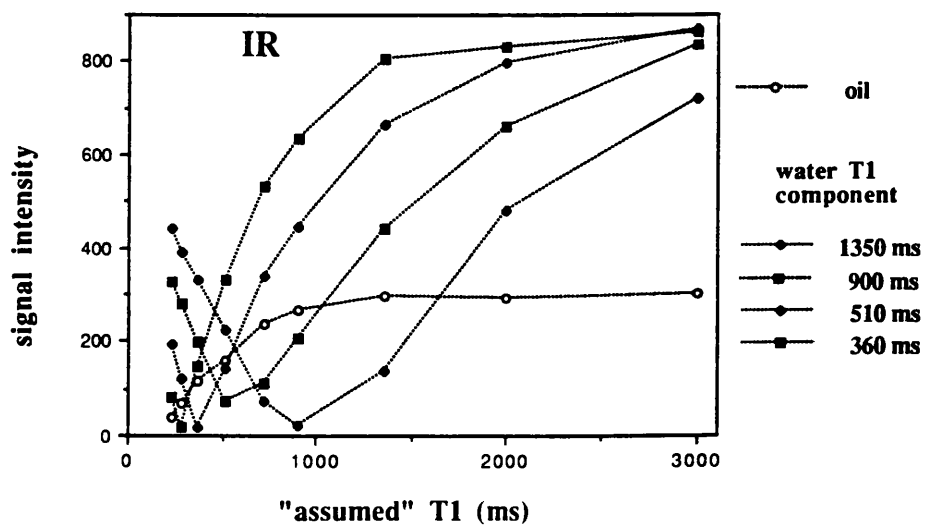


Figure 5.20. Measured signal intensity (arbitrary units) plotted against the "assumed" value of T1 (used to calculate the inversion time) for (A) the hybrid CSS-IR sequence with a non-selective inversion pulse, and (B) the conventional IR sequence.

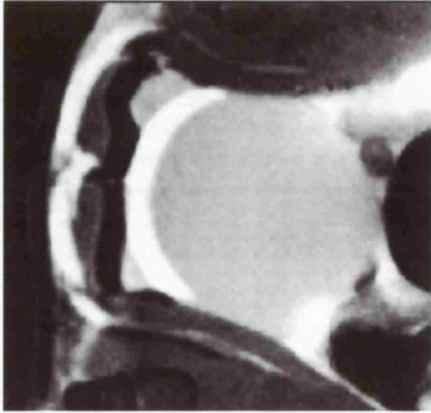
of ~280 ms, shows a residual signal intensity which is higher than the signal intensity of the longer T₁ water components, and is maximized for longer assumed T₁ values, i.e. higher than 1500 ms. However, as the suppression is relatively independent of the assumed T₁, the longer T₁ water components are efficiently suppressed for the relatively long assumed T₁ values of 2000 and 3000 ms. The signal from the compartment of the intermediate T₁ of 360 ms, however, is progressively increased for the longer assumed T₁ values of 2000 and 3000 ms. In summary, suppression of water magnetization in the T₁ range of 510-1350 ms is better than 95% for an assumed T₁ value of as long as 3000 ms, while the oil magnetization is only suppressed by 65%. Therefore, even in the extreme case of non-selective inversion pulse, the CSS-IR can give images with good suppression for relative long T₁ components, and significant residual oil signal (although with relatively degraded S/N). The results of the conventional IR sequence are shown in Fig. 5.20.B, for comparison. Once again, it is apparent that suppression of each T₁ component is strongly dependent on the accuracy of the assumed T₁ used to calculate the inversion recovery.

5.4.3 *In Vivo* Studies

Figure 5.21 shows images of a cross section at the level of the bladder of a normal rat as obtained by spin echo, and fat suppressed IR, PRESAT and CSS-IR sequences. In the spin echo image the chemical shift artifact is again apparent, with the signal of the abdominal fat being superimposed on the water signal, creating a bright ring at the left side of the bladder wall. Fat suppression in the following images has removed the artifact and the bladder is clearly outlined. Once again, in the IR image the low S/N ratio for the tissues surrounding the bladder results in a significant loss of the overall anatomical detail. Note that although the CSS-IR sequence gives efficient fat suppression, the PRESAT image still suffers from some chemical shift artifact, probably due to regional differences in B₁ homogeneity.

Figure 5.22 shows images of a cross section in the abdominal region of a normal rat obtained with a spin echo sequence, as well as water suppressed images acquired with the conventional IR and the modified IR, that is, the CSS-IR sequence with a non-selective inversion pulse. In the spin echo image the chemical shift artifact is again apparent, with the signal of the abdominal fat being superimposed on the water signal in several of the anatomical structures. Water suppression in the conventional IR image is efficient only for the bladder, with the signal from the rest of the tissues being reduced but not totally suppressed. The modified IR sequence, however, gives a true water suppressed image.

spin echo



inversion recovery



PRESAT



CSS-IR

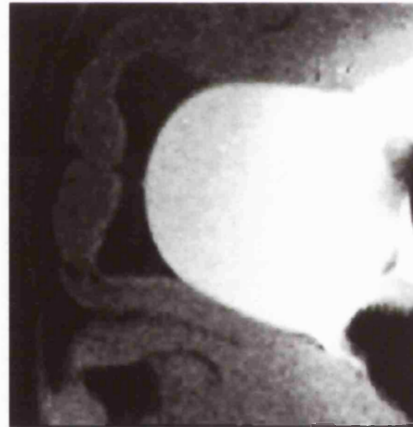
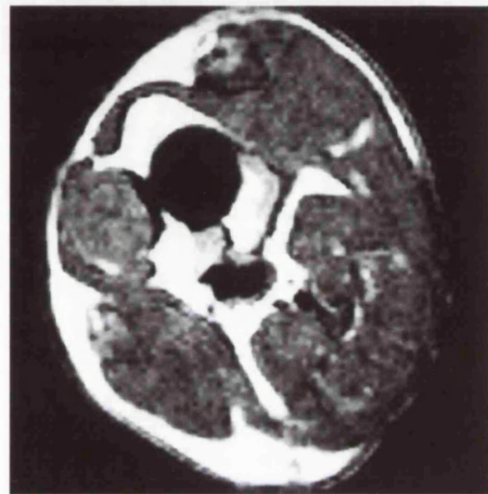


Figure 5.21. Transverse image of the normal abdominal region of a live normal rat at the level of the bladder, produced using a spin echo sequence, STIR, fat-suppressed PRESAT, and fat-suppressed CSS-IR.

spin echo



conventional inversion recovery



modified inversion recovery



Figure 5.22. Transverse images of the abdominal region of a live normal rat at the level of the bladder, produced using a spin echo, conventional inversion recovery with a long inversion time, and the hybrid sequence with non-selective inversion pulse and inversion time calculated to null long T1 components (modified IR).

5.5 CONCLUSIONS

A hybrid pulse sequence for fat and water suppression in proton magnetic resonance imaging has been investigated and a theoretical as well as experimental study is presented of the efficiency of the method as compared to its most closely related conventional fat and water differentiation techniques, namely T₁-null IR and PRESAT. The new sequence has proved to give the same efficient fat or water suppression as the other conventional methods employed, in both phantom and *in vivo* studies. In addition, the technique has shown better performance than IR or PRESAT in several situations where parameters, such as inversion time as well as tip angle and frequency bandwidth of the chemical shift selective pulse, were mis-set.

The hybrid CSS-IR sequence combines a selective pulse with the inversion recovery approach of IR. However, the inversion time is generally significantly shorter than that used in the conventional IR sequence, thus allowing shorter repetition times or, alternatively, more slices to be selected within the same imaging time. While in the IR sequence suppression is strongly dependent upon the T₁ of the component to be suppressed, both theory and experiments show that in the hybrid sequence the null-point is, in general, effectively independent of T₁ for a significant range of T₁ values. This ensures efficient suppression even in the cases where either the T₁ is not accurately known prior to imaging or there is a wide range of T₁ values for the unwanted component.

The CSS-IR sequence has been shown to provide good suppression for a wider range of mis-settings of the chemical shift selective pulse tip angle than the PRESAT sequence. It has already been reported that fat presaturation can be suboptimal in studies of liver disease due to inhomogeneous suppression of the superior and inferior aspect of the liver [5.17]. Even though modern instrumentation affords only a few percent variation in B₁ field homogeneity in the central imaging volume, the field may be rapidly degraded near the edges of the coil. This becomes particularly important, for example in the suppression of subcutaneous fat which is nearest to this inhomogeneous region. For example, in studies of breast imaging although the overall fat suppression was satisfactory, PRESAT gave a poor suppression near the skin surface [5.18]. One can also envisage future application of CSS-IR to fat and water imaging using surface or internal coils.

Chemical shift imaging requires a relatively high and homogeneous static magnetic field in order to resolve the fat and water resonances. Thus fat and water differentiation sequences that are based merely on this principle may give less acceptable results in cases where the static field is regionally degraded by susceptibility differences within the imaging object, for instance when imaging the optical nerve and musculoskeletal system. Even though the CSS-IR method uses chemical shift selection,

it has been shown that a wider selective pulse will always ensure good suppression while degrading the signal from the desired component considerably less than an equivalent PRESAT experiment. A modification of the CSS-IR sequence, with a non-selective inversion pulse was also used to provide multi-slice data sets with good suppression of intermediate and long T₁ water components, for example muscle tissue and body fluids. The use of non-selective inversion pulses, as well as the fact that the null point is not strongly dependent on the inversion time, should also give good suppression of signal arising from flowing spins.

CHAPTER 6

LONGITUDINAL RELAXATION TIME MEASUREMENTS IN MRI

6.1 INTRODUCTION

The measurement of relaxation times is common practice in NMR spectroscopy, where a relaxation time value is derived for each chemically shifted spectral peak. However, there are spins which may have the same chemical environment but subtly different physical surroundings, for example water protons in different tissues [6.1]. In such a case, spectroscopic relaxation time measurements of the total water resonance will yield only a weighted-mean value. Multi-exponential fitting of the experimental data is possible, but the resolution between different components may be very low, and it has been shown previously that a single exponential closely represents the variation of a multi-exponential decay unless the separate components differ by a factor greater than three [6.2].

In contrast, relaxation time measurements in MR imaging involve the generation of a "calculated" image, where each volume element holds the mean relaxation time value of all the spins confined to that region. The price to pay for this extra spatial information is that the chemical shift resolution is lost, at least for conventional imaging methods. The problem is further exasperated by the partial volume effect, that is, when the imaging voxel corresponds to an area that contains tissues with a range of relaxation time values. Although multi-exponential behaviour is expected, only the weighted mean value will be assigned to the imaging voxel. The relative misregistration of fat and water signals, due to their chemical shift difference, makes partial volume effects even more profound (depending on the static and gradient magnetic field strengths used). When small structures are involved, measurements could even become impossible. An example is the optic nerve with its surrounding orbital fat [6.3], and a diagrammatic representation of the partial volume effects in this case is shown in Fig. 6.1. As the spatial resolution is increased, partial volume effects diminish affording more accurate measurement of relaxation times (provided the signal-to-noise ratio remains the same, e.g. via increased signal averaging or better sample-receiver coupling). Another example is the kidney; MRI microscopy studies on rat kidneys, for example, have revealed five zones of tissue with distinctively different relaxation characteristics, while conventional MRI distinguishes only two regions [6.4].

Relaxation time maps in MRI are the primary subject matter of this chapter. After a brief discussion on their justification, the text focuses on longitudinal relaxation

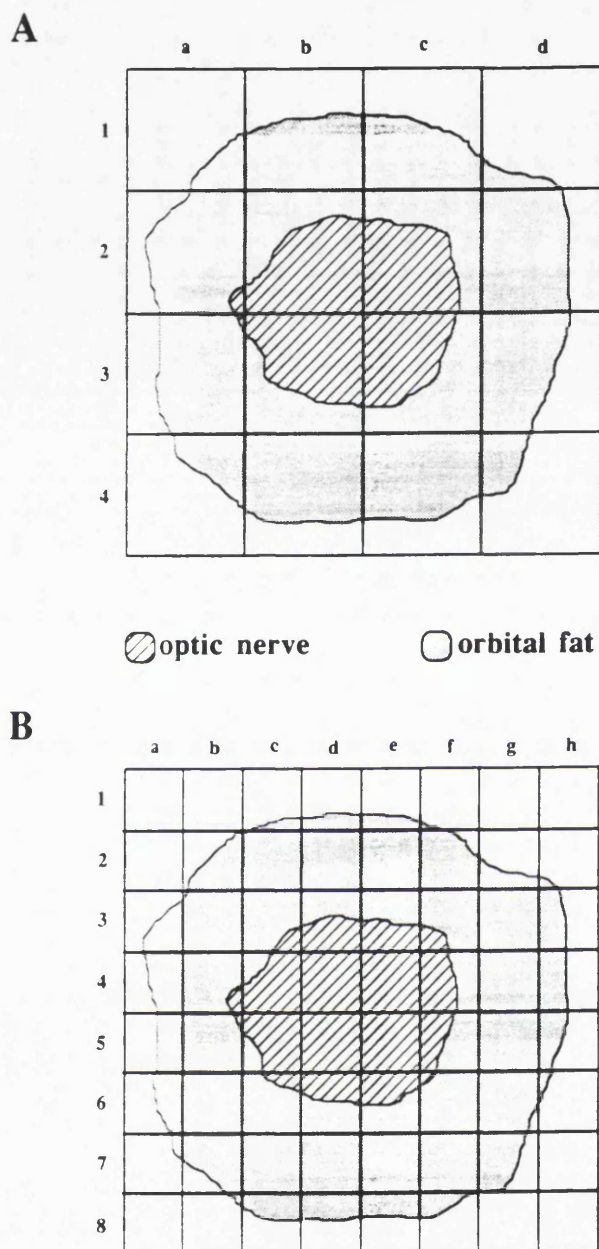


Figure 6.1. A schematic diagram of partial volume effect for the case of the optic nerve, a small structure surrounded by orbital fat. For simplicity, only the pixel area is considered, although the whole voxel is involved. **(A)** A low spatial resolution image matrix. The nervous tissue corresponds to the four central pixels, i.e. A[2b], A[2c], A[3b] & A[3c], which, however, also contain some orbital fat. The overall intensity of each individual pixel is, therefore, the weighted mean of the contributing fat and nervous tissue signals. **(B)** When the spatial resolution is increased one can resolve pixels which correspond only to nervous tissue, i.e. B[4d], B[4e], B[5d] & B[5e]. For simplicity, the mis-registration of the fat signal relative to water due to the chemical shift artifact has not been drawn.

time (T₁) calculated images and the various conventional techniques used to create them, and comments on the limitations, artifacts, corrections and practical considerations that relate to each method. This background work is intended as an introduction to the study of differential fat and water T₁ imaging presented in the next chapter.

6.2 REASONS FOR RELAXATION TIME MEASUREMENTS IN MRI

Much of the interest in tissue relaxation times has stemmed from the early observation of elevated T₁ and T₂ values in tumorous tissues of experimental animals [6.5, 6.6]. Since then, the need for relaxation time measurements in MRI has become even more profound, and the major reasons are detailed here.

Tissue Characterization and Quantitative Studies

Relaxation time maps have been used for tissue characterization in numerous circumstances, one obvious case being the differentiation between fat and the rest of the tissues on the basis of its markedly shorter T₁. Thus, calculated T₁ images have been used, for example, to assess the percentage of fetal fat (both subcutaneous and intra-abdominal) with respect to other fetal tissue in normal, as well as diabetic, pregnant women [6.7]. Recently, a new method has been proposed for quantitation of regional blood volumes based purely on T₁ maps generated before and after the injection of an intravascular contrast agent that enhances T₁ relaxation [6.8].

Contrast Manipulation in MRI: Pulse Sequence Optimization and Synthetic Images

Contrast in an MR image can be arranged to depend on various parameters and especially relaxation times [6.9]. If the relaxation times are known, then the imaging sequence and its timing parameters (such as repetition, echo or inversion time) can be chosen to give an image with the desired contrast and hence create the optimum imaging protocol to detect a certain pathology in the shortest possible scan time [6.10]. Furthermore, parameter optimization may be critical in sequences that differentiate between fat and water on the basis of their relaxation time differences, namely STIR [6.11] and FLAIR [6.12]; efficient suppression of the unwanted component can only be ensured when its T₁ is known prior to the experiment

Contrast in MRI can be further exploited by the use of synthetic images. Given the proton density and the relaxation time values, synthetic images can be generated for arbitrary timings in any pulse sequence, without requiring additional imaging time, thus allowing a rapid retrospective optimization of contrast through interactive control of the sequence and the imaging parameters [6.13].

Relaxation Times as Markers of Other Physical Parameters

Paramagnetic centres in a solution directly affect the relaxation processes of the solvent [6.14], therefore relaxation time measurements can be used to detect their pathological presence and measure their concentration in several clinical situations. For example, proton T₁ and T₂ relaxation maps have been used to obtain quantitative estimates of iron concentration in the liver in conditions like transfusion iron overload and haemochromatosis [6.15, 6.16], as well as to measure the ferritin content of brain tissue [6.17]. Several studies have also reported the potential of T₁ maps for 3-dimensional dosimetry of ionizing radiation. Such applications involve Fricke solutions where the ferrous ion Fe²⁺ is converted to the ferric ion Fe³⁺ which enhances T₁ relaxation [6.18, 6.19], or acrylamide-Bis-aragose gels where T₁ values are reduced due to polymerization and cross-linking induced by ionizing radiation [6.20].

Relaxation rates, particularly T₁, are temperature dependent, and it has been shown that T₁ maps can encode information relating to temperature distribution [6.21]. More recent studies have suggested that the temperature resolution obtained using T₁ calculated images (1-2 °C for a spatial resolution of 4-5 mm and 1s scan time) should be sufficient for non-invasive temperature mapping in clinical hyperthermia treatment of hypoxic tumours [6.22, 6.23].

There is also potential for the use of relaxation time maps to spatially encode the variation of any other physical processes that affect relaxation. For example, T₁ calculated images have been shown to correlate with pore size variations in brine saturated cores [6.24].

Diagnostic Information

It should have become clear from the above examples that relaxation times have a complex, leading role in MRI and a potential to become even more important. However, the possibility of reaching diagnosis based only on relaxation time maps is often regarded with scepticism, as most clinical studies indicate a large spread in relaxation time values for both normal and pathological tissues [6.25]. When performed over a period of time and on the same patient, however, relaxation measurements are sensitive, and can be directly correlated with certain pathologies. For example, it has been shown that the differential diagnosis of brain disease can be aided by relaxation time measurements when conventional imaging fails to distinguish them [6.26], while relaxation time maps proved to be important in evaluating the effect of interferon therapy in liver metastases [6.27].

6.3 T₁ MEASUREMENTS IN MRI

At present, the most commonly used methods for generation of T₁ maps are based on the basic pulse sequences used for T₁ measurements in spectroscopy, i.e. progressive saturation (PS) and inversion recovery (IR). These RF pulse sequences can be combined with a number of imaging techniques, including conventional spin-echo, spin-warp methods and fast imaging regimes such as echo-planar and low tip angle, gradient recalled echo imaging. In this section the principle of each technique is described and as an example, incorporation into the common spin echo, two-dimensional (2D) Fourier imaging regime is assumed. Alternative imaging methods for determining T₁ are also reviewed. These include stimulated echo (STE) imaging, as well as variable tip angle and multiple read-out imaging sequences. The latter have recently drawn much attention, primarily because imaging times can be considerably shortened albeit at the expense of reduced S/N.

6.3.1 Progressive Saturation (PS) and Saturation Recovery (SR)

The first published T₁ calculated image [6.28] was generated using progressive saturation [6.29]. In this method an initial 90° pulse perturbs the magnetization into the transverse plane and longitudinal relaxation occurs during the interval TR before the next sequence repetition. If TR is relatively long (i.e. ≥ 5T₁), the longitudinal magnetization has been allowed to recover completely during the intermediate time interval. However if the repetition time of the sequence is short, only a fraction of the thermal equilibrium magnetization recovers. Therefore, the transverse magnetization generated by the subsequent 90° pulse, as well as the acquired signal, is a function of T₁ and the repetition time TR. After a few sequence repetitions, a steady-state condition is reached and the signal strength I_{PS} for each pixel in the image is given by:

$$I_{PS} = C \rho \exp(-TE/T_2) [1 - \exp(-TR/T_1)] \quad (6.1)$$

where the first exponential term refers to the transverse relaxation during the echo time TE of a spin-echo experiment; had the 180°^{pulse} been omitted to give a gradient recalled version of the sequence, the decay time constant T₂ would have been replaced by the effective transverse relaxation time T₂*. C is a dimensionless constant that relates to the characteristics of the system, and ρ is the proton density averaged over the voxel, see also Eqn. (2.48). In the above analysis T₂* ≪ (TR-TE) is assumed, that is, any residual transverse magnetization is completely dephased prior to the next sequence repetition. Note that very short T₁ values (comparable to TE) cannot be accurately measured, as this magnetization is almost fully relaxed back to its thermal equilibrium value before data collection.

When all pulses are slice selective, data from several slices can be obtained within the repetition time [6.30]. However, there is a limit to the maximum number of slices that can be accommodated if the repetition time is required to be relatively short in order to obtain a data point early in the relaxation curve (especially when short T_1 values are interrogated).

If several images are obtained with different values of TR, the value of T_1 for each pixel can be calculated independently of the spin density and the transverse relaxation. This normally involves a non-linear, multi-parametric least-squares fit through iteration, which, considering the large number of pixels (e.g. 65,536 for an image of 256x256 resolution), may be a quite time-consuming process, although special fast algorithms have recently been developed [6.31]. Rapid non-least-squares processing techniques have also been described in the literature, however they generally sacrifice some accuracy for improved speed [6.32, 6.33].

It should be mentioned that in several publications progressive (or partial) saturation is incorrectly referred to as saturation recovery. The saturation recovery (SR) method as presented in the early days of NMR spectroscopy [6.34], involves an initial burst of radiofrequency pulses to completely saturate the system, that is, to zero the net magnetization. Then, after a time T_{sr} a 90° pulse samples the amount of relaxed magnetization and the final signal is given by an expression similar to Eqn. (6.1), where T_{sr} is used instead of TR. The time interval T_{sr} can be made as short as desired (the only limitation being the switching of electronics), so theoretically there is no lower limit to the accurate measurement of T_1 . However, many medical applications prefer to use the partial or progressive saturation method instead of saturation recovery, mainly because the initial burst of radiofrequency field can dissipate a considerable amount of energy into the subject, while the extra T_{sr} delay prolongs the overall imaging time. The problem of excessive energy deposition can be overcome using a version of the SR sequence where the saturating burst of pulses is replaced by a single 90° pulse to tip the spins into the transverse plane, followed by a delay which is long relative to T_2^* , or by a pulsed magnetic field gradient, to completely dephase the transverse magnetization [6.2, 6.35].

6.3.2 Inversion Recovery (IR)

Another popular method of data acquisition for T_1 maps is based on the inversion recovery (IR) sequence [6.36]. The spin system is initially inverted by means of a 180° pulse and longitudinal relaxation occurs. After a time TI a 90° pulse "reads" the relaxed magnetization. The final signal intensity IIR is proportional to the fraction of the magnetization that has recovered during the inversion time TI, and for a spin-echo experiment is given by:

$$I_{IR} = C \rho \exp(-TE/T_2) [1 - 2 \exp(-TI/T_1)] \quad (6.2)$$

Again it is assumed that $T_2^* \ll (TR - TE - TI)$. In order that Eqn. (6.2) holds, the repetition time of the sequence must be long enough for the perturbed magnetization to return to its thermal equilibrium value prior to the next inversion pulse. Practically, this means that a repetition time of at least 5 times the longest T_1 should be ensured (~99% recovery). However, this requirement is rarely met in the imaging context, as the imaging time would be lengthened to an unacceptable degree (e.g. $TR=10$ s *in vivo*). In practice, TR needs to be relatively short, so Eqn. (6.2) is modified to account for the partial recovery of the magnetization in the time interval between the read 90° pulse and the next sequence repetition [6.37]. Thus the observed signal intensity for each pixel in the image is given by the expression:

$$I_{IR} = C \rho \exp(-TE/T_2) [1 - 2 \exp(-TI/T_1) + \exp(-TR/T_1)] \quad (6.3)$$

In the analysis hereafter where the IR experiment is considered, Eqn. (6.3) is always assumed.

If several images are obtained with different inversion times (while other sequence timings are kept the same), then a non-linear, multi-parametric, least-squares fit for each pixel of the image matrix would again yield a T_1 map. Similar processing algorithms can be employed as in the case of the saturation methods. Note that the IR sequence can also function in a multi-slice mode in the same fashion as the PS experiment. Alternative, more complicated and more time efficient multi-slice schemes have also been proposed [6.38, 6.39], as described in Section 3.3.1.

The inversion recovery method is often preferred as it exhibits a wider dynamic range than the saturation techniques, since the magnetization is initially inverted and starts relaxing from a negative value. These negative signals, however, may induce a fundamental difficulty, known as contrast reversal [6.40]. In MRI experiments, data is generally presented as a magnitude image in order to avoid correcting phase shifts induced by pulse sequence timing errors, phase delay of electronic circuits, gradient ramping and eddy currents, static field inhomogeneity, and moving spins. In such a magnitude image, negative signal intensities are inverted. Figure 6.2 shows the actual relaxation curve of the magnetization following an inverting 180° pulse, and how this will appear when considering only the modulus of the intensity. It is apparent that the negative signal from a long T_1 component cannot be distinguished from positive signals of the same magnitude given by samples with shorter T_1 values. Several methods have, however, been used to restore signal polarity in IR images. A first approach is to search for the null point of the magnetization for each pixel in a set of IR images acquired with

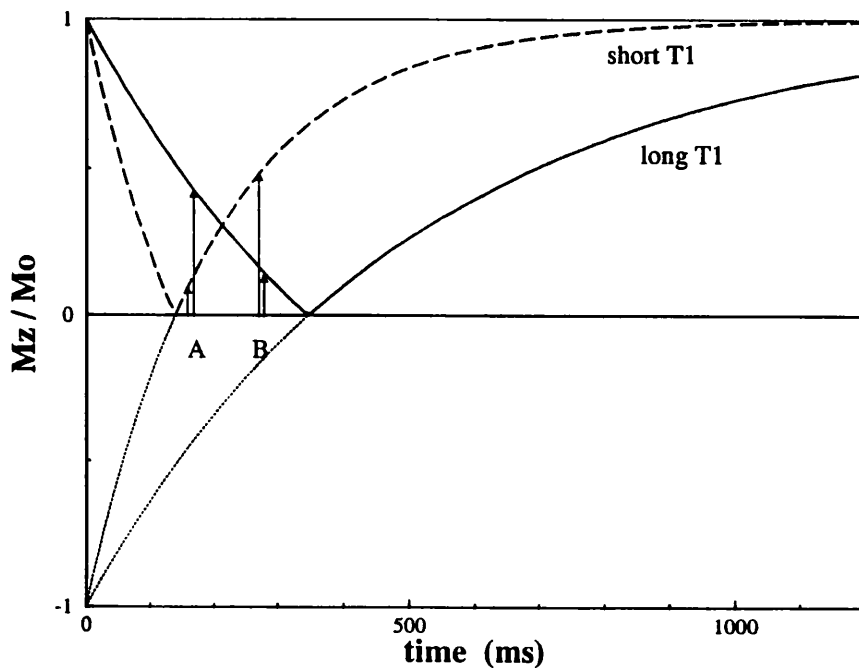


Figure 6.2. Relaxation curves for longitudinal magnetization following a 180° inverting pulse. The long-dashed and solid lines correspond to the magnitude representation of the relaxation curves for two components with different T_1 values ("short" $T_1 = 200$ ms, and "long" $T_1 = 500$ ms respectively). The dotted lines show the negative part of the curves when sign information is also considered. At an inversion time B, the long T_1 component gives a magnitude signal much lower than the short T_1 component. However, if the system is observed at time A, the contrast is reversed.

different inversion times [6.41]. At least four IR images are required, therefore this technique could not be incorporated in two-point or one-shot T_1 measurement regimes (as described in the following paragraphs). Alternatively, the sign information can be recovered if one considers and corrects for the phase shifts of the data prior to the T_1 map reconstruction. A simple method requires an additional partial saturation experiment, identical to the inversion recovery sequence except that the inversion pulse is omitted. Phase shifts due to hardware considerations are assumed to be the same for both data sets, however in the IR image any pixels corresponding to inverted magnetization will have an additional 180° phase shift. If the phase images of the two data sets are subtracted, the resulting image should yield a phase close to zero for pixels corresponding to short T_1 components, while regions where the signal is still inverted in the IR image should have a phase of $\sim 180^\circ$ [6.42]. Although noise and motion artifacts broaden the distribution of the phase differences around the two ideal values of 0° and 180° , this is not expected to significantly affect the sign restoration, as only a crude approximation of the phase difference is required. The IR magnitude image can then be made polarity sensitive by inverting the sign of the signal intensity in the pixels which are out of phase. In a similar approach, the phase information from the partial saturation data set is used to completely correct the inversion recovery data, so that the real part can then be used to reconstruct the image [6.43]. However, motion related or other random phase shifts cannot be corrected and may induce significant inaccuracies in the T_1 measurements. A regional phase correction algorithm has also been described, which involves the creation of a map of the gradual phase shifts due to hardware imperfections which is then used to phase correct the data [6.44]. The phase gradient between neighbouring pixels is calculated and any abrupt phase changes due to inverted spins are removed. Since the correction relies on information in adjacent pixels, noise areas may introduce errors which can then be propagated. To prevent this, empirical thresholds of pixel magnitude and phase coherence must be defined by the user.

Several studies have provided a comparison between saturation methods and the inversion recovery experiment, in terms of their achieved precision in the T_1 calculation within the same total experimental time, and suggest optimal parameter settings [6.45–6.47]. When systematic errors, such as pulse imperfections and slice profiles are not considered, IR experiments, with repetition time of about double the maximum estimated T_1 and T_2 values linearly spaced in time, have been shown to give better results than saturation sequences [6.46]. However, the prolonged imaging and processing times have led to the development and wide use of two-point measurement techniques, often employing hybrid, more efficient pulse sequence schemes, as described below.

6.3.3 Two Point Measurements and Hybrid Schemes

T_1 can be derived from only two images using the "intensity ratio" method [6.48]. In this approach, two different repetition times (if PS is considered), or two different values for the waiting time T_{sr} (for the SR sequence), or two different inversion times (for the IR sequence) are necessary. T_1 is then calculated from the ratio of the two signals. The measurements can only be precise if the pulse intervals are suitably chosen. In the PS sequence for example, if the data points are too early in the exponential recovery curve, then the intensity ratio becomes very insensitive to T_1 , whereas if the pulse intervals are both long in comparison with the relaxation time to be determined, the intensity ratio tends to unity. Near these limits any noise on the signals introduces large errors in the derived relaxation times. A large ratio of repetition times permits a wide range of relaxation times to be determined, but tends to be more time-consuming than a smaller ratio. In practice a repetition time ratio of 4 has been found to represent a reasonable compromise [6.48, 6.49]. In the inversion recovery case high precision is obtained when one of the experiments is near the null condition [6.48].

A hybrid two-point measurement scheme has, however, proven to be most efficient. It was suggested in the early days of NMR imaging [6.50] and still is the method of choice for many clinical studies. The method involves a partial saturation and an inversion recovery imaging experiment. Then the ratio of intensities for any pixel in the data matrix of the two images is given by:

$$\frac{I_{IR}}{I_{PS}} = \frac{1 - 2\exp(-TI/T_1) + \exp(-TR_{IR}/T_1)}{1 - \exp(-TR_{PS}/T_1)} \quad (6.4)$$

where I_{IR} and I_{PS} are the signal intensities for the IR and PS images with repetition times TR_{IR} and TR_{PS} , respectively. The two sequences can form two completely different experiments, or be performed in an interleaved fashion within the same sequence. The latter scheme is preferred, as it compensates for any mis-registration due to involuntary movement or shift in electronics during the different steps of the phase encoding procedure.

The most convenient method to generate the T_1 map is to refer to a computed "look-up" table, where the theoretically determined signal ratio, for the specific values of repetition and inversion times used in the experiment, is tabulated for various values of T_1 , using Eqn. (6.4). Then, the signal ratio for each pixel is calculated and compared to the computed values [6.51]. In theory, the inverse ratio I_{PS}/I_{IR} is equivalent for the purpose of T_1 measurement, however, it may create practical computational problems as it approaches infinity for combinations of TI and T_1 where the IR signal is zero.

This hybrid PS-IR method has been shown to be more efficient than other two-point measurement schemes for determining T_1 within a wide range of possible values

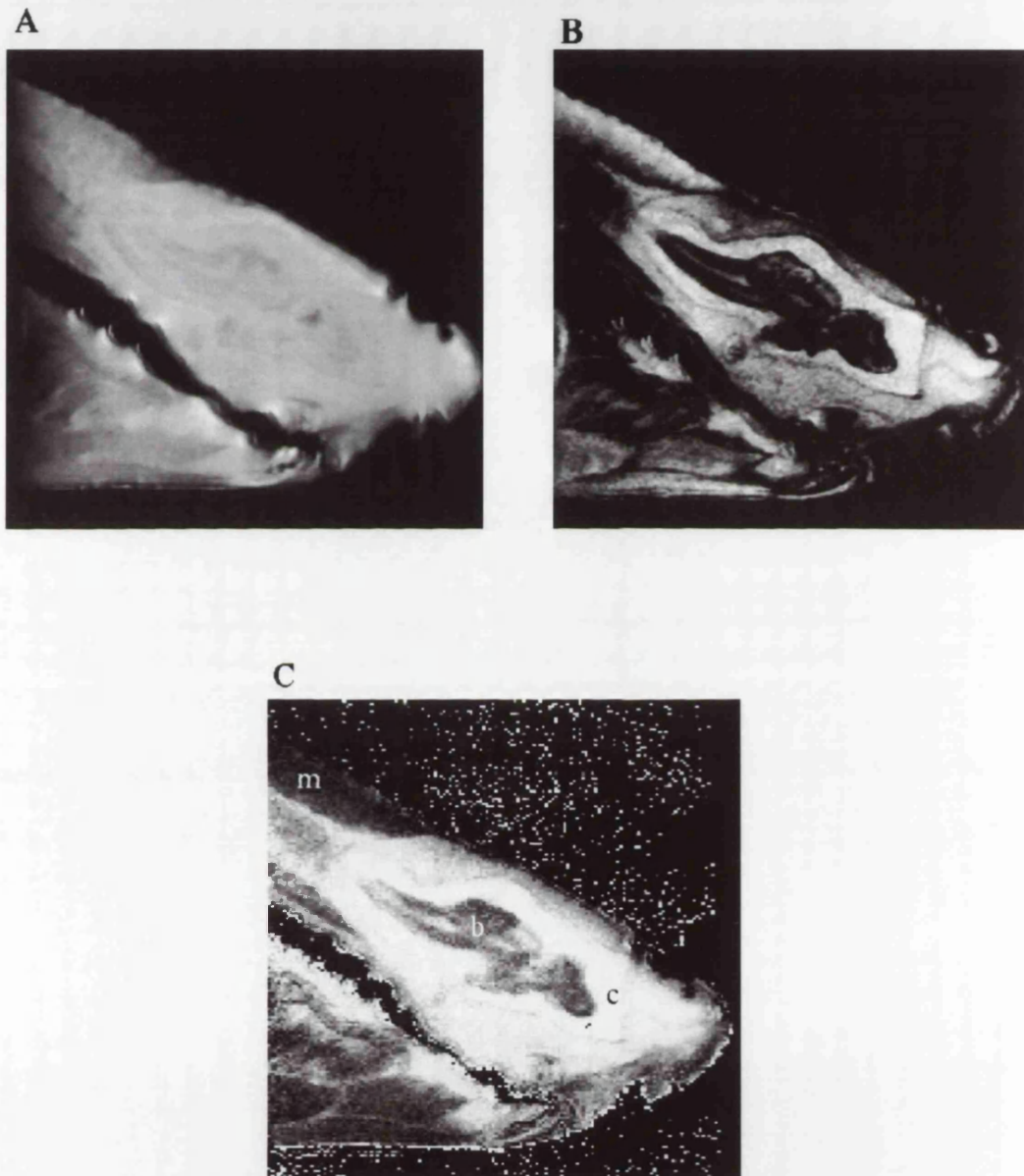


Figure 6.3 Longitudinal images of the head of a preserved shark species at 4.7 T.
 (A) Partial saturation, spin echo image, TR=4000 ms, TE=24 ms.
 (B) Inversion recovery, spin echo image, TR=6000 ms, TI=400 ms, TE=24 ms.
 (C) Calculated T1 map using the 2-point hybrid PS-IR method. T1 values for the three main tissues are: 1050 +/- 20 ms for brain (b)
 2124 +/- 20 ms for cartilage (c)
 767 +/- 16 ms for muscle (m).

[6.49]. Optimal parameter settings have also been suggested. For example, to measure T_1 within the ranges of 120-1200, 150-1500 and 200-1800 ms, the optimum TI should be about 280, 400, and 500 ms, respectively, while the same optimum TR_{IR}/TR_{PS} of about 2.5-3.0 would apply to all three bands [6.49]. Figure 6.3 is an example of a T_1 map of a shark head from The Natural History Museum (London) collection generated by the hybrid PS-IR method. Generation of this T_1 map was part of the initial imaging protocol for the first study of anatomical features of preserved shark species by MRI [6.52].

6.3.4 Variable Tip Angles

T_1 maps can also be generated by employing a variable tip angle pulse during the imaging experiment. In this method, a pulse of tip angle θ° is used to perturb the magnetization, which is then left to partially relax back to its thermal equilibrium value during the repetition time, which is generally short. As the excitation pulse is generally other than 90° , only a fraction of the thermal equilibrium magnetization is "tipped" into the transverse plane. This transverse magnetization is then a function of both the pulse tip angle θ° and the amount of longitudinal relaxation that has occurred during TR [6.53]. In this case the application of a 180° refocusing pulse to form a spin echo cannot be used, as such a pulse would also invert the magnetization which has remained along the longitudinal axis. Instead, an echo is formed through the use of gradients [6.54]. The transverse relaxation during the echo time TE is now described by the effective transverse relaxation time constant T_2^* and the signal intensity I_θ for any pixel in the data matrix is given by:

$$I_\theta = C \rho \exp(-TE/T_2^*) \frac{\sin\theta [1 - \exp(-TR/T_1)]}{1 - \cos\theta \exp(-TR/T_1)} \quad (6.5)$$

This assumes that pulses are applied along the same axis and that a steady state has been reached, which can generally be achieved within the first few sequence repetitions [6.55]. $TR \gg T_2^*$ is also assumed, so that the transverse magnetization is completely dephased prior to the next sequence repetition. Note that for a 90° pulse Eqn. (6.5) reduces to Eqn. (6.1) which describes the progressive saturation experiment, save for the transverse relaxation time constants. The two methods, therefore, are very similar, with the fundamental exception that Eqn. (6.5) can be re-arranged to allow linear data analysis to be employed for the T_1 calculations:

$$\frac{I_\theta}{\sin\theta} = \exp(-TR/T_1) \frac{I_\theta}{\tan\theta} + C \rho \exp(-TE/T_2^*) [1 - \exp(-TR/T_1)] \quad (6.6)$$

Following Eqn. (6.6), the plot of $I\theta/\sin\theta$ against $I\theta/\tan\theta$ is a straight line with a slope of $\exp(-TR/T_1)$. Because the rest of the unknown parameters, such as spin density and transverse relaxation constant, affect only the intercept of the linear plot, they do not interfere with the calculation of T_1 .

Studies for sequence parameter optimization have shown that two point measurements using only two images acquired at two different tip angles can be even more precise than a multiple point measurement with the same overall imaging time [6.56]. Additionally, simulation and experimental results have suggested that the optimum sequence parameters should involve a pair of tip angles well separated (e.g. 20° and 100°) and a short repetition time, such that $TR \leq T_1$. As a result, the method turns out to be quite fast, although care must be taken that the transverse magnetization is completely spoiled prior to the next sequence repetition. The variable tip angle method has also been shown to be of comparable or even greater efficiency and precision when compared to its most closely related technique, progressive saturation [6.56]. However, some limitations should also be considered. The most important is probably the fact that the sequence can not employ a 180° refocusing pulse for the echo formation, thus the final signal intensity may be prohibitively poor in a relatively inhomogeneous static magnetic field. Additionally, errors may arise in the calculation of the pulse tip angles, especially when one considers the variation of the tip angle across the slice thickness.

6.3.5 Single-Shot Techniques

All methods described so far require more than one imaging experiments in order to generate the calculated T_1 image. This is probably the most important limitation of T_1 mapping as it significantly increases the imaging time. One should note that sequences such as the hybrid PS-IR are often already performed in most clinical examinations in order to get images with a variable T_1 contrast, so that in these cases calculation of a T_1 map would give additional information without requiring extra imaging time. Nevertheless, several techniques have been devised to generate a T_1 map using information from only one sequence repetition.

One group of single-shot T_1 measurement methods involves stimulated echo (STE) imaging [6.57, 6.58]. The magnetization is initially tipped into the transverse plane by the first 90° pulse and dephases during the time interval $TE/2$. At the same time phase encoding is performed. A second 90° pulse causes half the magnetization to be stored in a plane parallel to the longitudinal axis, preserving its acquired phase information, while the other half of the magnetization rephases to form an echo after a further time $TE/2$. This echo is usually termed the primary echo (PE). The signal intensity for any given pixel in the PE image matrix is given by:

$$I_{PE} = \frac{1}{2} C \rho \exp(-TE/T_2) \quad (6.7)$$

which is the same as in the conventional, equivalent spin-echo experiment except for the factor of one-half. The other half of the magnetization that has been stored along the longitudinal axis is then brought back into the transverse plane by the application of a third 90° pulse (applied at time T_M after the second pulse) and refocuses to form an echo after a further time $TE/2$. This is commonly termed the stimulated echo. During the intermediate interval T_M the stored magnetization experiences only longitudinal relaxation. If T_M is too long (i.e. $\geq 5T_1$), practically all spins relax back to thermal equilibrium and by the time the third 90° pulse is applied no stored magnetization is left to form a stimulated echo. Thus, the signal intensity for any pixel in the STE image is dependent not only on T_2 relaxation during TE but also upon the T_1 relaxation during T_M :

$$I_{STE} = \frac{1}{2} C \rho \exp(-TE/T_2) \exp(-T_M/T_1) \quad (6.8)$$

Eqns. (6.7) and (6.8) assume the pulse sequence repetition time is sufficiently long to avoid additional T_1 dependence via partial saturation. Then, the ratio of STE signal intensity, to the intensity of the PE image is a direct measure of T_1 [6.59]:

$$\frac{I_{STE}}{I_{PE}} = \exp\left(-\frac{T_M}{T_1}\right) \quad (6.9)$$

An additional advantage of this two-point T_1 technique is that the two data sets are inherently interleaved, thus reducing the effect of motion or drift in electronics on the accuracy of the T_1 measurements. However, the signal intensities are at most only half those of the conventional spin echo and this poorer S/N can lead to larger errors in the T_1 measurements.

Perhaps the most interesting advantage of STE imaging is that the technique can be manipulated to give more than two points in the relaxation curve within a single imaging experiment, thus allowing the study of possible multi-exponential relaxation behaviour within a reasonable imaging time. For this purpose, the third 90° pulse is replaced by a number of small tip angle pulses that partially sample the stored magnetization at different T_M intervals. Each read pulse reduces the residual stored longitudinal magnetization (hence the magnitude of the next stimulated echo as well) by a factor of the cosine of the tip angle. The same tip angle dependence for all the stimulated echoes can be ensured by properly adjusting the tip angle of each read pulse, although this requires good B_1 field homogeneity. Detailed calculations show that,

ideally, the tip angles should increase from small values to reach 90° for the last pulse in the series [6.60, 6.61]. An alternative approach is to set all pulses to a very small angle (of the order of 5°), in which case the cosine can be approximated by 1 [6.60]. One should note however, that the lower the tip angle of the read pulse, the poorer the S/N of the resulting image. Another important consideration is that when using such a multi-pulse sequence several different and unwanted echoes may be formed during each acquisition interval. Phase cycling procedures and systematic application of magnetic field gradients have been employed to suppress this unwanted signal and give artifact free stimulated echo images [6.62].

Another group of single-shot methods for producing T_1 maps is based on the principle of multiple read-out pulses to sample the longitudinal magnetization during the transient region as it evolves towards a steady-state condition [6.63]. These multiple read-out sequences involve a series of evenly spaced, low tip angle ($\theta^\circ < 90^\circ$) pulses. Each θ° excitation pulse forces some of the magnetization into the transverse plane and produces a signal proportional to the amount of the longitudinal magnetization before the pulse. This signal is always recorded as a gradient-recalled echo because a 180° refocusing pulse would also invert the residual longitudinal magnetization. Between the pulses, which are applied with a short time interval T_d , the magnetization still relaxes with T_1 . However, the apparent overall decay towards a steady-state condition is characterized by an effective relaxation time $T_{1\text{eff}}$, which is related to the actual T_1 , the pulse tip angle θ° and the interpulse delay T_d by:

$$T_{1\text{eff}} = \frac{T_d}{T_d/T_1 - \ln(\cos\theta)} \quad (6.10)$$

The tip angle θ° must be less than 90° so that the logarithm of $\cos\theta$ is permissible in Eqn. (6.10). Other assumptions include the complete spoiling of the transverse magnetization prior to the application of the next read-out pulse, which can be satisfied by ensuring $T_d \gg T_2^*$, or by applying an appropriate spoiling field gradient pulse. It is apparent that the train of low-tip angle read-out pulses is used to both perturb the longitudinal magnetization from the thermal equilibrium condition and consecutively sample it as it gradually decays towards a steady-state value [6.63, 6.64]. In order to increase the dynamic range of the experiment, a saturating or inverting pulse can be employed to prepare the magnetization at some starting value [6.65–6.67]. The evolution of the longitudinal magnetization in all different versions of the preparation part of the sequence is characterized by the same effective relaxation time $T_{1\text{eff}}$ as it converges towards the same equilibrium value. A schematic description of the recovery of longitudinal magnetization for the multiple read-out sequence is shown in Fig. 6.4. As several read-out pulses are performed during each sequence repetition, a full

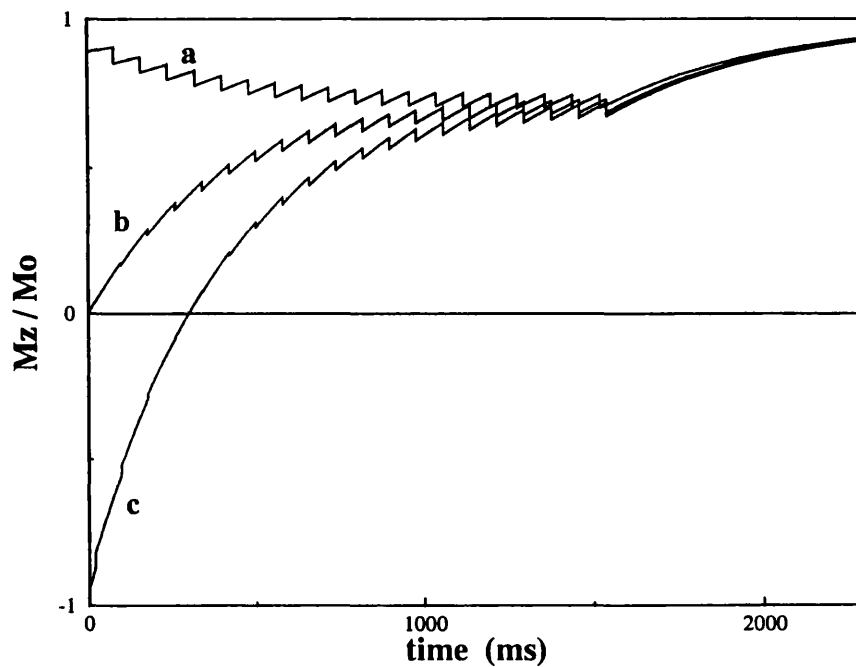


Figure 6.4. The recovery of the longitudinal magnetization during the course of the multiple read-out pulse sequence when the preparation pulse is omitted (a), when the preparation pulse is 90° (b) and when the preparation pulse is 180° (c). The calculations assume a T_1 value of 500 ms, a time interval of 20 ms between the preparation pulse and the read-out train, twenty read-out pulses of 20° tip angle and $T_d=80$ ms, and a repetition time of 2300 ms. The magnetization gradually approaches a steady-state, while the steps in the curves are due to the read-out pulses which bring some of the longitudinal magnetization into the transverse plane. It is apparent that the greatest change in the longitudinal magnetization (the dynamic range of the experiment) is obtained when the preparation pulse is 180° (c).

reconstruction of the decay curve is possible. When the pulse tip angle θ^* is not accurately known, a three parameter fit of the data can be employed to give a T_1 map as well as the spatial distribution of the RF field [6.64]. In the case of the inverting preparation pulse, signal polarity should be restored prior to T_1 calculations. The simple two-point algorithm described in Section 6.3.2 can be easily employed, where the inversion recovery and the partial saturation images required are substituted by the first and the last image, respectively, in the read-out train [6.42].

Studies on the optimization of the multiple read-out sequence parameters suggest tip angles in the range of 15° to 30° , and T_d values in the range of 70-100 ms for accurate measurements of T_1 values ranging from 150 to 900 ms [6.68–6.70]. Comparative studies have shown that within the same total imaging time, multiple read-out methods can produce calculated T_1 images with S/N comparable to that of T_1 maps generated by conventional multiple point methods, such as IR [6.71]. In the single-shot methods, the extra imaging time is used for signal averaging, and not for sampling more points in the relaxation curve, thus it is possible to trade off T_1 map S/N in order to reduce the overall imaging time if so desired. Nevertheless, in clinical examinations a conventional image with an acceptable S/N is also generally required for morphological inspection. In order to avoid the need to perform additional standard experiments for this purpose, one could take a weighted sum of all the images produced by the multiple read-out sequence and thus generate a composite image of clinical quality [6.64, 6.72]. Another approach involves modification of the sequence so that the last read-out pulse is adjusted to give an effective tip angle of 90° , yielding an image with the maximum possible S/N [6.73].

6.4 GENERAL CONSIDERATIONS

The first step towards more accurate T_1 measurements is the use of more elaborate signal calculations, derived with less approximations. For example, Eqns. (6.1) and (6.3) for the signal intensity of the SR and IR spin-echo experiments, respectively, assume that the T_1 is very long compared to TE. However, if the T_1 is comparable to TE/2 and some of the magnetization has relaxed during this time, the refocusing 180° pulse would invert any longitudinal magnetization, thus leading to a more complicated expression for the signal intensity [6.74–6.76].

Another important factor that may induce substantial inaccuracies in T_1 measurements is the effect of magnetization transfer contrast, i.e. the reduction of the longitudinal relaxation time of certain tissues when off-resonance pulses are applied [6.77]. Multi-slice imaging can effectively be regarded as off-resonance irradiation and it has been shown that the signal from tissues in such sequences decreases due to

magnetization transfer effects, the reduction being dependent upon the number of slices and other sequence parameters, such as repetition time [6.78, 6.79]. Such incidental magnetization transfer effects however, would not be observed in cases where off-resonance pulses are avoided, as in single-slice or 3D imaging techniques.

Other factors that may affect the expected signal and, thus, the T₁ calculations, include hardware imperfections, such as B₁ field inhomogeneity and imperfect slice profiles. Although in most clinical examinations modern instrumentation affords only a few percent variation in B₁ field homogeneity in the central imaging volume, the non-uniform excitation field of surface or internal coils, is still a major problem. In such cases, a practical solution would be to use a large, imaging transmitter coil for homogeneous excitation over the imaging volume, and a separate surface (or internal) receiver coil for maximum S/N for the volume of interest [6.80]. Alternatively, a map of the B₁ field could be used to correct the T₁ measurements during post-processing, although this requires additional experiments. Information about the tip angle distribution can be obtained together with the T₁ calculation when a multiple point method is used and the data are subsequently analyzed in terms of a two- or three-parameter exponential fit, one of the parameters being the pulse tip angle [6.47, 6.64, 6.81]. Such an approach would be rather time consuming when methods such as PS or IR are considered, but could be readily applied in the multiple read-out sequences (though a rather long processing time may be needed and the non-linear fitting required may not be sufficiently robust [6.68]). A more common solution to the problem of inhomogeneous B₁ field, however, is to use specially designed pulses that self-compensate for any B₁ inhomogeneity. Such an example is the broad category of composite pulses, initially designed for spectroscopic studies (detailed reviews are given in References [6.82] and [6.83]). One should note that although these pulses can be made frequency selective, the resulting slice profile can be far from the ideal rectangular shape. Adiabatic fast passage pulses are also B₁ insensitive (for a review, see Reference [6.84]). Such a pulse, achieved by a non-linear frequency sweep, has been used for inversion in the hybrid two-point PS-IR method to produce T₁ calculated images with increased accuracy [6.85]. In current clinical practice, most commonly used are the complex hyperbolic secant pulses, which can create a highly selective spin inversion or excitation which, above a critical threshold is independent of the pulse power and hence B₁ inhomogeneity [6.86]. The use of a hyperbolic secant 180° pulse for the inversion in the hybrid PS-IR method, as well as in the multiple read-out sequence, has been shown to give increased accuracy in T₁ measurements [6.70, 6.87]. The pulse can also be optimized to produce slice profiles much closer to the desired rectangular shape [6.88].

In conventional 2D imaging the slice selection is performed by application of a frequency selective pulse in the presence of a magnetic field gradient, thus the

distribution of tip angles across the slice is expected to be a simple reflection of the spectral "shape" of the pulse. As most conventional pulses exhibit frequency profiles different from the rectangular shape, assuming a uniform tip angle distribution across the slice would generally lead to erroneous T₁ measurements or even create an apparent multi-exponential relaxation behaviour [6.74, 6.89]. Slice profile effects can become more pronounced and complicated when multi-pulse sequences are considered because of the limited magnetization recovery during the interpulse delays [6.90, 6.91]. Similarly, deviations from the true values considerably increase when adjacent slices overlap [6.92]. It is possible to correct the T₁ measurements for the slice profile effects by substituting the nominal pulse tip angle with the appropriate expression derived from integrating through the selective pulse waveform [6.51, 6.70, 6.74, 6.93], or by estimating an average tip angle value across the slice profile from calibration experiments [6.94]. Direct measurements of the slice profile can also be used when deviations from the theoretical pulse waveform are intended or, due to operating system characteristics, suspected [6.74, 6.91]. The slice profile effects could be reduced by reducing the number of slice selective pulses within the sequence to a minimum, though this would result in single slice imaging. The problem could be avoided all together in a 3D imaging sequence, where "slice selection" is performed by phase encoding, although this again increases significantly the overall imaging time.

As all methods involve pixel-by-pixel manipulation of more than one image, any spatial mis-registration between consecutive images may introduce errors in the final T₁ map. The mis-registration can be induced either by an imbalance of the encoding gradients or by sample motion. The former may be cancelled out by applying the gradient pulses in exactly the same fashion for all images. This is readily applicable to sequences such as PS, IR, or variable tip angle, but can be more difficult in the case of single shot methods. In a similar sense, mass transfer in general (e.g. flow, diffusion and perfusion) should be considered, especially in single-shot methods where the reduction in the echo signal due to moving spins becomes more pronounced in the later echoes [6.58]. Signal mis-registration due to involuntary motion may prove to be more difficult to avoid but can be reduced by interleaving scans, which is inherent in single-shot sequences. Gating of the sequence to cardiac or respiratory cycle can also be employed, and such cardiac-gated T₁ maps have been demonstrated [6.95].

6.5 DISCUSSION

Relaxation time measurements are performed routinely in MRI. The process generally involves acquisition of several images such that a map of the spatial distribution of the relaxation time values can be calculated subsequently. Some of the methods for T_1 measurement, such as inversion recovery and stimulated echo imaging, involve an initial perturbation of the longitudinal magnetization and subsequent observation of the system as it relaxes back to thermal equilibrium. Another group of methods, namely saturation and variable tip angle imaging, force the magnetization into a steady-state condition, whose value depends on the longitudinal relaxation. Multiple read-out methods, finally, sample the magnetization as it progressively approaches this steady-state condition.

Longitudinal relaxation is generally an exponential process, but as multi-exponentiality is often expected (mainly due to partial volume effects) it would be most desirable to sample the relaxing magnetization several times during the relaxation process. In conventional methods such as progressive saturation, inversion recovery or variable tip angle sequences, this means several repetitions of the imaging experiment, resulting in a prohibitively long imaging time. As a consequence, in most clinical examinations only two-point measurements are performed. Single shot methods, namely stimulated echo and multiple read-out imaging, offer the opportunity to sample several points within the same repetition time. The penalty is a reduction in the S/N of the acquired images, thus, an increase of the stochastic errors in the subsequent T_1 measurements. However, the S/N can be increased by extensive averaging. Thus, when compared to IR, the multiple read-out sequence with a 180° preparation pulse is of similar efficiency within the same overall experimental time. One could conclude that a single shot method should be preferred in high S/N conditions, for example when the coil and the sample are well coupled (e.g. surface or internal coils) and the imaging voxel is relatively large. As the field of view is decreased (keeping the spatial resolution fixed) the IR, PS, or variable tip angle methods should become more desirable [6.71]. Generally, maximum achievable S/N is required in order to minimize stochastic errors in the T_1 measurements, therefore the echo time should be kept as short as possible. Potential problems may arise by the use of a gradient echo instead of a spin echo in the methods of variable tip angle and multiple read-out. Gradient echoes suffer from an inherent reduction in the S/N, depending upon the static magnetic field homogeneity and may exhibit artifacts at the interfaces of spins with different chemical shifts such as fat and water [6.96].

The extra imaging time generally needed in order to create T_1 maps is often a major problem especially in clinical routine MRI. The solution seems to lie with the use of high-speed imaging techniques, where there is the additional advantage of relatively

motion independent measurements and the potential for dynamic studies. Thus, the principle of saturation recovery has been incorporated into fast imaging sequences such as echo planar imaging (EPI) to yield real-time T₁ maps [6.97]. Additionally, the magnetization can be prepared by an 180° inverting pulse and a variable waiting period prior to the application of the fast imaging experiment, be it an EPI sequence or a fast low angle (FLASH) type method [6.98–6.100].

In conclusion, even though spin-lattice relaxation has been considered since the advent of NMR, new approaches to its measurement and manipulation in MRI continue to occupy much of the literature.

CHAPTER 7

METHODS FOR DIFFERENTIAL FAT AND WATER LONGITUDINAL RELAXATION TIME MEASUREMENTS IN MRI

7.1 INTRODUCTION

Summarizing the discussion presented in Chapter 3, fat and water differentiation in MRI is justified by the significance of the physiological distribution of the two components in several medical cases, and by the need for images free from chemical shift artifacts and dynamic range problems. When combined with the potential of relaxation time maps to afford information leading to quantitation, tissue characterization, sequence parameter optimization, and diagnosis, the need for separate fat and water relaxation time maps becomes apparent.

Multi-exponential analysis of the longitudinal relaxation time data is not often possible in routine MRI, as such a fitting procedure requires acquisition of many points in the curve and high signal-to-noise ratios [7.1] resulting in prohibitively long experimental times. Multi-exponentiality is not a major problem in most cases, as ^{the} literature suggests that such behaviour should only be expected in a limited number of tissues [7.2], mainly when fat and water are present in the same voxel, e.g. in bone marrow, mammary and fatty tissue [7.2–7.4]. A phantom study did, however, show that mono-exponential fitting of data corresponding to a mixture of water and "human-equivalent" fat can result in grossly inaccurate measurement of T_1 values [7.5]. Multi-exponential fitting of the same data could decompose the fat and water T_1 , but proved inadequate to further resolve the two T_1 components of fat, as both were relatively similar when compared with the much higher water T_1 value [7.5].

The need for differential fat and water maps has been expressed in various publications, and one example is in quantitative studies of regional blood volume based on T_1 maps, where the model used is valid only under the assumption that any fat signal that contributes to the image is suppressed [7.6]. Several studies have addressed the problem of creating separate T_1 maps for the two components by combining the asymmetric echo chemical shift imaging technique (and hybrid modifications) with the principle of partial saturation to produce differential fat and water T_1 maps, yielding T_1 values for phantoms within 10% of the spectroscopically derived ones [7.7–7.9]. Although multi-slice, a major drawback of these techniques is the extended overall imaging time. Firstly, several data points in the relaxation curve are required (usually 4 to 6) to give a good T_1 estimation due to the reduced dynamic range of the partial saturation

method with respect to inversion recovery. Additionally, the conventional asymmetric echo experiment requires at least two repetitions of the sequence, even if only one of the components is of interest. Furthermore, any mis-registration errors between the in-phase and opposed-phase images are expected to propagate into the calculated images.

Recently, fat and water T₁ maps have been generated using the two-point IR technique while differentiating between the two components on the basis of their phase difference in a gradient echo [7.10]. Although evaluation of the technique in phantoms was not presented, its application in a comparative clinical study showed that reduced T₁ values of skeletal muscle, often associated with muscular dystrophy and congenital myopathies, was caused by partial volume effects due to secondary fatty infiltration.

In this chapter, new pulse sequence schemes are proposed for the generation of separate fat and water T₁ maps. The proposed methods are evaluated for their ability to produce accurate T₁ measurements in direct comparison with spectroscopic and conventional imaging techniques. Technical considerations that relate to each technique are also presented.

7.2 THE SEQUENCES

The proposed techniques were primarily designated for direct application in relatively high resolution imaging experiments (submillimeter voxel dimensions) on the 4.7 T imaging system of the University of London Intercollegiate Research Service, where on a daily basis a diverse range of objects are imaged (ranging in size and shape from a cockroach to a coconut!), using a limited number of conventional radiofrequency coils. In order to account for the relatively low S/N (due to small voxel size and variable coupling between the coil and the sample), T₁ measurements are based on the robust, two-point PS-IR method [7.11].

The PS-IR regime can be readily incorporated into simple, single slice chemical shift selective imaging [7.12], and such a sequence is shown in Fig. 7.1. The component of interest is selectively excited by the chemical shift selective 90° pulse. Magnetization within a single slice is then refocused by the slice selective 180° pulse. The inversion pulse is neither spatially nor chemical shift selective. Only one PS-IR experiment is required in order to generate the T₁ map of one chemical shift, however if both fat and water T₁ information is desired the imaging time is double that of the conventional method. Due to the single slice selective pulse (per excitation), time efficient multi-slice schemes cannot be employed, and acquisition of a second slice requires repetition of the entire experiment. However, the effects of any deviations from the ideal square slice profile are kept to the minimum, as they are not enhanced by propagation through multiple slice selective pulses, and accuracy in T₁ measurements is ensured.

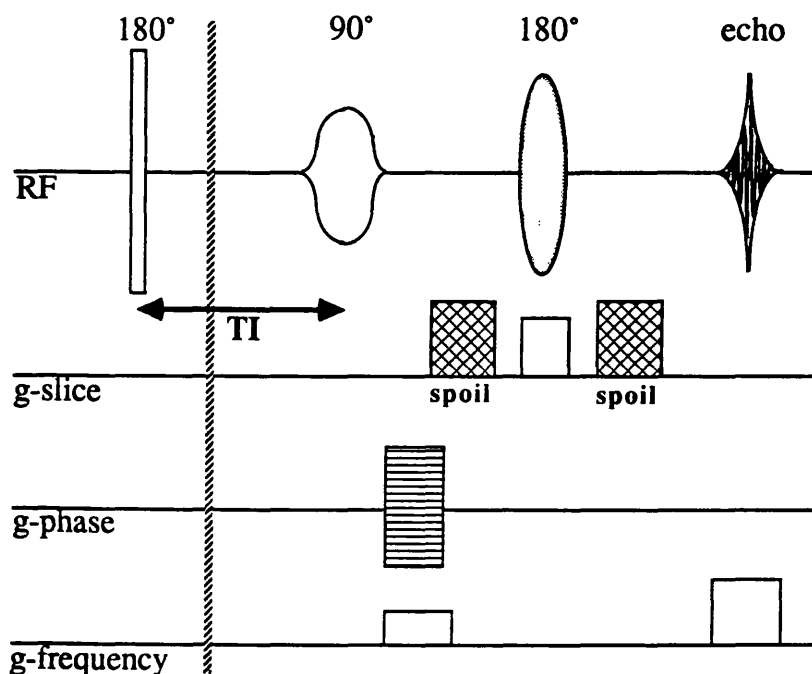


Figure 7.1. Diagrammatic representation of a single slice chemical shift selective, PS-IR imaging sequence. The experiment is repeated twice, with and without the initial inversion pulse. Slice selection is performed with the refocusing pulse.

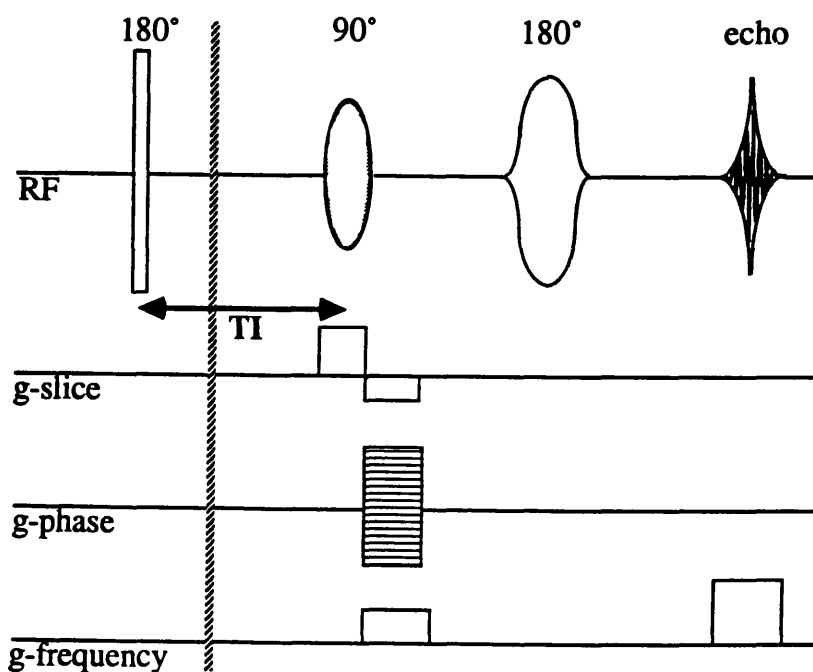


Figure 7.2. Diagrammatic representation of a single slice chemical shift selective, PS-IR imaging sequence. The experiment is repeated twice, with and without the initial inversion pulse. Slice selection is performed with the excitation pulse.

However, one should consider the effect of the non-slice-selective excitation pulse, which generates transverse magnetization (of the desired component) over the entire imaging volume. Such magnetization is spatially encoded, but generally is quickly dephased by the slice selection, phase and frequency encoding gradients (the latter, only when its compensating part is applied prior to the refocusing pulse). However, it is possible that transverse magnetization outside the selected slice is still of sufficient amplitude during acquisition, thus inducing a signal and generating artifacts in the resulting image. In order to completely spoil such magnetization, additional magnetic field gradients can be applied, with lobes of the same sign and total area positioned on either side of the refocusing pulse so that the desired magnetization is not affected. Alternatively, the PS-IR scheme can be incorporated in a chemical shift selective refocusing sequence [7.13], where the slice selection is performed by the excitation pulse, and only the desired resonance is refocused, as shown in the pulse sequence diagram of Fig. 7.2.

In an attempt to improve the time efficiency of differential fat and water T₁ maps, a more complex PS-IR method is proposed, and the pulse sequence is shown in Fig. 7.3. In this scheme, two slices are selected within the same repetition time. The first chemical shift selective 90° pulse excites only the fat magnetization over the entire imaging volume and the subsequent slice selective 180° pulse refocuses the excited spins within a single slice. In order to completely dephase signal arising outside the slice of interest, a spoil gradient is again applied around the refocusing pulses. The same experiment is repeated immediately, with the excitation pulse on the water resonance and the frequency of the slice selective 180° pulse adjusted to refocus a different slice. The inverting pulse in the IR part of the experiment is again non-selective. Note that the inversion time is different for the two resonances, and this has to be incorporated in the T₁ calculating program. In theory, the two components can be selected in either order. Studies on the optimization of PS-IR sequence parameters for accurate T₁ measurements [7.14], however, suggest that a shorter inversion time should be used for the measurement of a shorter T₁ component. Considering that typical fat T₁ values in biological systems are expected to be in the range of 150-300 ms [7.2], the optimal TI for fat would be 280 ms, while a TI of 400 ms or 500 ms can be used to measure the generally longer T₁ values of water. This choice of inversion delays can also afford relatively long echo times if so desired. One should note that while fat magnetization is refocused within a slice by the first slice selective pulse, water is inverted and its longitudinal relaxation disturbed. Therefore, care should be taken that the second slice selective pulse refocuses water in a slice other than the previous one. This can be ensured by slice selective pulses with a frequency difference equal to or greater than their bandwidth.

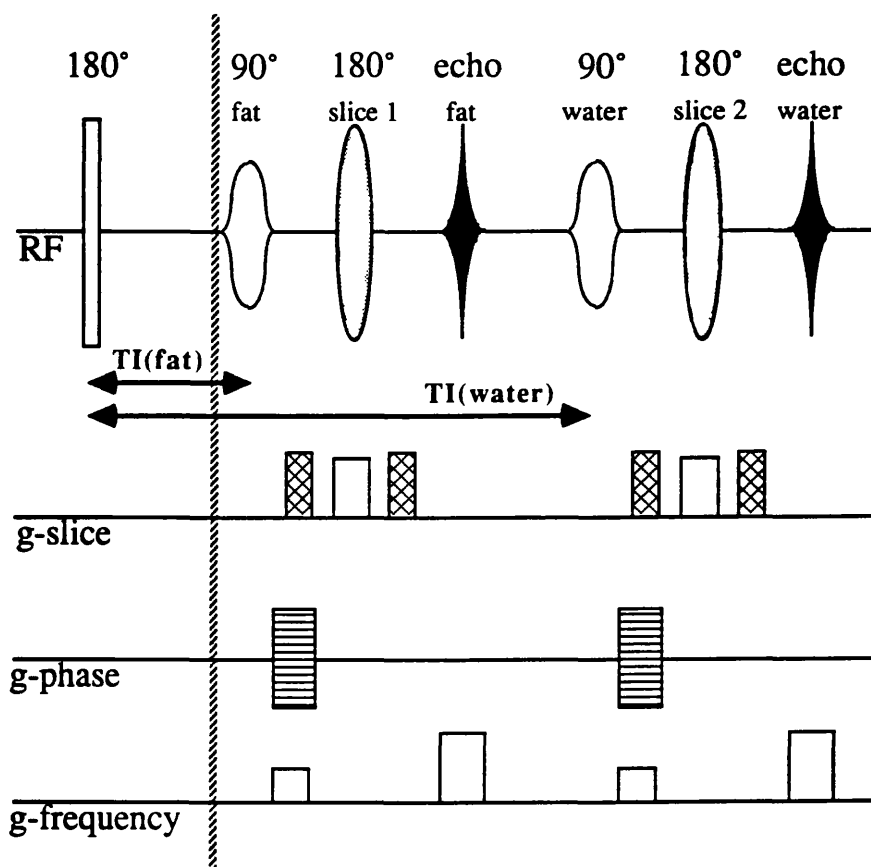


Figure 7.3. Diagrammatic representation of a double spin-echo chemical shift selective, PS-IR imaging sequence. The experiment is repeated twice, with and without the initial inversion pulse. Slice selection is performed with the refocusing pulses.

An important point to mention is that due to the chemical shift of the two components it is possible to create fat and water images of the same spatial position. Consider a selective pulse of bandwidth ΔF_p (in Hz) around the frequency F_p in the presence of a linear magnetic field gradient of amplitude G applied along the r direction. The gradient creates a linear frequency distribution:

$$F(r) = \frac{\gamma}{2\pi} (1-\sigma) (B_0 + Gr) = F_{res} + \frac{\gamma}{2\pi} (1-\sigma) Gr \quad (7.1)$$

where σ and F_{res} are the shielding constant and the resonance frequency (in Hz) in a homogeneous magnetic field, respectively, of the species to be imaged. The selected slice is then centred at:

$$r = 2\pi \frac{F_p - F_{res}}{\gamma (1-\sigma) G} \approx 2\pi \frac{F_p - F_{res}}{\gamma G} \quad (7.2)$$

The thickness of the slice, Δr , is given by:

$$\Delta r = 2\pi \frac{\Delta F_p}{\gamma G} \quad (7.3)$$

Considering the chemical shift of $\delta=3.6$ ppm between the fat and water protons, their resonances have a frequency difference of ΔF (720 Hz for a 4.7T static magnetic field), that is, $F_{res}(\text{water}) = F_{res}(\text{fat}) + \Delta F$. Then, following from Eqn. (7.2), the first slice selective pulse of frequency F_p , will refocus fat spins in a slice centred at:

$$r_1(\text{fat}) = 2\pi \frac{F_p - F_{res}(\text{fat})}{\gamma G} \quad (7.4)$$

and invert water spins in a slice centred at:

$$\begin{aligned} r_1(\text{water}) &= 2\pi \frac{F_p - F_{res}(\text{water})}{\gamma G} = 2\pi \frac{F_p - F_{res}(\text{fat}) - \Delta F}{\gamma G} = \\ &= r_1(\text{fat}) - 2\pi \frac{\Delta F}{\gamma G} \end{aligned} \quad (7.5)$$

If the second slice selective pulse has a frequency of $F_p + \Delta F$, it will refocus water spins in a slice centred at:

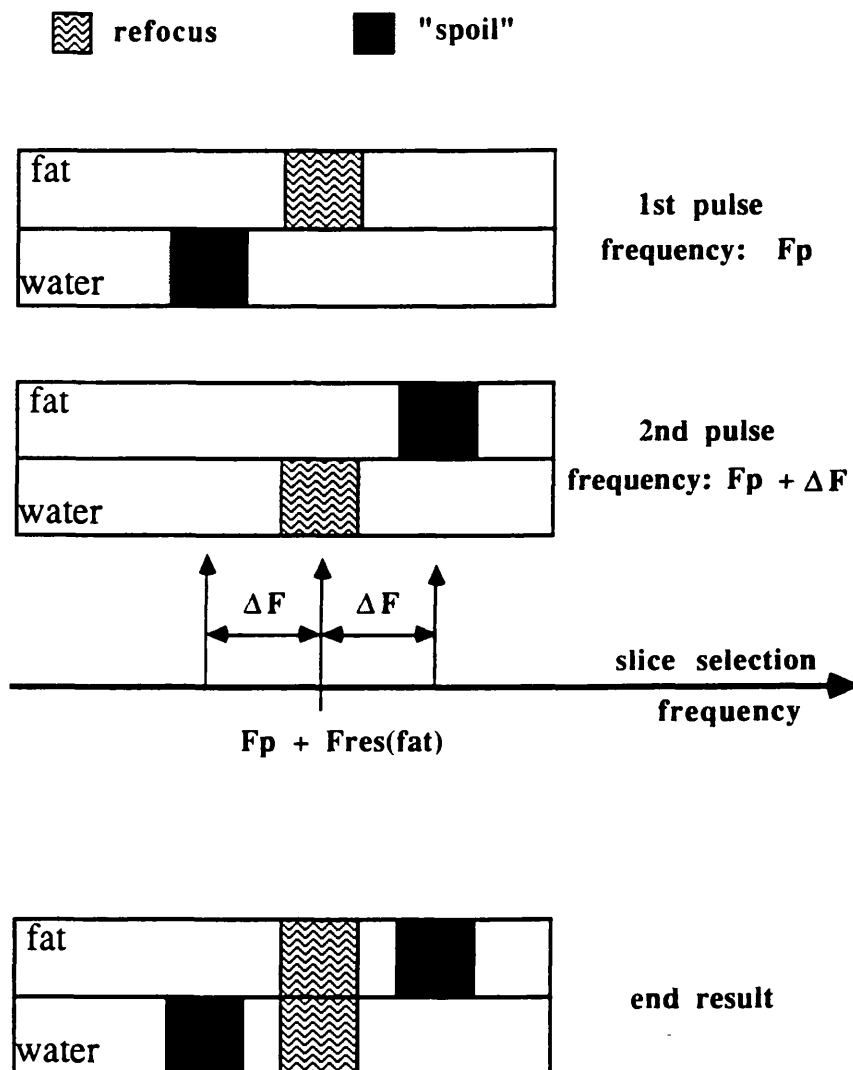


Figure 7.4. Schematic representation of chemical shift dependent slice selection in the proposed double spin echo PS-IR sequence of Fig. 7.3. Following fat selective excitation, the 1st slice selective refocusing pulse has a frequency of F_p Hz, refocusing fat in a slice centred at $F_p - F_{res}(fat)$ Hz and "spoiling" water magnetization in a slice with relative separation of $-\Delta F$ Hz. Following water selective excitation, the 2nd slice selective refocusing pulse has a frequency of $(F_p + \Delta F)$ Hz, refocusing water in the same slice as the previously generated fat image, and "spoiling" fat magnetization in a slice with relative separation of $+\Delta F$ Hz. ΔF is the chemical shift (in Hz) between fat and water protons.

$$\begin{aligned} r2(\text{water}) &= 2\pi \frac{F_p + \Delta F - F_{\text{res}}(\text{water})}{\gamma G} = 2\pi \frac{F_p - F_{\text{res}}(\text{fat})}{\gamma G} = \\ &= r1(\text{fat}) \end{aligned} \quad (7.6)$$

while fat spins will be inverted in a slice centred at:

$$r2(\text{fat}) = 2\pi \frac{F_p + \Delta F - F_{\text{res}}(\text{fat})}{\gamma G} = r1(\text{fat}) + 2\pi \frac{\Delta F}{\gamma G} \quad (7.7)$$

It is apparent that fat and water images as generated by the first and second spin echo experiment with slice selective pulses of frequencies F_p and $F_p + \Delta F$, respectively, correspond to the same spatial position, that is, a slice centred at $(2\pi/\gamma G)\{F_p - F_{\text{res}}(\text{fat})\}$. The slices with the inverted fat and water magnetization are centred at $\pm(2\pi/\gamma G)\Delta F$ around the slice of interest. A schematic representation of the effect of the two slice selective pulses is shown in Fig. 4.4. Care should be taken that the slice of interest does not overlap with inverted magnetization of either component. Following from Eqns. (7.5) and (7.7), and assuming rectangular slice profiles, this can be ensured if the slice thickness, Δr , is:

$$\Delta r \leq 2\pi \frac{\Delta F}{\gamma G} \quad (7.8)$$

which, considering Eqn. (7.3), is equivalent to $\Delta F_p \leq \Delta F$, that is when the frequency bandwidth of the slice selective pulses is less than the relative chemical shift of the two components. As before, slice selection can also be performed during excitation, with the refocusing pulses being chemical shift selective.

7.3 EXPERIMENTS AND RESULTS

The proposed PS-IR methods were evaluated for their ability to produce accurate differential fat and water T₁ maps in direct comparison to conventional spectroscopic and imaging sequences. This phantom study was performed on a SISCO-200 NMR imaging spectrometer (Spectroscopy Imaging Systems Corporation, Fremont, California), equipped with a 4.7 T, 33 cm bore superconducting magnet and the standard SISCO magnetic field gradient set (20 mT/m, 33 cm inner diameter). An imaging coil with an inner diameter of 9 cm was used for all spectroscopic and imaging experiments.

The phantom consisted of several glass tubes (~1 cm outer diameter, ~4 cm height), each one containing either mineral oil (Aldrich Chemical Co. Ltd., Gillingham

SP8 4JL, England) or distilled water doped with different concentrations of copper sulphate to give water T_1 values in a range similar to that found in biological systems.

7.3.1 Spectroscopic T_1 Measurements

The T_1 value of each phantom component was measured separately by the standard spectroscopic version of the inversion recovery technique [7.15], as implemented by the manufacturer. The experiment involved 7 repetitions of the sequence with inversion times logarithmically spaced well over the relaxation curve, while $TR \gg 5T_1$ was ensured by a crude measurement of the T_1 prior to the actual experiment. The phantom was left to reach thermal equilibrium within the centre of the magnet, which had been kept at a constant temperature of 18.5 °C throughout the experiment. The spectroscopically measured T_1 values, calculated using the mono-exponential fitting procedure supplied by the manufacturer, are shown in Table 7.1. It should be noted that in the oil spectrum two resonance peaks could be partially resolved with a relative shift of 0.4 ppm (with an overall 2 ppm peak width), each one being characterized by a different T_1 relaxation constant. The value shown in Table 7.1 is the weighted mean, the two T_1 components being 245 ± 2 ms and 285 ± 1 ms, corresponding to peaks with normalized areas of 0.61 and 0.39, respectively.

7.3.2 Conventional T_1 Maps

For the imaging experiments the individual phantom tubes were mounted together in a glass beaker. A pilot spectrum from the phantom, acquired prior to imaging, showed that the oil resonance frequencies occurred within a ~ 2 ppm range, centred ~ 3.6 ppm upfield from the water peak (shimmed to 0.5 ppm full width at half maximum height). A single cross sectional slice was selected through the middle of the phantom, by means of 5000 μ s, five-lobe, sinc shaped pulses in the presence of 11.7 mT/m linear magnetic field gradient, giving a slice thickness of 2 mm. All imaging experiments were performed with a 6x6 cm field of view, 128x128 data matrix and 4 signal averages per phase encoding step. The echo and acquisition times were kept constant at 30 ms and 5 ms, respectively.

Following the suggested optimal parameter setting for accurate T_1 measurements using the PS-IR method [7.14], the inversion time was 400 ms, while the repetition times of the partial saturation and the inversion recovery experiments were 1600 ms and 4000 ms, respectively (see Section 6.3.3). The signal polarity in the inversion recovery image was restored using the simple two-point algorithm based on the gross differences in the phase images of the PS and IR experiment [7.16] (see Section 6.3.2). This algorithm was implemented using macros developed in the "viewit" programming environment and C programmes based on the UNC image processing software and libraries. Calculation of the T_1 maps was performed using existing software developed at the Institute of

TABLE 7.1				
phantom no.	component	CuSO ₄ conc. (g/l)	spectroscopic T1 (ms)	± SD (ms)
1	water	0.1	1352	3
2	water	0.2	826	3
3	water	0.4	511	3
4	water	0.6	353	1
5	water	0.8	276	2
6	water	1.0	225	1
7	oil	–	261	1

Table 7.1. Spectroscopic T1 measurements of the phantom compartments.

The concentration of CuSO₄ for the water solutions is also shown.

64 averages were acquired.

Neurology, London. The T_1 value for each phantom component was calculated from the T_1 maps by measuring the mean value (\pm SEM) from a 14 mm^2 (i.e. 64 pixels) region of interest. The linear correlation coefficient, r , as well as the slope, β , and intercept, α , (at the 99% confidence limit) of the regression line of each image derived T_1 set on the spectroscopic values were computed, as described in Appendix 3.

The conventional PS-IR imaging experiment was firstly performed with all pulses being slice selective, and the results are shown in Table 7.2. Although the t-test shows a linear correlation between the two sets of values higher than the 99.95% significance level, the confidence limits for the coefficients of the regression line show a significant deviation of the ideal condition, suggesting the presence of a systematic error in one of the measurement sets. This error appears as a reduction in the image derived T_1 values, in the range of 10-26% of the spectroscopic measurement, and may be due to non-ideal slice profiles, which are enhanced by multiple slice selective pulses. In order to minimize the effects of non-ideal slice, the sequence was repeated in a single slice version, where inversion and excitation were performed by broad-band (12 ppm), square pulses, while a single slice was selected by the refocusing pulse (similar to the pulse sequence diagram in Fig. 7.1, save for the chemical shift selection). The experiment was repeated three times with different frequency offsets for the non-selective pulses, being on resonance for either water, fat, or in between. This was intended in order to study the off-resonance effects of the simple square pulse employed. No spoil gradients around the refocusing pulse were used in this experiment. The results are shown in Table 7.3.

The t-test shows good linear correlation between each set of image derived values and the spectroscopic measurements. When the non-selective pulses are on resonance with the component of interest, the image derived T_1 for all the phantom components are within 2% of the equivalent spectroscopic value and both regression line coefficients have values corresponding to the ideal situation. However, there is a significant deviation from the desired identity line when the non-selective pulses are not on resonance, as also shown in Fig. 7.5. For non-selective pulses with frequency between the fat and water resonances (~ 1.8 ppm off resonance) the error in the T_1 measurements is in the order of 10-20%, while in the case of non-selective pulses 3.6 ppm off-resonance (selecting the other component) the error in T_1 measurements is in the range of 20-60% of the spectroscopic values.

Figure 7.6 depicts both the partial saturation and inversion recovery images as well as the T_1 map, as derived from the conventional multi-slice PS-IR experiment and the single slice version where slice selection is applied by the refocusing pulse. An artifact, in the form of streak, present in some of the images is due to intermittent external RF interference. Additionally, both images acquired by the single slice sequence are degraded by artifacts, which also propagate into the T_1 map. The origin of this artifact is

TABLE 7.2		
phantom	method spectroscopy	conventional multi-slice PS-IR
# 1	1352	1002 ± 3
# 2	826	651 ± 1
# 3	511	405 ± 1
# 4	353	290 ± 1
# 5	276	225 ± 1
# 6	225	183 ± 2
# 7	261	235 ± 2
r	1	0.999167
α	0	33.9 ± 86.4
β	1	0.724 ± 0.041

Table 7.2. T₁ values (in ms ± SEM) of the phantom compartments, as measured by multi-slice PS-IR imaging.

TABLE 7.3				
method	spectroscopy	conventional slice selection with 180° on resonance	conventional slice selection with 180° 1.8 ppm off	conventional slice selection with 180° 3.6 ppm off
phantom				
# 1	1352	1356 ± 4	1052 ± 3	530 ± 3
# 2	826	824 ± 2	676 ± 3	406 ± 1
# 3	511	509 ± 1	449 ± 2	328 ± 1
# 4	353	360 ± 2	322 ± 1	257 ± 1
# 5	276	273 ± 1	252 ± 1	208 ± 1
# 6	225	227 ± 1	208 ± 1	182 ± 2
# 7	261	266 ± 1	249 ± 1	214 ± 3
r	1	0.999954	0.999471	0.985479
α	0	1.5 ± 8.8	53.8 ± 22.2	139.2 ± 47.85
β	1	1.000 ± 0.013	0.744 ± 0.33	0.303 ± 0.072

Table 7.3. T₁ values (in ms ± SEM) of the phantom compartments, as measured by single-slice PS-IR imaging. The slice selection is performed by the refocusing pulse, while the frequency of the non-selective pulses is on resonance with either of the two components or in the middle.

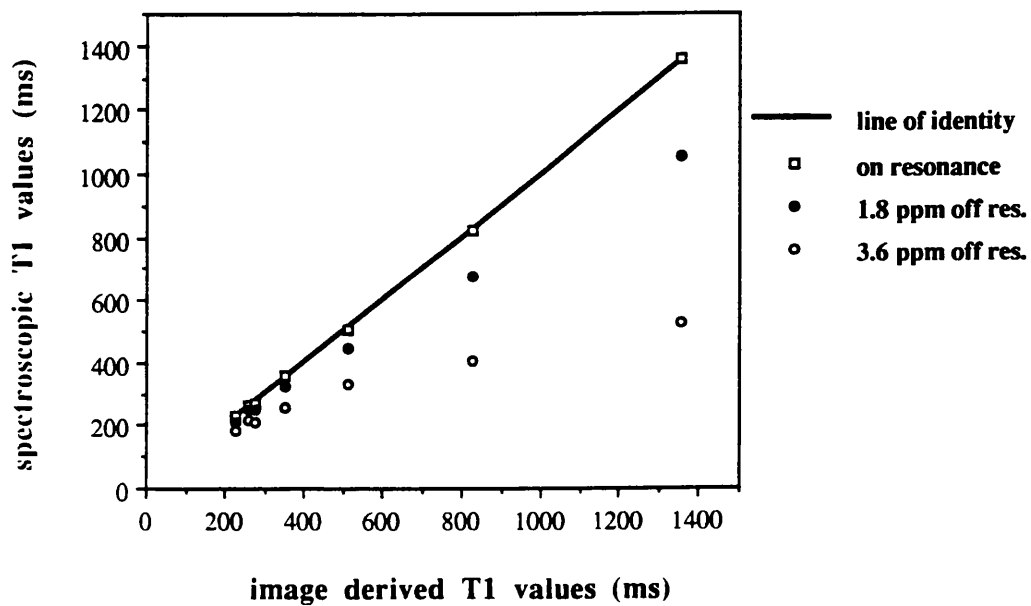


Figure 7.5. Conventional single slice PS-IR image derived T1 values for the various phantom components plotted against the equivalent spectroscopic values. When all non-selective pulses are on resonance with the component of interest, the values fall onto the identity line. In the off resonance condition, the image derived T1 values are significantly lower than in spectroscopy.

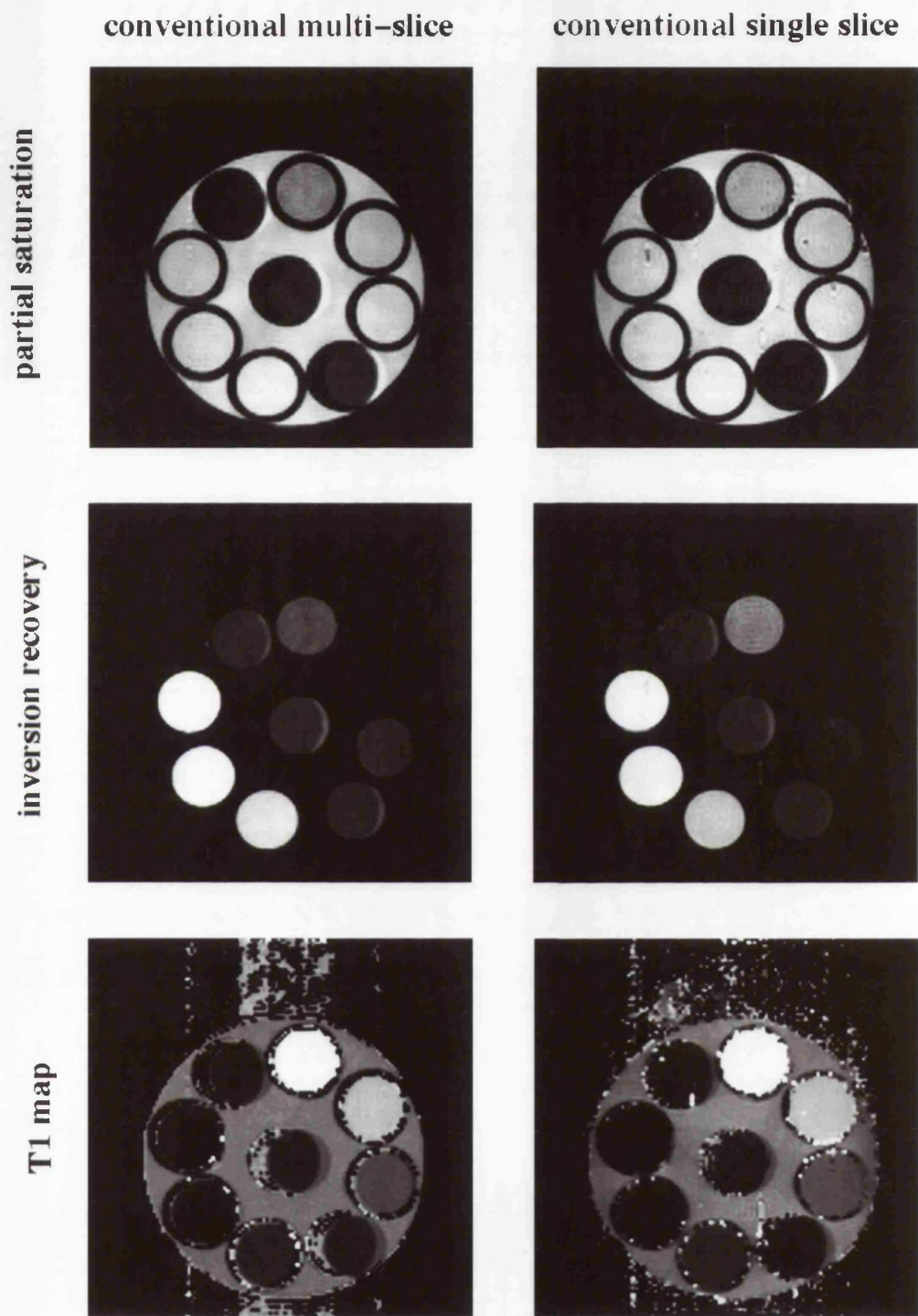


Figure 7.6. Partial saturation and inversion recovery images and the corresponding T1 maps generated using the conventional multi-slice PS-IR experiment and the single slice version where the slice is selected during refocusing. No spoiler gradients are employed.

due to magnetization outside the slice of interest, which is excited by the non-selective 90° but not completely dephased. To demonstrate this effect, a separate experiment was performed using a less complex phantom, that is, a single glass tube with doped distilled water (T_1 of 353 ms). Imaging experiments were performed as before, using the conventional multi-slice partial saturation sequence and two versions with a single slice selective pulse, either the refocusing or the excitation pulse. The sequences were also repeated with the power of the refocusing pulse set to zero, while the rest of the imaging parameters were kept constant. This experiment should give an image of noise, unless some of the excited magnetization is not completely dephased at the time of signal acquisition. The results are shown in Fig. 7.7. The artifact is apparent only in the image which involves non-selective excitation, and the signal that generates it is also shown in the image acquired with the refocusing pulse switched off. On the other hand, all images that involve slice selective excitation are artifact free. The artifact in the images acquired using non-selective excitation can also be significantly reduced by employing a spoil gradient, with lobes of the same sign and equal areas before and after the refocusing pulse so that the magnetization in the slice of interest is not affected. This is shown in Fig. 7.8, where the signal in the images acquired with the refocusing pulse switched off is progressively reduced as the strength of the spoil gradient lobes around the 180° increases from zero up to 17.6 mT/m. The spoil gradient was applied in the slice selection direction and each lobe was of 6 ms duration.

The PS-IR method was then performed using the conventional single slice sequence with slice selection on the refocusing 180° pulse and the spoil gradients, as well as the version with the slice selection on the excitation pulse. The corresponding T_1 measurements for the case of non-selective pulses being on resonance with the component of interest, are shown in Table 7.4. All image derived T_1 measurements correlate well with spectroscopy, while the regression coefficients show good agreement of the imaging methods with spectroscopy. In fact, all image T_1 measurements are within 2% of the corresponding spectroscopic value.

7.3.3 Fat and Water T_1 Maps

The proposed single slice sequences for differential fat and water T_1 maps (shown in Figs. 7.1 and 7.2) were performed whilst maintaining the same imaging parameters as in the conventional experiments. Chemical shift selective pulses of 600 Hz (3 ppm) bandwidth were employed. The differential T_1 maps are shown in Fig. 7.9. The sequence with the slice selection on the refocusing pulse again suffers from artifacts, while incorporation of a spoil gradient or a slice selective excitation pulse results in artifact free maps. The T_1 values for each phantom component as derived from the differential T_1

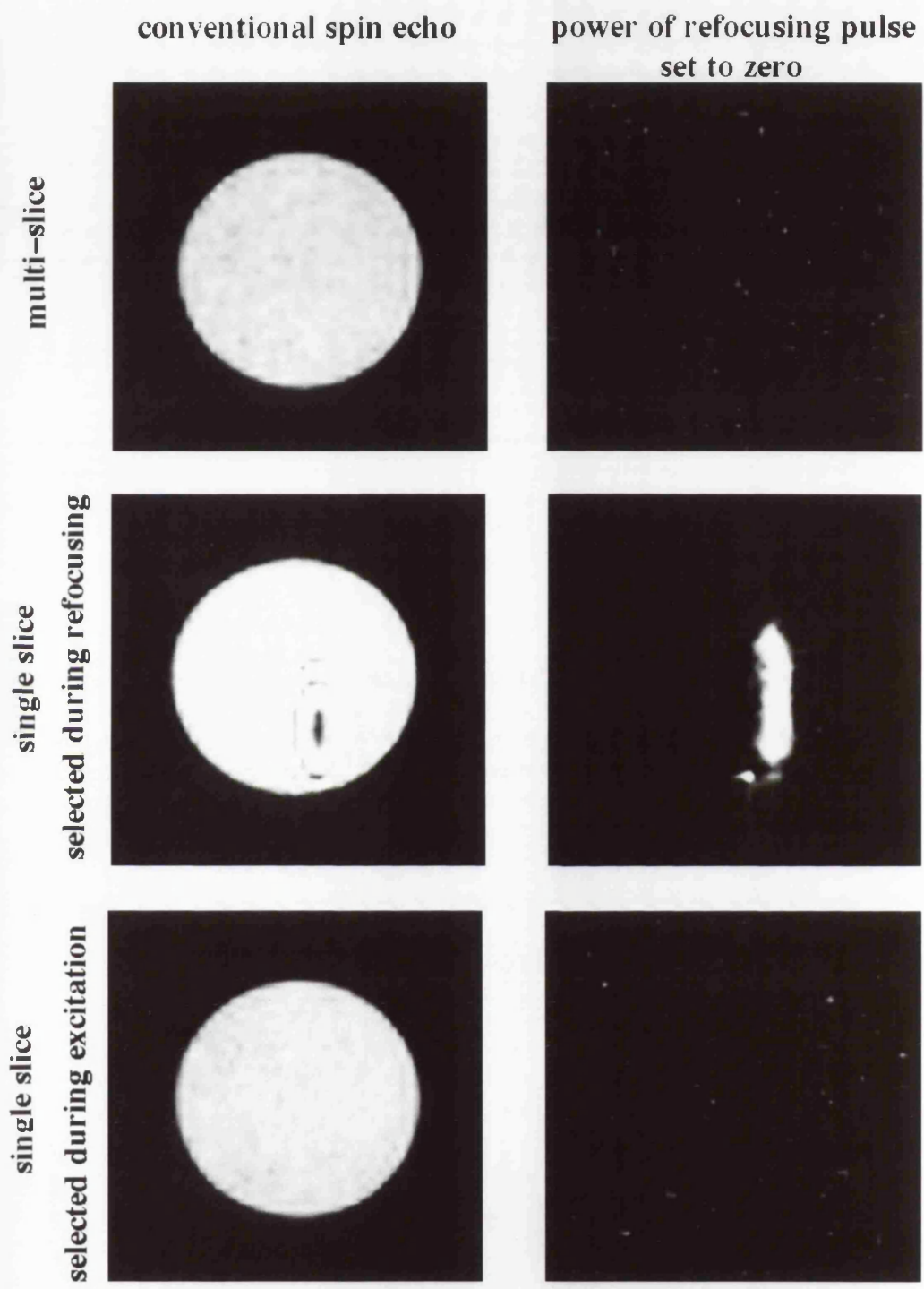


Figure 7.7. Partial saturation, spin echo images of a single tube of water acquired using the conventional multi-slice sequence and two single slice versions where the slice is being selected either with the refocusing of the excitation pulse. The images on the right correspond to the same experiment as in the left but with the power of the refocusing pulse set to zero.

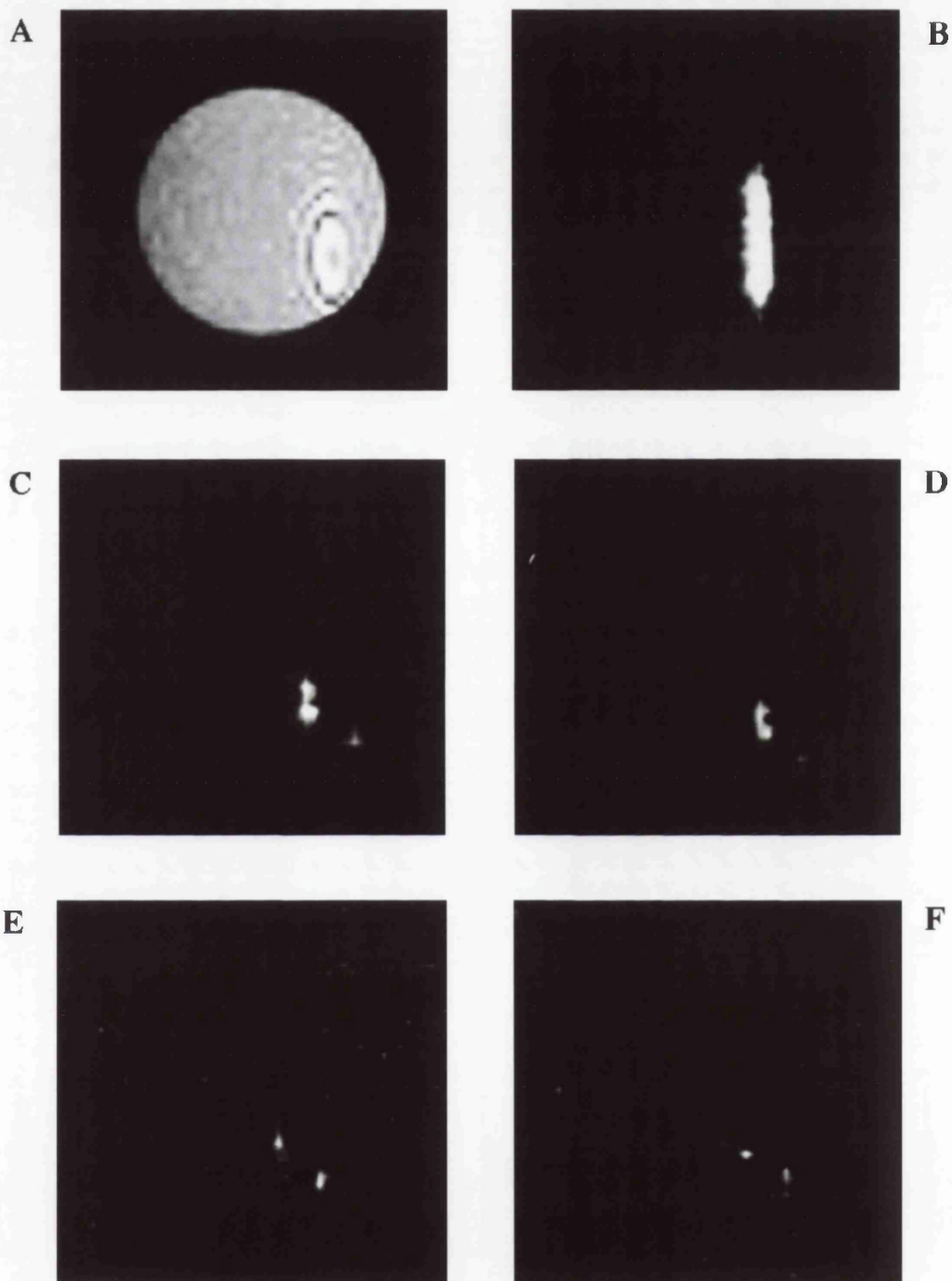


Figure 7.8. (A) Partial saturation, spin echo image of a single tube of water acquired using the single slice version of the conventional sequence, with slice selection during refocusing and no spoiler gradients. (B) The same experiment but with the power of the refocusing pulse set to zero. (C) – (F) The same experiment as in (B) but with spoiler gradients of total duration 12 ms and strength of 12.7, 14.6, 16.6, and 17.6 mT/m, respectively.

TABLE 7.4				
method	spectroscopy	conventional slice selection with 180° no spoil	conventional slice selection with 180° + spoil	conventional slice selection with 90°
phantom				
# 1	1352	1356 ± 4	1341 ± 1	1347 ± 3
# 2	826	824 ± 2	818 ± 2	836 ± 2
# 3	511	509 ± 1	513 ± 1	510 ± 3
# 4	353	360 ± 2	360 ± 3	349 ± 1
# 5	276	273 ± 1	273 ± 1	272 ± 1
# 6	225	227 ± 1	224 ± 1	223 ± 1
# 7	261	266 ± 1	265 ± 2	263 ± 2
r	1	0.999954	0.999952	0.999920
α	0	1.5 ± 8.8	5.2 ± 8.9	-0.9 ± 11.6
β	1	1.000 ± 0.013	0.988 ± 0.013	1.001 ± 0.017

Table 7.4. T₁ values (in ms ± SEM) of the phantom compartments, as measured by single-slice PS-IR imaging, where the refocusing 180° pulse is slice selective with or without spoil gradients, or the excitation pulse is slice selective.

All non-selective pulses are on resonance.

maps are shown in Table 7.5. The measurements correlate well with spectroscopy, and are within 2% of the corresponding spectroscopic value.

The proposed double spin-echo sequence for differential fat and water T₁ maps (shown in Fig. 7.3) was performed maintaining the same imaging parameters as before. The fat T₁ map was generated by the first spin echo experiment with an inversion time of 280 ms, while a TI of 400 ms was used for the water map. The sequence was then repeated employing the set of spoil gradients around the refocusing pulses. Finally, the double spin-echo PS-IR experiment was performed with the excitation pulses being slice selective while chemical shift selection was accomplished by the refocusing pulses. The differential T₁ maps are shown in Fig. 7.10. The T₁ values for each phantom component as derived from the differential T₁ maps are shown in Table 7.6. The measurements correlate well with spectroscopy, but the regression coefficients once again indicate a systematic error. This is due to the fact that the frequency of the non-selective inversion pulse was set between the two resonances, effectively being 1.8 ppm off-resonance for both components. The result is a 4%-17% reduction in the image derived T₁ values. However, when compared to the equivalent conventional imaging experiment (see Table 7.3), the off-resonance effect on the T₁ measurements is less, as this differential fat and water PS-IR experiment employs only one non-selective pulse, the rest being either on-resonance chemical shift selective pulses or used for slice selection.

7.4 DISCUSSION

Longitudinal relaxation time measurements are a powerful tool in MRI. However, their potential may be limited in cases where fat and water are present within the same imaging voxel due to their physiological distributions or as a result of chemical shift artifact. In this chapter two groups of methods have been proposed that generate differential fat and water T₁ maps. The T₁ measurements are based on the hybrid, two point PS-IR sequence, while the differentiation between the two components employs chemical shift selective pulses.

The first group of sequences involve single slice chemical shift selective imaging, where the chemical shift selection is performed by either the excitation or the refocusing pulse. Both schemes have been used to create differential T₁ maps of a fat and water phantom, and the image derived measurements were within 2% of the spectroscopic values. The equivalent conventional PS-IR imaging techniques resulted in a poorer accuracy, because of non-ideal slice profiles (in the multi-slice version) or due to off resonance effects of the non-selective pulses (in the single slice version). In the proposed methods, deviations from the ideal slice profile are minimum, as only one slice selective

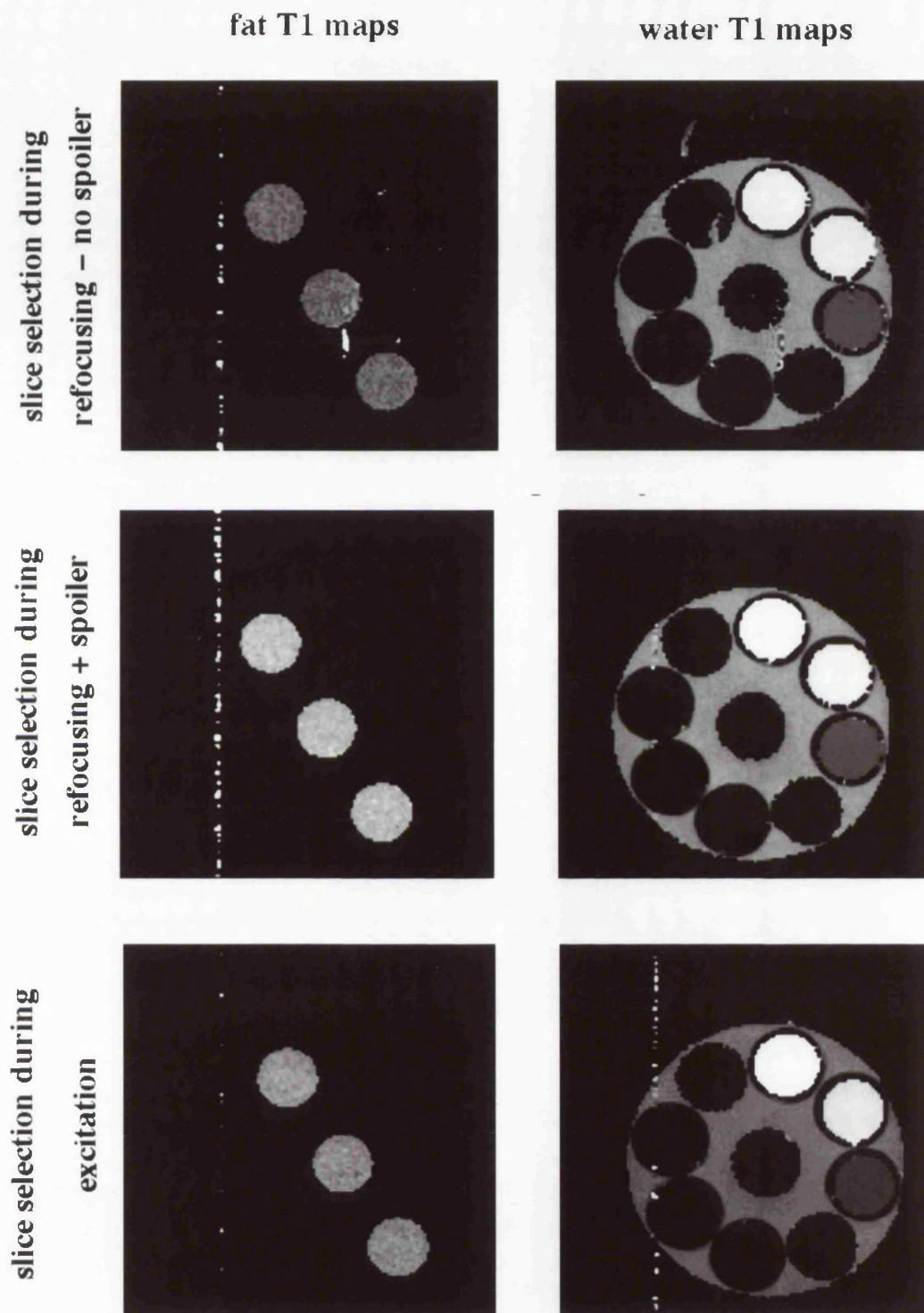


Figure 7.9. Differential fat and water T1 maps as generated by the proposed single slice, chemical shift selective PS-IR methods. The slice selection is performed with the refocusing pulse (with or without spoiler gradients), or with the excitation pulse.

TABLE 7.5				
method	spectroscopy	fat & water slice selection with 180° no spoil	fat & water slice selection with 180° + spoil	fat & water slice selection with 90°
phantom				
# 1	1352	1360 ± 4	1340 ± 4	1352 ± 3
# 2	826	827 ± 1	823 ± 1	825 ± 2
# 3	511	511 ± 1	512 ± 1	510 ± 1
# 4	353	352 ± 2	356 ± 3	352 ± 1
# 5	276	268 ± 1	267 ± 2	272 ± 2
# 6	225	222 ± 2	227 ± 1	220 ± 1
# 7	261	263 ± 2	266 ± 4	262 ± 3
r	1	0.999974	0.999933	0.999989
α	0	-5.2 ± 6.7	3.9 ± 10.5	-2.8 ± 4.3
β	1	1.009 ± 0.010	0.989 ± 0.015	1.002 ± 0.006

Table 7.5. T₁ values (in ms ± SEM) of the phantom compartments, as measured by the proposed methods for single-slice, differential fat and water T₁ imaging.

The slice selection is performed with the 180° refocusing pulse, with or without spoil gradients, or during the excitation pulse.

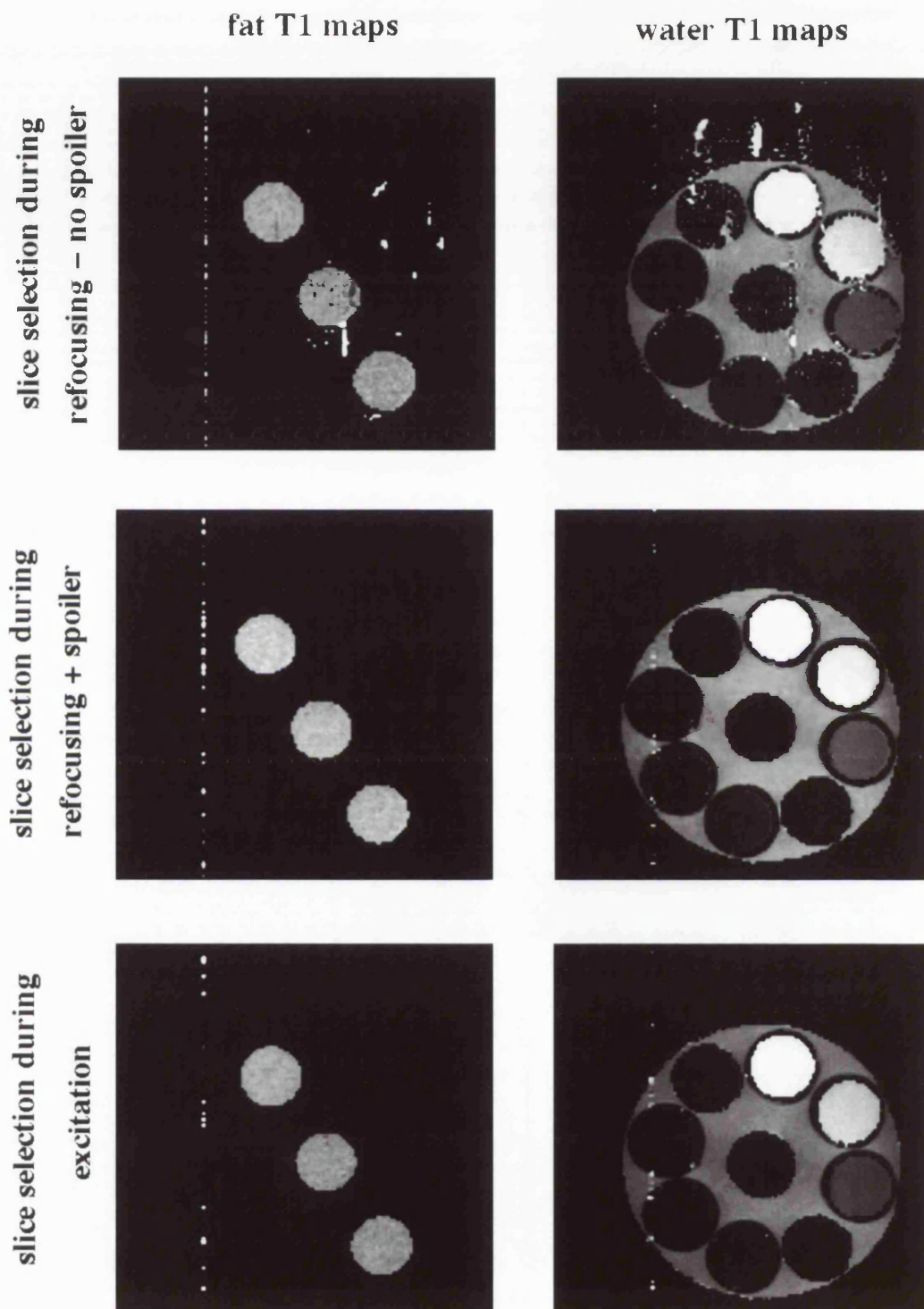


Figure 7.10. Differential fat and water T1 maps as generated by the proposed double spin echo, chemical shift selective PS-IR methods. The slice selection is performed with the refocusing pulse (with of without spoiler gradients), or with the excitation pulse.

TABLE 7.6				
method	spectroscopy	double fat & water slice selection with 180°	double fat & water slice selection with 180°	double fat & water slice selection with 90°
phantom		no spoil	+ spoil	
# 1	1352	1154 ± 4	1149 ± 2	1143 ± 2
# 2	826	690 ± 1	685 ± 3	679 ± 2
# 3	511	450 ± 1	457 ± 1	453 ± 2
# 4	353	317 ± 2	320 ± 1	324 ± 1
# 5	276	239 ± 2	244 ± 2	246 ± 1
# 6	225	207 ± 1	211 ± 1	215 ± 1
# 7	261	247 ± 3	251 ± 1	249 ± 3
r	1	0.999563	0.999394	0.999331
α	0	18.8 ± 22.6	26.0 ± 26.4	29.4 ± 27.4
β	1	0.83 ± 0.03	0.82 ± 0.04	0.81 ± 0.04

Table 7.6. T₁ values (in ms ± SEM) of the phantom compartments, as measured by the proposed double spin-echo method for differential fat and water T₁ imaging.

The slice selection is performed with the 180° refocusing pulse, with or without spoil gradients, or during the excitation pulse.

pulse (per excitation) is applied, while all pulses are on resonance for the component of interest.

The second group of sequences involve two chemical shift selective spin echo experiments within the same repetition time, each one selecting a different component in a different slice. Although the measurements show a good correlation with spectroscopy, the image derived T₁ values are systematically lower than those measured by spectroscopic methods due to the off resonance effect of the single non-selective pulse in the sequence, that is, the inversion pulse in the IR experiment. Further work should involve elimination of this systematic error using specially designed pulses, for example composite or adiabatic broadband inversion pulses [7.17, 7.18]. An important characteristic of these double spin echo sequences is that the relative frequency displacement of the two components in the slice selection direction can be used to create differential fat and water maps from the same slice within a single PS-IR experiment. Future work will involve phantom evaluation of the method using slice selective pulses with frequency offsets and bandwidths to allow for differential fat and water T₁ maps of the same slice. Subsequently, the method will be applied *in-vivo*, as part of an on-going study of spongiform encephalopathy [7.19].

SUMMARY

This thesis has concentrated on the detection and discrimination between fat and water signals in nuclear magnetic resonance imaging. Although primarily directed towards biological systems, the concepts under discussion and the proposed methods can be readily extended to encompass MRI applications in other areas that involve "fat" and "water" systems, such as the petroleum industry. Since the early days of MRI, numerous studies have been oriented towards differential imaging of the two components. As the field of MRI is currently heading towards new frontiers, including quantitative studies, texture analysis, and mapping of several physical processes such as motion, metabolism and functionality, the need to differentiate between fat and water is as important as ever. A critical review of the present state of the field (as presented in Chapter 3) indicates that no method has yet proven to be suitable for all imaging applications and on every system configuration. The current trend towards medium and higher static magnetic field systems, however, favours chemical shift imaging techniques and the work presented in this thesis has involved, in the main, chemical shift selective methods.

Work concerning improvements on conventional techniques for fat and water differentiation has been presented. Slice cycling techniques have been proposed to reduce the differential suppression across the slices in the original version of the chemical shift selective presaturation technique (Chapter 4). Similar procedures may prove useful in any method that involves an initial preparation period followed by acquisition of a number of slices. Continuation of this work should be directed towards devising more efficient cycling schemes, as well as exploring the potential of the proposed 4-step procedure to yield longitudinal relaxation time maps of the suppressed component.

A hybrid chemical shift selective inversion recovery sequence for fat or water suppressed MRI has been presented (Chapter 5). Theoretical analysis and comparative experimental evaluation have showed that the technique is robust in normal use and more tolerant than its closely related conventional methods to mis-settings of parameters such as inversion time, as well as tip angle and frequency bandwidth of the chemical shift selective pulse. The proposed method requires only minor alteration of the standard inversion recovery or presaturation experiments, thus it can be readily applied in clinical imaging. Implementation of the sequence will be especially beneficial when the unwanted component exhibits a range of T₁ values, or there are regional susceptibility differences, as well as when surface or internal coils are used.

Finally, initial work on differential fat and water relaxation time measurements has been presented. As a background, conventional methods for generation of longitudinal relaxation time maps have been discussed (Chapter 6). Subsequently, simple sequences

have been proposed for creating differential T₁ calculated images (Chapter 7). Initial experimental validation of the proposed methods has shown that accurate T₁ measurements can be obtained, that do not suffer from non-ideal slice profiles or off resonance effects of the RF pulses by as much as equivalent conventional techniques. However, more work is invited in devising more time efficient regimes for differential fat and water T₁ measurements. Future work should also be directed towards differential mapping of transverse and rotating frame relaxation processes.

This thesis is the result of my own work.

PUBLICATIONS ARISING FROM THIS WORK

1. E. Kaldoudi, S.C.R. Williams, G.J. Barker, and P.S. Tofts
"A Chemical Shift Selective Inversion Recovery Sequence for Fat-Suppressed MRI: Theory and Experimental Validation"
Magn. Reson. Imaging, vol. 11, 341-355, 1993.
2. E. Kaldoudi, S.C.R. Williams, G.J. Barker, and P.S. Tofts
"A Modified IR Sequence for Multi-Slice Fluid Attenuated MRI"
Abstr. 12th SMRM, vol. 3, 1231, 1993.
3. E. Kaldoudi, S.C.R. Williams, G.J. Barker, and P.S. Tofts
"Fat-Suppression in MRI: Comparison of a Robust, Hybrid Method with Conventional Techniques"
Proceedings of the British Institute of Radiology,
Br. J. Radiology, vol. 66, 957, 1993.
4. E. Kaldoudi, and S.C.R. Williams
"Relaxation Time Measurements in NMR Imaging. Part I: Longitudinal Relaxation Time"
Concepts Magn. Reson., vol. 5, 217-242, 1993.
5. E. Kaldoudi, and S.C.R. Williams
"Fat and Water Differentiation by Nuclear Magnetic Resonance Imaging"
Concepts Magn. Reson., vol. 4, 53-71, 1992.
6. E. Kaldoudi, and S.C.R. Williams
"Chart: Fat and Water Differentiation by Nuclear Magnetic Resonance Imaging"
Concepts Magn. Reson., vol. 4, 162-165, 1992.
7. G.N.H. Waller, S.C.R. Williams, M.J. Cookson, and E. Kaldoudi
"Preliminary Analysis of Elasmobranch Tissue Using Magnetic Resonance Imaging"
Magn. Reson. Imaging, vol. 12, no. 3, 1994 (in press).

APPENDICES

APPENDIX 1

PHASE CYCLING

An important feature of many conventional pulse sequences is a phase cycling procedure to remove unwanted components of the signal on the basis of their phase properties. These unwanted signals may be due to receiver circuit imperfections, or can be generated during the pulse sequence, for example because of imperfect pulses. A phase cycling routine generally involves repeating the pulse sequence keeping all the parameters constant apart from the relative phases of the radiofrequency pulses and the receiver.

The phase cycling routine employed in all imaging pulse sequences presented in this study is summarized in Table A.1. It is based on the four-step CYCLOPS (CYCLically Ordered Phase Sequence) procedure [A.1], with an additional cycling of the refocusing 180° pulse through the phase encoding steps [A.2]. It is apparent that this routine involves phase shifts of the excitation and refocusing pulse, as well as the receiver. The phase of any other pulse (e.g. a 180° inversion pulse) is kept constant. It should be noted that in the SISCO imaging spectrometer used in this study, the receiver phase is actually fixed. Any shift of the receiver phase during the phase cycle merely changes the "mode" of the receiver. Thus, a 180° receiver phase shift sets the system to subtract instead of adding the data, while a 90° phase shift swaps the two channels of the receiver. This is shown within the parentheses in the 4th column of Table A.1. The "R" and "I" symbols indicate that the acquired signal in the real channel of the receiver will be stored in the data block labelled as "real" and "imaginary", respectively, while the sign indicates addition (+) or subtraction (-).

The pair of the 1st and 2nd repetition (or 3rd & 4th) is designed to remove the "dc-offset" artifact, which appears as a bright streak at the centre of the frequency encoding direction (i.e. a signal of 0 Hz frequency) and it is due to any constant voltage (dc) offset in the amplifier of the receiver circuit. In the second repetition of this two-step cycle, any part of the signal that arises from the sample experiences a relative 180° shift, therefore subtraction (-R) in the data blocks reverses the phase and results in signal accumulation. On the contrary, any constant component of the signal arising from the amplifiers in the receiver circuit, does not experience the phase reversal induced by the phase cycling of the RF sequence. Thus, subtraction in the data blocks results in its cancellation. A diagrammatic representation of the dc-offset and its correction is shown in Fig. A.1.

TABLE A.1			
transmitter no. of repetition	excitation pulse phase	refocusing pulse phase	receiver phase real channel
1st & subsequent "odd-numbered" phase encoding steps			
1	0°	90°	0° (+R)
2	180°	90°	180° (-R)
3	90°	180°	90° (+I)
4	270°	180°	270° (-I)
2nd & subsequent "even-numbered" phase encoding steps			
1	0°	270°	0° (+R)
2	180°	270°	180° (-R)
3	90°	0°	90° (+I)
4	270°	0°	270° (-I)

TABLE A.1. The phase cycling procedure used in the imaging sequences presented in this study.

The pair of 1st and 4th repetitions (or 2nd & 3rd) is designed to remove the ghost images induced as a result of a mismatch in the gain and the relative phases of the two channels in the quadrature receiver circuit. Such a mismatch "contaminates" the complex free induction decay. The subsequent complex Fourier transformation of this signal gives rise to ghost signals at "mirror" resonance frequencies with respect to the transmitter frequency. For example, a real signal at frequency offset $\Delta\omega$, where ω is the transmitter frequency, will produce a ghost signal at frequency offset $-\Delta\omega$, its relative intensity being dependent on the degree of the phase and gain mismatch of the two channels [A.3]. To overcome the problem, the receiver channels are interchanged in the second step of the cycle. However, this induces a phase difference in the signals to be accumulated. In order to make the signals coherent, the relative phase of the refocusing pulse in respect to the excitation pulse is also shifted by 90°, and the sign of the signal in the imaginary channel is reversed. Figure A.2 gives a diagrammatic explanation of how this 2-step cycle corrects for gain imbalances and relative shift deviation in the receiver channels. A more rigorous treatment can be found elsewhere [A.1, A.4].

Finally, the 180° shift of the refocusing pulse for every second phase encoding step removes the "dc-offset-like" artifact in the phase encoding direction, which is due to

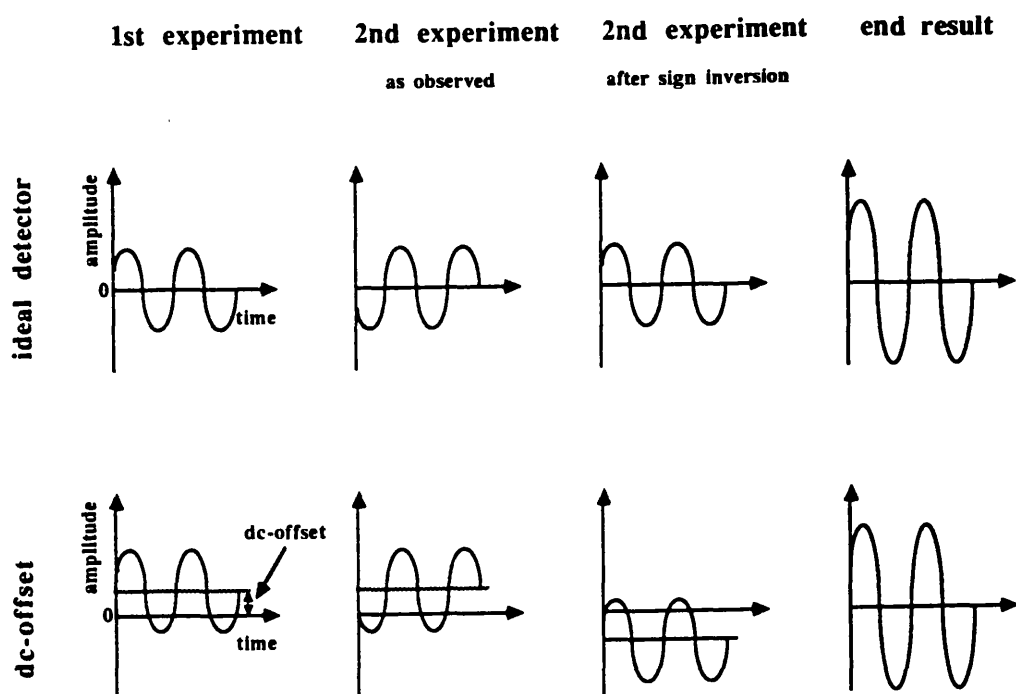


Figure A.1. Graphical representation of the dc-offset induced to an NMR signal by receiver circuit electronics and its cancellation through a two-step phase cycling procedure. For simplicity, any damping effects due to transverse relaxation and field inhomogeneities have been ignored.

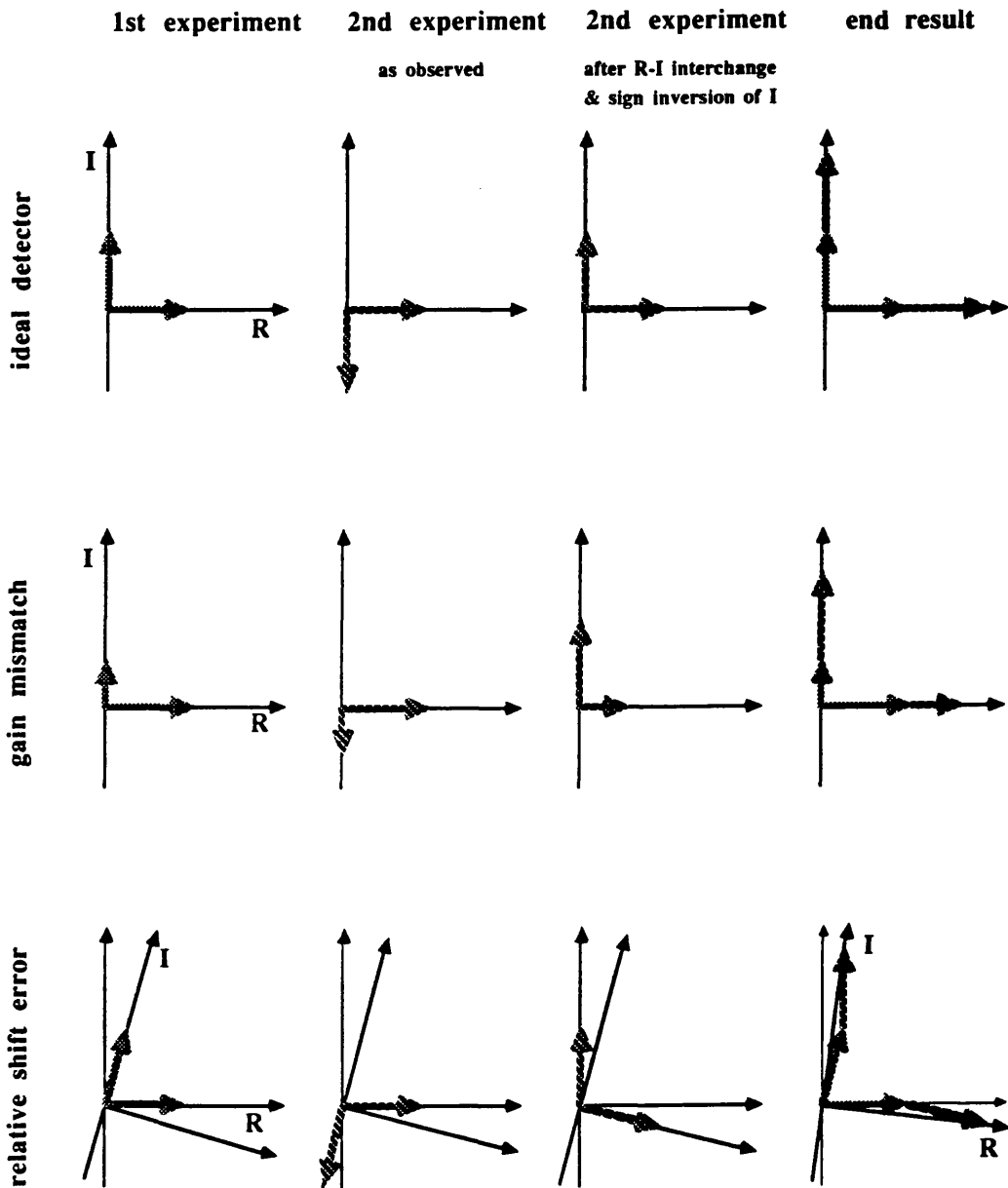


Figure A.2. Graphical representation of cancellation of quadrature errors through a two-step phase cycling procedure. In the second experiment the phase of the refocusing pulse is shifted by 90° . Then, the sign of the imaginary channel is inverted and the real and imaginary channels are interchanged. After signal accumulation, the two channels of the receiver are balanced.

RF pulse imperfections. If the excitation pulse is not exactly 90° , it leaves some residual longitudinal magnetization, which will not be phase encoded. A refocusing pulse that is not exactly 180° , will then excite some of this residual longitudinal magnetization into the transverse plane. As this magnetization has not been phase encoded, it will appear as if it has experienced zero phase encoding gradient, i.e. it will give rise to a streak along the centre of the phase encoding direction. Alteration of the phase of the refocusing pulse by 180° does not affect the phase encoded signal, however, it will invert the phase of the residual magnetization component by 180° . In the end, this residual component would appear to have the maximum possible rate of phase accumulation (i.e. 180° per phase encoding step), therefore it will be interpreted as signal coming from the edges of the field of view in the phase encoding direction. A more rigorous explanation of this artifact and its correction can be found elsewhere [A.2].

APPENDIX 2

LONGITUDINAL MAGNETIZATION AFTER A TRAIN OF β° PULSES

Consider a train of β° pulses applied with a repetition time T , assuming that steady-state-free-precession effects are negligible, i.e. $T_2 \ll T$. Let $M^-(n)$ and $M^+(n)$ be the longitudinal magnetization just before and just after the n th pulse respectively. Then,

$$M^+(n) = M^-(n) \cos(\beta) \quad (\text{A.1})$$

The behaviour of the longitudinal relaxation M_z can be calculated using the Bloch equation:

$$\frac{dM_z}{dt} = -\frac{M_z - M_0}{T_1} \quad (\text{A.2})$$

where M_0 is the thermal equilibrium magnetization. Thus, considering the interval T between the $n-1$ and the n th pulse, Equation (A.2) becomes:

$$\int_{M^+(n-1)}^{M^-(n)} \frac{dM_z}{M_z - M_0} = -\int_0^T \frac{dt}{T_1}$$

Thus,

$$\frac{M_0 - M^-(n)}{M_0 - M^+(n-1)} = \exp(-T/T_1)$$

and substituting from Eqn. (A.1), for $\beta \neq (2k+1)90^\circ$, $\beta = 0, 1, 2, \dots$,

$$M^+(n) = M_0 \cos(\beta) - M_0 \cos(\beta) \exp(-T/T_1) + M^+(n-1) \cos(\beta) \exp(-T/T_1) \quad (\text{A.3})$$

Equation (A.3) describes a recurrence relation, of the type:

$$M^+(n) = A + B M^+(n-1), \quad \text{with first term: } M^+(1) = M_0 \cos(\beta) \quad (\text{A.4})$$

$$\text{where } A = M_0 \cos(\beta) - M_0 \cos(\beta) \exp(-T/T_1) \quad (\text{A.5a})$$

$$B = \cos(\beta) \exp(-T/T_1) \quad (\text{A.5b})$$

The recurrence relation (A.4) can be developed as follows:

$$M^+(1) = M_0 \cos(\beta)$$

$$M^+(2) = A + B M^+(1) = A + B M_0 \cos(\beta)$$

$$\begin{aligned} M^+(3) &= A + B M^+(2) = A + B [A + B M_0 \cos(\beta)] = \\ &= A (1 + B) + B^2 M_0 \cos(\beta) \end{aligned}$$

$$\begin{aligned} M^+(4) &= A + B M^+(3) = A + B [A (1 + B) + B^2 M_0 \cos(\beta)] = \\ &= A (1 + B + B^2) + B^3 M_0 \cos(\beta) \end{aligned}$$

$$\begin{aligned} M^+(5) &= A + B M^+(4) = A + B [A (1 + B + B^2) + B^3 M_0 \cos(\beta)] = \\ &= A (1 + B + B^2 + B^3) + B^4 M_0 \cos(\beta) \end{aligned}$$

and finally

$$\begin{aligned} M^+(n) &= A (1 + B + B^2 + B^3 + \dots + B^{n-2}) + B^{n-1} M_0 \cos(\beta) = \\ &= A \frac{1 - B^{n-1}}{1 - B} + B^{n-1} M_0 \cos(\beta) = \\ &= \frac{A (1 - B^{n-1}) + (B^{n-1} - B^n) M_0 \cos(\beta)}{1 - B} \end{aligned}$$

and considering Eqns. (A.5),

$$M^+(n) = \frac{M_0 \cos(\beta) (1 - e^{-T/T_1}) + M_0 \cos^n(\beta) e^{-n(T/T_1)} (1 - \cos(\beta))}{1 - \cos(\beta) e^{-T/T_1}} \quad (\text{A.6})$$

Given that:

$$\lim_{n \rightarrow \infty} x^n = 0, \quad \forall x \in \mathfrak{R}, |x| < 1,$$

then

$$(a) \quad \lim_{n \rightarrow \infty} e^{-n(T/T_1)} = 0, \quad \text{and}$$

$$(b) \quad \lim_{n \rightarrow \infty} \cos^n(\beta) = 0, \quad \text{if } \beta \neq k 180^\circ \quad k = 0, 1, 2, 3, \dots$$

$$\cos^n(\beta) = 1, \quad \text{if } \beta = (2k) 180^\circ$$

$$\cos^n(\beta) = (-1)^n, \quad \text{if } \beta = (2k+1) 180^\circ$$

Thus $M^+(n)$ converges to a finite limit as $n \rightarrow \infty$, and this is given by:

$$\lim_{n \rightarrow \infty} M^+(n) = M_{ss} = M_0 \cos(\beta) \frac{1 - e^{-T/T_1}}{1 - \cos(\beta) e^{-T/T_1}} \quad (A.7)$$

The fact that for $n \rightarrow \infty$ $M^+(n)$ converges to a finite limit, shows that after infinite pulse repetitions the longitudinal magnetization reaches a steady-state whose value is M_{ss} , as given by Eqn. (A.7). Note that in the case of $\beta=90^\circ$ (or generally, $\beta=(2k+1)90^\circ$, $k=0, 1, 2, \dots$), the longitudinal magnetization just after each pulse in the train is always zero, Eqn. (A.3). (It should be stressed once again that SSFP effects are assumed to negligible.) Therefore the steady-state value is $M_{ss}=0$, and it is reached after the 1st pulse. For any other value of the tip angle β , one can define an approximate steady-state condition which is reached when the difference between the magnetization $M^+(n)$ and the steady-state value M_{ss} , is less than or equal to a predetermined value $\alpha\%$ of M_{ss} , that is, assuming that $\beta \neq (2k+1)90^\circ$,

$$\frac{|M^+(n) - M_{ss}|}{|M_{ss}|} \leq \frac{\alpha}{100}$$

Thus, considering Eqns. (A.6) & (A.7),

$$\frac{|\cos^n(\beta) e^{-n(T/T_1)}| |1 - \cos(\beta)|}{|1 - e^{-T/T_1}| |\cos(\beta)|} \leq \frac{\alpha}{100}$$

and, assuming $\beta \neq (2k)180^\circ$, $k=0, 1, 2, \dots$,

$$|\cos^n(\beta) e^{-n(T/T_1)}| \leq \frac{\alpha}{100} \frac{|1 - e^{-T/T_1}| |\cos(\beta)|}{|1 - \cos(\beta)|}$$

and finally,

$$n \geq \frac{\ln \left[\frac{\alpha}{100} \frac{|1 - e^{-T/T_1}| |\cos(\beta)|}{|1 - \cos(\beta)|} \right]}{\ln \left[\frac{|e^{T/T_1}|}{|\cos(\beta)|} \right]} \quad (A.8)$$

Note that the previous analysis does not hold at the limit where $(T/T_1) \rightarrow 0$, that is, it assumes a finite pulse repetition time greater than zero.

In the specific case of $\beta=180^\circ$, Eqns. (A.6) and (A.7), and inequality (A.8), become respectively:

$$M_{180^\circ}^+(n) = M_0 \frac{e^{-T/T_1} - 1 + 2(-1)^n e^{-n(T/T_1)}}{1 + e^{-T/T_1}} \quad (\text{A.9})$$

$$M_{ss180^\circ} = M_0 \frac{e^{-T/T_1} - 1}{e^{-T/T_1} + 1} \quad (\text{A.10})$$

$$n_{180^\circ} \geq -\frac{T_1}{T} \ln\left[\frac{\alpha}{200} (1 - e^{-T/T_1})\right] \quad (\text{A.11})$$

As this magnetization relaxes, it passes through a null point at time T_I , which can be calculated using the Bloch equation, (A.1). Thus, integrating

$$\int_{M_{ss}}^0 \frac{dM_z}{M_z - M_0} = - \int_0^{T_I} \frac{dt}{T_1}$$

gives:

$$T_I = T_1 \ln 2 - T_1 \ln[1 + e^{-T/T_1}] \quad (\text{A.12})$$

APPENDIX 3

STATISTICAL ANALYSIS

In experimental studies, a common situation involves the validation of a new method for the measurement of a physical property by applying it to a population already studied by another standard procedure. In making such a comparison, the principal interest is to show that the experimental measurements as obtained by the new method are not significantly different from those derived by the established procedure. When a standard method, X, and a new one, Y, are applied on a population of N members, producing N pairs of measurements (x_i, y_i) , a common comparison involves a two-step statistical procedure [A.5, A.6]:

- (i) Firstly, the degree of linear correlation between the quantities x and y has to be established, in other words one must determine how well the experimental points fit a straight line. This is determined by the linear correlation coefficient, r.
- (ii) Subsequently, the experimental points have to ^{be} fitted onto the regression line of y on x, which is then compared to the desired identity line corresponding to the ideal case when $x_i = y_i$. This comparison involves calculating the slope and the intercept of the regression line.

The linear correlation coefficient is given by:

$$r = \frac{N \sum_i (x_i y_i) - \sum_i x_i \sum_i y_i}{\sqrt{N \sum_i (x_i)^2 - (\sum_i x_i)^2} \sqrt{N \sum_i (y_i)^2 - (\sum_i y_i)^2}}$$

where x_i and y_i are the values of the property for the i th member of the population of N members as measured by method X and Y, respectively. The correlation coefficient can take values in the range $-1 \leq r \leq +1$. A coefficient of +1 indicates a perfect correlation, that is, the experimental points lie exactly on a straight line with positive slope, while a coefficient of zero indicates complete lack of linear correlation.

To determine whether a value of r is of sufficient magnitude to indicate correlation or is simply a chance deviation from zero, the null hypothesis is used, stating that the population coefficient is zero. For a small number of pairs ($N < 30$), the t-test is applied with $N-2$ degrees of freedom, and the t-value is then given by:

$$t = |r| \sqrt{\frac{N-2}{1-r^2}}$$

The critical t-values for preset significance levels can be obtained by published tables, e.g. [A.5, A.6]. If the calculated t-value is greater than the tabulated critical t-value at the desired significance level, then the null hypothesis can be rejected. As the direction of difference between the calculated correlation coefficient and 0 is important, a one-sided test should be employed.

Once a linear correlation is established, the least squares method can be used to fit the experimental points into the "best" straight line [A.5, A.6]. The slope, β , and the intercept, α , of this line are then given by:

$$\beta = \frac{N \sum_i (x_i y_i) - \sum_i x_i \sum_i y_i}{N \sum_i (x_i)^2 - (\sum_i x_i)^2}$$

and

$$\alpha = \frac{\sum_i y_i - \beta \sum_i x_i}{N}$$

A measure of the extent to which the y values estimated from the line deviate from those actually observed is given by the standard error of estimate, s_{yx} :

$$s_{yx} = \sqrt{\frac{L_{xx} L_{yy} - (L_{xy})^2}{(N-2) N L_{xx}}}$$

where

$$L_{xx} = N \sum_i (x_i)^2 - (\sum_i x_i)^2$$

$$L_{yy} = N \sum_i (y_i)^2 - (\sum_i y_i)^2$$

and

$$L_{xy} = N \sum_i (x_i y_i) - \left(\sum_i x_i \right)^2 \left(\sum_i y_i \right)^2$$

If \bar{x} is the arithmetic mean of the x-values, the standard deviations for the slope, s_β , and the intercept, s_α , can then be calculated by:

$$s_\beta = \frac{S_{xy}}{\sqrt{\sum_i (x_i - \bar{x})^2}}$$

and

$$s_\alpha = S_{xy} \frac{\sqrt{\sum_i (x_i)^2}}{\sqrt{N \sum_i (x_i - \bar{x})^2}}$$

These values of s_β and s_α are used to estimate the confidence limits for the slope and the intercept, which are given by:

$$\beta \pm t_p s_\beta \quad \text{and} \quad \alpha \pm t_p s_\alpha$$

where t_p is the t-value at the desired confidence level p , for $(N-2)$ degrees of freedom. As the direction of distribution for the values of the slope and the intercept of the regression line is of no concern, a two-sided t-distribution is assumed.

It is apparent that if each measurement yields an identical result with both methods the regression line will have a zero intercept, and a slope and a correlation coefficient of 1. A line with a slope significantly different from 1 indicates the presence of systematic errors, while a non-zero intercept shows that one of the methods gives results higher or lower than the other. The case of the correlation coefficient being significantly different from 1, even though the slope and the intercept are close to their ideal values, suggests very poor precision for either one or both of the experimental methods. It should be mentioned that the above analysis is strictly valid under the assumption that the x-direction errors are zero, while the error in the y-values is constant.

REFERENCES

CHAPTER 1

- 1.1. F. Bloch, W.W. Hansen, and M. Packard, "Nuclear Induction", *Phys. Rev.*, vol. 69, 127, 1946.
- 1.2. E.M. Purcell, H.C. Torrey, and R.V. Pound, "Resonance Absorption by Nuclear Magnetic Moments in a Solid", *Phys. Rev.*, vol. 69, 37-38, 1946.
- 1.3. N. Bloembergen, E.M. Purcell, and R.V. Pound, "Relaxation Effects in Nuclear Magnetic Resonance Absorption", *Phys. Rev.*, vol. 73, 679-712, 1948.
- 1.4. D. Pines, and C.P. Slichter, "Relaxation Times in Magnetic Resonance", *Phys. Rev.*, vol. 100, 1014-1020, 1955.
- 1.5. A. G. Redfield, "On the Theory of Relaxation Processes", *IBM J.*, vol. 1, 19-31, 1957.
- 1.6. G.E. Pake, "Nuclear Resonance Absorption in Hydrated Crystals: Fine Structure of the Proton Line", *J. Chem. Phys.*, vol. 16, 327-336, 1948.
- 1.7. W.G. Proctor, and F.C. Yu, "The Dependence of a Nuclear Magnetic Resonance Frequency upon Chemical Compound", *Phys. Rev.*, vol. 77, 717, 1950.
- 1.8. W.G. Dickinson, "Dependence of the F-19 Nuclear Magnetic Resonance Position on Chemical Compound", *Phys. Rev.*, vol. 77, 736-737, 1950.
- 1.9. E. L. Hahn, "Spin Echoes", *Phys. Rev.*, vol. 80, 580-594, 1950.
- 1.10. R.R. Ernst, and W.A. Anderson, "Application of Fourier Transform Spectroscopy to Magnetic Resonance", *Rev. Scient. Instr.*, vol. 37, 93-102, 1966.
- 1.11. J. Jeener, International Ampere Summer School, Basko Polje, Yugoslavia, 1971. (unpublished).
- 1.12. G. P. Collins, "Nobel Chemistry Prize Recognizes the Importance of Ernst's NMR Work", *Physics Today*, vol. 44, no. 12, 19-21, 1991.
- 1.13. P.C. Lauterbur, "Image Formation by Induced Local Interactions: Examples Employing Nuclear Magnetic Resonance", *Nature*, vol. 242, 190-191, 1973.
- 1.14. P. Mansfield, P.K. Grannel, "NMR Diffraction in Solids?", *J. Phys. C. Solid State Phys.*, vol. 6, L422-L426, 1973.
- 1.15. P.T. Callaghan, "Principles of Nuclear Magnetic Resonance Microscopy", Clarendon Press, 1991.

- 1.16. E.J. Potchen, E.M. Haacke, J.E. Siebert, and A. Gottschalk, "Magnetic Resonance Angiography. Concepts and Applications", Mosby Year Book Inc., 1993.
- 1.17. J.W. Belliveau, D.N. Kennedy, R.C. McKinstry, B.R. Buchbinder, R.M. Weisskoff, M.S. Cohen, J.M. Vevea, T.J. Brady, and B.R. Rosen, "Functional Imaging of the Human Visual Cortex by Magnetic Resonance Imaging", *Science*, vol. 254, 716-719, 1991.
- 1.18. S.C.R. Williams, "Nuclear Magnetic Resonance Imaging", *Nuclear Magn. Reson.*, vol. 21, 415-454, 1992.
- 1.19. E. Kaldoudi, and S.C.R. Williams, "Fat and Water Differentiation by Nuclear Magnetic Resonance Imaging", *Concepts Magn. Reson.*, vol. 4, 53-71, 1992.
- 1.20. E. Kaldoudi, and S.C.R. Williams, "Chart: Fat and Water Differentiation by Nuclear Magnetic Resonance Imaging", *Concepts Magn. Reson.*, vol. 4, 162-165, 1992.
- 1.21. E. Kaldoudi, S.C.R. Williams, G.J. Barker, and P.S. Tofts, "A Chemical Shift Selective Inversion Recovery Sequence for Fat-Suppressed MRI: Theory and Experimental Validation", *Magn. Reson. Imaging*, vol. 11, 341-355, 1993.
- 1.22. E. Kaldoudi, S.C.R. Williams, G.J. Barker, and P.S. Tofts, "A Modified IR Sequence for Multi-Slice Fluid Attenuated MRI", *Abstr. 12th SMRM*, vol. 3, 1231, 1993.
- 1.23. E. Kaldoudi, S.C.R. Williams, G.J. Barker, and P.S. Tofts, "Fat Suppression in MRI: Comparison of a Robust, Hybrid Method with Conventional Techniques", *Br. J. Radiology*, vol. 66, 957, 1993.
- 1.24. E. Kaldoudi, and S.C.R. Williams, "Relaxation Time Measurements in NMR Imaging. Part I: Longitudinal Relaxation Time", *Concepts Magn. Reson.*, vol. 5, 217-242, 1993.

CHAPTER 2

- 2.1. P.A.M. Dirac, "The Principles of Quantum Mechanics", Clarendon Press, 1930, 4th ed. 1958.
- 2.2. [S. Trachanas, "Quantum Mechanics", Creta University Press, Greece, 1985.]
- 2.3. A. Abragam, "Principles of Nuclear Magnetism", Clarendon Press, 1961.
- 2.4. R.R. Ernst, G. Bodenhausen, and A. Wokaun, "Principles of Nuclear Magnetic Resonance in One and Two Dimensions", Clarendon Press, 1987.
- 2.5. M. Goldman, "Quantum Description of High-Resolution NMR in Liquids", Clarendon Press, 1988.

- 2.6. C.P. Slichter, "Principles of Magnetic Resonance", Springer-Verlag, 1978, 3rd ed. 1990.
- 2.7. R.K. Harris, "Nuclear Magnetic Resonance Spectroscopy", Longman Scientific & Technical, 1983.
- 2.8. J.W. Hennel, and J. Klinowski, "Fundamentals of Nuclear Magnetic Resonance", Longman Scientific & Technical, 1993.
- 2.9. P.G. Morris, "Nuclear Magnetic Resonance Imaging in Medicine and Biology", Clarendon Press, 1986.
- 2.10. P.T. Callaghan, "Principles of Nuclear Magnetic Resonance Microscopy", Clarendon Press, 1991.
- 2.11. C.-N. Chen, and D.I. Hoult, "Biomedical Magnetic Resonance Technology", Adam Hilger, 1989.
- 2.12. R.N. Bracewell, "The Fourier Transform and its Applications", McGraw-Hill, 1965, 2nd ed. 1986.
- 2.13. A.G. Marshall, and F.R. Verdun, "Fourier Transforms in NMR, Optical, and Mass Spectrometry", Elsevier, 1990.
- 2.14. R.H.T. Bates, and M.J. McDonnell, "Image Restoration and Reconstruction", Clarendon Press, 1986.
- 2.15. M.R. Spiegel, "Schaum's Outline Series: Schaum's Outline of Theory and Problems of Advanced Calculus", McGraw-Hill, 1963.
- 2.16. A. Jeffrey, "Mathematics for Engineers and Scientists", Van Nostrand Reinhold, 1969, 4th ed. 1989.
- 2.17. N. Zumbuladis, "Whence Spin?", Concepts Magn. Reson., vol. 3, 89-107, 1991.
- 2.18. D.I. Hoult, "The Magnetic Resonance Myth of Radio Waves", Concepts Magn. Reson., vol. 1, 1-5, 1989.
- 2.19. D.C. Look, and I.J. Lowe, "Nuclear Magnetic Dipole-Dipole Relaxation along the Static and Rotating Magnetic Field: Application to Gypsum", J. Chem. Phys., vol. 44, 2995-3000, 1966.
- 2.20. E.L. Hahn, "Spin Echoes", Phys. Rev., vol. 80, 580-594, 1950.
- 2.21. A. Abragam, and B. Bleaney, "Electron Paramagnetic Resonance of Transition Ions", Oxford University Press, 1970.
- 2.22. U. Fano, "Description of States in Quantum Mechanics by Density Matrix and Operator Techniques", Rev. Modern Phys., vol. 29, 74-93, 1957.
- 2.23. M.D. Harpen, "The Density Matrix Formalism of Nuclear Relaxation: A Review", Med. Phys., vol. 15, 538-550, 1988.

- 2.24. O.W. Sorensen, G.W. Eich, M.H. Levitt, G. Bodenhausen, and R.R. Ernst, "Product Operator Formalism for the Description of NMR Pulse Experiments", *Progr. NMR Spectr.*, vol. 16, 163-192, 1983.
- 2.25. R. Freeman, "A Handbook of Nuclear Magnetic Resonance", Longman Scientific & Technical, 1987.
- 2.26. F. Bloch, "Dynamic Theory of Nuclear Induction", *Phys. Rev.*, vol. 102, 104-135, 1956.
- 2.27. D.I. Hoult, "The NMR Receiver: A Description and Analysis of Design", *Progress NMR Spectr.*, vol. 12, 41-77, 1978.
- 2.28. D.D. Traficante, "Phase-Sensitive Detection. Part II: Quadrature Phase Detection", *Concepts Magn. Reson.*, vol. 2, 181-195, 1990.
- 2.29. J.W. Cooley, and J.W. Tukey, "An Algorithm for the Machine Calculation of Complex Fourier Series", *Math. Comput.*, vol. 19, 297-301, 1965.
- 2.30. G.D. Bergland, "A Fast Fourier Transform Algorithm for Real-Valued Series", *Commun. A. C. M.*, vol. 11, 703-710, 1968.
- 2.31. E. Fukushima, and S.B.W. Roeder, "Experimental Pulse NMR. A Nuts and Bolts Approach", Addison-Wesley, 1981.
- 2.32. D.D. Traficante, "Phase-Sensitive Detection. Part I: Phase, Gates, Phase-Sensitive Detectors, Mixers, and the Rotating Frame", *Concepts Magn. Reson.*, vol. 2, 151-167, 1990.
- 2.33. H.Y. Carr, and E.M. Purcell, "Effects of Diffusion on Free Precession in Nuclear Magnetic Resonance Experiments", *Phys. Rev.*, vol. 94, 630-638, 1954.
- 2.34. S. Meiboom, and D. Gill, "Modified Spin-Echo Method for Measuring Nuclear Relaxation Times", *Rev. Sci. Instrum.*, vol. 29, 688-691, 1958.
- 2.35. E.L. Hahn, and D.E. Maxwell, "Spin Echo Measurements of Nuclear Spin Coupling in Molecules", *Phys. Rev.*, vol. 88, 1070-1084, 1952.
- 2.36. W.A. Edelstein, J.M.S. Hutchison, G. Johnson, and T. Redpath, "Spin Warp NMR Imaging and Applications to Human Whole-Body Imaging", *Phys. Med. Biol.*, vol. 25, 751-756, 1980.
- 2.37. E.M. Haacke, "The Effects of Finite Sampling in Spin-Echo or Field-Echo Magnetic Resonance Imaging", *Magn. Reson. Med.*, vol. 4, 407-421, 1987.
- 2.38. E.M. Haacke, Z.-P. Liang, and J.A. Tkach, "T₂ Deconvolution in MR Imaging and NMR Spectroscopy", *J. Magn. Reson.*, vol. 76, 440-457, 1988.
- 2.39. R. Gabillard, "A Steady State Transient Technique in Nuclear Magnetic Resonance", *Phys. Rev.*, vol. 85, 694-695, 1952.
- 2.40. P.C. Lauterbur, "Image Formation by Induced Local Interactions: Examples Employing Magnetic Resonance", *Nature*, vol. 242, 190-191, 1973.

- 2.41. P. Mansfield, and P.K. Grannel, "NMR 'Diffraction' in Solids?", *J. Phys. C: Solid State Phys.*, vol. 6, L422-L426, 1973.
- 2.42. R. Damadian, M. Goldsmith, and L. Minkoff, "NMR in Cancer: XVI. FONAR Image of the Live Human Body", *Physiol. Chem. Phys.*, vol. 9, 97-100, 1977.
- 2.43. P. Mansfield, and P.K. Grannel, "Diffraction and Microscopy in Solids and Liquids by NMR", *Phys. Rev. (Solid State)*, vol. 12, 3618-3634, 1975.
- 2.44. D.B. Twieg, "The k-Trajectory Formulation of the NMR Imaging Process with Applications in Analysis and Synthesis of Imaging Methods", *Med. Phys.*, vol. 10, 610-621, 1983.
- 2.45. S. Ljunggren, "A Simple Graphical Representation of Fourier-Based Imaging Methods", *J. Magn. Reson.*, vol. 54, 338-343, 1983.
- 2.46. D.B. Twieg, J. Katz, and R.M. Peshock, "A General Treatment of NMR Imaging with Chemical Shifts and Motion", *Magn. Reson. Med.*, vol. 5, 32-46, 1987.
- 2.47. P. Mansfield, "Imaging by Nuclear Magnetic Resonance", *J. Phys. E: Sci. Instrum.*, vol. 21, 18-30, 1988.
- 2.48. F.W. Wehrli, "Fast-Scan Magnetic Resonance: Principles and Applications" *Magn. Reson. Quart.*, vol. 6, 165-236, 1990.
- 2.49. H.R. Brooker, and W.S. Hinshaw, "Thin-Section NMR Imaging", *J. Magn. Reson.*, vol. 30, 129-131, 1978.
- 2.50. A.N. Garroway, P.K. Grannell, and P. Mansfield, "Image Formation in NMR by a Selective Irradiative Process", *J. Phys. C., Solid State Phys.*, vol 7, L457-L462, 1974.
- 2.51. R.J. Sutherland, and J.M.S. Hutchison, "Three-Dimensional NMR Imaging Using Selective Excitation", *J. Phys. E: Sci. Instrum.*, vol. 11, 79-83, 1978.
- 2.52. R.A. Brooks, and G. Di Chiro, "Principles of Computer Assisted Tomography (CAT) in Radiographic and Radioisotopic Imaging", *Phys. Med. Biol.*, vol. 21, 689-732, 1976.
- 2.53. A. Kumar, D. Welti, and R.R. Ernst, "NMR Fourier Zeugmatography", *J. Magn. Reson.*, vol. 18, 69-83, 1975.
- 2.54. J. Frahm, K.D. Merboldt, W. Hanicke, and A. Haase, "Stimulated Echo Imaging", *J. Magn. Reson.*, vol. 64, 81-93, 1985.
- 2.55. W. Sattin, T.H. Mareci, and K.N. Scott, "Exploiting the Stimulated Echo in Nuclear Magnetic Resonance Imaging. I. Method", *J. Magn. Reson.*, vol. 64, 177-182, 1985.
- 2.56. H.Y. Carr, "Steady-State Free Precession in Nuclear Magnetic Resonance", *Phys. Rev.*, vol. 112, 1693-1701, 1958.

- 2.57. S. Patz, "Steady-State Free Precession: An Overview of Basic Concepts and Applications", *Adv. Magn. Reson. Imaging*, vol. 1, 73-102, 1989.
- 2.58. A. Haase, J. Frahm, D. Matthaei, W. Hanicke, and K.-D. Merboldt, "FLASH Imaging: Rapid NMR Imaging Using Low Flip-Angle Pulses", *J. Magn. Reson.*, vol. 67, 258-266, 1986.
- 2.59. J. Hennig, A. Nauerth, and H. Friedburg, "RARE Imaging: A Fast Imaging Method for Clinical MR", *Magn. Reson. Med.*, vol. 3, 823-833, 1986.
- 2.60. P. Mansfield, "Multi-Planar Image Formation Using NMR Spin Echoes", *J. Phys. C, Solid State Phys.*, vol. 10, L55-L58, 1977.
- 2.61. A.M. Houseman, M.K. Stehling, B. Chapman, R. Coxon, R. Turner, R.J. Ordidge, M.G. Cawley, P. Glover, P. Mansfield, and R.E. Coupland, "Improvements in Snapshot NMR Imaging", *Br. J. Radiol.*, vol. 61, 822-828, 1988.
- 2.62. E.R. McVeigh, R.M. Henkelman, and M.J. Bronskill, "Noise and Filtration in Magnetic Resonance Imaging", *Med. Phys.*, vol. 12, 586-591, 1985.
- 2.63. H.D.W. Hill, and R.E. Richards, "Limits of Measurement in Magnetic Resonance", *J. Phys. E: J. Sci. Instr.*, vol. 1, 977-983, 1968.
- 2.64. D.I. Hoult, and R.E. Richards, "The Signal-to-Noise Ratio of the Nuclear Magnetic Resonance Experiment", *J. Magn. Reson.*, vol. 24, 71-85, 1976.
- 2.65. D.I. Hoult, and P.C. Lauterbur, "The Sensitivity of the Zeugmatographic Experiment Involving Human Samples", *J. Magn. Reson.*, vol. 34, 425-433, 1979.
- 2.66. W.A. Edelstein, G.H. Glover, C.J. Hardy, and R.W. Redington, "The Intrinsic Signal-to-Noise Ratio in NMR Imaging", *Magn. Reson. Med.*, vol. 3, 604-618, 1986.
- 2.67. D.D. Traficante, "Time Averaging. Does the Noise Really Average Toward Zero?", *Concepts Magn. Reson.*, vol. 3, 83-87, 1991.
- 2.68. J.C. Miller, and J.N. Miller, "Statistics for Analytical Chemistry", Ellis Horwood Ltd., 1988.
- 2.69. W.A. Edelstein, P.A. Bottomley, and L.M. Pfeifer, "A Signal-to-Noise Calibration Procedure for NMR Imaging Systems", *Med. Phys.*, vol. 11, 180-185, 1984.
- 2.70. R.M. Henkelman, "Measurement of Signal Intensities in the Presence of Noise in MR Images", *Med. Phys.*, vol. 12, 232-233, 1985. Erratum: *Med. Phys.*, vol. 13, 544, 1986.
- 2.71. P.S. Tofts, and G. Johnson, "Correction for Rayleigh Noise in an NMR Magnitude Image when Measuring T₂ at Low Values of Signal to Noise Ratio", *Abstr. 5th SMRM*, 1450-1451, 1986.

CHAPTER 3

- 3.1. M. A. Horsfield, "Nuclear Magnetic Resonance in Petroleum Engineering", Ph.D. Thesis, University of Cambridge, 1989.
- 3.2. P. G. Morris, "Nuclear Magnetic Resonance Imaging in Medicine and Biology", Clarendon Press, 1986.
- 3.3. R.O. Scow, and S.S. Chernick, "Mobilization, Transport and Utilization of Free Acids", in: M. Florkin, and E.H. Stotz (eds.), "Comprehensive Biochemistry, Vol. 18, Lipid Metabolism", Elsevier Publishing Company, pages 19-49, 1970.
- 3.4. M. K. Campbell, "Biochemistry", Saunders College Publishing, 1991.
- 3.5. G.C. Hill, and J.S. Holman, "Chemistry in Context", Nelson, 1978.
- 3.6. E.B. Cady, "Clinical Magnetic Resonance Spectroscopy", Plenum Press, 1990.
- 3.7. R.J. Abraham, and P. Loftus, "Proton and Carbon-13 NMR Spectroscopy. An Integrated Approach", Heyden, 1978.
- 3.8. P.A. Bottomley, T.H. Foster, R.E. Argersinger, and L.M. Pfeifer, "A Review of Normal Tissue Hydrogen NMR Relaxation Time and Relaxation Mechanisms from 1-100 MHz: Dependence on Tissue Type, NMR Frequency, Temperature, Species, Excision, and Age", *Med. Phys.*, vol. 11, 425-448, 1984.
- 3.9. P.C. Lauterbur, D.M. Kramer, W.V. House, and C.-N. Chen, "Zeugmatographic High Resolution Nuclear Magnetic Resonance Spectroscopy: Images of Chemical Inhomogeneity within Macroscopic Objects", *J. Am. Chem. Soc.*, vol. 97, 6866-6868, 1975.
- 3.10. S.J. Cox, and P. Styles, "Towards Biomedical Imaging", *J. Magn. Reson.*, vol. 40, 209-212, 1980.
- 3.11. B.R. Rosen, I.L. Pykett, T.J. Brady, E. Carter, A. Ratner, and J. Wands, "NMR Proton Chemical Shift Imaging of the Experimentally Induced Fatty Liver Disease: Enhanced Sensitivity over Conventional NMR Imaging", *Magn. Reson. Med.*, vol. 1, 238-239, 1984.
- 3.12. J.S. Kriegshausler, P.R. Julsrud, and J.T. Lund, "MR Imaging of Fat in and around the Heart", *Am. J. Roentgenol.*, vol. 155, 271-274, 1990.
- 3.13. S.G. Moore, and K.L. Dawson, "Red and Yellow Marrow in the Femur: Age Related Changes in Appearance at MR Imaging", *Radiology*, vol. 175, 219-223, 1990.
- 3.14. S.K. Stevens, S.G. Moore, and M.D. Amylon, "Repopulation of Marrow after Transplantation: MR Imaging with Pathologic Correlation", *Radiology*, vol. 175, 213-218, 1990.

- 3.15. S.K. Stevens, S.G. Moore, and I.D. Kaplan, "Early and Late Bone-Marrow Changes after Irradiation: MR Evaluation", *Am. J. Roentgenol.*, vol. 154, 745-750, 1990.
- 3.16. A. Leroy-Willig, J. Bittoun, J.P. Luton, A. Louvel, J.E. Lefevre, A. Bonnin, and J.C. Roucayrol, "In Vivo MR Spectroscopic Imaging of the Adrenal Glands: Distinction between Adenomas and Carcinomas Larger than 15 mm Based on Lipid Content", *Am. J. Roentgenol.*, vol. 153, 771-773, 1989.
- 3.17. C.P. Hawkins, S.C.R. Williams, G.J. Barker, B. Youl, T. Revesz, J. Newcombe, A. Brar, D.G. MacManus, E.P.G.H. du Boulay, and W.I. McDonald, "Lipid Imaging to Detect Myelin Breakdown in Multiple Sclerosis", *Neuroradiol.*, vol. 33(suppl.), 404-405, 1991.
- 3.18. H.E. Deans, F.W. Smith, D.J. Lloyd, A.N. Law, and H.W. Sutherland, "Fetal Fat Measurement by Magnetic Resonance Imaging", *Br. J. Radiol.*, vol. 62, 603-607, 1989.
- 3.19. C.-N. Chen, and D.I. Hoult, "Biomedical Magnetic Resonance Technology", IOP Publishing Ltd, 1989.
- 3.20. M.A. Foster, J.M.S. Hutchison, J.R. Mallard, and M. Fuller, "Nuclear Magnetic Resonance Pulse Sequence and Discrimination of High- and Low-Fat Tissues", *Magn. Reson. Imaging.*, vol. 2, 187-192, 1984.
- 3.21. J. Hennig, A. Nauerth, and H. Friedburg, "RARE: A Fast Imaging Method for Clinical MR", *Magn. Reson. Med.*, vol. 3, 823-833, 1986.
- 3.22. R.T. Constable, A.W. Anderson, J. Zhong, and J.C. Gore, "Mechanisms Influencing Contrast in FSE MR Imaging", *Abstr. 11th SMRM*, vol. 1, 436, 1992.
- 3.23. G.A. Wright, and A. Macovski, "Lipid Signal Enhancement in Spin-Echo Trains", *Abstr. 11th SMRM*, vol.1, 437, 1992.
- 3.24. R.S. Hinks, and D. Martin, "Bright Fat, Fast Spin Echo, and CPMG", *Abstr. 11th SMRM*, vol. 2, 4503, 1992.
- 3.25. E.E. Babcock, L. Brateman, J.C. Weinreb, S.D. Horner, and R.L. Nunnally, "Edge Artifacts in MR Images: Chemical Shift Effect", *J. Comput. Assist. Tomogr.*, vol. 9, 252-257, 1985.
- 3.26. D.B. Twieg, J. Katz, and R.M. Peshock, "A General Treatment of NMR Imaging with Chemical Shifts and Motion", *Magn. Reson. Med.*, vol. 5, 32-46, 1987.
- 3.27. F.W. Wehrli, T.G. Perkins, A. Shimakawa, and F. Roberts, "Chemical Shift-Induced Amplitude Modulations in Images Obtained with Gradient Refocusing", *Magn. Reson. Imaging*, vol. 5, 157-158, 1987.

- 3.28. F.W. Wehrli, "Fast-Scan Magnetic Resonance: Principles and Applications", *Magn. Reson. Quart.*, vol. 6, 165-236, 1990.
- 3.29. A.T. Watanabe, G.P. Teitelbaum, R.B. Lufkin, J.S. Tsuruda, J.R. Jenkins, and W.G. Bradley, "Gradient-Echo MR Imaging of the Lumbar Spine: Comparison with Spin Echo Technique", *J. Comput. Assist. Tomogr.*, vol. 14, 410-414, 1990.
- 3.30. L.D. Hall, and S.L. Talagala, "Slice Selection in the Presence of Chemically Shifted Species", *J. Magn. Reson.*, vol. 71, 180-186, 1987.
- 3.31. R.H. Wachsberg, D.G. Mitchell, M.D. Rifkin, S. Vinitzki, and T.A. Tasciyan, "Chemical Shift Artifact Along the Slice-Select Axis", *Abst. SMRM 10th Meeting*, vol. 2, 895, 1991.
- 3.32. G.M. Bydder, and I.R. Young, "MR Imaging: Clinical Use of the Inversion Recovery Sequence", *J. Comput. Assist. Tomogr.*, vol. 9, 659-675, 1985.
- 3.33. H.W. Park, M.H. Cho, and Z.H. Cho, "Time-Multiplexed Multislice Inversion-Recovery Techniques for NMR Imaging", *Magn. Reson. Med.*, vol. 2, 534-539, 1985.
- 3.34. J.V. Hajnal, B. de Coene, P.D. Lewis, C.J. Baudouin, F.M. Cowan, J.M. Pennock, I.R. Young, and G.M. Bydder, "High Signal Regions in Normal White Matter Shown by Heavily T₂-Weighted CSF Nulled IR Sequences", *J. Comput. Assist. Tomogr.*, vol. 16, 506-513, 1992.
- 3.35. B. de Coene, J. V. Hajnal, P. Gatehouse, D.B. Longmore, S.J. White, A. Oatridge, J.M. Pennock, I.R. Young, and G.M. Bydder, "MR of the Brain Using Fluid-Attenuated Inversion Recovery (FLAIR) Pulse Sequences", *AJNR*, vol. 13, 1555-1564, 1992.
- 3.36. C.H. Oh, S.K. Hilal, I.K. Mun, and Z.H. Cho, "An Optimized Multislice Acquisition Sequence for the Inversion-Recovery MR Imaging", *Magn. Reson. Imaging*, vol. 9, 903-908, 1991.
- 3.37. J.L. Fleckenstein, B.T. Archer, B.A. Barker, J.T. Vaughan, R.W. Parkey, and R.M. Peshock, "Fast Short-Tau Inversion Recovery MR Imaging", *Radiology*, vol. 179, 499-504, 1991.
- 3.38. C.J.G. Bakker, T.D. Witkamp, and W.M. Janssen, "Short TI Short TR Inversion Recovery Imaging Using Reduced Flip Angles", *Magn. Reson. Imaging*, vol. 9, 323-330, 1991.
- 3.39. G. Johnson, D.H. Miller, D. MacManus, P.S. Tofts, D. Barnes, E.P.G.H. du Boulay, and W.I. McDonald, "STIR Sequences in NMR Imaging of the Optic Nerve", *Neuroradiol.*, vol. 29, 238-245, 1987.

- 3.40. K. Gersonde, T. Tolxdorff, and L. Felsberg, "Identification and Characterization of Tissues by T₂-Selective Whole-Body Proton NMR Imaging", *Magn. Reson. Med.*, vol. 2, 390-401, 1985.
- 3.41. J. Mao, H. Yan, W.W. Brey, W.D. Bidgood Jr., J.J. Steinbach, and A. Mancuso, "Fat Tissue and Fat Suppression", *Magn. Reson. Imaging*, vol. 11, 385-393, 1993.
- 3.42. L.D. Hall, S. Sukumar, and S.L. Talagala, "Chemical-Shift-Resolved Tomography Using Frequency-Selective Excitation and Suppression of Specific Resonances", *J. Magn. Reson.*, vol. 56, 275-278, 1984.
- 3.43. P.M. Joseph, "A Spin Echo Chemical Shift Imaging Technique", *J. Comput. Assist. Tomogr.*, vol. 9, 651-658, 1985.
- 3.44. J.A.B. Lohman, R.J. Ordidge, and A. Connelly, "Spin Echo Imaging of Multiple Chemical Shifts", *Magn. Reson. Med.*, vol. 5, 83-86, 1987.
- 3.45. B.R. Rosen, V.J. Wedeen, and T.J. Brady, "Selective Saturation NMR Imaging", *J. Comput. Assist. Tomogr.*, vol. 8, 813-818, 1984.
- 3.46. A. Haase, J. Frahm, W. Hanicke, and D. Matthaei, "H-1 NMR Chemical Shift Selective (CHESS) Imaging", *Phys. Med. Biol.*, vol. 30, 341-344, 1985.
- 3.47. P.J. Keller, W.W. Hunter, and P. Schmalbrock, "Multisection Fat-Water Imaging with Chemical Shift Selective Presaturation", *Radiology*, vol. 164, 539-541, 1987.
- 3.48. E.L. Hahn, "Spin Echoes", *Phys. Rev.*, vol. 80, 580-594, 1950.
- 3.49. A. Haase, and J. Frahm, "Multiple Chemical-Shift-Selective NMR Imaging Using Stimulated Echoes", *J. Magn. Reson.*, vol. 64, 94-102, 1985.
- 3.50. R.J. Sutherland, and J.M.S. Hutchison, "Three-Dimensional NMR Imaging Using Selective Excitation", *J. Phys. E: Sci. Instrum.*, vol. 11, 79-83, 1978.
- 3.51. S. Alexander, "Spin-Echo Method for Measuring Relaxation Times in Two-Line NMR Spectra", *Rev. Sci. Instr.*, vol. 32, 1066-1067, 1961.
- 3.52. P. Mansfield, A.A. Maudsley, and T. Baines, "Fast Scan Proton Density Imaging", *J. Phys. E: Sci. Instrum.*, vol. 9, 271-278, 1976.
- 3.53. J. Mao, W.D. Bidgood Jr., P.G.P. Ang, A. Mancuso, and H. Yan, "A Clinically Viable Technique of Fat Suppression for Abdomen and Pelvis", *Magn. Reson. Med.*, vol. 21, 320-326, 1991.
- 3.54. J. Mao, H. Yan, and W.D. Bidgood Jr., "Fat Suppression with an Improved Selective Presaturation Pulse", *Magn. Reson. Imaging*, vol. 10, 49-53, 1992.
- 3.55. P.J. Hore, "A New Method for Water Suppression in the Proton NMR Spectra of Aqueous Solutions", *J. Magn. Reson.*, vol. 54, 539-542, 1983.
- 3.56. J.F. Martin, and C.G. Wade, "Chemical-Shift Encoding in NMR Images", *J. Magn. Reson.*, vol. 61, 153-157, 1985.

- 3.57. C.L. Dumoulin, "A Method for Chemical-Shift -Selective Imaging", *Magn. Reson. Med.*, vol. 2, 583-585, 1985.
- 3.58. W.T. Dixon, "Simple Proton Spectroscopic Imaging", *Radiology*, vol. 153, 189-194, 1984.
- 3.59. D.D. Blatter, A.H. Morris, D.C. Ailion, A.G. Cutillo, and T.A. Case, "Asymmetric Spin Echo Sequences. A Simple New Method for Obtaining NMR H-1 Spectral Images", *Invest. Radiology*, vol. 20, 845-853, 1985.
- 3.60. H.N. Yeung, and D.W. Kormos, "Separation of True Fat and Water Images by Correcting Magnetic Field Inhomogeneity in Situ", *Radiology*, vol. 159, 783-786, 1986.
- 3.61. G.H. Glover, and E. Schneider, "Three-Point Dixon Technique for True Water/Fat Decomposition with B₀ Inhomogeneity Correction", *Magn. Reson. Med.*, vol. 18, 371-383, 1991.
- 3.62. J.A. Borrello, T.L. Chenevert, C.R. Meyer, A.M. Aisen, and G.M. Glazer, "Chemical Shift-Based True Water and Fat Images: Regional Phase Correction of Modified Spin-Echo MR Images", *Radiology*, vol. 164, 531-537, 1987.
- 3.63. S.C.R. Williams, M.A. Horsfield, and L.D. Hall, "True Water and Fat MR Imaging with Use of Multiple-Echo Acquisition", *Radiology*, vol. 173, 249-253, 1989.
- 3.64. A.G. Webb, and L.D. Hall, "A General Formalism for the Manipulation of Multiple-Echo Data Sets, and Application to Chemical Shift Editing", *Magn. Reson. Med.*, vol. 18, 411-416, 1991.
- 3.65. P. Bendel, C.-M. Lai, and P.C. Lauterbur, "P-31 Spectroscopic Zeugmatography of Phosphorous Metabolites", *J. Magn. Reson.*, vol. 38, 343-356, 1980.
- 3.66. L.D. Hall, and S. Sukumar, "A New Image-Processing Method for NMR Chemical Microscopy", *J. Magn. Reson.*, vol. 56, 326-333, 1984.
- 3.67. L. Axel, G. Glover, and N. Pelc, "Chemical-Shift Magnetic Resonance Imaging of Two-Line Spectra by Gradient Reversal", *Magn. Reson. Med.*, vol. 2, 428-436, 1985.
- 3.68. A. Volk, B. Tiffon, J. Mispelter, and J.M. Lhoste, "Chemical Shift-Specific Slice Selection. A New Method for Chemical Shift Imaging at High Magnetic Field", *J. Magn. Reson.*, vol. 71, 168-174, 1987.
- 3.69. H.W. Park, D.J. Kim, and Z.H. Cho, "Gradient Reversal Technique and Its Applications to Chemical-Shift-Related NMR Imaging", *Magn. Reson. Med.*, vol. 4, 526-536, 1987.

- 3.70. L.D. Hall, and S. Sukumar, "Chemical Microscopy Using a High-Resolution NMR Spectrometer. A Combination of Tomography/Spectroscopy Using either H-1 or C-13", *J. Magn. Reson.*, vol. 50, 161-164, 1982.
- 3.71. L.D. Hall, and S. Sukumar, "Three Dimensional Fourier Transform NMR Imaging. High Resolution Chemical Shift Resolved Planar Imaging", *J. Magn. Reson.*, vol. 56, 314-317, 1984.
- 3.72. E.L. Hahn, and D.E. Maxwell, "Spin Echo Measurements of Nuclear Spin Coupling in Molecules", *Phys. Rev.*, vol. 88, 1070-1084, 1952.
- 3.73. A.G. Webb, S.C.R. Williams, and L.D. Hall, "Generation of Coupled Spin-Only Images Using Multiple-Echo Acquisition", *J. Magn. Reson.*, vol. 84, 159-165, 1989.
- 3.74. L.D. Hall, T.J. Norwood, and S.C.R. Williams, "Coupled-Spin-Filtered Imaging in an Inhomogeneous Magnetic Field", *J. Magn. Reson.*, vol. 79, 363-368, 1988.
- 3.75. C.L. Dumoulin, and D. Vatis, "Water Suppression in H-1 Magnetic Resonance Images by the Generation of Multiple-Quantum Coherence", *Magn. Reson. Med.*, vol. 3, 282-288, 1986.
- 3.76. C.L. Dumoulin, "Suppression of Water and Other Noncoupled Spins by Homonuclear Polarization Transfer in Magnetic Resonance Imaging", *Magn. Reson. Med.*, vol. 3, 90-96, 1986.
- 3.77. D.W. Kormos, and H.N. Yeung, "NMR Imaging of C-13 in Animal Tissues", *Magn. Reson. Med.*, vol. 4, 500-505, 1987.
- 3.78. M.I. Altbach, M.A. Mattingly, M.F. Brown, and A.F. Gmitro, "Magnetic Resonance Imaging of Lipid Deposits in Human Atheroma via a Stimulated-Echo Diffusion-Weighted Technique", *Magn. Reson. Med.*, vol. 20, 319-326, 1991.
- 3.79. R. Golfieri, H. Baddeley, J.S. Pringle, and R. Souhami, "The Role of the STIR Sequence in Magnetic Resonance Imaging Examination of Bone Tumours", *Br. J. Radiol.*, vol. 63, 251-256, 1990.
- 3.80. B. Tamler, F.G. Sommer, G.H. Glover, and E. Schneider, "Prostatic MR Imaging Performed with the Three-Point Dixon Technique", *Radiology*, vol. 179, 43-47, 1991.
- 3.81. H.-U. Kauczor, B. Dietl, G. Brix, M.V. Knopp, M. Wannemacher, G. van Kaick, and W. Semmler, "Radiation Induced Bone Marrow Damage in Hodgkin's Disease: Quantification of Long-Term Changes by Chemical Shift Imaging", *Abstr. 10th SMRM*, vol. 2, 959, 1991.

- 3.82. R.F. Thoeri, D.P. Gorczyca, and R. de Marco, "Fatsaturation Versus Spin Echo Imaging for Focal Liver Disease", *Abst. SMRM 10th Meeting*, vol. 1, 97, 1991.
- 3.83. M. Komu, A. Alanen, J. Tyrkko, and M. Alanen, "Preoperative Tissue Characterization with Chemical Shift Imaging: A Case Report of an Epidermal Cyst", *Magn. Reson. Imaging*, vol. 10, 161-163, 1992.
- 3.84. M. Moyle, T. Matsuda, and G.M. Pohost, "SLIP, A Lipid Suppression Technique to Improve Image Contrast in Inflow Angiography", *Magn. Reson. Med.*, vol. 21, 71-81, 1991.
- 3.85. C.H. Meyer, J.M. Pauly, A. Macovski, and D.G. Nishimura, "Simultaneous Spatial and Spectral Selective Excitation", *Magn. Reson. Med.*, vol. 15, 287-304, 1990.
- 3.86. J. Szumowski, J.K. Eisen, S. Vinitzki, P.W. Haake, and D.B. Plewes, "Hybrid Methods of Chemical-Shift Imaging", *Magn. Reson. Med.*, vol. 9, 379-388, 1989.
- 3.87. S. Vinitzki, D.G. Mitcell, J. Szumowski, D.L. Burk, and M.D. Rifkin, "Variable Flip Angle Imaging and Fat Suppression in Combined Gradient and Spin-Echo (GREASE) Techniques", *Magn. Reson. Imaging*, vol. 8, 131-139, 1990.
- 3.88. D.N. Guilfoyle, and P. Mansfield, "Chemical-Shift Imaging", *Magn. Reson. Med.*, vol. 2, 479-489, 1985.
- 3.89. D.N. Guilfoyle, A. Blamire, B. Chapman, R.J. Ordidge, and P. Mansfield, "PEEP. A Rapid Chemical-Shift Imaging Method", *Magn. Reson. Med.*, vol. 10, 282-287, 1989.
- 3.90. D.B. Twieg, "Multiple-Output Chemical Shift Imaging (MOSCI): A Practical Technique for Rapid Spectroscopic Imaging", *Magn. Reson. Med.*, vol. 12, 64-73, 1989.
- 3.91. A. Haase, "Snapshot FLASH MRI. Applications to T₁, T₂, and Chemical-Shift Imaging", *Magn. Reson. Med.*, vol. 13, 77-89, 1990.

CHAPTER 4

- 4.1. P.J. Keller, W.W. Hunter, and P. Schmalbrock, "Multisection Fat-Water Imaging with Chemical Shift Selective Presaturation", *Radiology*, vol. 164, 539-541, 1987.
- 4.2. A.M.K. Simmons, "Segmentation of Neuroanatomy in Magnetic Resonance Images", Ph.D. Thesis, University of London, 1992.

- 4.3. P.A. Bottomley, and E.R. Andrew, "RF Magnetic Field Penetration, Phase Shift and Power Dissipation in Biological Tissue: Implications for NMR Imaging", *Phys. Med. Biol.*, vol. 23, 630-643, 1978.
- 4.4. P.A. Bottomley, and W.A. Edelstein, "Power Deposition in Whole-Body NMR Imaging", *Med. Phys.*, vol. 8, 510-512, 1981.
- 4.5. E.L. Hahn, "An Accurate Nuclear Magnetic Resonance Method for Measuring Spin-Lattice Relaxation Times", *Phys. Rev.*, vol. 76, 145-146, 1949.
- 4.6. L.L. Baker, S.B. Goodman, I. Perkash, B. Lane, and D.R. Enzmann, "Benign versus Pathologic Compression Fractures of Vertebral Bodies: Assessment with Conventional Spin-Echo, Chemical-Shift, and STIR MR Imaging", *Radiology*, vol. 174, 495-502, 1990.
- 4.7. R.F. Thoeni, D.P. Gorczyca, and R. de Marco, "Fatsaturation versus Spin Echo Imaging for Focal Liver Disease", *Abst. 10th SMRM*, vol. 1, 97, 1991.
- 4.8. J. Mao, H. Yan, W.W. Brey, W.D. Bidgood Jr., J.J. Steinbach, and A. Mancuso, "Fat Tissue and Fat Suppression", *Magn. Reson. Imaging*, vol. 11, 385-393, 1993.
- 4.9. C.J.G. Bakker, and J. Vriend, "Multi-Exponential Water Proton Spin-Lattice Relaxation in Biological Tissues and Its Implications for Quantitative NMR Imaging", *Phys. Med. Biol.*, vol. 29, 509-518, 1984.
- 4.10. J.V. Hajnal, B. de Coene, P.D. Lewis, C.J. Baudouin, F.M. Cowan, J.M. Pennock, I.R. Young, and G.M. Bydder, "High Signal Regions in Normal White Matter Shown by Heavily T₂-Weighted CSF Nulled IR Sequences", *J. Comput. Assist. Tomogr.*, vol. 16, 506-513, 1992.
- 4.11. B. de Coene, J. V. Hajnal, P. Gatehouse, D.B. Longmore, S.J. White, A. Oatridge, J.M. Pennock, I.R. Young, and G.M. Bydder, "MR of the Brain Using Fluid-Attenuated Inversion Recovery (FLAIR) Pulse Sequences", *AJNR*, vol. 13, 1555-1564, 1992.

CHAPTER 5

- 5.1. B.R. Rosen, V.J. Wedeen, and T.J. Brady, "Selective Saturation NMR Imaging", *J. Comput. Assist. Tomogr.*, vol. 8, 813-818, 1984.
- 5.2. A. Haase, J. Frahm, W. Hanicke, and D. Matthaei, "H-1 NMR Chemical Shift Selective (CHESS) Imaging", *Phys. Med. Biol.*, vol. 30, 341-344, 1985.
- 5.3. P.J. Keller, W.W. Hunter, and P. Schmalbrock, "Multisection Fat-Water Imaging with Chemical Shift Selective Presaturation", *Radiology*, vol. 164, 539-541, 1987.

- 5.4. M.A. Foster, J.M.S. Hutchison, J.R. Mallard, and M. Fuller, "Nuclear Magnetic Resonance Pulse Sequence and Discrimination of High- and Low-Fat Tissues", *Magn. Reson. Imaging*, vol. 2, 187-192, 1984.
- 5.5. G.M. Bydder, and I.R. Young, "MR Imaging: Clinical Use of the Inversion Recovery Sequence", *J. Comput. Assist. Tomogr.*, vol. 9, 659-675, 1985.
- 5.6. J.V. Hajnal, B. De Coene, P.D. Lewis, C.J. Baudouin, F.M. Cowan, J.M. Pennock, I.R. Young, and G.M. Bydder, "High Signal Regions in Normal White Matter Shown by Heavily T₂-Weighted CSF Nulled Sequence", *J. Comput. Assist. Tomogr.*, vol. 16, 506-513, 1992.
- 5.7. B. De Coene, J.V. Hajnal, P. Gatehouse, D.B. Longmore, S.J. White, A. Oatridge, J.M. Pennock, I.R. Young, and G.M. Bydder, "MR of the Brain Using Fluid-Attenuated Inversion Recovery (FLAIR) Pulse Sequences", *AJNR*, vol. 13, 1555-1564, 1992.
- 5.8. C.H. Oh, S.K. Hilal, and Z.H. Cho, "Selective Partial Inversion Recovery (SPIR) in Steady State for Selective Saturation Magnetic Resonance Imaging (MRI)", *Abstr. 7th SMRM*, vol. 2, 1042, 1988.
- 5.9. T.E. Merchant, G.R.P. Thelissen, H.C.E. Kievit, L.J.M.P. Oosterwaal, C.J.G. Bakker, and P.W. de Graaf, "Breast Disease Evaluation with Fat-Suppressed Magnetic Resonance Imaging", *Magn. Reson. Imag.*, vol. 10, 335-340, 1992.
- 5.10. H.W. Park, M.H. Cho, and Z.H. Cho, "Time-Multiplexed Multislice Inversion-Recovery Techniques for NMR Imaging", *Magn. Reson. Med.*, vol. 2, 534-539, 1985.
- 5.11. G. Johnson, D.H. Miller, D. MacManus, P.S. Tofts, D. Barnes, E.P.G.H. du Boulay, and W.I. McDonald, "STIR Sequences in NMR Imaging of the Optic Nerve", *Neuroradiology*, vol. 29, 238-245, 1987.
- 5.12. L.D. Hall, S. Sukumar, and S.L. Talagala, "Chemical-Shift-Resolved Tomography Using Frequency-Selective Excitation and Suppression of Specific Resonances", *J. Magn. Reson.*, vol. 56, 275-278, 1984.
- 5.13. E.L. Hahn, "An Accurate Nuclear Magnetic Resonance Method for Measuring Spin-Lattice Relaxation Times", *Phys. Rev.*, vol. 76, 145-146, 1949.
- 5.14. J.C. Miller, and J.N. Miller, "Statistics for Analytical Chemistry", Ellis Horwood Ltd., 1988.
- 5.15. R.M. Henkelman, "Measurement of Signal Intensities in the Presence of Noise in MR Images", *Med. Phys.*, vol. 12, 232-233, 1985.
- 5.16. P.S. Tofts, and G. Johnson, "Correction for Rayleigh Noise in an NMR Magnitude Image when Measuring T₂ at Low Values of Signal-to-Noise Ratio", *Abstr. 5th SMRM*, vol. 2, 1450-1451, 1986.

- 5.17. R.C. Semelka, M. Kroeker, J.P. Shoenut, F.C. Simm, H.M. Greenberg, and A.B. Micflikier, "MRI of the Liver: T₂-Weighted Fat Suppression, Breath-Hold FLASH and Dynamic Gd-DTPA Enhanced FLASH at 1.5T with Comparison to CT in 40 Patients", Abstr. 10th SMRM, vol. 1, 99, 1991.
- 5.18. H. Hiramatsu, K. Oshio, E.D. Waitzkin, T.H. Frenna, C.M. Denison, J.E. Meyer, D.F. Adams, and F.A. Jolesz, "High Resolution Breast Imaging Using T₁/T₂ RARE with Fat Suppression", Abstr. 12th SMRM, vol. 2, 860, 1993.

CHAPTER 6

- 6.1. P.A. Bottomley, T.H. Foster, R.E. Argersinger, and L.M. Pfeifer, "A Review of Normal Tissue Hydrogen NMR Relaxation Times and Relaxation Mechanisms from 1-100 MHz: Dependence on Tissue Type, NMR Frequency, Temperature, Species, Excision, and Age", *Med. Phys.*, vol. 11, 425-448, 1984.
- 6.2. D.S. Hickey, D. Checkley, R.M. Aspden, A. Naughton, J.P.R. Jenkins, and L. Isherwood, "A Method for the Clinical Measurement of Relaxation Times in Magnetic Resonance Imaging", *Br. J. Radiology*, vol. 59, 565-576, 1986.
- 6.3. G. Johnson, D.H. Miller, D. MacManus, P.S. Tofts, D. Barnes, E.P.G.H. du Boulay, and W.I. McDonald, "STIR Sequences in NMR Imaging of the Optic Nerve", *Neuroradiol.*, vol. 29, 238-245, 1987.
- 6.4. S.E. Dockery, S.A. Suddarth, and G.A. Johnson, "Relaxation Measurements at 300 MHz Using MR Microscopy", *Magn. Reson. Med.*, vol. 11, 182-192, 1989.
- 6.5. R. Damadian, "Tumor Detection by Nuclear Magnetic Resonance", *Science*, vol. 171, 1151-1153, 1971.
- 6.6. C.F. Hazlewood, D.C. Chang, D. Medina, G. Cleveland, and B.L. Nichols, "Distinction Between the Preneoplastic and Neoplastic State of Murine Mammary Glands", *Proc. Nat. Acad. Sci. USA*, vol. 69, 1478-1480, 1972.
- 6.7. H.E. Deans, F.W. Smith, D.J. Lloyd, A.N. Law, and H.W. Sutherland, "Fetal Fat Measurement by Magnetic Resonance Imaging", *Br. J. Radiology*, vol. 62, 603-607, 1989.
- 6.8. C. Schwarzbauer, J. Syha, and A. Haase, "Quantification of Regional Blood Volume by Rapid T₁ Mapping", *Magn. Reson. Med.*, vol. 29, 709-712, 1993.
- 6.9. W.H. Perman, S.K. Hilal, H.E. Simon, and A.A. Maudsley, "Contrast Manipulation in NMR Imaging", *Magn. Reson. Imaging*, vol. 2, 23-32, 1984.
- 6.10. K.J. van Lom, J.J. Brown, W.H. Perman, J.C. Sandstrom, and J.K.T. Lee, "Liver Imaging at 1.5 Tesla: Pulse Sequence Optimization Based on Improved

- Measurement of Tissue Relaxation Times", *Magn. Reson. Imaging*, vol. 9, 165-171, 1991.
- 6.11. G.M. Bydder, and I.R. Young, "MR Imaging: Clinical Use of the Inversion Recovery Sequence", *J. Comput. Assist. Tomogr.*, vol. 9, 659-675, 1985.
 - 6.12. J.V. Hajnal, B. de Coene, P.D. Lewis, C.J. Baudouin, F.M. Cowan, J.M. Pennock, I.R. Young, and G.M. Bydder, "High Signal Regions in Normal White Matter Shown by Heavily T₂-Weighted CSF Nulled IR Sequences", *J. Comput. Assist. Tomogr.*, vol. 16, 506-513, 1992.
 - 6.13. S.A. Bobman, S.J. Riederer, J.N. Lee, T. Tasciyan, F. Farzaneh, and H.Z. Wang, "Pulse Sequence Extrapolation with MR Image Synthesis", *Radiology*, vol. 159, 253-258, 1986.
 - 6.14. I. Solomon, "Relaxation Processes in a System of Two Spins", *Phys. Rev.*, vol. 99, 559-565, 1955.
 - 6.15. H. Perrimond, C. Chagnon, I. Moulanier, G. Michel, H. Guidicelli, and P.J. Bernard, "[The Value of Nuclear Magnetic Resonance in the Study of Iron Overload in Thalassemia Patients]", *Ann. Pediatr. Paris*, vol. 38, 175-184, 1991.
 - 6.16. G.K. Radda, "Ions, Control and Disease", *Book of Abstr., NMR: New Applications to Materials and Medical Imaging*, The British Radio Spectroscopy Group, University of Nottingham, 1992.
 - 6.17. G. Bartzokis, J. Mintz and W. Oldendorf, "Brain Iron Levels Correlate with Field Dependent T₂ Relaxation Time Shortening", *Abst. 10th SMRM*, #1264, 1991.
 - 6.18. J.C. Gore, Y.S. Kang, and R.J. Schulz, "Measurement of Radiation Dose Distributions by Nuclear Magnetic Resonance", *Phys. Med. Biol.*, vol. 29, 1189-1197, 1984.
 - 6.19. M.B. Podgorsak, and L.J. Schreiner, "Nuclear Magnetic Relaxation Characterization of Irradiated Fricke Solution", *Med. Phys.*, vol. 19, 87-95, 1992.
 - 6.20. M.J. Maryanski, J.C. Gore, R.P. Kennan, and R.J. Schulz, "NMR Relaxation Enhancement in Gels Polymerized and Cross-Linked by Ionizing Radiation: A New Approach to 3D Dosimetry by MRI", *Magn. Reson. Imaging*, vol. 11, 253-258, 1993.
 - 6.21. D.L. Parker, V. Smith, P.Sheldon, L.E. Crooks, and L. Fussell, "Temperature Distribution Measurements in Two-Dimensional NMR Imaging", *Med. Phys.*, vol. 10, 321-325, 1983.

- 6.22. R.J. Dickinson, A.S. Hall, A.J. Hind, and I.R. Young, "Measurement of Changes in Tissue Temperature Using MR Imaging", *J. Comput. Assist. Tomogr.*, vol. 10, 468-472, 1986.
- 6.23. A.S. Hall, M.V. Prior, J.W. Hand, I.R. Young, and R.J. Dickinson, "Observation by MR Imaging of In Vivo Temperature Changes Induced by Radio Frequency Hyperthermia", *J. Comput. Assist. Tomogr.*, vol. 14, 430-436, 1990.
- 6.24. J.J. Attard, T.A. Carpenter, L.D. Hall, S. Davies, M.J. Taylor, and K.J. Packer, "Spatially Resolved T₁ Relaxation Measurements in Reservoir Cores", *Magn. Reson. Imaging*, vol. 9, 815-819, 1991.
- 6.25. P.A. Bottomley, C.J. Hardy, R.E. Argersinger, and G. Allen-Moore, "A Review of H-1 Nuclear Magnetic Resonance Relaxation in Pathology: Are T₁ and T₂ Diagnostic?", *Med. Phys.*, vol. 14, 1-36, 1987.
- 6.26. P.S. Tofts, and E.P.G.H. du Boulay, "Towards Quantitative Measurements of Relaxation Times and Other Parameters in the Brain", *Neuroradiol.*, vol. 32, 407-415, 1990.
- 6.27. T. Andersson, A. Ericsson, B. Eriksson, A. Hemmingsson, E. Lindh, R. Nyman, and K. Oberg, "Relative Proton Density and Relaxation Times in Liver Metastases during Interferon Treatment", *Br. J. Radiology*, vol. 62, 433-437, 1989.
- 6.28. I.L. Pykett, and P. Mansfield, "A Line Scan Image Study of a Tumorous Rat Leg by NMR", *Phys. Med. Biol.*, vol. 23, 961-967, 1978.
- 6.29. R. Freeman, and H.D.W. Hill, "Fourier Transform Study of NMR Spin-Lattice Relaxation by Progressive Saturation", *J. Chem. Phys.*, vol. 54, 3367-3377, 1971.
- 6.30. L.E. Crooks, D.A. Ortendahl, L. Kaufman, J. Hoenninger, M. Arakawa, J. Watts, C.R. Cannon, M. Brant-Zawadski, P.L. Davis, and A.R. Margulis, "Clinical Efficiency of Nuclear Magnetic Resonance Imaging", *Radiology*, vol. 146, 123-128, 1983.
- 6.31. J. Gong, and J.P. Hornak, "A Fast T₁ Algorithm", *Magn. Reson. Imaging*, vol. 10, 623-626, 1992.
- 6.32. G.O. Sperber, A. Ericsson and A. Hemmingsson, "A Fast Method for T₁ Fitting", *Magn. Reson. Med.*, vol. 9, 113-117, 1989.
- 6.33. A. Jesmanowicz, E.C. Wong, J.C. Wu, and J.S. Hyde, "Fast Algorithm for Computation of T₁, T₂ and Diffusion Coefficient Images", *Abst. 10th SMRM*, vol. 1, 740, 1991.

- 6.34. J.L. Markley, W.J. Horsley, and M.P. Klein, "Spin-Lattice Relaxation Measurements in Slowly Relaxing Complex Spectra", *J. Chem. Phys.*, vol. 55, 3604-3605, 1971.
- 6.35. G.G. McDonald, and J.S. Leigh Jr., "A New Method for Measuring Longitudinal Relaxation Times", *J. Magn. Reson.*, vol. 9, 358-362, 1973.
- 6.36. E.L. Hahn, "An Accurate Nuclear Magnetic Resonance Method for Measuring Spin-Lattice Relaxation Times", *Phys. Rev.*, vol. 76, 145-146, 1949.
- 6.37. D. Canet, G.C. Levy, and I.R. Peat, "Time Saving in C-13 Spin-Lattice Relaxation Measurements by Inversion-Recovery", *J. Magn. Reson.*, vol. 18, 199-204, 1975.
- 6.38. H.W. Park, M.H. Cho, and Z.H. Cho, "Time-Multiplexed Multislice Inversion-Recovery Techniques for NMR Imaging", *Magn. Reson. Med.*, vol. 2, 534-539, 1985.
- 6.39. C.H. Oh, S.K. Hilal, I.K. Mun, and Z.H. Cho, "An Optimized Multislice Acquisition Sequence for the Inversion-Recovery MR Imaging", *Magn. Reson. Imaging*, vol. 9, 903-908, 1991.
- 6.40. I.R. Young, D.R. Bailes, and G.M. Bydder, "Apparent Changes of Appearance of Inversion-Recovery Images", *Magn. Reson. Med.*, vol. 2, 81-85, 1985.
- 6.41. C.J.G. Bakker, C.N. de Graaf, and P. van Dijk, "Restoration of Signal Polarity in a Set of Inversion Recovery NMR Images", *IEEE Trans. Med. Imaging*, vol. MI-3, 197-202, 1984.
- 6.42. P.A. Gowland, and M.O. Leach, "A Simple Method for the Restoration of Signal Polarity in Multi-Image Inversion Recovery Sequences for Measuring T_1 ", *Magn. Reson. Med.*, vol. 18, 224-231, 1991.
- 6.43. H.W. Park, M.H. Cho, and Z.H. Cho, "Real-Value Representation in Inversion-Recovery NMR Imaging by Use of a Phase-Correction Method", *Magn. Reson. Med.*, vol. 3, 15-23, 1986.
- 6.44. J.A. Borrello, T.L. Chenevert, and A.M. Aisen, "Regional Phase Correction of Inversion-Recovery MR Images", *Magn. Reson. Med.*, vol. 14, 56-67, 1990.
- 6.45. G.H. Weiss, R.K. Gupta, J.A. Ferretti, and E.D. Becker, "The Choice of Optimal Parameters for Measurement of Spin-Lattice Relaxation Times. I. Mathematical Formulation", *J. Magn. Reson.*, vol. 37, 369-379, 1980.
- 6.46. E.D. Becker, J.A. Ferretti, R.K. Gupta, and G.H. Weiss, "The Choice of Optimal Parameters for Measurement of Spin-Lattice Relaxation Times. II. Comparison of Saturation Recovery, Inversion Recovery, and Fast-Inversion Recovery Experiments", *J. Magn. Reson.*, vol. 37, 381-394, 1980.

- 6.47. H. Hanssum, "Optimization of Fast Inversion-Recovery Fourier Transform Experiments", *J. Magn. Reson.*, vol. 45, 461-475, 1981.
- 6.48. R. Freeman, H.D.W. Hill, and R. Kaptein, "An Adaptive Scheme for Measuring NMR Spin-Lattice Relaxation Times", *J. Magn. Reson.*, vol. 7, 82-98, 1972.
- 6.49. M.S. Lin, J.W. Fletcher, and R.M. Donati, "Two-Point T₁ Measurement: Wide-Coverage Optimizations by Stochastic Simulations", *Magn. Reson. Med.*, vol. 3, 518-533, 1986.
- 6.50. W.A. Edelstein, J.M.S. Hutchison, G. Johnson, and T. Redpath, "Spin Warp NMR Imaging and Applications to Human Whole-Body Imaging", *Phys. Med. Biol.*, vol. 25, 751-756, 1980.
- 6.51. T.W. Redpath, "Calibration of the Aberdeen NMR Imager for Proton Spin-Lattice Relaxation Time Measurements In Vivo", *Phys. Med. Biol.*, vol. 27, 1057-1065, 1982.
- 6.52. G.N.H. Waller, S.C.R. Williams, M.J. Cookson, and E. Kaldoudi, "Preliminary Analysis of Elasmobranch Tissue Using Magnetic Resonance Imaging", *Magn. Reson. Imaging* (in press)
- 6.53. R.K. Gupta, "A New Look at the Method of Variable Nutation Angle for the Measurement of Spin-Lattice Relaxation Times Using Fourier Transform NMR", *J. Magn. Reson.*, vol. 25, 231-235, 1977.
- 6.54. E.K. Fram, R.J. Herfkens, G.A. Johnson, G.H. Glover, J.P. Karis, A. Shimakawa, T.G. Perkins and N.J. Pelc, "Rapid Calculation of T₁ Using Variable Flip Angle Gradient Refocused Imaging", *Magn. Reson. Imaging*, vol. 5, 201-208, 1987.
- 6.55. J. Homer, and M.S. Beevers, "Driven-Equilibrium Single-Pulse Observation of T₁ Relaxation. A Reevaluation of a Rapid 'New' Method for Determining NMR Spin-Lattice Relaxation Times", *J. Magn. Reson.*, vol. 63, 287-297, 1985.
- 6.56. H.Z. Wang, S.J. Riederer, and J.N. Lee, "Optimizing the Precision in T₁ Relaxation Estimation Using Limited Flip Angles", *Magn. Reson. Med.*, vol. 5, 399-416, 1987.
- 6.57. J. Frahm, K.D. Merboldt, W. Hanicke, and A. Haase, "Stimulated Echo Imaging", *J. Magn. Reson.*, vol. 64, 81-93, 1985.
- 6.58. W. Sattin, T.H. Mareci, and K.N. Scott, "Exploiting the Stimulated Echo in Nuclear Magnetic Resonance Imaging. I. Method", *J. Magn. Reson.*, vol. 64, 177-182, 1985.

- 6.59. W. Sattin, T.H. Mareci, and K.N. Scott, "Exploiting the Stimulated Echo in Nuclear Magnetic Resonance Imaging. II. Applications", *J. Magn. Reson.*, vol. 65, 298-307, 1985.
- 6.60. A. Haase, and J. Frahm, "NMR Imaging of Spin-Lattice Relaxation Using Stimulated Echoes", *J. Magn. Reson.*, vol. 65, 481-490, 1985.
- 6.61. T.H. Mareci, W. Sattin, and K.N. Scott, "Tip-Angle-Reduced T₁ imaging", *J. Magn. Reson.*, vol. 67, 55-65, 1986.
- 6.62. G.J. Barker, and T.H. Mareci, "Suppression of Artifacts in Multiple-Echo Magnetic Resonance", *J. Magn. Reson.*, vol. 83, 11-28, 1989.
- 6.63. D.C. Look, and D.R. Locker, "Time Saving in Measurement of NMR and EPR Relaxation Times", *Rev. Sci. Instrum.*, vol. 41, 250-251, 1970.
- 6.64. W.H. Hinson, and W.T. Sobol, "A New Method of Computing Spin-Lattice Relaxation Maps in Magnetic Resonance Imaging Using Fast Scanning Protocols", *Med. Phys.*, vol. 15, 551-561, 1988.
- 6.65. R. Kaptein, K. Dijkstra, and C.E. Tarr, "A Single-Scan Fourier Transform Method for Measuring Spin-Lattice Relaxation Times", *J. Magn. Reson.*, vol. 24, 295-300, 1976.
- 6.66. R. Graumann, M. Deimling, T. Heilmann, and A. Oppelt, "A New Method for Fast and Precise T₁ Determination", *Abstr. 5th SMRM*, p. 922-923, 1986.
- 6.67. G. Brix, L.R. Schad, M. Deimling, and W.J. Lorenz, "Fast and Precise T₁ Imaging Using a TOMROP Sequence", *Magn. Reson. Imaging*, vol. 8, 351-356, 1990.
- 6.68. I. Kay, and R.M. Henkelman, "Practical Implementation and Optimization of One-Shot T₁ Imaging", *Magn. Reson. Med.*, vol. 22, 414-424, 1991.
- 6.69. Y.T. Zhang, H.N. Yeung, P.L. Carson, and J.H. Ellis, "Experimental Analysis of T₁ Imaging with a Single-Scan, Multiple-Point, Inversion-Recovery Technique", *Magn. Reson. Med.*, vol. 25, 337-343, 1992.
- 6.70. P.A. Gowland, and M.O. Leach, "Fast and Accurate Measurements of T₁ Using a Multi-Readout Single Inversion-Recovery Sequence", *Magn. Reson. Med.*, vol. 26, 79-88, 1992.
- 6.71. A.P. Crawley, and R.M. Henkelman, "A Comparison of One-Shot and Recovery Methods in T₁ Imaging", *Magn. Reson. Med.*, vol. 7, 23-34, 1988.
- 6.72. J.N. Lee, and S.J. Riederer, "The Contrast-to-Noise in Relaxation Time, Synthetic, and Weighted-Sum MR Images", *Magn. Reson. Med.*, vol. 5, 13-22, 1987.
- 6.73. I.R. Young, A.S. Hall, and G.M. Bydder, "The Design of a Multiple Inversion Recovery Sequence for T₁ Measurement", *Magn. Reson. Med.*, vol. 5, 99-108, 1987.

- 6.74. B.R. Rosen, I.L. Pykett, and T.J. Brady, "Spin Lattice Relaxation Time Measurements in Two-Dimensional Nuclear Magnetic Resonance Imaging: Corrections for Plane Selection and Pulse Sequence", *J. Comput. Assist. Tomogr.*, vol. 8, 195-199, 1984.
- 6.75. C.J.G. Bakker, C.N. de Graaf, and P. van Dijk, "Derivation of Quantitative Information in NMR Imaging: A Phantom Study", *Phys. Med. Biol.*, vol. 29, 1511-1525, 1984.
- 6.76. G.O. Sperber, A. Ericsson, A. Hemmingsson, B. Jung, and K.-A. Thuomas, "Improved Formulae for Signal Amplitudes in Repeated NMR Sequences: Applications in NMR Imaging", *Magn. Reson. Med.*, vol. 3, 685-698, 1986.
- 6.77. S.D. Wolff, and R.S. Balaban, "Magnetization Transfer Contrast (MTC) and Tissue Water Proton Relaxation in Vivo", *Magn. Reson. Med.*, vol. 10, 135-144, 1989.
- 6.78. W.T. Dixon, H. Engels, M. Castillo, and M. Sardashti, "Incidental Magnetization Transfer Contrast in Standard Multislice Imaging", *Magn. Reson. Imaging*, vol. 8, 417-422, 1990.
- 6.79. G.E. Santyr, "Magnetization Transfer Effects in Multislice MR Imaging", *Magn. Reson. Imaging*, vol. 11, 521-532, 1993.
- 6.80. C.J. Hardy, W.A. Edelstein, and O.M. Mueller, "Surface-Coil T₁ Images", *Magn. Reson. Med.*, vol. 3, 935-940, 1986.
- 6.81. J.L. Evelhoch, and J.J.H. Ackerman, "NMR T₁ Measurements in Inhomogeneous B₁ with Surface Coils", *J. Magn. Reson.*, vol. 53, 52-64, 1983.
- 6.82. M.H. Levitt, "Composite Pulses", *Progr. NMR Spectr.*, vol. 18, 61-122, 1986.
- 6.83. E. Gaggelli, and G. Valensin, "Methods of Single- and Double-Selective Excitation: Theory and Applications. Part I", *Concepts Magn. Reson.*, vol. 4, 339-360, 1992.
- 6.84. M. Garwood, and K. Ugurbil, "B₁ Insensitive Adiabatic RF Pulses", In: "NMR, Basic Principles and Progress", Eds. P. Diehl, E. Fluck, H. Gunther, R. Kosfeld, and J. Seelig, Springer-Verlag, vol. 26, 109-147, 1992.
- 6.85. C.J. Hardy, W.A. Edelstein, D. Vatis, R. Harms, and W.J. Adams, "Calculated T₁ Images Derived From a Partial Saturation-Inversion Recovery Pulse Sequence with Adiabatic Fast Passage", *Magn. Reson. Imaging*, vol. 3, 107-116, 1985.
- 6.86. M.S. Silver, R.I. Joseph, and D.I. Hoult, "Selective Spin Inversion in Nuclear Magnetic Resonance and Coherent Optics through an Exact Solution of the Bloch-Riccati Equation", *Phys. Rev. A*, vol. 31, 2753-2755, 1985.

- 6.87. P.A. Gowland, M.O. Leach, and J.C. Sharp, "The Use of an Improved Inversion Pulse with the Spin-Echo/Inversion-Recovery Sequence to Give Increased Accuracy and Reduced Imaging Time for T₁ Measurements", *Magn. Reson. Med.*, vol. 12, 261-267, 1989.
- 6.88. J. Mao, C. Virapongse, and J.R. Fitzsimmons, "A Study of Optimization of the Complex Hyperbolic Secant Inversion Pulses", *Magn. Reson. Med.*, vol. 13, 293-298, 1990.
- 6.89. M.D. Harpen, and J.P. Williams, "Longitudinal Relaxation Time Measurements with Non-Uniform Tilt Angles", *Phys. Med. Biol.*, vol. 31, 1229-1236, 1986.
- 6.90. I.R. Young, D.J. Bryant, and J.A. Payne, "Variations in Slice Shape and Absorption as Artifacts in the Determination of Tissue Parameters in NMR Imaging", *Magn. Reson. Med.*, vol. 2, 355-389, 1985.
- 6.91. D.W. McRobbie, R.A. Lerski, and K. Straughan, "Slice Profile Effects and Their Calibration and Correction in Quantitative NMR Imaging", *Phys. Med. Biol.*, vol. 32, 971-983, 1987.
- 6.92. M. Just, H.P. Higer, and P. Pfannenstiel, "Errors in T₁ Determination Using Multislice Technique and Gaussian Slice Profiles", *Magn. Reson. Imaging*, vol. 6, 53-56, 1988.
- 6.93. J.M.S. Hutchison, W.A. Edelstein, and G. Johnson, "A Whole-Body NMR Imaging Machine", *J. Phys. E: Sci. Instrum.*, vol. 13, 947-955, 1980.
- 6.94. F.S. Prato, D.J. Drost, T. Keys, P. Laxon, B. Comissiong, and E. Sestini, "Optimization of Signal-to-Noise Ratio in Calculated T₁ Images Derived from Two Spin-Echo Images", *Magn. Reson. Med.*, vol. 3, 63-75, 1986.
- 6.95. M.A. Smith, J.P. Ridgway, J.W.E. Brydon, M. Been, R.H.B. Douglas, D.M. Kean, A.L. Muir, and J.J.K. Best, "ECG-Gated T₁ Images of the Heart", *Phys. Med. Biol.*, vol. 3, 771-778, 1986.
- 6.96. F.W. Wehrli, "Fast-Scan Magnetic Resonance: Principles and Applications", *Magn. Reson. Quart.*, vol. 6, 165-236, 1990.
- 6.97. P. Mansfield, D.N. Guilfoyle, R.J. Ordidge, and R.E. Coupland, "Measurement of T₁ by Echo-Planar Imaging and the Construction of Computer-Generated Images", *Phys. Med. Biol.*, vol. 31, 113-124, 1986.
- 6.98. M.K. Stehling, R.J. Ordidge, R. Coxon, and P. Mansfield, "Inversion-Recovery Echo-Planar Imaging (IR-EPI) at 0.5 T", *Magn. Reson. Med.*, vol. 13, 514-517, 1990.
- 6.99. A. Haase, "Snapshot FLASH MRI. Applications to T₁, T₂, and Chemical-Shift Imaging", *Magn. Reson. Med.*, vol. 13, 77-89, 1990.

- 6.100. S. Nekolla, T. Gneiting, J. Syha, R. Deichmann, and A. Haase, "Improving T₁ Determination in MRI by k-Space-Reduced Snapshot-FLASH Images", Abstr. 10th SMRM, # 1216, 1991.

CHAPTER 7

- 7.1. N.J. Clayden, and B.D. Hesler, "Multiexponential Analysis of Relaxation Decays", *J. Magn. Reson.*, vol. 98, 271-282, 1992.
- 7.2. P.A. Bottomley, T.H. Foster, R.E. Argersinger, and L.M. Pfeifer, "A Review of Normal Tissue Hydrogen NMR Relaxation Times and Relaxation Mechanisms from 1-100 MHz: Dependence on Tissue Type, NMR Frequency, Temperature, Species, Excision, and Age", *Med. Phys.*, vol. 11, 425-448, 1984.
- 7.3. C.J.G. Bakker, and J. Vriend, "Multi-Exponential Water Proton Spin-Lattice Relaxation in Biological Tissues and Its Implications for Quantitative NMR Imaging", *Phys. Med. Biol.*, vol. 29, 509-518, 1984.
- 7.4. J. Mao, H. Yan, W.W. Brey, W.D. Bidgood Jr., J.J. Steinbach, and A. Mancuso, "Fat Tissue and Fat Suppression", *Magn. Reson. Imaging*, vol. 11, 385-393, 1993.
- 7.5. R.L. Kamman, C.J.G. Bakker, P. van Dijk, G.P. Stomp, A.P. Heiner, and H.J.C. Berendsen, "Multi-Exponential Relaxation Analysis with MR Imaging and NMR Spectroscopy Using Fat-Water Systems", *Magn. Reson. Imaging*, vol. 5, 381-392, 1987.
- 7.6. C. Schwarzbauer, J. Syha, and A. Haase, "Quantification of Regional Blood Volume by Rapid T₁ Mapping", *Magn. Reson. Med.*, vol. 29, 709-712, 1993.
- 7.7. R.B. Buxton, G.L. Wismer, T.J. Brady, and B.R. Rosen, "Quantitative Proton Chemical-Shift Imaging", *Magn. Reson. Med.*, vol. 3, 881-900, 1986.
- 7.8. C.S. Poon, J. Szumowski, D.B. Plewes, P. Ashby, and R.M. Henkelman, "Fat/Water Quantitation and Differential Relaxation Time Measurement Using Chemical Shift Imaging Technique", *Magn. Reson. Imaging*, vol. 7, 369-382, 1989.
- 7.9. J.P. Hornak, A.C. Smith, and J. Szumowski, "Spin-Lattice Relaxation Time Measurements Using a Hybrid CSI - Phantom Study", *Magn. Reson. Med.*, vol. 13, 398-406, 1990.
- 7.10. A.E. Lamminen, J.I. Tantt, R.E. Sepponen, I.J.I. Suramo, and H. Pihko, "Magnetic Resonance of Diseased Skeletal Muscle: Combined T₁ Measurements and Chemical Shift Imaging", *Br. J. Radiology*, vol. 63, 591-596, 1990.

- 7.11. W.A. Edelstein, J.M.S. Hutchison, G. Johnson, and T. Redpath, "Spin Warp NMR Imaging and Applications to Human Whole-Body Imaging", *Phys. Med. Biol.*, vol. 25, 751-756, 1980.
- 7.12. L.D. Hall, S. Sukumar, and S.L. Talagala, "Chemical-Shift-Resolved Tomography Using Frequency-Selective Excitation and Suppression of Specific Resonances", *J. Magn. Reson.*, vol. 56, 275-278, 1984.
- 7.13. P.M. Joseph, "A Spin Echo Chemical Shift Imaging Technique", *J. Comput. Assist. Tomogr.*, vol. 9, 651-658, 1985.
- 7.14. M.S. Lin, J.W. Fletcher, and R.M. Donati, "Two-Point T₁ Measurement: Wide-Coverage Optimizations by Stochastic Simulations", *Magn. Reson. Med.*, vol. 3, 518-533, 1986.
- 7.15. E.L. Hahn, "An Accurate Nuclear Magnetic Resonance Method for Measuring Spin-Lattice Relaxation Times", *Phys. Rev.*, vol. 76, 145-146, 1949.
- 7.16. P.A. Gowland, and M.O. Leach, "A Simple Method for the Restoration of Signal Polarity in Multi-Image Inversion Recovery Sequences for Measuring T₁", *Magn. Reson. Med.*, vol. 18, 224-231, 1991.
- 7.17. M.H. Levitt, "Composite Pulses", *Progr. NMR Spectr.*, vol. 18, 61-122, 1986.
- 7.18. J. Baum, R. Tycko, and A. Pines, "Broadband and Adiabatic Inversion of a Two-Level System by Phase-Modulated Pulses", *Phys. Rev. A*, vol. 32, 3435-3447, 1985.
- 7.19. J.D. Bell, S.C.R. Williams, I.J. Cox, P.S. Belton, and J. Hope, "*In-vivo/In-vitro* NMR Studies of a Mouse Model of Scrapie", *Abstr. 10th SMRM*, vol. 1, 431, 1991.

APPENDICES

- A.1. D.I. Hoult, and R.E. Richards, "Critical Factors in the Design of Sensitive High Resolution Nuclear Magnetic Resonance Spectrometers", *Proc. Roy. Soc. Lond.*, vol. A344, 311-340, 1975.
- A.2. R. Graumann, A. Oppelt, and E. Stetter, "Multiple-Spin-Echo Imaging with a 2D Fourier Method", *Magn. Reson. Med.*, vol. 3, 707-721, 1986.
- A.3. S.W. Homans, "A Dictionary of Concepts in NMR", Clarendon Press, Oxford, 1989.
- A.4. D.D. Traficante, "Phase-Sensitive Detection. Part II: Quadrature Phase Detection", *Concepts Magn. Reson.*, vol. 2, 181-195, 1990.
- A.5. J.C. Miller, and J.N. Miller, "Statistics for Analytical Chemistry", Ellis Horwood Ltd., 1988.

- A.6. R.D. Remington, and M.A. Schork, "Statistics with Applications to the Biological and Health Sciences", Pentice-Hall, 1970, 2nd ed. 1985.